Lars Martin Sandvik Aas

Mueller Matrix Imaging and Spectroscopy

Thesis for the degree of Philosophiae Doctor

Trondheim, November 2013

Norwegian University of Science and Technology
The Faculty of Natural Sciences and Technology
Department of Physics

NTNU – Trondheim
Norwegian University of
Science and Technology

NTNU
Norwegian University of Science and Technology

Thesis for the degree of Philosophiae Doctor

The Faculty of Natural Sciences and Technology
Department of Physics

ISBN 978-82-471-4783-2 (printed ver.)
ISBN 978-82-471-4785-6 (electronic ver.)
ISSN 1503-8181

Doctoral theses at NTNU, 2013:323

Printed by NTNU-trykk

Abstract

This thesis presents experimental work on the following topics in Mueller matrix polarimetry; instrument design and implementation, and selected applications of liquid crystal based Mueller matrix polarimeters (MMP) and spectroscopic Mueller matrix ellipsometry (MME).

In particular MMPs were designed using ferroelectric liquid crystals (FLC) and liquid crystal variable retarders (LCVR) as polarization changing components. The polarimeters were optimized by using genetic algorithms with the system matrix condition numbers as figures of merit. A calibration routine was adapted to calibrate an overdetermined MMP based on LCVRs. The temporal response of the FLC based MMP was studied in order to investigate its potential as a high speed MMP.

The FLC based MMP was implemented as an imaging MMP. Applications studied with the imaging MMP were strain mapping in multi crystalline silicon, directional mapping of collagen fibers, polarizing properties of an anisotropic plasmonic polarizer and nematic textures in colloidal dispersions of synthetic clay.

Spectroscopic MME was used to study two types of nanopatterned plasmonic samples. Optical and structural properties of biaxial in plane gold nanowires were found through parametrization of the dielectric tensor of the layer. Strong localized surface plasmon resonances (LSPR) were found in the plane normal to the wires and in the plane along the wires. A small resonance was also found in the out of plane direction. The ellipsometric modelling allowed for determining parameters of the local geometry. Anisotropic Cu nanoparticles embedded in mixed oxide (Cu_2O and SiO_2) nanopillars were also studied using MME. Cu nanoparticles were localized as discs on the top, as droplets inside and as needles on the side of the nanopillars. MME allowed for detecting the splitting of the modes in wavelength and in $p-$ and $s-$polarized modes originating from the nanoparticle shapes.

Finally, measurement and modeling of GaSb nanopillars using spectroscopic MME allowed for the determination of small tilt angles of only a few degrees.

Preface

This dissertation is submitted as a partial fulfillment of the requirements for the degree of Philosophiae Doctor (Ph.D.) at the Norwegian University of Science and Technology (NTNU). The thesis is based on work performed at the Department of Physics, NTNU from August 2009 to September 2013. The work was supervised by Professor Morten Kildemo. Professor Mikael Lindgren served as a co-supervisor.

There are many people I would like to thank, some have contributed directly to this thesis, others were more important in motivating me through long days at work and short afternoons at home.

First of all I would like to express my gratitude to Morten, who learned me to do research. I could not have done it without you. Thank you for believing in me and giving the opportunity to work in your lab.

I am very much obliged to my fellow Ph.D. student and friend Pål G. Ellingsen, you have been a lifesaver during long days in the lab and over the computer. We have had many interesting projects and fruitful discussions together over the past four years.

The lunches and Friday beers would not have been the same without my other colleagues Jérôme, Ingar, Daniel, Zahra, Paul Anton and Tor. Thank you for making the optics group a fun place to work.

I am grateful to people from other labs whom I have been collaborating with over the last years: Mari, Mustafa, Mohammadreza, Donny, Turid, Francesco, Elin, Yann, Ellen, Kristin, Dag, Enric, Razvigor, Henrik, Elisabeth, Jon Otto, Øyvind and Magnus, thank you.

The master students I had the pleasure to learn to know and co-supervise, Kjetil, Bent Even, Erik, Andreas, Øystein and Thomas, thank you.

My family mamma Elin and pappa Øyvind, Paul Fredrik and Ottar, thank you for your unreserved trust and always believing in me.

Birgit, André, Lars-Kristian, Kristi and Svein, thank you for your support and patience.

Assi, you bring joy in my life, thank you for putting a smile on my face every day. You are an inspiration for dedicated work, success, kindness and love.

"The Norwegian Research Center for Solar Cell Technology" (project num. 193829) and all the people therein are acknowledged for my financial support and making this project possible.

List of papers

This section includes a complete list of papers resulting from the work conducted in the pursuit of the Ph.D. degree. For the reasoning of completeness, some papers were excluded from the thesis, they are still listed as *Papers not included in the thesis*. In order to fulfill §7.4 of the Ph.D. regulations of NTNU, the contribution of the authors are clarified in detail below each entry.

Paper 1

L. M. S. Aas, P. G. Ellingsen, M. Kildemo, and M. Lindgren, Dynamic Response of a fast near infra-red Mueller matrix ellipsometer, J. Mod. Optic. **57**, 1603–1610 (2010)

The paper is a study of the dynamic response of a ferroelectric liquid crystal-based Mueller matrix ellipsometer (MME). The time dependent intensity response of the MME is measured and simulated. The fast instrument allowed us to measure the temporal response of the Mueller matrix and the retardance of a liquid crystal variable retarder upon changing state.

The experimental work was performed by me and PGE. MK wrote a draft to the paper which I finalized and prepared for publication. ML took part in the final discussion.

Paper 2

P. A. Letnes, I. S. Nerbø, L. M. S. Aas, P. G. Ellingsen, and M. Kildemo, Fast and optimal broad-band Stokes/Mueller polarimeter design by the use of a genetic algorithm, Opt. Express **18**, 23095–23103 (2010)

The ideas to this paper came over lunch. PAL took a course in genetic programing and was looking for a practical problem to solve. The optimization of polarimeters turned out to be a suitable problem.

PAL was the main contributor to this paper, he wrote the Python code and wrote the parts of the paper related to genetic algorithm and the results. ISN wrote most of the other parts. I wrote about solutions for calibration of the overdetermined system. PGE and I used our own software to confirm the results. All authors took part in the discussions of the paper.

Paper 3

L. M. S. Aas, P. G. Ellingsen, B. E. Fladmark, P. A. Letnes, and M. Kildemo, Overdetermined broadband spectroscopic Mueller matrix polarimeter designed by genetic algorithms, Opt. Express **21**, 8753 (2013)

This paper took up the ideas of Paper 2 to realize the first "genetic polarimeter".

A new software was developed by PGE and PAL to optimize using in principle any polarization changing component, as long as the dispersion is known. BEF had a master project in our group. I supervised him in the lab and we realized this project together. I wrote the first draft to the paper, MK and PGE was helping with revisions.

Paper 4

L. M. S. Aas, D. G. Skåre, P. G. Ellingsen, P. A. Letnes, and M. Kildemo, Design, optimization and realization of FLC based Stokes polarimeters and Mueller matrix ellipsometer using a genetic algorithm, Preprint, subm. to Thin Solid Films (2013)

From Paper 2 we saw that it was possible to improve the commercially available MM16 Mueller matrix ellipsometer from *Horiba*.

The experimental work of the project was mainly performed by DGS. I wrote the paper, did the simulations and was in general involved in the instrumentation. The simulation code was written by PGE and PAL. MK took part in discussions in all parts of the project.

Paper 5

L. M. S. Aas, P. G. Ellingsen, and M. Kildemo, Near infra-red Mueller matrix imaging system and application to retardance imaging of strain, Thin Solid Films **519**, 2737–2741 (2010)

This paper demonstrates a near infrared Mueller matrix imager based on ferroelectric liquid crystal retarders, and the application to transmission imaging of strain in multi crystalline silicon.

I did the experimental work and wrote the paper, PGE and MK took part in the discussions and helping finalizing the paper.

Paper 6

L. M. S. Aas, I. S. Nerbø, M. Kildemo, D. Chiappe, C. Martella, and F. Buatier de Mongeot, Mueller matrix imaging of plasmonic polarizers on nanopatterned surface, Proc. SPIE **8082**, 80822W (2011)

The paper reports polarizing properties of an anisotropic nanopatterned film of gold nanoparticles on a SiO_2 substrate using transmission Mueller matrix imaging. The spatial homogeneity of polarizability, depolarization and retardance is studied.

ISN and I did the measurements and the analysis, and wrote the paper together. The samples were prepared by FBdM, DC and CM at the University of Genova. FBdM wrote the parts of the paper describing the sample preparation. MK took part in the discussions.

Paper 7

P. G. Ellingsen, M. B. Lilledahl, L. M. S. Aas, C. d. L. Davies, and M. Kildemo, Quantitative characterization of articular cartilage using Mueller matrix imaging and multiphoton microscopy, J. Biomed. Opt. **16**, 116002 (2011)

Collagen fiber meshworks in articular cartilage of chicken knee were studied using transmission Mueller matrix imaging and multiphoton microscopy. By looking on the collagen network as a birefringent effective medium the long axis of the fibers was analysed as the slow axis of the medium.

PGE and MBL wrote all parts of the paper. PGE took the Mueller matrix images and did the analysis of them, MBL did the multiphoton imaging. MK

and I took part in the discussions and analysis.

Paper 8

P. G. Ellingsen, L. M. S. Aas, V. S. Hagen, R. Kumar, M. B. Lilledahl, and M. Kildemo, Mueller matrix 3D directional imaging of collagen fibers, Preprint, subm. to J. Biomed. Opt. (2013)

Following up on Paper 7, where we here demonstrate three dimensional directional mapping of collagen fibers.

Most of the work was done by PGE. I took part in the discussion of and development of the model.

Paper 9

M. Kildemo, L. M. S. Aas, P. G. Ellingsen, H. Hemmen, E. L. Hansen, and J. O. Fossum, Mueller matrix imaging of nematic textures in colloidal dispersions of Na-fluorohectorite synthetic clay, Proc. SPIE **8082**, 808221 (2011)

Near infrared Mueller matrix imaging was used to study nematic textures in colloidal dispersions of synthetic clay particles. The particles organize into phases of strong birefringence. By analyzing the Mueller matrix images we find the orientation of the particles within ordered domains.

This paper was mainly written by MK. HH and ELH prepared the samples. I had the idea to this paper, did the measurements and made the figures. JOF read and commented the paper before submission.

Paper 10

L. M. S. Aas, M. Kildemo, Y. Cohin, and E. Søndergård, Determination of small tilt angles of short GaSb nanopillars using UV–visible Mueller matrix ellipsometry, Thin Solid Films **541**, 97–101 (2013)

Ultraviolet to infrared spectroscopic Mueller matrix ellipsometry was used to find small tilt angles of ~ 40 nm high GaSb nanopillars.

The measurement and analysis were made by me and MK. We also wrote the paper together. The samples were made in the lab of ES and YC.

Paper 11

K. Høydalsvik, L. M. S. Aas, E. Døli, E. Søndergård, M. Kildemo, and D. W. Breiby, Combining surface X-ray scattering and ellipsometry for non-destructive area-averaged characterisation of ion beam-induced GaSb surface nanostructures, Accepted for publication in Thin Solid Films (2013)

The paper explores the combination of surface X-ray scattering and Mueller matrix ellipsometry for the characterization of GaSb nanopillars.

ED and I wrote the first draft to this paper, which was finalized by KH. ED did the GISAXS measurements under the supervision of KH and DWB. I was responsible for the ellipsometry part of the paper.

Paper 12

L. M. S. Aas, , M. Kildemo, C. Martella, M. C. Giordano, D. Chiappe, and F. Buatier de Mongeot, Optical properties of biaxial nanopatterned gold plasmonic nanowired grid polarizer, Preprint, subm. to Opt. Express (2013)

Optical and structural properties of thermally deposited in plane gold nanowires on SiO_2 substrate were characterized by Mueller matrix ellipsometry.

The samples were prepared by FBdM, CM and DC. I did all measurements, analysis and wrote the paper.

Paper 13

Z. Ghadyani, M. Kildemo, L. M. S. Aas, Y. Cohin, and E. Søndergård, Spectroscopic Mueller matrix ellipsometry of plasmonic resonant Cu in mixed oxide nanopillars, Preprint, subm. to Opt. Express (2013)

The characterization of localized surface plasmon properties of Cu nano particles on oxide nano pillars is shown to be possible by Mueller matrix ellipsometry. I did all ellipsometry measurements, made several figures, took part in the discussions and revised the paper before submission. ZG did SEM and ellipsometry data analysis. MK did the analysis of the Mueller matrix measurements. MK and ZG wrote the paper together. ES and YC made the samples and did proofreading.

Papers not included in the thesis

Paper 14

M. Kildemo, J. Maria, P. G. Ellingsen, and L. M. S. Aas, Parametric model of the Mueller matrix of a Spectralon white reflectance standard deduced by polar decomposition techniques, Opt. Express **21**, 18509 (2013)

Paper 15

J. Maria, L. M. S. Aas, and M. Kildemo, In and out of incidence plane Mueller matrix scattering ellipsometry of rough mc-Si, Preprint, subm. to Thin Solid Films (2013)

Paper 16

O. Svensen, J. J. Stamnes, M. Kildemo, L. M. S. Aas, S. R. Erga, and O. Frette, Mueller matrix measurements of algae with different shape and size distributions, Appl. Opt. **50**, 5149–5157 (2011)

Paper 17

P. A. Letnes, I. S. Nerbø, L. M. S. Aas, P. G. Ellingsen, and M. Kildemo, Genetic invention of fast and optimal broad-band stokes/mueller polarimeter designs, in Proceedings of the 13th annual conference companion on Genetic and evolutionary computation, (2011), pp. 237–238

Contents

1. Introduction

Polarization is one of the fundamental properties of light. Most natural light sources emit light with a polarization which is not well defined. The light is then said to be unpolarized. Interactions with matter may change the polarization state. An every day example is the polarization of light upon reflection from a smooth surface. This effect can be used by *e.g.* sports fishermen and car drivers to block reflections from water surfaces using polarization filtering sunglasses. The same principal (the change of polarization by reflection) is used in the material characterization technique called ellipsometry.

Ellipsometry is a polarimetric technique, where polarimetry is the general method to measure the polarization state of light. Because the reflected polarization state depends on the refractive index of the reflecting material, ellipsometry has become the key technology to measure refractive indices. A modern ellipsometer can measure the polarization properties of the material in a range of wavelengths and incidence angles. By taking advantage of interference, which is an effect that can be observed as color variations on a thin film *e.g.* after a small oil spill on water, refractive indices and film thicknesses can be measured very precisely. The latter has made ellipsometry a key non-invasive technology in the semiconductor industry's chase after Moore's law [18].

With standard ellipsometry it is assumed that the materials under investigation are smooth and isotropic. If they are not isotropic, generalized or Mueller matrix ellipsometry must be employed [19, 20]. Some materials have intrinsic anisotropic properties originating from an anisotropic crystal lattice. Other originally isotropic materials can have an anisotropy induced by *e.g.* strain, or the local nanostructure. Nanostructures are objects of size ranging from one to a few hundred nanometers, *i.e.* larger than an atom, but smaller than what can be resolved optically. Nanoscience has received an increasing interest [21], mainly due to the possibility of tailoring properties which has been further enhanced through the development of production and characterization technology. In particular, the self-assembled nanostructures are promising due to

their cost efficiency and the potential for manufacturing large surface areas.

Advanced modeling allows generalized and Mueller matrix ellipsometry to be used to determine material compositions, dimension and shape of anisotropic nanostructures [22–25]. Ellipsometry is widely used as an *in-situ* characterization method for thin film and nano structure growth [22, 26, 27].

A more recent application of generalized and Mueller matrix ellipsometry is the characterization of plasmonic nanomaterials. Plasmons are collective oscillations of free electrons, which can, in the optical regime, be exited as propagating waves on the surface of noble metals such as gold and silver [28]. In nanostructured plasmonic materials the plasmons are localized. At the surface plasmon resonance (SPR) the electromagnetic field is enhanced and confined close to the surface making plasmonic material useful in non-linear optical technology [29,30] and sensor applications [31]. Commonly the plasmon resonance frequency is detected through enhanced absorption at the plasmon resonance. The absorption is, however, polarization dependent [28], making ellipsometry highly sensitive for the latter [32]. Designing novel plasmonic materials has received much recent attention, in particular due to the proven increased photon absorption and thus efficiency of photovoltaic devices covered by a plasmonic film [33]. Furthermore, anisotropic plasmonic materials [34,35] are metamaterial candidates for anomalous refractive materials [36, 37].

In biophysical characterization, optical methods have become important. But, even though many biological samples have typical polarization signatures, polarization sensitive characterization methods are not commonly applied. On the research level it has been shown that polarimetry and Mueller matrix imaging in particular can advantageously be employed as an additional tool to diagnose cancerous tissue and fibrosis [38–41]. Polarimetry can in addition be used to characterize other biological materials, whereas in this thesis, collagen fiber meshworks have been studied by the imaging Mueller matrix polarimeter. In remote sensing applications, the polarization properties of biological materials compared to others can be used for target detection [42, 43]. As most sources of circular light are biological [44], one of the more peculiar applications in remote sensing is the search for extraterrestrial life by looking for circular polarized light from distant planets [45].

Many everyday technological progresses are based on polarimetry, from liquid crystal displays (LCD) and 3D cinema, to our current capacity of electronic semiconductor devices. Taking some steps back in time, the Vikings used polarimetry, when they on cloudy days navigated on the sea, using their bire-

fringent calcite "sólarsteinn" (sun stone) to locate the sun [46, 47]. A glimpse into the future of digital security, information might be secured by quantum cryptography based on polarized light [48].

This thesis contains 13 papers. The papers describe methods, results and conclusions obtained in the thesis. This introduction to the papers are organized in five chapters. Chapter 2 gives a short introduction to how polarized light can be described by the Stokes vector, and how the change of the polarization state can be described by the Mueller matrix. Further, selected methods of analysing the Mueller matrix are described. Polarimetry, the measurement of the Mueller matrix and the development of polarimeters are presented in Chapter 3. Here the imaging Mueller matrix polarimeter is also explained, and an overview of results are given. In Chapter 4 the formalism for using Mueller matrix polarimeters in reflection, in particular spectroscopic Mueller matrix ellipsometry, is described. A brief overview of the results are also given here. Chapter 5 contains conclusions and an outlook.

2. Background

In this chapter an introduction to the notation for polarized light and its interaction with matter is provided. Furthermore, an introduction to methods for analyzing the Mueller matrix is presented.

2.1. Polarized light and the Stokes-Mueller calculus

Polarization is a fundamental property of transverse waves. It describes their specific orientation in space as the wave propagates. Light, and monochromatic electromagnetic plane waves in general, are commonly expressed in a Cartesian coordinate system as a time dependent harmonic electric field. The wave is propagating in the $\hat{z}$ direction and is expressed by a superposition of electric field oscillating in the $\hat{x}$ and $\hat{y}$ direction

$$\vec{E}(z,t) = \Re\left\{E_{0x}\mathrm{e}^{i(\omega t - 2\pi z/\lambda + \delta_x)}\right\}\hat{x} + \Re\left\{E_{0y}\mathrm{e}^{i(\omega t - 2\pi z/\lambda + \delta_y)}\right\}\hat{y}, \tag{2.1}$$

where λ, ω and δ are the wavelength, angular frequency and the phase shifts respectively. Here the sign convention of Hauge [49] is used. The equation above can be rewritten as

$$\vec{E} = \Re\left\{\begin{bmatrix} E_{0x}\mathrm{e}^{i\delta_x} \\ E_{0y}\mathrm{e}^{i\delta_y} \end{bmatrix} \cdot \mathrm{e}^{i(\omega t - 2\pi z/\lambda)}\right\}. \tag{2.2}$$

The polarization state of the plane wave is in general determined by the field amplitudes E_{0x} and E_{0y} and the relative phase difference $\delta = (\delta_y - \delta_x)$ between the two components. The polarization can thus be expressed using the Jones vector

$$\vec{J} = \begin{bmatrix} E_x \\ E_y \end{bmatrix} = \begin{bmatrix} E_{0x}\mathrm{e}^{i\delta_x} \\ E_{0y}\mathrm{e}^{i\delta_y} \end{bmatrix}. \tag{2.3}$$

The change of the polarization state upon interaction, *e.g.* reflection or transmission, can then in an elegant manner be expressed by a Jones transfer matrix

$$\vec{J}^{\,\mathrm{out}} = \mathbf{J}\vec{J}^{\,\mathrm{in}}, \tag{2.4}$$

$$\begin{bmatrix} E_x \\ E_y \end{bmatrix}^{\mathrm{out}} = \begin{bmatrix} a & b \\ c & d \end{bmatrix} \begin{bmatrix} E_x \\ E_y \end{bmatrix}^{\mathrm{in}}. \tag{2.5}$$

Here a, b, c and d are complex transmission or reflection coefficients and translates linear interactions of coherent light.

In many practical cases light is not a plane wave, it may have a finite bandwidth ($\Delta\lambda$ and $\Delta\omega$) and time dependent electric field amplitudes and phases

$$\vec{E} = \Re\left\{ \begin{bmatrix} E_{0x}(t)\mathrm{e}^{i\delta_x(t)} \\ E_{0y}(t)\mathrm{e}^{i\delta_y(t)} \end{bmatrix} \cdot \mathrm{e}^{i(\Delta\omega t - 2\pi z/\Delta\lambda)} \right\}. \tag{2.6}$$

In these cases light is said to be quasi-monochromatic and the Jones vector is time dependent. A practical way to deal with the latter complexity is the Mueller-Stokes formalism, where the polarization state is defined by the difference in intensity of orthogonal field components

$$\vec{S} = \begin{bmatrix} s_1 \\ s_2 \\ s_3 \\ s_4 \end{bmatrix} = \begin{bmatrix} I_x + I_y \\ I_x - I_y \\ I_{+45^\circ} - I_{-45^\circ} \\ I_R - I_L \end{bmatrix} = \begin{bmatrix} \left\langle E_{0x}(t)^2 \right\rangle + \left\langle E_{0y}(t)^2 \right\rangle \\ \left\langle E_{0x}(t)^2 \right\rangle - \left\langle E_{0y}(t)^2 \right\rangle \\ 2\left\langle E_{0x}(t)E_{0y}(t)\cos\delta(t) \right\rangle \\ 2\left\langle E_{0x}(t)E_{0y}(t)\sin\delta(t) \right\rangle \end{bmatrix}. \tag{2.7}$$

Here $\langle\ \rangle$ denotes time-averages, meaning that s_1 is the total intensity, s_2, s_3, s_4 are the difference between the intensity of linear x- and y-polarized light, light linearly polarized $+45^\circ$ and -45° with respect to the x-axis, and right and left handed circular polarized light, respectively.

Now the degree of polarization (DOP) can be defined as the ratio of the length of the polarized intensity vector $[s_2, s_3, s_4]^T$ to the total intensity,

$$\mathrm{DOP} = \frac{\sqrt{s_2^2 + s_3^2 + s_4^2}}{s_1}. \tag{2.8}$$

A DOP equal to one means that the the light is totally polarized, while a DOP equal to zero means that the light is unpolarized.

A linear transformation (reflection/transmission) of a Stokes vector can be

expressed using a Mueller matrix

$$\vec{S}^{\text{out}} = \mathbf{M} \cdot \vec{S}^{\text{ in}}, \tag{2.9}$$

$$\begin{bmatrix} s_1 \\ s_2 \\ s_3 \\ s_4 \end{bmatrix}^{\text{out}} = \begin{bmatrix} m_{11} & m_{12} & m_{13} & m_{14} \\ m_{21} & m_{22} & m_{23} & m_{24} \\ m_{31} & m_{32} & m_{33} & m_{34} \\ m_{41} & m_{42} & m_{43} & m_{44} \end{bmatrix} \begin{bmatrix} s_1 \\ s_2 \\ s_3 \\ s_4 \end{bmatrix}^{\text{in}}. \tag{2.10}$$

Hence, a cascade of N separate interactions can be expressed by multiplication the individual Mueller matrices to a system Mueller Matrix

$$\mathbf{M}_{\text{sys.}} = \mathbf{M}_N \mathbf{M}_{N-1} \dots \mathbf{M}_1, \tag{2.11}$$

where $\mathbf{M}_1$ is the first interaction.

An important property of a Mueller matrix is the depolarization properties. There exist several definitions of depolarization of a Mueller matrix, in this thesis the depolarization index from Gil and Bernabeu [50] has been used

$$P_d = \sqrt{\frac{\sum_{i,j} m_{ij}^2 - m_{11}^2}{3m_{11}^2}} \begin{cases} 1, & \text{non-depolarizing} \\ 0, & \text{completely depolarizing} \end{cases} \tag{2.12}$$

Another name for a non-depolarizing Mueller matrix is a Mueller-Jones matrix (*i.e.* a Mueller matrix that can be expressed as a Jones matrix). A Mueller-Jones matrix can be calculated from a Jones matrix by

$$\mathbf{M} = \mathbf{A} \left(\mathbf{J} \otimes \mathbf{J}^* \right) \mathbf{A}^{-1}, \tag{2.13}$$

where,

$$\mathbf{A} = \begin{bmatrix} 1 & 0 & 0 & 1 \\ 1 & 0 & 0 & -1 \\ 0 & 1 & 1 & 0 \\ 0 & i & -i & 0 \end{bmatrix}, \tag{2.14}$$

and * denotes the complex conjugate of the matrix.

A third mathematical description of polarized light, which will not be discussed any further, is the density matrix formalism [51] where the polarization

state is expressed in terms of the correlation of the electric field components.

$$\mathbf{J}_M = \begin{bmatrix} \langle E_x(t)E_x^*(t)\rangle & \left\langle E_x(t)E_y^*(t)\right\rangle \\ \langle E_y(t)E_x^*(t)\rangle & \left\langle E_y(t)E_y^*(t)\right\rangle \end{bmatrix}. \tag{2.15}$$

The density matrix and the Stokes vector contains the same information, thus both may be used to describe partially polarized light.

2.2. Analyzing the Mueller matrix

Decomposition methods are widely used for the retrieval of relevant quantities in a generally complicated Mueller matrix. Two types of decomposition regimes are here considered, product decompositions and the differential decomposition.

Depolarization is an important measurable quantity in Mueller matrices. It is commonly quantified using the depolarization index of Gil and Bernabeu [50], Equation (2.12). Other definitions of the depolarizing properties of a Mueller matrix are *e.g.* Chipman's definition of average degree of polarization [52] and the Mueller matrix entropy [53].

Some properties can be directly extracted without any assumptions and decompositions. These are diattenuation, polarizance, transmittance/reflectance, and as mentioned previously, depolarization. A shorthand notation for the Mueller matrix is

$$\mathbf{M} = m_{11}\begin{bmatrix} 1 & \vec{D}^T \\ \vec{P} & \mathbf{m} \end{bmatrix}, \tag{2.16}$$

where $\mathbf{m}$ is a 3×3 sub-matrix, $\vec{D}$ is the diattenuation vector defined as

$$\vec{D} = \begin{bmatrix} D_{\mathrm{H}} \\ D_{45} \\ D_{\mathrm{C}} \end{bmatrix} = \frac{1}{m_{11}}\begin{bmatrix} m_{12} \\ m_{13} \\ m_{14} \end{bmatrix}, \tag{2.17}$$

and $\vec{P}$ is the polarizance vector

$$\vec{P} = \begin{bmatrix} P_{\mathrm{H}} \\ P_{45} \\ P_{\mathrm{C}} \end{bmatrix} = \frac{1}{m_{11}}\begin{bmatrix} m_{21} \\ m_{31} \\ m_{41} \end{bmatrix}. \tag{2.18}$$

The diattenuation describes the polarization dependent dichroism of the material, while the polarizance describes the conversion from unpolarized incident light to the resulting Stokes vector. The transmittance/reflectance comes directly from m_{11}.

2.2.1. Product decompositions

Product decomposition, also called polar decomposition, is a class of Mueller matrix decomposition methods where the Mueller matrix is separated into basic depolarization, retardance and diattenuation Mueller matrices. It is assumed that the polarizing effects occur in a specific order. There are currently three types of product decompositions, the so called forward, reverse and symmetric decomposition.

The forward polar decomposition for Mueller matrices, originally proposed by Lu and Chipman [54], decomposes the Mueller matrix assuming that the diattenuating effect occurs before the depolarization, resulting in the following equations

$$\mathbf{M} = \mathbf{M}_\Delta \mathbf{M}_\mathrm{R} \mathbf{M}_\mathrm{D}, \tag{2.19a}$$
$$\mathbf{M} = \mathbf{M}_\Delta \mathbf{M}'_\mathrm{D} \mathbf{M}_\mathrm{R}, \tag{2.19b}$$
$$\mathbf{M} = \mathbf{M}_\mathrm{R} \mathbf{M}'_\Delta \mathbf{M}_\mathrm{D}. \tag{2.19c}$$

$\mathbf{M}_\Delta$, $\mathbf{M}_\mathrm{R}$ and $\mathbf{M}_\mathrm{D}$ are the Mueller matrices of a pure depolarizer, retarder and diattenuater respectively. Morio and Goudail [55] showed that they were all equivalent, but Equation (2.19a) was the originally solved problem and is chosen as the normal form.

The reverse product decomposition proposed by Ossikovski *et al.* [56] is considering the case where the depolarization is happening before the diattenuation

$$\mathbf{M} = \mathbf{M}_\mathrm{D} \mathbf{M}_\mathrm{R} \mathbf{M}_\Delta, \tag{2.20a}$$
$$\mathbf{M} = \mathbf{M}_\mathrm{R} \mathbf{M}_\mathrm{D} \mathbf{M}''_\Delta, \tag{2.20b}$$
$$\mathbf{M} = \mathbf{M}_\mathrm{D} \mathbf{M}''_\Delta \mathbf{M}_\mathrm{R}. \tag{2.20c}$$

The normal form is here Equation (2.20a).

The symmetric decomposition, proposed by Ossikovski [57], is the last form of the product decomposition. It treats the case where a diagonal depolarizing

Mueller matrix is arranged between two pairs of retarders and diattenuators

$$\mathbf{M} = \mathbf{M}_{\mathrm{D2}}\mathbf{M}_{\mathrm{R2}}\mathbf{M}_{\Delta\mathrm{d}}\mathbf{M}_{\mathrm{R1}}^{T}\mathbf{M}_{\mathrm{D1}}. \tag{2.21}$$

The symmetric decomposition requires that $\mathbf{M}$ is a so called Stokes diagonalizable matrix [58, 59], which means that $\mathbf{M}_{\Delta}$ must be a diagonal depolarizer. As the symmetric decomposition was not applied in this work its detailed description is omitted from the thesis.

Forward polar decomposition

The normal form of the forward decomposition (Equation (2.19a)) is solved by first defining the general matrices of a depolarizer, a retarder and a diattenuator

$$\mathbf{M}_{\Delta} = \begin{bmatrix} 1 & \vec{0}^{T} \\ \vec{P}_{\Delta} & \mathbf{m}_{\Delta} \end{bmatrix}, \mathbf{M}_{\mathrm{R}} = \begin{bmatrix} 1 & \vec{0}^{T} \\ \vec{0} & \mathbf{m}_{\mathrm{R}} \end{bmatrix}, \mathbf{M}_{\mathrm{D}} = \begin{bmatrix} 1 & \vec{D}^{T} \\ \vec{D} & \mathbf{m}_{\mathrm{D}} \end{bmatrix}. \tag{2.22}$$

Here $\mathbf{m}_{\Delta}$, $\mathbf{m}_{R}$ and $\mathbf{m}_{D}$ are 3×3 sub matrices, $\vec{0}$ is a three element vector of zeros, $\vec{P}_{\Delta}$ is defined as the polarizing properties of the depolarizer, and $\vec{D}$ is the diattenuation vector of Equation (2.17).

The sub matrix of the diattenuator can be found by considering the total diattenuation and the unity vector $\hat{D} = \vec{D}/|\vec{D}|$ as

$$\mathbf{m}_{\mathrm{D}} = \sqrt{1 - |\vec{D}|^{2}}\mathbf{I} + \left(1 - \sqrt{1 - |\vec{D}|^{2}}\right)\hat{D}\hat{D}^{T}, \tag{2.23}$$

here $\mathbf{I}$ is the 3×3 identity matrix. The diattenuation can be removed from the original matrix by multiplying by the inverse of $\mathbf{M}_{\mathrm{D}}$

$$\mathbf{M}' = \mathbf{M}\mathbf{M}_{\mathrm{D}}^{-1} = \mathbf{M}_{\Delta}\mathbf{M}_{\mathrm{R}} = \begin{bmatrix} 1 & \vec{0}^{T} \\ \vec{P}_{\Delta} & \mathbf{m}_{\Delta}\mathbf{m}_{\mathrm{R}} \end{bmatrix} = \begin{bmatrix} 1 & \vec{0}^{T} \\ \vec{P}_{\Delta} & \mathbf{m}' \end{bmatrix}, \tag{2.24}$$

resulting in the polarizance vector of the depolarization matrix

$$\vec{P}_{\Delta} = \frac{\vec{P} - \mathbf{m}\vec{D}}{1 - \vec{D}^{2}}. \tag{2.25}$$

Now, the problem is reduced to decompose the 3×3 matrix $\mathbf{m}' = \mathbf{m}_{\Delta}\mathbf{m}_{\mathrm{R}}$.

Because $\mathbf{m}_\Delta$ is diagonal and the eigenvalues of $\mathbf{m}'(\mathbf{m}')^T$ are λ_1, λ_2 and λ_3, the eigenvalues of $\mathbf{m}_\Delta$ are $\sqrt{\lambda_1}$, $\sqrt{\lambda_2}$ and $\sqrt{\lambda_3}$ [54]. The depolarizing sub-matrix can now be constructed as [54]

$$\mathbf{m}_\Delta = \pm\left\{\mathbf{m}'^T\mathbf{m}' + \left(\sqrt{\lambda_1\lambda_2} + \sqrt{\lambda_2\lambda_3} + \sqrt{\lambda_3\lambda_1}\right)\mathbf{I}\right\}^{-1} \times \left\{\left(\sqrt{\lambda_1} + \sqrt{\lambda_2} + \sqrt{\lambda_3}\right)\mathbf{m}'^T\mathbf{m}' + \sqrt{\lambda_1\lambda_2\lambda_3}\mathbf{I}\right\}. \quad (2.26)$$

The retardance matrix is now found as

$$\mathbf{M}_\mathrm{R} = \mathbf{M}_\Delta^{-1}\mathbf{M}'. \quad (2.27)$$

The total retardance R can be found by

$$R = \arccos\left(\frac{\mathrm{Tr}(\mathbf{M}_\mathrm{R})}{2} - 1\right), \quad (2.28)$$

and a retardance vector separating linear retardance and optical rotation can be constructed as

$$\vec{R} = \begin{bmatrix} R_\mathrm{H} \\ R_{45} \\ R_\mathrm{C} \end{bmatrix} = \begin{bmatrix} r_1 \\ r_2 \\ r_3 \end{bmatrix}, r_i = \frac{R}{2\sin R}\sum_{j,k=1}^{4}\epsilon_{ijk}[\mathbf{m}_\mathrm{R}]_{jk}, \quad (2.29)$$

where ϵ_{ijk} is the Levi-Civita permutation symbol. By following Manhas *et al.* [60], the retardance Mueller matrix can be written as the product of a rotated linear retardance Mueller matrix $\mathbf{M}_\mathrm{LR}$ and an optical rotation Mueller

matrix $\mathbf{M}_{\mathrm{OR}}$

$$\mathbf{M}_{\mathrm{R}} = \mathbf{M}_{\mathrm{LR}}(\delta,\theta)\mathbf{M}_{\mathrm{OR}}(\alpha) = \begin{bmatrix} 1 & 0 & 0 & 0 \\ 0 & \cos^2 2\theta + \sin^2 2\theta \cos\delta & (1-\cos\delta)\cos 2\theta \sin 2\theta & -\sin 2\theta \sin\delta \\ 0 & (1-\cos\delta)\cos 2\theta \sin 2\theta & \sin^2 2\theta & \cos 2\theta \sin\delta \\ 0 & \sin 2\theta \sin\delta & \cos 2\theta \sin\delta & \cos\delta \end{bmatrix} \times \begin{bmatrix} 1 & 0 & 0 & 0 \\ 0 & \cos(2\alpha) & \sin(2\alpha) & 0 \\ 0 & -\sin(2\alpha) & \cos(2\alpha) & 0 \\ 0 & 0 & 0 & 1 \end{bmatrix}. \quad (2.30)$$

Applying Equation (2.28), the total retardance can be found in terms of the linear retardance δ and optical rotation α

$$R = \arccos\left\{2\cos^2\alpha\cos^2(\delta/2) - 1\right\}. \quad (2.31)$$

If the square of R_{C} is written out

$$R_{\mathrm{C}}^2 = \frac{\sin^2\alpha\cos^2(\delta/2)}{1-\cos^2\alpha\cos^2(\delta/2)}, \quad (2.32)$$

the linear retardance can be calculated as

$$\delta = 2\arccos\sqrt{R_{\mathrm{C}}^2\left(1-\cos^2(R/2)\right)+\cos^2(R/2)}, \quad (2.33)$$

and the optical rotation as

$$\alpha = \frac{1}{2}\arcsin\frac{2R_C\sin R}{1+\cos(\delta)}. \quad (2.34)$$

Finally the orientation of the fast axis of the linear retarder can be calculated by the relation between R_{H} and R_{45}

$$\theta = \frac{1}{2}\arctan\frac{R_{45}}{R_{\mathrm{H}}}, \quad \theta \in [0^\circ, 180^\circ]. \quad (2.35)$$

Reverse polar decomposition

The reverse decomposition, with its normal form in Equation (2.20a), suggested by Ossikovski *et al.* [56] follows somewhat the same procedure as for the forward decomposition. The important difference is that the Mueller matrix of the depolarizer $\mathbf{M}_\Delta$ and diattenuator in Equation (2.22) must be slightly modified to a *reverse* version

$$\mathbf{M}_{\Delta r} = \begin{bmatrix} 1 & \vec{D}_{\Delta r}^T \\ \vec{0} & \mathbf{m}_{\Delta r} \end{bmatrix}, \quad \mathbf{M}_\mathrm{D} = \begin{bmatrix} 1 & \vec{P}^T \\ \vec{P} & \mathbf{m}_\mathrm{P} \end{bmatrix}. \tag{2.36}$$

The depolarizer is now having a diattenuating form, while the diattenuator matrix is constructed by the polarizance vector (Equation (2.18)) of the original Mueller matrix and a sub-matrix $\mathbf{m}_\mathrm{P}$. Following the procedure from the forward decomposition, $\mathbf{M'} = \mathbf{M}_\mathrm{D}^{-1}\mathbf{M} = \mathbf{M}_\mathrm{R}\mathbf{M}_{\Delta r}$, the depolarizing diattenuation vector is

$$\vec{D}_{\Delta r} = \frac{\vec{D} - \mathbf{m}\vec{P}}{1 - \vec{P}^2}. \tag{2.37}$$

The diagonal sub-depolarizing matrix $\mathbf{m}_{\Delta r}$ can now be calculated using Equation (2.26).

As shown in [56], the reverse decomposition can be solved by applying the forward polar decomposition on the transpose of the Mueller matrix (Equation (2.19a)),

$$\begin{aligned} \mathbf{M}^T &= (\mathbf{M}_\Delta \mathbf{M}_\mathrm{R} \mathbf{M}_\mathrm{D})^T \\ &= \mathbf{M}_\mathrm{D}^T \mathbf{M}_\mathrm{R}^T \mathbf{M}_\Delta^T. \end{aligned} \tag{2.38}$$

The reverse decomposed matrices can now be found by transposing the resulting matrices back to their normal form.

2.2.2. Differential decomposition

In the product decomposition methods the assumption is always that the polarizing effects apply in a specific order. If the effects are simultaneous, the differential decomposition of Mueller matrices, recently refined by Ossikovski [61], can be applied.

Here the differential matrix $\mathbf{m}$, relates the transmission Mueller matrix of

a depolarizing anisotropic medium, with propagation in the z-direction to the spatial derivative in this direction

$$\frac{d\mathbf{M}}{dz} = \mathbf{m}\mathbf{M}. \tag{2.39}$$

The elementary polarizing properties are the elements of the differential matrix given by

$$\mathbf{m} = \begin{bmatrix} \alpha & \beta & \gamma & \partial \\ \beta' & \alpha_1 & \mu & -\nu \\ \gamma' & -\mu' & \alpha_2 & \eta \\ \partial' & \nu' & -\eta' & \alpha_3 \end{bmatrix}. \tag{2.40}$$

Where β and γ are the dichroism of the linear horizontal-vertical, linear $\pm 45°$ axes respectively, and ∂ is the circular dichroism . η, ν and μ are the linear horizontal-vertical, linear $\pm 45°$ and circular retardance. α is the isotropic absorption, and α_1, α_2 and α_3 are the depolarization for the linear horizontal-vertical, linear $\pm 45°$ and circular polarization. The value of each variable is the mean of the primed and un-primed, where they are only different in the case of depolarization.

If the Mueller matrix of the sample is uniform in the direction of propagation, $\mathbf{m}$ is independent of Z. The integral over Equation (2.39) can be written as the logarithm of $\mathbf{M}$

$$\mathbf{L} = \ln \mathbf{M} = \mathbf{m}l, \tag{2.41}$$

where l is the optical path length of the sample.

The properties of the sample can be calculated by splitting $\mathbf{L}$ into an anti-symmetric ($\mathbf{L}_m$) and a symmetric ($\mathbf{L}_u$) part, such that $\mathbf{L} = \mathbf{L}_m + \mathbf{L}_u$ by

$$\begin{aligned} \mathbf{L}_m &= \frac{1}{2}\left(\mathbf{L} - \mathbf{G}\mathbf{L}^T\mathbf{G}\right), \\ \mathbf{L}_u &= \frac{1}{2}\left(\mathbf{L} + \mathbf{G}\mathbf{L}^T\mathbf{G}\right), \end{aligned} \tag{2.42}$$

where $\mathbf{G}$ is a diagonal matrix $\mathbf{G} = \mathrm{diag}(1, -1, -1, -1)$. The off-diagonal elements of $\mathbf{L}_m$ are the mean of the respective properties in Equation (2.40), while the same elements in $\mathbf{L}_u$ are the respective uncertainties. The depolarization

factors are those found on the diagonal of $\mathbf{L}_u$.

The common polarization parameters can then be calculated similarly as for the other methods of decomposition. The dichroism $d_{\mathbf{L}_m}$, linear retardance $\delta_{\mathbf{L}_m}$ and its orientation $\theta_{\mathbf{L}_m}$, depolarization $\Delta_{\mathbf{L}_u}$, optical rotation $\alpha_{\mathbf{L}_m}$, and total retardance $R_{\mathbf{L}_m}$ are found through the following relations [62]

$$d_{\mathbf{L}_m} = \sqrt{\beta_{\mathbf{L}_m}^2 + \gamma_{\mathbf{L}_m}^2 + \partial_{\mathbf{L}_m}^2}, \tag{2.43a}$$

$$\delta_{\mathbf{L}_m} = \sqrt{\nu_{\mathbf{L}_m}^2 + \eta_{\mathbf{L}_m}^2}, \tag{2.43b}$$

$$\theta_{\mathbf{L}_m} = \frac{1}{2} \arctan \frac{\mu_{\mathbf{L}_m}}{\nu_{\mathbf{L}_m}}, \tag{2.43c}$$

$$\Delta_{\mathbf{L}_u} = \frac{1}{3}|\alpha_1 + \alpha_2 + \alpha_3|, \tag{2.43d}$$

$$\alpha_{\mathbf{L}_m} = \frac{1}{2}\mu_{\mathbf{L}_m} \qquad \text{and} \tag{2.43e}$$

$$R_{\mathbf{L}_m} = \sqrt{\nu_{\mathbf{L}_m}^2 + \eta_{\mathbf{L}_m}^2 + \mu_{\mathbf{L}_m}^2} = \sqrt{\delta_{\mathbf{L}_m}^2 + 4\alpha_{\mathbf{L}_m}^2}. \tag{2.43f}$$

The standard deviation of the parameters, except for the depolarization, are found in the same manner by employing Equation (2.43) to $\mathbf{L}_u$. In Equation (2.43) the parameters are accumulated over the distance l such that the values for the retardance is similar to what is obtained from the polar decomposition. The limiting values for diattenuation and depolarization in the polar decomposition is between 0 and 1. To accomplish the same limiting values for the values from the differential decomposition, the following relations are employed [62]

$$D = \tanh(d_{\mathbf{L}_m}), \tag{2.44a}$$

$$\Delta = 1 - \frac{1}{3}\left(\mathrm{e}^{\alpha_1} + \mathrm{e}^{\alpha_2} + \mathrm{e}^{\alpha_3}\right). \tag{2.44b}$$

It is noted that the differential decomposition is currently only working for measurements in transmission (forward scattering), while for Mueller matrices in the backscattering regime the decomposition breaks down [14]. The Mueller matrix roots decomposition proposed by Noble *et al.* [63, 64], where large roots are taken over the Mueller matrix is equivalent to the differential decomposition.

2.2.3. Physical realizability

A measured Mueller matrix can in some cases, due to small measurement errors, be non-physical. Two main constraints apply for Mueller matrices [65].

- A Mueller matrix can never over polarize, *i.e.* generate a Stokes vector with a degree of polarization greater than one.
- A Mueller matrix can not have gain, *i.e.* the intensity can not increase through a Mueller matrix.

The polarization constraint can be checked through the eigenvalues of the hermitian coherency matrix [66, 67], which in [67] is defined as

$$\mathbf{H} = \frac{1}{2}\sum_{i=1}^{4}\sum_{j=1}^{4} m_{ij}\sigma_i \otimes \sigma_j^*, \tag{2.45}$$

where $\sigma_{i/j}$ are the Pauli spin matrices given as

$$\sigma_1 = \begin{bmatrix} 1 & 0 \\ 0 & 1 \end{bmatrix}, \quad \sigma_2 = \begin{bmatrix} 1 & 0 \\ 0 & -1 \end{bmatrix}, \quad \sigma_3 = \begin{bmatrix} 0 & 1 \\ 1 & 0 \end{bmatrix}, \quad \sigma_4 = \begin{bmatrix} 0 & -i \\ i & 0 \end{bmatrix}. \tag{2.46}$$

The Mueller matrix is non-physical if $\mathbf{H}$ has negative eigenvalues. Cloude [66] defined a measure for how close a measured matrix is a physical Mueller matrix through the coherency fidelity

$$H_{\text{fid.}} = -10\log_{10}\frac{\sum \lambda_+}{\sum \lambda_-}, \tag{2.47}$$

where λ_+ and λ_- are the positive and negative eigenvalues of $\mathbf{H}$, calculated through a spectral decomposition

$$\mathbf{H} = \mathbf{V}\mathbf{D}\mathbf{V}^*. \tag{2.48}$$

$\mathbf{V}$ is the eigenvector matrix and $\mathbf{D}$ is a matrix with the eigenvalues on the diagonal. The fidelity is useful to control a measured matrix for unphysical artifacts.

Any real Mueller matrix polarimeter will sometimes return Mueller matrices with a negative eigenvalue. The closest physical Mueller matrix can then be

calculated by replacing the negative eigenvalues in $\mathbf{D}$ by zeros. If the new eigenvalue matrix is $\mathbf{D}'$, a filtered Coherency matrix can be calculated by

$$\mathbf{H}' = \mathbf{V}\mathbf{D}'\mathbf{V}^*, \tag{2.49}$$

which can further be used to calculate the filtered Mueller matrix.

The gain constraint can be analyzed using the definition of the transmittance in a Mueller matrix [65]

$$g_f = m_{11} + \left(m_{12}^2 + m_{13}^2 + m_{14}^2\right)^{\frac{1}{2}} \leq 1 \tag{2.50}$$

$$g_r = m_{11} + \left(m_{21}^2 + m_{31}^2 + m_{41}^2\right)^{\frac{1}{2}} \leq 1, \tag{2.51}$$

where the subscripts f and r indicate forward and, the more special, reverse transmittance [65]. Note that the gain constraint can only be applied before any normalization to m_{11}.

3. Polarimetry

A Mueller matrix polarimeter consists of four main parts, a light source, a Polarization State Generator (PSG), a Polarization State Analyzer (PSA) and a detector. The PSG and PSA comprise polarization and analyzing optics. Figure 3.1 shows a sketch of a general Mueller matrix polarimeter configuration, in both reflection and transmission mode (dashed lines). The polarization optics of the PSG and PSA consist of a linear polarizer and at least one phase retarding device, such as *e.g.* wave-plates, liquid crystals, compensators, Pockels cells or electro-optical retarders.

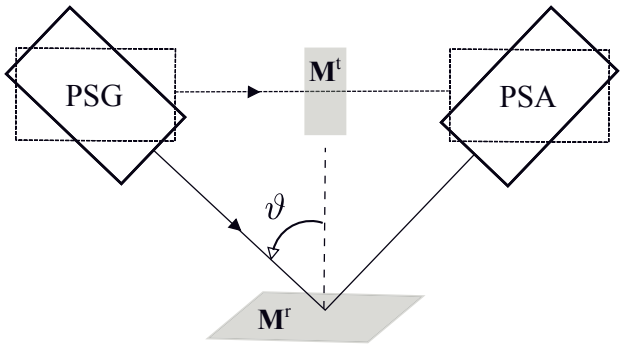

Figure 3.1.: Sketch of a general polarimeter in reflection (with incidence angle ϑ) and transmission (dashed) mode.

Two main concepts of Mueller matrix polarimeters exist, one where the polarization state is continuously modulated and analyzed, and the other where a discrete number of states are generated and analyzed.

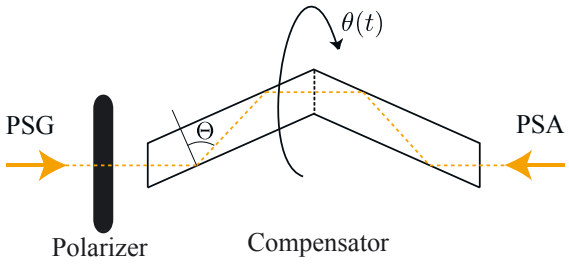

Figure 3.2.: A sketch of a rotating compensator polarimeter. The retardance of the compensator is determined by the angle Θ, and the azimuth orientation by θ.

3.1. Continuously rotating compensator Mueller matrix polarimeter

In a continuously rotating compensator polarimeter the PSG and PSA consists of a polarizer and a compensator. Figure 3.2 illustrates the PSG and PSA using the compensator. The advantage of using compensators as wave retarding devices, is the very low dispersion and the wide working wavelength range, nominally only limited by the absorption of the material. Such compensators are commonly implemented using two Fresnel rhombs, where the retardance is determined by the angle Θ of the rhombs and the isotropic refractive index of the material [68].

The continuously rotating compensator Mueller matrix multichannel polarimeter was developed by Collins *et al.* [69], and further commercialized by JA Woollam Company under the name RC2. The system is a so-called 3-5 dual rotating compensator polarimeter, where the compensator of the PSG and PSA rotate continuously with a frequency $\omega_1 = 3\omega$ and $\omega_2 = 5\omega$ respectively. By letting the time dependent azimuth orientation of the compensator of the PSG be $\omega_1 t$, the resulting time dependent Stokes vector is

$$\vec{S}(\omega_1 t, \Theta, \lambda) = \mathbf{M}_{\text{ret.}}(\omega_1 t, \delta(\Theta, \lambda))\mathbf{M}_{\text{pol.}}[1, 0, 0, 0]^T. \tag{3.1}$$

The optimal retardance for a rotating compensator polarimeter is 132° [70], which for the UV to the infrared correspond to $\Theta \approx 66°$ for CaF_2 and fused

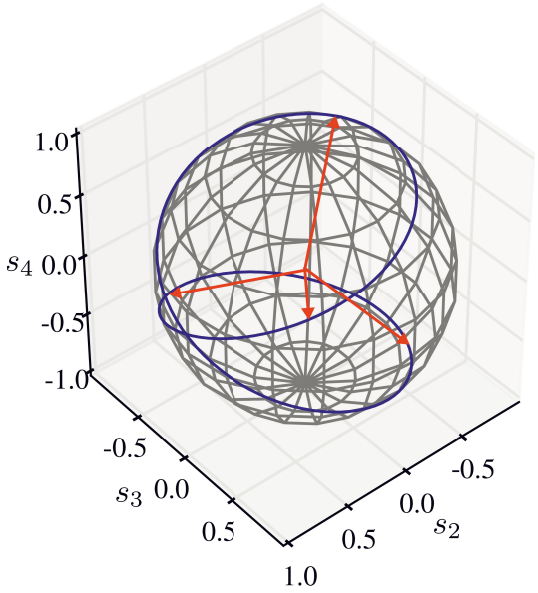

Figure 3.3.: The polarization state of the continuously rotating compensator Mueller matrix polarimeter plotted as a trajectory on the Poincare sphere (blue line). The polarization states of an optimal discrete state rotating compensator polarimeter are plotted as red vectors.

silica prisms [71]. In Figure 3.3 the Stokes vector of Equation (3.1) is plotted on the Poincare sphere upon a full revolution for $\delta = 132°$. On the Poincare sphere, the elements s_2, s_3 and s_4 of the normalized Stokes vector represent the axes, such that the north and the south pole represents right and left circular polarized light, and equator linearly polarized light. The retardance of 132° ensures that the polarization space (here represented by the Poincare sphere) is spanned.

Further, the expression describing the interaction with the sample ($\mathbf{M}_{\text{Sample}}$) and the polarization state analyzer of the PSA is

$$\vec{A}(\omega_2 t, \omega_1 t, \Theta, \lambda) = \mathbf{M}_{\text{pol.}}\mathbf{M}_{\text{ret.}}(\omega_2 t, \delta(\Theta, \lambda))\mathbf{M}_{\text{Sample}}\vec{S}(\omega_1 t, \Theta, \lambda). \tag{3.2}$$

It is assumed that the retardance of the compensator in the PSG and PSA are

the same. Because the last optical element is a polarizer the final polarization state is only determined by its orientation. The intensity, however, is time dependent and a function of ω, Θ, λ and the elements of the Mueller matrix. By performing the matrix multiplications in the equations above, one can for each wavelength λ find the time dependent intensity expressed as a Fourier sum [69]

$$I'(t) = I'_0 \left(1 + \sum_{n=1}^{16} (\alpha'_{2n} \cos 2n\omega t + \beta'_{2n} \sin 2n\omega t) \right), \tag{3.3}$$

where I'_0 is the average intensity and α'_{2n} β'_{2n} are 32 normalized Fourier coefficients. Eight of these are always zero, while the remaining coefficients and the average intensity are functions of the Mueller matrix elements of the sample [69]. In practice the Mueller matrix is normally found by taking the fast Fourier transform of the recorded intensity.

3.2. Discrete states Mueller matrix polarimeters

A Mueller matrix polarimeter can also be accomplished by using discrete polarization states in the PSG and PSA. At least 16 intensity measurements are needed, corresponding to four probing states, and four analysis states. For a unique measurement of the Mueller matrix the polarization states of the PSG and PSA must span the polarization space, which can be visualized on the Poincare sphere. As an example, for a dual rotating compensator ellipsometer, four discrete Stokes vectors can be generated by selecting four azimuth angles of the compensators. Sabatke *et al.* [72] showed that the four optimal Stokes vectors make up a tetrahedron when plotted on the Poincare sphere, see Figure 3.3.

Two system matrices $\mathbf{W}$ and $\mathbf{A}$ are constructed for the PSG and PSA, respectively. The Stokes vectors generated in the PSG are organized as the columns in $\mathbf{W}$. $\mathbf{A}$ is constructed by the analysing Stokes vectors as rows. An intensity matrix $\mathbf{B}$ is obtained by matrix multiplication of the system matrices and the Mueller matrix

$$\mathbf{B} = \mathbf{AMW}. \tag{3.4}$$

By inverting $\mathbf{A}$ and $\mathbf{W}$ and multiplying these from each side, the Mueller matrix can be found

$$\mathbf{M} = \mathbf{A}^{-1}\mathbf{B}\mathbf{W}^{-1}. \tag{3.5}$$

The noise in $\mathbf{M}$ is related to the noise in $\mathbf{B}$ and the inverse of $\mathbf{W}$ and $\mathbf{A}$. More specific, Stabo-Eeg *et al.* [73] found an expression for the relative error in the Mueller matrix

$$\frac{\|\Delta\mathbf{M}\|}{\|\mathbf{M}\|} \lesssim \kappa_{\mathbf{W}}\kappa_{\mathbf{A}}\frac{\|\Delta\mathbf{B}\|}{\|\mathbf{B}\|} + \kappa_{\mathbf{A}}\frac{\|\Delta\mathbf{A}\|}{\|\mathbf{A}\|} + \kappa_{\mathbf{W}}\frac{\|\Delta\mathbf{W}\|}{\|\mathbf{W}\|}, \tag{3.6}$$

where $\kappa_{\mathbf{A}}$ and $\kappa_{\mathbf{W}}$ are the condition numbers of $\mathbf{A}$ and $\mathbf{W}$. The condition number of a square non-singular matrix is defined as $\kappa_{\mathbf{A}} = ||\mathbf{A}||/||\mathbf{A}^{-1}||$ where $||\cdot||$ denotes the second norm [74]. $\Delta\mathbf{W}$ and $\Delta\mathbf{A}$ are calibration errors, and $\Delta\mathbf{B}$ is intensity measurement errors. If $\mathbf{A}$ and $\mathbf{W}$ are similar matrices, the relative error in $\mathbf{M}$ is proportional to the square of the condition number. Thus, by minimizing the condition numbers the error is minimized. The lowest possible condition number for a matrix constructed from four Stokes vector, and hence the best polarimeter possible is $\kappa = \sqrt{3}$ [75].

3.2.1. Overdetermined polarimetry

Because of dispersion in the retardance of optical components, four Stokes vectors are not always enough to construct a well conditioned broadband polarimeter. One solution to improve the conditioning is to increase the number of Stokes vectors in the polarimeter. Paper 3 describes the optimization (using genetic algorithms) and implementation of a spectroscopic overdetermined polarimeter based on six voltage states in the the PSA and PSG. The system matrices ($\mathbf{W}$ and $\mathbf{A}$) are now of sizes 4×6 and 6×4. Equation (3.4) still holds, but since non-square matrices are singular, the inverse does not uniquely exist. For physical matrices with noise, the numerical most accurate solution is found by the Moore-Penrose pseudo-inverse [76], commonly noted †. In overdetermined form Equation (3.5) now reads

$$\mathbf{M} = \mathbf{A}^{\dagger}\mathbf{B}\mathbf{W}^{\dagger}. \tag{3.7}$$

3.3. Optimization of polarimeters

Designing polarimeters with an optimal condition number for one wavelength is a trivial task. The common use of polarimeters nowadays is though for spectroscopic purposes, and the optimization of these is complicated due to dispersion in the optical components. Optimization of the spectral condition number of polarimeters have commonly been accomplished through semi-direct [77] and Monte-Carlo searches [78]. When the complexity of the polarimeter design is increased, the number of variables becomes too large for efficient direct searches. Genetic algorithms [79] were therefore suggested for efficient design of polarimeters (Paper 2 and 3).

Polarimeters based on ferroelectric liquid crystals, and liquid crystal variable retarders were designed. In the following sections brief explanations of their working principles are given.

3.3.1. Ferroelectric liquid crystal based polarimeters

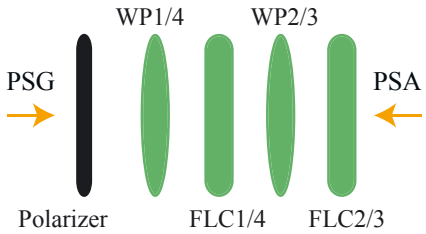

Figure 3.4.: A sketch of a FLC based polarimeter. A minimum of two FLCs are needed for the PSG/PSA in order to generate four states. The fixed waveplates are included to compensate for the dispersion.

Ferroelectric liquid crystals (FLC) are smectic C liquid crystals (LC) [80], a LC phase which has long molecules arranged in layers. Within each layer the molecules are all oriented in the same direction. The chirality of the molecules induces a dipole moment used to control the direction of the molecules. By

switching the polarity of an electric field over the crystal, the molecules changes direction and the effective fast axis of the LC changes orientation. FLCs can be modeled as a normal phase retarder, or waveplate, with two stable voltage controlled azimuth orientations. The retardance is proportional to the physical thickness of the device.

As each FLC has two stable states, at least four FLCs are needed to generate enough states in the Mueller matrix polarimeter. Each state corresponds to an azimuth orientation angle in the set

$$\hat{\theta} = \left\{ \begin{array}{cccc} \theta_{1,\mathrm{FLC1}} & \theta_{1,\mathrm{FLC2}} & \theta_{1,\mathrm{FLC3}} & \theta_{1,\mathrm{FLC4}} \\ \theta_{2,\mathrm{FLC1}} & \theta_{2,\mathrm{FLC2}} & \theta_{2,\mathrm{FLC3}} & \theta_{2,\mathrm{FLC4}} \end{array} \right\}. \tag{3.8}$$

The $\mathbf{W}$ matrix is then constructed by the four Stokes vectors

$$\mathbf{W} = [\vec{S}_1, \vec{S}_2, \vec{S}_3, \vec{S}_4], \tag{3.9}$$

generated by the combination of the orientation states

$$\begin{aligned} \vec{S}_k(\lambda, \hat{\theta}) = \mathbf{M}_{\mathrm{ret.}}(\theta_{i,\mathrm{FLC2}}, \delta_{\mathrm{FLC2}}(\lambda))\mathbf{M}_{\mathrm{ret.}}(\theta_{\mathrm{WP2}}, \delta_{\mathrm{WP2}}(\lambda)) \\ \times \mathbf{M}_{\mathrm{ret.}}(\theta_{j,\mathrm{FLC1}}, \delta_{\mathrm{FLC1}}(\lambda))\mathbf{M}_{\mathrm{ret.}}(\theta_{\mathrm{WP1}}, \delta_{\mathrm{WP1}}(\lambda))\mathbf{M}_{\mathrm{pol.}}[1,0,0,0]^T, \end{aligned} \tag{3.10}$$

where also two fixed retarders ($\mathbf{M}_{\mathrm{ret.}}(\theta_{\mathrm{WP}}, \delta_{\mathrm{WP}}(\lambda))$) are included to ensure a broadband low condition number. $\mathbf{M}_{\mathrm{ret.}}$ is the Mueller matrix of the retarder with dispersive retardance $\delta(\lambda)$, oriented at an angle θ relative to the transmission axis of the polarizer ($\mathbf{M}_{\mathrm{pol.}}$). The indices j and i refer to the state of FLC1 and FLC2 respectively. Similarly, the system matrix of the PSA is constructed from four analyzing Stokes vectors ($\vec{A}$)

$$\mathbf{A} = [\vec{A}_1, \vec{A}_2, \vec{A}_3, \vec{A}_4]^T. \tag{3.11}$$

Accounting for the reverse order of the components, the polarization states are found in the same manner as above

$$\begin{aligned} \vec{A}_k(\lambda, \hat{\theta}) = [1,0,0,0]^T\mathbf{M}_{\mathrm{pol.}}\mathbf{M}_{\mathrm{ret.}}(\theta_{\mathrm{WP4}}, \delta_{\mathrm{WP4}}(\lambda))\mathbf{M}_{\mathrm{ret.}}(\theta_{j,\mathrm{FLC4}}, \delta_{\mathrm{FLC4}}(\lambda)) \\ \times \mathbf{M}_{\mathrm{ret.}}(\theta_{\mathrm{WP3}}, \delta_{\mathrm{WP3}}(\lambda))\mathbf{M}_{\mathrm{ret.}}(\theta_{i,\mathrm{FLC3}}, \delta_{\mathrm{FLC3}}(\lambda)). \end{aligned} \tag{3.12}$$

Figure 3.4 shows a sketch of the FLC based polarimeter. The arrows show the direction of the light beam for the PSG and PSA.

3.3.2. Liquid crystal variable retarder based polarimeter

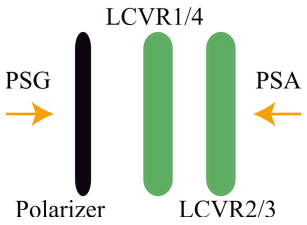

Figure 3.5.: A sketch of a polarimeter based on two LCVRs in the PSG and PSA. The retardance of each LCVR, and thus the polarization state of the instrument, can be controlled electrically.

The liquid crystal variable retarders (LCVR) are nematic LCs, where the molecules are disordered in position, but are all pointing in the same direction. At resting states they are aligned with the windows of the device, giving a high birefringence. When an electric field is applied, the molecules change alignment orientation to an angle depending of the electric field strength. The form birefringence of the LC ensures a minimum retardance at maximum field strength.

A broadband Mueller matrix polarimeter can be made by using a total of four LCVRs, as illustrated in Figure 3.5. The optimization of this polarimeter is related to choosing the azimuth orientation of the two components, relative to the polarizer, and selecting a combination of voltages giving the best condition number of the system matrices. The calculation and modeling of the system is accomplished by considering the Stokes vectors generated for a set of voltages $\hat{V}$ by

$$\vec{S}_k(\lambda, \hat{V}) = \mathbf{M}_{\text{ret.}}(\theta_{\text{LC2}}, \delta_{\text{LC2}}(V_i, \lambda))\mathbf{M}_{\text{ret.}}(\theta_{\text{LC1}}, \delta_{\text{LC1}}(V_j, \lambda)) \times \mathbf{M}_{\text{pol.}}[1, 0, 0, 0]^T \quad (3.13)$$

for the PSG, and

$$\vec{A}_k(\lambda, \hat{V}) = [1,0,0,0]^T \mathbf{M}_{\text{pol.}} \mathbf{M}_{\text{ret.}}(\theta_{\text{LC4}}, \delta_{\text{LC4}}(V_j, \lambda)) \times \mathbf{M}_{\text{ret.}}(\theta_{\text{LC3}}, \delta_{\text{LC3}}(V_i, \lambda)) \quad (3.14)$$

for the PSA. Note that for a system based on four LCVRs it is possible to generate more than the minimum four states in the PSG and PSA. The system is then said to be overdetermined.

3.4. Eigenvalue calibration for overdetermined polarimeters

For the calibration of the discrete state polarimeters described above the eigenvalue calibration method (ECM), developed by Compain *et al.* [81], was implemented. The only requirements of the calibration method are to have appropriate reference samples, and that at least one of their orientations are known. In order to probe all parts of $\mathbf{W}$ and $\mathbf{A}$, the properties of the reference samples must be sufficiently different. The instruments developed here were calibrated in transmission using two polarizers and one waveplate as calibration samples, in addition to the transmission measurement of air. A further development of the ECM to also handle overdetermined polarimeters with n states in the PSG and PSA was outlined in Paper 3, and is explained in more detail here. This calibration also works for systems with $n = 4$ states.

Let $\{\mathbf{M}\}$ be the set of reference samples and $\{\mathbf{B}\}$ the corresponding set of intensity matrices generated by Equation (3.7). The intensity matrix of air is simply $\mathbf{B}_0 = \mathbf{AW}$. Note that $\mathbf{B}_0$ is a matrix of size n^2.

Two sets of matrices $\{\mathbf{C}\}$ and $\{\mathbf{C}'\}$ are constructed as

$$\begin{aligned} \mathbf{C}_i &= \mathbf{B}_0^\dagger \mathbf{B}_i = (\mathbf{AW})^\dagger \mathbf{A} \mathbf{M}_i \mathbf{W} = \mathbf{W}^\dagger \mathbf{M} \mathbf{W}, \\ \mathbf{C}'_i &= \mathbf{B}_i \mathbf{B}_0^\dagger = \mathbf{A} \mathbf{M}_i \mathbf{W} (\mathbf{AW})^\dagger = \mathbf{AMA}^\dagger. \end{aligned} \quad (3.15)$$

Note that $\mathbf{C}$ is independent of $\mathbf{W}$ and $\mathbf{C}'$ of $\mathbf{A}$. $\mathbf{C}_i$ and $\mathbf{C}'_i$ are of sizes $n \times n$ and holds n eigenvalues. In the special case when $n = 4$, $\mathbf{C}_i$ and $\mathbf{C}'_i$ are similar to $\mathbf{M}_i$, and have similar eigenvalues, only modified by numerical and measurement noise. A general non-depolarizing Mueller matrix, with both diattenuation and retardance (*e.g.* reflection from a surface), has two real and two complex

eigenvalues. In terms of the transmission coefficient τ and the ellipsometry angles Ψ and Δ, of the non-depolarizing Mueller matrix in Equation 4.6, the eigenvalues are

$$\begin{aligned} \lambda_{r1} &= 2\tau\cos^2\Psi, & \lambda_{r2} &= 2\tau\sin^2\Psi, \\ \lambda_{c1} &= \tau\sin^2(2\Psi)\mathrm{e}^{-i\Delta}, & \lambda_{c2} &= \tau\sin^2(2\Psi)\mathrm{e}^{i\Delta}. \end{aligned} \tag{3.16}$$

By solving for τ, Ψ and Δ in the eigenvalues of $\mathbf{C}_i$, corresponding Mueller matrices of the reference samples can be constructed. The subscripts r and c denotes real and complex values respectively. One should note that for a pure polarizer the transmission coefficient can be found by taking the trace of $\mathbf{C}_i$

$$\tau_p = \mathrm{Tr}(\mathbf{C}_i). \tag{3.17}$$

For $n > 4$ the four eigenvalues of $\mathbf{C}_i$ and $\mathbf{C}'_i$ corresponding to the eigenvalues of $\mathbf{M}_i$ can in principal, when no noise is present, be found by comparing them to what is expected for the particular reference sample. However, noise makes this difficult. A suggested solution is to calculate a 4×4 matrix $\mathbf{C}_i^0$ and $\mathbf{C}_i'^0$ by choosing the 4×4 subset of $\mathbf{B}_0$ and $\mathbf{B}_i$ which has the lowest condition number in $\mathbf{B}_0$, ensuring minimal noise propagation when taking the inverse in the calculation of $\mathbf{C}_i^0$ and $\mathbf{C}_i'^0$.

The eigenvalues of $\mathbf{C}$ and $\mathbf{C}'$ do not directly give the orientations of the reference samples. They are, however, found in the process of calculating the system matrices $\mathbf{A}$ and $\mathbf{W}$. The system matrices are found by solving the sets of linear equations from Equation (3.15)

$$\begin{aligned} \mathbf{M}_i\mathbf{W} - \mathbf{W}\mathbf{C}_i &= 0, \\ \mathbf{A}\mathbf{M}_i - \mathbf{C}'_i\mathbf{A} &= 0. \end{aligned} \tag{3.18}$$

Letting $\vec{w}$ and $\vec{a}$ being $\mathbf{W}$ and $\mathbf{A}$ on vector form, Equation (3.18) can be rewritten as

$$\begin{aligned} \mathbf{H}_i\vec{w}^{4n} &= 0, \\ \mathbf{H}'_i\vec{a}^{4n} &= 0. \end{aligned} \tag{3.19}$$

Here $\mathbf{H}_i$ and $\mathbf{H}'_i$ are matrices of size $4n \times 4n$ calculated through linear trans-

formations of Equation (3.18)

$$\begin{array}{l} \mathbf{H}_i = \left[\begin{array}{cccc} \vec{g}_i^{\,1} & \vec{g}_i^{\,2} & \dots & \vec{g}_i^{\,4n} \end{array} \right], \\ \mathbf{H}'_i = \left[\begin{array}{cccc} \vec{g}_i^{\,\prime 1} & \vec{g}_i^{\,\prime 2} & \dots & \vec{g}_i^{\,\prime 4n} \end{array} \right], \end{array} \tag{3.20}$$

where $\vec{g}_i$ and $\vec{g}'_i$ are vectors constructed from the elements of the matrices $\mathbf{G}_i$ and $\mathbf{G}'_i$

$$\begin{array}{cc} \mathbf{G}_i^1 = \mathbf{M}_i\mathbf{U}^1 - \mathbf{U}^1\mathbf{C}_i, & \mathbf{G}_i'^1 = \mathbf{U}^1\mathbf{M}_i - \mathbf{C}_i\mathbf{U}^1, \\ \vdots & \vdots \\ \mathbf{G}_i^{4n} = \mathbf{M}_i\mathbf{U}^{4n} - \mathbf{U}^{4n}\mathbf{C}_i, & \mathbf{G}_i'^{4n} = \mathbf{U}^{4n}\mathbf{M}_i - \mathbf{C}_i\mathbf{U}^{4n}, \end{array} \tag{3.21}$$

where

$$\begin{array}{c} \mathbf{U}^1 = \left[\begin{array}{cccc} 1 & 0 & \dots & 0 \\ 0 & 0 & \dots & 0 \\ 0 & 0 & \dots & 0 \\ 0 & 0 & \dots & 0 \end{array} \right], \mathbf{U}^2 = \left[\begin{array}{cccc} 0 & 1 & \dots & 0 \\ 0 & 0 & \dots & 0 \\ 0 & 0 & \dots & 0 \\ 0 & 0 & \dots & 0 \end{array} \right], \\ \mathbf{U}^{n+1} = \left[\begin{array}{cccc} 0 & 0 & \dots & 0 \\ 1 & 0 & \dots & 0 \\ 0 & 0 & \dots & 0 \\ 0 & 0 & \dots & 0 \end{array} \right], \dots, \mathbf{U}^{4n} = \left[\begin{array}{cccc} 0 & 0 & \dots & 0 \\ 0 & 0 & \dots & 0 \\ 0 & 0 & \dots & 0 \\ 0 & 0 & \dots & 1 \end{array} \right]. \end{array} \tag{3.22}$$

At last, a total measurement matrix for all reference samples i can be constructed as

$$\begin{array}{l} \mathbf{K} = \sum_i \mathbf{H}_i^T \mathbf{H}_i, \\ \mathbf{K}' = \sum_i \mathbf{H}_i'^T \mathbf{H}'_i. \end{array} \tag{3.23}$$

The overdetermined solution to the system can then be found by solving the equations

$$\begin{array}{l} \mathbf{K}\vec{w} = 0, \\ \mathbf{K}'\vec{a} = 0 \end{array} \tag{3.24}$$

for $\vec{w}$ and $\vec{a}$, and arranging them into matrices again. In practice, when noise is present, the solutions are found by taking the eigenvector with the smallest eigenvalue (λ_{4n}). The orientation of the reference samples are also found by

minimizing the smallest eigenvalue of $\mathbf{K}$ and $\mathbf{K}'$, yielding the error functions

$$\epsilon_{\mathbf{W}} = \sum_{k=1}^{4n-1} \frac{\lambda_{4n}}{\lambda_k}, \qquad \epsilon_{\mathbf{A}} = \sum_{k=1}^{4n-1} \frac{\lambda'_{4n}}{\lambda'_k}. \tag{3.25}$$

In the case for the implementations in Papers 1, 3 and 5, the orientation of one polarizer was assumed known.

3.5. Mueller matrix imaging

Mueller matrix imaging provides information about lateral polarization properties of samples. By applying the decomposition methods to Mueller matrix images, physical parameters of the sample system can be analyzed. In this thesis Mueller matrix imaging was applied to mapping of strain fields in multi crystalline silicon, polarizing properties of anisotropic plasmonic thin films on quartz substrates, nematic textures in colloidal dispersions of synthetic clay and directional mapping of collagen fibers.

There are two main approaches to realize a Mueller matrix imager, the serial and parallel approach. In the serial approach the image is constructed by scanning the sample or the light beam, while in the parallel configuration an array detector is used. The easiest is to scan the sample, which is also the most time consuming. By using a scanning mirror to set the position of the light beam, fast serial acquisition can be accomplished. Parallel measurements using a 2D array detector have the advantage of no extra moving parts. The resolution and imaging area can also be chosen and changed easily by imaging optics.

When using a 2D array detector it can be advantageous to use a polarimeter technology with no mechanically moving parts. If a rotating compensator polarimeter was adapted to imaging purposes, extremely careful alignment would be necessary to avoid image wobble. Liquid crystal based polarimeters (FLCs and LCVRs) are better suited for the application. By using discrete states polarimeters for imaging purposes the integration time of the detector can be adjusted without having to change the speed of the rotating compensators.

3.5.1. Strain mapping in crystalline silicon wafers

Material waste is a limiting factor in the continuous effort for lower prices in the production of solar cells based on multi crystalline silicon. The major waste sources are wafer cutting and breakage. One of the main reasons for the latter is residual material strain and stress.

Strain is a displacement of the crystal structure of the material, induced by a force applied to the material over a given area, known as stress. Strain is also a major source for crystal dislocations [82], which degrades the quality of the electron transport and the recombination rate, and hence the efficiency. As silicon has a cubic diamond crystal lattice it is optically isotropic if the material is not strained.

Mueller matrix polarimetry is sensitive to the retardance (cf. Section 2.2). The retardance δ is simply the birefringence, which is the difference in refractive index $(n_e - n_o)$ for two axes of the material, for a medium thickness d, at at given wavelength λ

$$\delta = \frac{2\pi d}{\lambda}|\Delta n| = \frac{2\pi d}{\lambda}|n_e - n_o|. \tag{3.26}$$

The relation between strain and birefringence can be found by first considering the quadratic representation of the impermeability tensor

$$\sum_{i,j=1}^{3} \eta_{ij} x_i x_j = 1. \tag{3.27}$$

The elements η_{ij} are related to the dielectric tensor elements (ε_{ij}) and the refractive index (n_{ij}) of the material by $\eta_{ij} = \varepsilon_0/\varepsilon_{ij} = 1/n_{ij}^2$ [83]. In Figure 3.6, the refractive index ellipsoid is plotted using Equation (3.27), with the principle axes of the tensor $\boldsymbol{\eta}$ as the coordinate system.

A second rank strain tensor can be defined as [83]

$$\boldsymbol{\epsilon} = \begin{bmatrix} \epsilon_{11} & \epsilon_{12} & \epsilon_{13} \\ \epsilon_{12} & \epsilon_{22} & \epsilon_{23} \\ \epsilon_{13} & \epsilon_{23} & \epsilon_{33} \end{bmatrix} = \begin{bmatrix} \epsilon_1 & \epsilon_6 & \epsilon_5 \\ \epsilon_6 & \epsilon_2 & \epsilon_4 \\ \epsilon_5 & \epsilon_4 & \epsilon_3 \end{bmatrix}, \tag{3.28}$$

where the diagonal elements are the normal strain and the off-diagonal elements the shear strain. Within the elastic limits, a fourth rank photoelastic

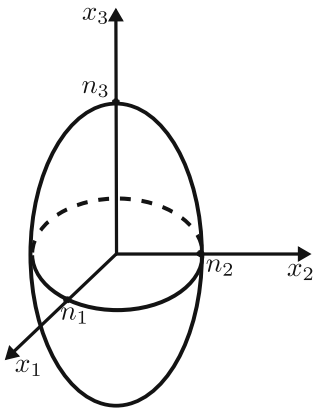

Figure 3.6.: The refractive index ellipsoid.

tensor $\boldsymbol{p}$, relating the strain to the change in the impermeability tensor, from the undeformed state $\boldsymbol{\eta^0}$ to deformed state $\boldsymbol{\eta}$ can be defined as

$$\boldsymbol{\eta} - \boldsymbol{\eta^0} = \boldsymbol{p\epsilon}. \tag{3.29}$$

In principal all 36 elements of $\boldsymbol{p}$ can be independent. The symmetry of the crystal will, however, in most cases reduce the number of independent parameters. For silicon, which has a diamond crystal structure with a full octahedral symmetry, the photoelastic tensor has only three independent parameters, resulting in [83],

$$\begin{bmatrix} \eta_1 - \eta_1^0 \\ \eta_2 - \eta_2^0 \\ \eta_3 - \eta_3^0 \\ \eta_4 - \eta_4^0 \\ \eta_5 - \eta_5^0 \\ \eta_6 - \eta_6^0 \end{bmatrix} = \begin{bmatrix} p_{11} & p_{12} & p_{12} & 0 & 0 & 0 \\ p_{12} & p_{11} & p_{12} & 0 & 0 & 0 \\ p_{12} & p_{12} & p_{11} & 0 & 0 & 0 \\ 0 & 0 & 0 & p_{44} & 0 & 0 \\ 0 & 0 & 0 & 0 & p_{44} & 0 \\ 0 & 0 & 0 & 0 & 0 & p_{44} \end{bmatrix} \begin{bmatrix} \epsilon_1 \\ \epsilon_2 \\ \epsilon_3 \\ \epsilon_4 \\ \epsilon_5 \\ \epsilon_6 \end{bmatrix}. \tag{3.30}$$

Because silicon is an anisotropic material, the values of the photoelastic tensor is not equal for all crystal orientations. For simplicity, the tensor is usually given in the lattice frame. The tensor can be rotated using Euler rotations to the particular crystal orientation.

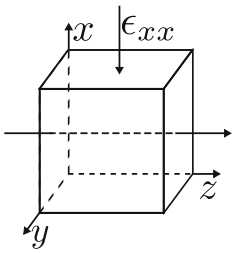

Figure 3.7.: Normal strain applied in the x-direction of a cubic solid with light propagating in the z-direction.

Let for simplicity a linear normal strain $\epsilon_{xx} = \epsilon_1$ be applied to a solid in the x-direction. If light is passing through the solid in the z-direction, illustrated in Figure 3.7, a simple expression can be found for the induced birefringence. In terms of the index ellipsoid, using the principal axes as the coordinate system, the surface perpendicular to the direction of light propagation is

$$\eta_1 x^2 + \eta_3 y^2 = 1. \tag{3.31}$$

By assuming that the crystal is optically isotropic in the undeformed state, the birefringence can be found by

$$\eta_1 - \eta_2 = (p_{11} - p_{12})\epsilon_1. \tag{3.32}$$

The left-hand side of the expression can be rewritten as

$$\begin{aligned} \eta_1 - \eta_2 &= \frac{1}{n_1^2} - \frac{1}{n_2^2}, \\ &= \frac{n_2^2 - n_1^2}{n_1^2 n_2^2}, \\ &\approx -\frac{(n_1 - n_2)(n_1 + n_2)}{n_0^4}, \\ &\approx -\frac{2\Delta n}{n_0^3}, \end{aligned} \tag{3.33}$$

Here it was assumed that the refractive indices are only slightly perturbed.

Solving for the birefringence yields

$$\Delta n = \frac{n_0^3}{2}(p_{11} - p_{12})\epsilon_1. \tag{3.34}$$

The retardance can now be found using Equation (3.26). The retardance gives the magnitude of the strain, while the orientation of the fast axis (see Section 2.2) gives the direction.

The disadvantage of using Mueller matrix imaging to image strain fields in bulk material is that the atomic displacement is not measured directly, as can be done by x-ray scattering [84] and electron microscopy [85]. Hence, polarimetry requires that one direction in the material is undeformed.

3.6. Overview of results

Design and implementation of spectroscopic Stokes and Mueller matrix polarimeters is a large part of this thesis, as described in Paper 1, 2, 3 and 4. A ferroelectric liquid crystal based polarimeter was adapted to imaging, and applied to the characterization of strain in multi-crystalline silicon (Paper 5), a plasmonic polarizer (Paper 6), collagen fiber meshwork (Paper 7 and 8) and nematic textures in colloidal dispersions of synthetic clay (Paper 9).

3.6.1. Polarimeter design

In order to optimize the Stokes and Mueller polarimeters using FLCs and LCVRs, the properties of the components have to be known very precisely. Both the intrinsic retardance of the FLCs and the voltage dependent retardance of the LCVRs were characterized in the visible and the near infrared spectral range. The dynamic response of the FLC based Mueller matrix polarimeter was studied in order to realize fast measurements. When waiting for steady state upon FLCs switching, a complete Mueller matrix could be measured in 16 ms. By not waiting for the steady state, the measurement time could be decreased to 8 ms within reasonable accuracy. Using these settings, the temporal Mueller matrix of a LCVR during the (150 ms long) switching could be measured.

FLC based Mueller matrix polarimeters have the advantage of being fast. LCVRs have a much longer transition time when changing states, but are

more modular as the retardance can be varied continuously within a predefined range. For the optimization of polarimeters based on both FLCs and LCVRs, a genetic algorithm was developed. Several designs for overdetermined polarimetry were explored, resulting in an improved condition number over a broader spectral range. Genetic algorithms were used because of the strong efficiency when searching in large search spaces with many local minima. In particular, Figure 3.8 shows the search landscape for two of the 12 dimensions of an overdetermined Stokes polarimeter based on three FLCs.

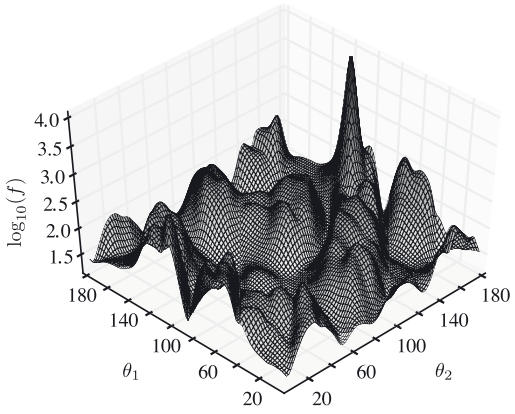

Figure 3.8.: The fitness landscape for two of the in total 12 dimensions for the optimized design using three FLCs. θ_1 and θ_2 are the azimuth orientation of one of the FLCs and waveplates respectively. The figure is from Paper 4.

Figure 3.9(a) shows the spectral inverse condition number of simulated LCVR designs using four, six and eight states in the Stokes polarimeter. In Figure 3.9(b), the simulated, measured and calibrated inverse condition number for the realized six states Stokes polarimeter are shown. For a full Mueller matrix measurement, the three designs require 4×4, 6×6 and 8×8 intensity measurements. By going from four to six states the condition number is improved considerably on the edge of the spectrum, while the increase from six

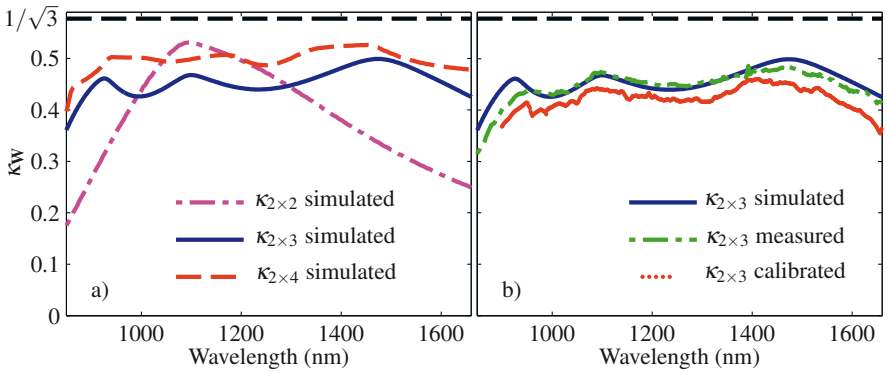

Figure 3.9.: Spectral inverse condition number for the LCVR polarimeter. a) shows the simulated spectral condition number for designs using four, six and eight states in the PSG and PSA. b) shows the simulated, experimentally measured and calibrated spectral condition numbers for the realized six states design. The figure is from Paper 3.

to eight states does not improve the condition number enough compared to the increased measurement time when going from 36 to 64 intensity measurements.

3.6.2. Mueller matrix imaging

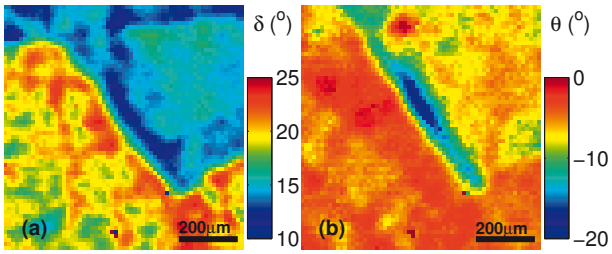

Figure 3.10.: Figure (a) shows the linear retardance (δ), while (b) shows the orientation of the slow axis (θ) of the same area. In this particular there are two grains of different orientation. The figure is from Paper 5.

Through the arguments of Section 3.5.1, the Mueller matrix imaging polarimeter was applied to strain mapping of a multi-crystalline silicon wafer. For a proof of concept, strain was induced through buckling, while the wafer was mounted in a custom made sample holder. Figure 3.10 shows the linear retardance and the orientation of the slow axis at the boundary area between two crystal grains. There is a large difference in retardance between the two grains. In the present study, the grain orientations were not known, such that an estimate of the explicit strain could not be found. At the grain boundary the retardance is lower, and the orientation of the strain is remarkably different compared to inside the grain. Currently, it can only be speculated if there is a relaxation of strain at the boundary.

Mueller matrix imaging was applied to directional mapping of collagen fibers in biological tissue in Paper 7 and 8. Collagen fibers form as bundles of long

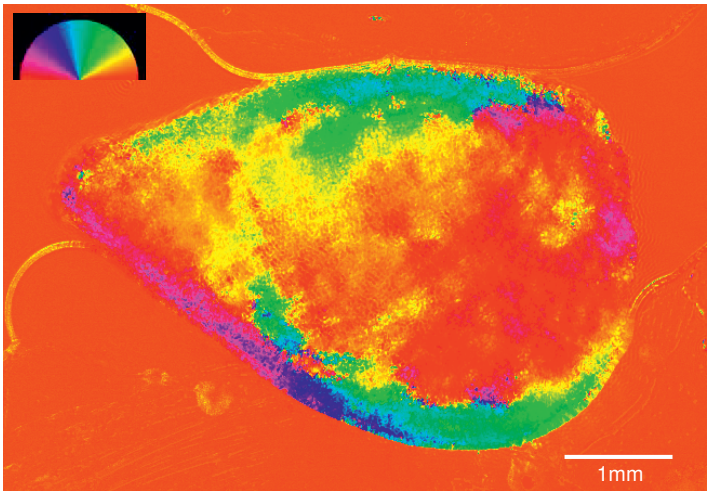

Figure 3.11.: The orientation of the slow axis of the decomposed Mueller matrix retardation image. The same axis correspond to the orientation of the collagen fibers. The figure is from Paper 7.

were studied by Mueller matrix imaging. The clay particles are discs with thickness 1 nm, with a lateral size up to 1μm. In an aqueous solution, under the influence of gravity, the particles separate into phases with distinct regions of different concentration and ordering. The shape of the particles results in a birefringent effective medium, where the retardance depends on the concentration and orientations of the particles. Figure 3.12 shows a retardance map of the transition from an isotropic domain to an anisotropic domain. The red lines show the direction of the fast axis, corresponding to the direction of the normal axis of the particles.

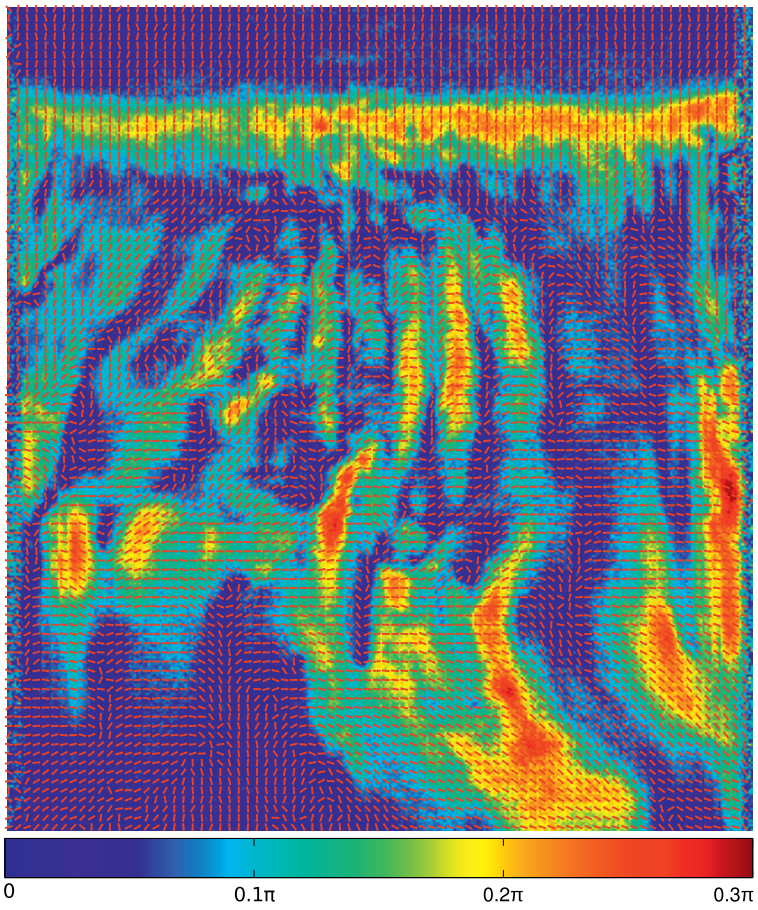

Figure 3.12.: The retardance image (color map) and the orientation of the fast axis (red lines) for a transitional area in the synthetic clay. The figure is from Paper 9.

4. Spectroscopic Mueller matrix ellipsometry

Ellipsometry is a polarimetric measurement technique referred to when measuring the change in amplitude and phase between two orthogonal electric field components upon specular reflection from a smooth surface. In ellipsometry the orthogonal field components are usually defined as parallel ($\vec{E}_p$) and perpendicular ($\vec{E}_s$) to the plane of incidence, as illustrated in Figure 4.1. There are three different classes of ellipsometry. In order of increasing number of measured parameters they are denoted: *standard*, *generalized* and *Mueller matrix* ellipsometry.

4.1. Standard ellipsometry

By considering the boundary conditions of Maxwell's equation, one can arrive at Fresnel's reflection coefficients for $\vec{E}_s$ and $\vec{E}_p$

$$r_p = \frac{\tilde{n}_2 \cos\vartheta_1 - \tilde{n}_1 \cos\vartheta_2}{\tilde{n}_2 \cos\vartheta_1 + \tilde{n}_1 \cos\vartheta_2}, \qquad r_s = \frac{\tilde{n}_1 \cos\vartheta_1 - \tilde{n}_2 \cos\vartheta_2}{\tilde{n}_1 \cos\vartheta_1 + \tilde{n}_2 \cos\vartheta_2}, \tag{4.1}$$

where $\tilde{n}_1$ and $\tilde{n}_2$ are the complex refractive indices of the two materials, and ϑ_1 and ϑ_2 are the incident and refracted angles, see Figure 4.1. These can be inserted into the Jones transfer matrix, resulting in

$$\begin{bmatrix} E_p \\ E_s \end{bmatrix}^{\text{refl.}} = \begin{bmatrix} r_p & 0 \\ 0 & r_s \end{bmatrix} \begin{bmatrix} E_p \\ E_s \end{bmatrix}^{\text{in}}, \tag{4.2}$$

which is used to calculate the reflected polarization state.

For a stack of isotropic thin films, the so called Abeles 2×2 transfer matrix formalism [19], or the similar 2×2 scattering matrix formalism [19] can be used to calculate the reflection coefficients r_p and r_s for the multilayer system.

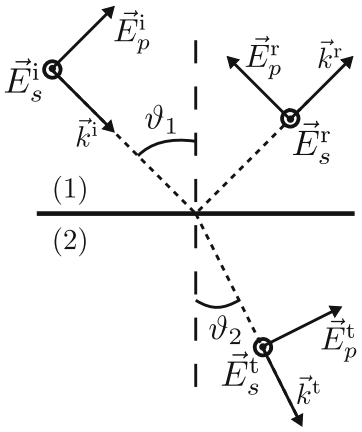

Figure 4.1.: Sketch of the electric field components for light reflected and refracted by a smooth interface between two materials [22]. The superscripts i, r and t denotes incident, reflected and transmitted field respectively.

Another common approach is to use the recursive Airy type formulas for the reflection coefficients [19, 86].

In the *standard* ellipsometry configuration, one commonly set $\vec{J}^{\mathrm{in}} = [1, 1]^T$, and measure the relative difference in amplitude ($\tan\Psi$) and phase (Δ) for the two reflected components. This results in a relation for the ratio of the two reflection coefficients

$$\rho = \frac{r_p}{r_s} = \tan\Psi \mathrm{e}^{i\Delta}. \tag{4.3}$$

The ellipsometric angles Ψ and Δ are typically found through a Fourier analysis of the reflected light modulated by a photoelastic modulator (PEM) or a rotating polarizer compensator.

4.2. Generalized ellipsometry

For reflections from materials having anisotropic properties, *i.e.* the index of refraction is direction dependent, there will be a coupling between the orthog-

onal field components. The Jones matrix is then generalized to

$$\begin{bmatrix} E_p \\ E_s \end{bmatrix}^{\text{refl.}} = \begin{bmatrix} r_{pp} & r_{ps} \\ r_{sp} & r_{ss} \end{bmatrix} \begin{bmatrix} E_p \\ E_s \end{bmatrix}^{\text{in}}. \tag{4.4}$$

The normalized Jones matrix can be obtained in the same manner as for the isotropic case, giving the generalized ratios, and generalized ellipsometric parameters

$$\rho_{pp} = \frac{r_{pp}}{r_{ss}} = \tan\Psi_{pp} e^{i\Delta_{pp}},\ \rho_{ps} = \frac{r_{ps}}{r_{ss}} = \tan\Psi_{ps} e^{i\Delta_{ps}},\ \rho_{sp} = \frac{r_{sp}}{r_{ss}} = \tan\Psi_{sp} e^{i\Delta_{sp}}. \tag{4.5}$$

These parameters can in principle be measured using a *standard* ellipsometer. For example, the PEM based ellipsometer (*e.g.* the UVISEL, commercialized by Horiba Jobin Yvon) can be generalized to measure the three first columns of the Mueller matrix [25,87]. Similarly, the common rotating analyzer with fixed compensator system (*e.g.* the VASE system commercialized by J.A. Woollam) can be generalized to measure the 3 first rows of the Mueller matrix. The complete Mueller Jones matrix (Equation (2.13)) may in both cases be estimated, and hence the corresponding general Jones matrix can be derived [25]. Dedicated configurations with continuously rotating compensator does also exist (*e.g.* the M2000, commercialized by J.A. Woollam).

4.3. Mueller matrix ellipsometry

In terms of the ellipsometric angles, the Mueller matrix corresponding to a reflection from an isotropic interface is

$$\mathbf{M}_{\text{iso}} = \frac{|r_p|^2 + |r_s|^2}{2} \begin{bmatrix} 1 & -\cos 2\Psi & 0 & 0 \\ \cos 2\Psi & 1 & 0 & 0 \\ 0 & 0 & \sin 2\Psi \cos\Delta & \sin 2\Psi \sin\Delta \\ 0 & 0 & -\sin 2\Psi \sin\Delta & \sin 2\Psi \cos\Delta \end{bmatrix}. \tag{4.6}$$

Note that the matrix is usually reported normalized to the m_{11} element. The unnormalized m_{11} is the reflectance for unpolarized light.

For reflection from anisotropic samples, the Mueller matrix can be calculated in terms of the reflection coefficients using Equation (2.14)

$$\mathbf{M}_{\text{aniso}} = \begin{bmatrix} \frac{1}{2}(|r_{pp}|^2 + |r_{sp}|^2 + |r_{ps}|^2 + |r_{ss}|^2) & \frac{1}{2}(|r_{pp}|^2 + |r_{sp}|^2 - |r_{ps}|^2 - |r_{ss}|^2) & \dots \\ \frac{1}{2}(|r_{pp}|^2 - |r_{sp}|^2 + |r_{ps}|^2 - |r_{ss}|^2) & \frac{1}{2}(|r_{pp}|^2 - |r_{sp}|^2 - |r_{ps}|^2 + |r_{ss}|^2) & \dots \\ \mathrm{Re}(r_{pp}r_{sp}^* + r_{ps}r_{ss}^*) & \mathrm{Re}(r_{pp}r_{sp}^* - r_{sp}r_{ss}^*) & \dots \\ -\mathrm{Im}(r_{pp}r_{sp}^* + r_{ps}r_{ss}^*) & -\mathrm{Im}(r_{pp}r_{sp}^* - r_{ps}r_{ss}^*) & \dots \end{bmatrix}$$

$$\begin{bmatrix} \mathrm{Re}(r_{pp}r_{ps}^* + r_{sp}r_{ss}^*) & \mathrm{Im}(r_{pp}r_{ps}^* + r_{sp}r_{ss}^*) \\ \mathrm{Re}(r_{pp}r_{ps}^* - r_{sp}r_{ss}^*) & \mathrm{Im}(r_{pp}r_{ps}^* - r_{sp}r_{ss}^*) \\ \mathrm{Re}(r_{pp}r_{ss}^* + r_{ps}r_{sp}^*) & \mathrm{Im}(r_{pp}r_{ss}^* - r_{ps}r_{sp}^*) \\ -\mathrm{Im}(r_{pp}r_{ss}^* + r_{ps}r_{sp}^*) & \mathrm{Re}(r_{pp}r_{ss}^* - r_{ps}r_{sp}^*) \end{bmatrix}. \quad (4.7)$$

In generalized ellipsometry only a subset of the Mueller matrix is measured, typically three rows or three columns. This is enough to calculate the normalized Jones matrix, and the rest of the elements of the Mueller matrix, if, and only if there is no depolarization. Depolarization may arise from thickness inhomogeneity, angular spread of the incoming light, the finite bandwidth of the instrument, backside reflections from thick layers or substrates, or scattering effects due to roughness. If the complete Mueller matrix is measured, the depolarizing effects can be taken into account when modeling the sample.

Certain depolarization phenomena can be handled accurately in standard ellipsometry as long as the sample is isotropic. However, when the sample is additionally anisotropic, standard ellipsometry cannot properly separate the two effects, and a complete Mueller matrix is required in order for an accurate modeling of the optical response of the sample.

4.4. Ellipsometric modelling

For the simplest case illustrated in Figure 4.1, *i.e.* reflection from a smooth clean and infinitely thick substrate, the refractive index can be calculated directly from an ellipsometric measurement, using Equation (4.1) and (4.3). When introducing layered structures, solving the system is commonly done by making a model and simulating the measurement. The model parameters resulting in the best fit between measurements and simulated data are commonly found iteratively. Not only dielectric functions and thicknesses of the layers, but also derived parameters such as surface roughness, material composition, crystallinity, anisotropy, uniformity and interface mixing, can be used

as model parameters.

4.4.1. Dielectric functions

The dielectric function ε is a frequency dependent intrinsic property of a material describing the relation between an applied electric field and the induced displacement field (in Gaussian units) [88]

$$\begin{aligned} \vec{D} &= \varepsilon_0 \varepsilon \vec{E}, \\ &= \vec{E} + 4\pi \vec{P}, \end{aligned} \tag{4.8}$$

where ε_0 is the electric permittivity in vacuum, and $\vec{P}$ the polarization field. In general, ε is complex and a function of the frequency of the electric field $\varepsilon(\omega) = \varepsilon_1(\omega) + i\varepsilon_2(\omega)$. From the dielectric function the complex refractive index is calculated as

$$\tilde{n}^2 = (n - i\kappa)^2 = \varepsilon = \varepsilon_1 + i\varepsilon_2, \tag{4.9}$$

In the classical Lorentz theory of optical properties for matter, charged particles are treated as simple harmonic oscillators subject to a driving force from an applied electromagnetic field. This classical approach gives the same results as for the quantum mechanical approach. The Lorentz model for the dielectric function as a function of photon energy is [89]

$$\tilde{\varepsilon}_{\text{Lor.}}(E) = \varepsilon_1 + i\varepsilon_2 = 1 + \frac{E_p^2}{E_0^2 - E^2 - i\gamma E}, \tag{4.10}$$

where the oscillator amplitude is defined by the plasma energy E_p, the center energy E_0 and the broadening of the oscillator γ. It can be used to describe many features of optical excitations, although, in some cases corrections are required in order to resemble experimental data better. One such correction is the Tauc-Lorentz oscillator [90], which is a Kramers-Kronig consistent modification of the Forouhi-Bloomer oscillator [91]. The Tauc-Lorentz model adds a correction to the imaginary part of the dielectric function near the band-gap

E_g of the material

$$\varepsilon_{\text{2Tauc-L.}} = \begin{cases} \frac{(E_0-E_g)^2}{E_0^2} \cdot \varepsilon_{\text{2Lor.}}, & E > E_g \\ 0, & E < E_g. \end{cases} \tag{4.11}$$

The real part of the dielectric function is found by Kramers–Kronig integration of $\varepsilon_{\text{2Tauc-L.}}$ [90]. It is mainly used for parametrization of the dielectric function of amorphous materials.

Applying the classical approach of Lorentz to free electrons, the dielectric function is found to be similar to the Lorentz oscillator when letting the center energy be zero. It then becomes the Drude oscillator, with the dielectric function given by [89]

$$\varepsilon_{\text{Drude}}(E) = 1 - \frac{E_p^2}{E^2 + i\gamma E}. \tag{4.12}$$

Parametrization of the dielectric function of materials using Kramers-Kronig consistent oscillator models is a common method where properties such as electronic band structures, doping levels, band-gap and conductivity, among others, can be estimated.

Anisotropic dielectric function tensor

For non-cubic solids and other anisotropic media, the dielectric function must be represented by a complex-valued second rank tensor $\boldsymbol{\varepsilon}$, which, expressed in Cartesian coordinates, is [92]

$$\vec{D} = \tilde{\varepsilon}_0 \boldsymbol{\varepsilon} \vec{E} = \tilde{\varepsilon}_0 \begin{pmatrix} \varepsilon_{xx} & \varepsilon_{xy} & \varepsilon_{xz} \\ \varepsilon_{yx} & \varepsilon_{yy} & \varepsilon_{yz} \\ \varepsilon_{zx} & \varepsilon_{zy} & \varepsilon_{zz} \end{pmatrix} \vec{E}. \tag{4.13}$$

Here the displacement field $\vec{D}$ and electric field $\vec{E}$ are defined along the unit directions $\hat{x}$, $\hat{y}$ and $\hat{z}$.

The relation between the laboratory frame of reference (x, y, z) and that of the material (ξ, η, ζ), can be obtained by an Euler rotation [93]

$$\boldsymbol{\varepsilon}(x, y, z) = \mathbf{A}(\varphi, \theta, \psi) \boldsymbol{\varepsilon}(\xi, \eta, \zeta) \mathbf{A}(-\varphi, -\theta, -\psi), \tag{4.14}$$

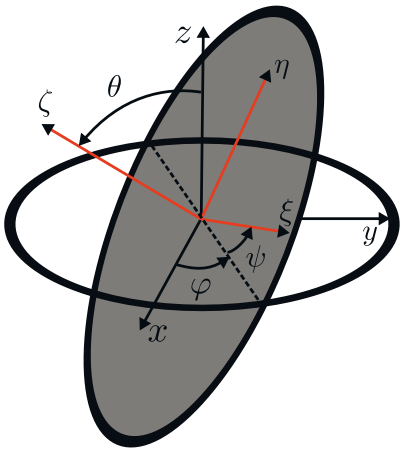

Figure 4.2.: Schematic defining the generalized Euler angles φ, θ and ψ used for a general Cartesian coordinate system rotation.

where the rotation angles (φ, θ, ψ) are defined in Figure 4.2, and the rotation matrix defined as [93]

$$\mathbf{A}(\varphi,\theta,\psi) = \begin{bmatrix} \cos\psi & \sin\psi & 0 \\ -\sin\psi & \cos\psi & 0 \\ 0 & 0 & 1 \end{bmatrix} \begin{bmatrix} 1 & 0 & 0 \\ 0 & \cos\theta & \sin\theta \\ 0 & -\sin\theta & \cos\theta \end{bmatrix} \begin{bmatrix} \cos\varphi & \sin\varphi & 0 \\ -\sin\varphi & \cos\varphi & 0 \\ 0 & 0 & 1 \end{bmatrix} \tag{4.15}$$

For orthorhombic, tetragonal, hexagonal and trigonal symmetries, the rotation angles can be found such that $\boldsymbol{\varepsilon}$ is diagonal in (ξ, η, ζ)

$$\boldsymbol{\varepsilon} = \mathbf{A}(\varphi,\theta,\psi) \begin{pmatrix} \varepsilon_\xi & 0 & 0 \\ 0 & \varepsilon_\eta & 0 \\ 0 & 0 & \varepsilon_\zeta \end{pmatrix} \mathbf{A}(-\varphi,-\theta,-\psi). \tag{4.16}$$

4.4.2. Effective medium theories

Heterogeneous materials with a local structure sufficiently smaller than the wavelength of the probing electromagnetic field can be considered as a homogeneous material with effective optical properties. This makes it possible,

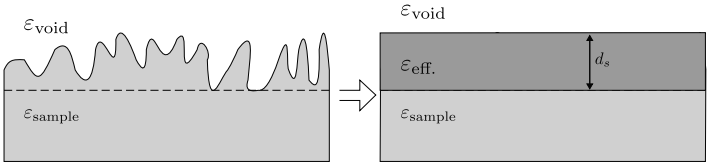

Figure 4.3.: Surface roughness is commonly modeled using effective medium theories.

using ellipsometry, to measure and analyze *e.g.* nanostructured surfaces (Paper 10 and 11) or roughness of smooth surfaces, as illustrated in Figure 4.3. Different effective medium theories and formulas for the mixing of the materials exist [94, 95]. These may give access to volume fill factors and inclusion shapes. The common effective medium theories are all based on the Clausius-Mossotti relation which relates the microscopic electric field response from a lattice structure of dipoles to the macroscopic observable response, the dielectric function [95].

Following the derivation of Aspnes [95] (using Gaussian units), it is assumed that a uniform internal electric field $\vec{E}_{\text{int}}$ is applied to a microscopic lattice structure of dipoles (quasi-static approximation), with polarizability α, extending to infinity. Resulting in a local dipole $\vec{p}_i = \alpha\vec{E}(\vec{R}_i)$ at every lattice point $\vec{R}_i$. Assuming a cubic lattice, symmetry ensures that the electric field at each lattice point is the same local field $\vec{E}(\vec{R}_i) = \vec{E}_{\text{loc.}}$.

The electric field at an arbitrary location in space $\vec{E}(\vec{r})$ can be found by the sum of the applied electric field and the electric field induced by all dipoles [95]

$$\vec{E}(\vec{r}) = \vec{E}_{\text{int}} + \sum_i \vec{E}(\vec{p}_i, \vec{r} - \vec{R}_i), \tag{4.17}$$

where

$$\vec{E}(\vec{p}, \vec{r}) = -\nabla\left(\frac{\vec{p}\cdot\hat{r}}{r^2}\right) = \frac{3(\vec{p}\cdot\hat{r}) - \vec{p}}{r^3}$$

is the electric field at a distance $\vec{r}$ from a dipole with dipole moment $\vec{p}$. Simi-

is the electric field at a distance $\vec{r}$ from a dipole with dipole moment $\vec{p}$. Similarly the polarizability at the position $\vec{r}$ is

$$\vec{p}(\vec{r}) = \sum_i \alpha \vec{E}(\vec{R}_i)\delta(\vec{r} - \vec{R}_i), \tag{4.18}$$

where the delta function (δ) is introduced because the dipoles are only located on the lattice sites.

The local electric field at the origin ($\vec{r} = 0$) can now be calculated as [95]

$$\begin{aligned} E_{\text{loc}} = \vec{E}(0) &= \vec{E}_{\text{int}} + \sum_{i \neq 0} \vec{E}(\alpha \vec{E}_{\text{loc}}, \vec{R}_i) \\ &= \vec{E}_{\text{int}}, \quad \text{for high symmetries.} \end{aligned} \tag{4.19}$$

In Equation (4.19), the sum is over all dipoles except the singular point of $\vec{R} = 0$. Because of the symmetry of the cubic lattice this sum goes to zero. Thus, the local dipole moment and electric field can be found for all $\vec{r}$ in terms of the local microscopic parameters and the applied electric field

$$\vec{E}(\vec{r}) = \vec{E}_{\text{loc}} + \sum_i \vec{E}(\alpha \vec{E}_{\text{loc}}, \vec{r} - \vec{R}_i), \tag{4.20a}$$

$$\vec{p} = (\vec{r}) = \sum_i \alpha \vec{E}_{\text{loc}} \delta(\vec{r} - \vec{R}_i). \tag{4.20b}$$

The macroscopic polarization $\vec{P}$ is found by taking the appropriate volume integral of Equation (4.20b)

$$\vec{P} = \frac{1}{V} \int_V d^3 r \, \vec{p}(\vec{r}) = N \alpha \vec{E}_{\text{loc}}, \tag{4.21}$$

where N is the number of dipoles per unit volume. Similarly the macroscopic electric field can be found by integrating Equation (4.20a)

$$\begin{aligned} \vec{E} = \int_V \vec{E}(\vec{r}) &= \vec{E}_{\text{loc}} - \frac{4\pi}{3} N \alpha \vec{E}_{\text{loc}} \\ &= \vec{E}_{\text{loc}} - \frac{4\pi}{3} \vec{P}. \end{aligned} \tag{4.22}$$

A result which shows that, due to the local opposing electric field generated

by the dipoles, the applied microscopically uniform field $\vec{E}_{\text{int}}$ is actually larger than the apparently applied macroscopic uniform field $\vec{E}$ [95].

By substituting Equations (4.22) and (4.21) in the equation for the macroscopic response (4.8), the Clausius-Mossotti relation is found [95]

$$\frac{\varepsilon - 1}{\varepsilon + 2} = \frac{4\pi}{3} N\alpha. \tag{4.23}$$

The Clausius-Mossotti relation is derived for a homogeneous material, but the microscopical approach above may also be used to treat heterogeneous materials.

Letting two different polarizabilities α_a and α_b be assigned uniformly at random lattice sites in the cubic lattice, Equations (4.17) and (4.18) will remain the same. Also, the high symmetry argument of Equation (4.19) still holds such that $\vec{E}_{\text{loc}} = \vec{E}_{\text{int}}$. The volume averages are then

$$\vec{P} = (N_a\alpha_a + N_b\alpha_b)\vec{E}_{\text{loc}}, \tag{4.24a}$$

$$\vec{E} = \vec{E}_{\text{loc}} - \frac{4\pi}{3}\vec{P}, \tag{4.24b}$$

where N_a and N_b are the number of dipoles per unit volume of each type. It follows that

$$\frac{\varepsilon - 1}{\varepsilon + 2} = \frac{4\pi}{3}(N_a\alpha_a + N_b\alpha_b). \tag{4.25}$$

The Clausius-Mossotti equation can be used to rewrite the material a and b in terms of their dielectric function ε_a and ε_a and their volume fill fractions f_a and f_b

$$\frac{\varepsilon - 1}{\varepsilon + 2} = f_a\frac{\varepsilon_a - 1}{\varepsilon_a + 2} + f_b\frac{\varepsilon_b - 1}{\varepsilon_b + 2}, \tag{4.26}$$

which is known as the Lorentz-Lorenz effective medium equation [95]. By adding more terms, Equation (4.26) can be expanded to any number of materials.

The Lorentz-Lorenz equation assumes a uniform mixing of the dipoles of the constituent materials. More commonly, heterogeneous materials consists of microscopic regions sufficiently smaller than the wavelength of light, but large enough to have a defined dielectric property, as for the surface roughness

illustrated in Figure 4.3.

The simplest case is to consider spherical inclusions with dielectric function ε_a and radius r_a embedded in a medium with dielectric function ε_b. For an applied electric field $\vec{E}_0$, the local electric field at position $\vec{r}$ is [88]

$$\vec{E}(\vec{r}) = \begin{cases} \frac{3\varepsilon_b}{\varepsilon_a+2\varepsilon_b}\vec{E}_0 & |\vec{r}| < r_a \\ \vec{E}_0 + \vec{E}(\vec{p}_a, \vec{r}) & |\vec{r}| > r_a, \end{cases}, \tag{4.27}$$

and the dipole moment of the sphere is [88]

$$\vec{p}_a = \alpha_a \vec{E}_0 = \frac{\varepsilon_a - \varepsilon_b}{\varepsilon_a + 2\varepsilon_b} r_a^3 \vec{E}_0, \tag{4.28}$$

where α_a is the polarizability of the sphere. By rewriting Equation (4.8) to $\vec{P}_i(\vec{r}) = \frac{\varepsilon_i - 1}{4\pi}\vec{E}(\vec{r})$, where $i = a$ or b, and taking the volume averages, the expression for the Maxwell-Garnett effective medium equation is found

$$\frac{\varepsilon - \varepsilon_b}{\varepsilon + 2\varepsilon_b} = f_a \frac{\varepsilon_a - \varepsilon_b}{\varepsilon_a + 2\varepsilon_b}, \tag{4.29}$$

where f_a is the volume fraction of phase a.

In the Maxwell-Garnett effective medium equation the effective dielectric function is different when interchanging the two media. For some systems the latter is correct, but for example, in the case of surface roughness (Figure 4.3) it is not clear which is embedded in the other. Bruggeman [96] suggested that the two media both were inclusions in the effective medium itself. Which can be accomplished by comparing the Lorentz-Lorenz and Maxwell-Garnett equations and acknowledging that they are in fact of the same form, where a more general effective medium equation can be considered as

$$\frac{\varepsilon - \varepsilon_h}{\varepsilon + 2\varepsilon_h} = f_a \frac{\varepsilon_a - \varepsilon_h}{\varepsilon_a + 2\varepsilon_h} + f_a \frac{\varepsilon_b - \varepsilon_h}{\varepsilon_b + 2\varepsilon_h}, \tag{4.30}$$

where ε_h is the dielectric function of the host medium. By letting $\varepsilon_h \equiv \varepsilon$ in Equation (4.30) the Bruggeman effective medium approximation is

$$0 = f_a \frac{\varepsilon_a - \varepsilon}{\varepsilon_a + 2\varepsilon} + f_a \frac{\varepsilon_b - \varepsilon}{\varepsilon_b + 2\varepsilon}. \tag{4.31}$$

In principle, the effective medium approximations presented are all of the form

of Equation (4.30) and only differs by the choice of host material.

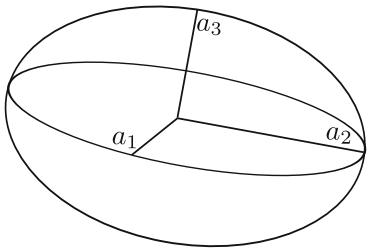

Figure 4.4.: An ellipsoid defining the three semi-axis a_1, a_2 and a_3

Spherical symmetry was assumed for all the derivations of the effective medium approximation above, if the inclusions have an ellipsoidal shape the induced microscopic polarization and electric field will depend on the polarization of the electric field. In specific, the polarizability along each semi-axis a_i of the ellipsoid (see Figure 4.4) is [94, 97]

$$\alpha_i = \frac{a_1 a_2 a_3}{3} \frac{\varepsilon_a - \varepsilon_b}{\varepsilon_b + L_i(\varepsilon_a - \varepsilon_b)}, \tag{4.32}$$

where L_i is the depolarization factor for each direction

$$L_i = \frac{a_1 a_2 a_3}{2} \int_0^\infty \frac{ds}{(s + a_i^2)\sqrt{(s + a_1^2)(s + a_2^2)(s + a_1^3)}}. \tag{4.33}$$

L_i must be in the range 0 to 1. The depolarization factors must also satisfy $\sum L_i = 1$. For a sphere, where $a_1 = a_2 = a_3$, the depolarization factors will be $[1/3, 1/3, 1/3]$. Considering the two limits of a disc and a needle, the depolarization factors are $[1, 0, 0]$ and $[0, 1/2, 1/2]$.

The Maxwell-Garnett generalized effective medium equation for ellipsoidal inclusions is [94, 98]

$$\frac{\varepsilon_i - \varepsilon_b}{\varepsilon_i + 3\varepsilon_b} = \frac{f_a}{3} \frac{\varepsilon_a - \varepsilon_b}{\varepsilon_b + L_i(\varepsilon_a - \varepsilon_b)}. \tag{4.34}$$

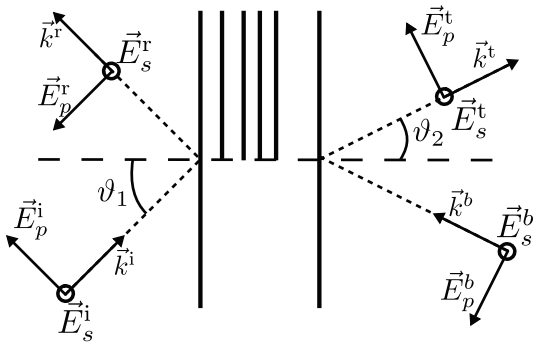

Figure 4.5.: Schematic illustration of the incidence, reflected, transmitted and back-travelling plane waves of a general multi layer structure [92].

Similarly, the generalized Bruggeman effective medium equation is [94,99–101]

$$0 = f_a \frac{\varepsilon_a - \varepsilon_i}{\varepsilon_i + L_i(\varepsilon_a - \varepsilon_i)} + f_b \frac{\varepsilon_b - \varepsilon_i}{\varepsilon_i + L_i(\varepsilon_b - \varepsilon_i)} \tag{4.35}$$

The effective medium is now anisotropic, and the dielectric function is a tensor, see Equations (4.13) and (4.16).

In all the effective medium models discussed above a semi-infinite three dimensional material is assumed. When the medium is a two dimensional film, of *e.g.* nano particles on a substrate, substrate interactions may give anisotropic effective dielectric properties, even if every particle has a spherical symmetry and they are arranged isotropically. Yamaguchi *et al.* [102, 103] extended the Maxwell-Garnett equation to treat such cases. One other approach was the introduction of effective substrate and near-field dependent depolarization factors by Granqvist and Hunderi [104]. More rigorous approaches to solve the latter have been proposed by Simonsen *et al.* [105] and Letnes *et al.* [106].

4.4.3. Optical response of anisotropic layered structures

The reflected electromagnetic fields from a stack of stratified layers consists of the superposition of the reflected fields from all layers, including multiple reflections. For thin films, interference of the reflected fields from the various layers can be modeled to find the dielectric functions and thicknesses of the

A global transfer matrix $\mathbf{T}$, describing the total response of the enitre stack of films, is defined as

$$\begin{bmatrix} E_s^i \\ E_s^r \\ E_p^i \\ E_p^r \end{bmatrix} = \mathbf{T} \cdot \begin{bmatrix} E_s^t \\ E_s^b \\ E_p^t \\ E_p^b \end{bmatrix} = \begin{bmatrix} T_{11} & T_{12} & T_{13} & T_{14} \\ T_{21} & T_{22} & T_{23} & T_{24} \\ T_{31} & T_{32} & T_{33} & T_{34} \\ T_{41} & T_{42} & T_{43} & T_{44} \end{bmatrix} \cdot \begin{bmatrix} E_s^t \\ E_s^b \\ E_p^t \\ E_p^b \end{bmatrix}, \tag{4.36}$$

where E^i, E^r, E^t and E^b are complex amplitudes of the incoming, reflected, transmitted and back-traveling fields for p and s polarized light, as illustrated in Figure 4.5. In the case where the stack of films are supported on an infinite substrate, there will be no back-travelling modes ($E_s^b = E_p^b = 0$). The complex reflection coefficients for the stack can then be calculated as

$$\begin{aligned} r_{pp} &= \left(\frac{E_p^r}{E_p^i}\right)_{E_s^i=0} = \frac{T_{11}T_{43} - T_{41}T_{13}}{T_{11}T_{33} - T_{13}T_{31}}, \\ r_{ps} &= \left(\frac{E_p^r}{E_s^i}\right)_{E_p^i=0} = \frac{T_{41}T_{33} - T_{43}T_{31}}{T_{11}T_{33} - T_{13}T_{31}}, \\ r_{ss} &= \left(\frac{E_s^r}{E_s^i}\right)_{E_p^i=0} = \frac{T_{21}T_{33} - T_{23}T_{31}}{T_{11}T_{33} - T_{13}T_{31}}, \\ r_{sp} &= \left(\frac{E_s^r}{E_p^i}\right)_{E_s^i=0} = \frac{T_{11}T_{23} - T_{21}T_{13}}{T_{11}T_{33} - T_{13}T_{31}}. \end{aligned} \tag{4.37}$$

The total transfer matrix of the stack of N layers, each with a thickness d_i, is found by the multiplication of the partial transfer matrix of each layer

$$\mathbf{T} = \mathbf{L}_a^{-1} \prod_{i=1}^{N} [\mathbf{T}_{ip}(d_i)]^{-1} \mathbf{L}_f = \mathbf{L}_a^{-1} \prod_{i=1}^{N} [\mathbf{T}_{ip}(-d_i)] \mathbf{L}_f. \tag{4.38}$$

$\mathbf{L}_a^{-1}$ is a matrix describing the ambient

$$\mathbf{L}_a^{-1} = \frac{1}{2} \begin{bmatrix} 0 & 1 & -(\tilde{n}_a \cos\vartheta_1)^{-1} & 0 \\ 0 & 1 & (\tilde{n}_a \cos\vartheta_1)^{-1} & 0 \\ (\cos\vartheta_1)^{-1} & 0 & 0 & 1/\tilde{n}_a \\ -(\cos\vartheta_1)^{-1} & 0 & 0 & 1/\tilde{n}_a \end{bmatrix}, \tag{4.39}$$

where ϑ is the incidence angle and $\tilde{n}_a$ the isotropic refractive index of the ambient. The matrix of the isotropic substrate is [22]

$$\mathbf{L}_f = \begin{bmatrix} 0 & 0 & \cos\vartheta_2 & 0 \\ 1 & 0 & 0 & 0 \\ -\tilde{n}_s \cos\vartheta_2 & 0 & 0 & 0 \\ 0 & 0 & \tilde{n}_s & 0 \end{bmatrix}. \tag{4.40}$$

In the case of an anisotropic substrate, the E^t modes may couple, and $\mathbf{L}_f$ will take a form which is derived and given in [108].

In order to calculate the partial transfer matrix of each layer, a characteristic coefficient matrix $\mathbf{\Delta}$ is first found by solving four differential equations from first order Maxwell equations derived by Berreman [109]. The in plane components of the electric and magnetic field, for a Cartesian coordinate system in Gaussian units, can for every position z be found by

$$\vec{\Psi}(z) = [E_x, E_y, H_x, H_y]^T(z), \tag{4.41}$$

$$\partial_z \vec{\Psi}(z) = ik_0 \mathbf{\Delta}(z)\vec{\Psi}(z), \quad k_0 = \frac{\omega}{c}, \tag{4.42}$$

where ω is the angular frequency of the fields and c the vacuum speed of light [92]. The characteristic coefficient matrix is given by the dielectric tensor $\boldsymbol{\varepsilon}$ of the medium and the x-component of the incident wave vector ($k_x = \tilde{n}_a \sin\vartheta_1$)

$$\mathbf{\Delta} = \begin{bmatrix} -k_x \frac{\varepsilon_{zx}}{\varepsilon_{zz}} & -k_x \frac{\varepsilon_{zy}}{\varepsilon_{zz}} & 0 & 1 - \frac{k_x^2}{\varepsilon_{zz}} \\ 0 & 0 & -1 & 0 \\ \varepsilon_{yz}\frac{\varepsilon_{zx}}{\varepsilon_{zz}} - \varepsilon_{yx} & k_x^2 + \varepsilon_{yz}\frac{\varepsilon_{zy}}{\varepsilon_{zz}} - \varepsilon_{yy} & 0 & k_x \frac{\varepsilon_{yz}}{\varepsilon_{zz}} \\ \varepsilon_{xx} - \varepsilon_{xz}\frac{\varepsilon_{zx}}{\varepsilon_{zz}} & \varepsilon_{xy} - \varepsilon_{xz}\frac{\varepsilon_{zy}}{\varepsilon_{zz}} & 0 & -k_x \frac{\varepsilon_{xz}}{\varepsilon_{zz}} \end{bmatrix} \tag{4.43}$$

The solution to Equation (4.42) is an exponential, and can be expressed by the partial transfer matrix as

$$\vec{\Psi}(z) = \mathrm{e}^{ik_0 \mathbf{\Delta} d}\vec{\Psi}(z_0) = \mathbf{T}_p \vec{\Psi}(z_0), \tag{4.44}$$

$$\mathbf{T}_p = \mathrm{e}^{ik_0 \mathbf{\Delta} d}. \tag{4.45}$$

The partial transfer matrix describes the linear translation of the field components from position z_0 to z by a distance $d = z - z_0$. By applying Cayley-

Hamilton's theorem [22, 110], the exponential matrix $\mathbf{T}_p$ can be expressed as

$$\mathbf{T}_p = \beta_0 \mathbf{I} + \beta_1 \mathbf{\Delta} + \beta_2 \mathbf{\Delta}^2 + \beta_3 \mathbf{\Delta}^3, \tag{4.46}$$

where β_i is found by solving [110]

$$\mathrm{e}^{-ik_0\lambda_k d} = \sum_{j=0}^{3} \beta_j \lambda_k, \quad k = 0, \ldots, 3. \tag{4.47}$$

Here λ_k are the four eigenvalues of $\mathbf{\Delta}$.

For an isotropic layer, $\mathbf{T}_p$ is simplified to

$$\mathbf{T}_p = \begin{bmatrix} \cos(k_0 d\lambda) & 0 & 0 & \frac{i\lambda}{\varepsilon}\sin(k_0 d\lambda) \\ 0 & \cos(k_0 d\lambda) & \frac{-i}{\lambda}\sin(k_0 d\lambda) & 0 \\ 0 & -i\lambda \sin(k_0 d\lambda) & \cos(k_0 d\lambda) & 0 \\ (i\varepsilon/\lambda)\sin(k_0 d\lambda) & 0 & 0 & \cos(k_0 d\lambda) \end{bmatrix} \tag{4.48}$$

where $\pm\lambda$ are the degenerated eigenvalues of $\mathbf{\Delta}$,

$$\lambda_1 = \lambda_2 = -\lambda_3 = -\lambda_4 \equiv \lambda = \sqrt{\varepsilon - k_x^2} = \sqrt{\tilde{n}^2 - \tilde{n}_a^2 \sin^2 \vartheta_a} \tag{4.49}$$

4.4.4. Figure of merit

When analyzing ellipsometric data and comparing the data to simulated values, a measure for the goodness of the fit is needed. The common and well established methods are the χ^2 and mean squared error (MSE) figures of merit. They are of similar form, but differs in that χ^2 also takes into account a wavelength and parameter dependent standard deviation of the observables. In terms of the Mueller matrix elements, the two functions are defined by

$$\chi^2 = \frac{1}{N \cdot J - M} \sum_{i=1}^{N} \sum_{j=1}^{J} \left(\frac{m_j^{\mathrm{mod}}(i) - m_j^{\mathrm{exp}}(i)}{\sigma_j(i)} \right)^2, \tag{4.50}$$

$$\mathrm{MSE} = 1000 \sqrt{\frac{1}{N \cdot J - M} \sum_{i=1}^{N} \sum_{j=1}^{J} \left(m_j^{\mathrm{mod}}(i) - m_j^{\mathrm{exp}}(i) \right)^2}, \tag{4.51}$$

where N is the number of wavelengths, J the number of observables (here the Mueller matrix elements), M the number of fit parameters, $\sigma_j(i)$ the standard deviation, and m_j^{mod} and m_j^{exp} are the simulated and experimental Mueller matrix elements respectively. The MSE is multiplied by a factor of 1000, which is equivalent to a standard deviation of 0.001 in the χ^2 function. When working with spectroscopic Mueller matrices using multiple incidence angles and planes it can be difficult to estimate a correct standard deviation for all observables. The MSE is therefore used in many applications.

4.5. Overview of results

In this thesis, nanopatterned GaSb substrates and plasmonic anisotropic nanostructures of Au and Cu are studied using spectroscopic dual rotating compensator Mueller matrix ellipsometry. The spectroscopic range of the instrument is from 210 nm (5.9 eV) to 1700 nm (0.73 eV). A complete ellipsometric characterization of these films can only be made by measuring the spectroscopic Mueller matrix for several incidence planes and angles. The incidence plane is selected by rotating the sample plane, as illustrated in Figure 4.6.

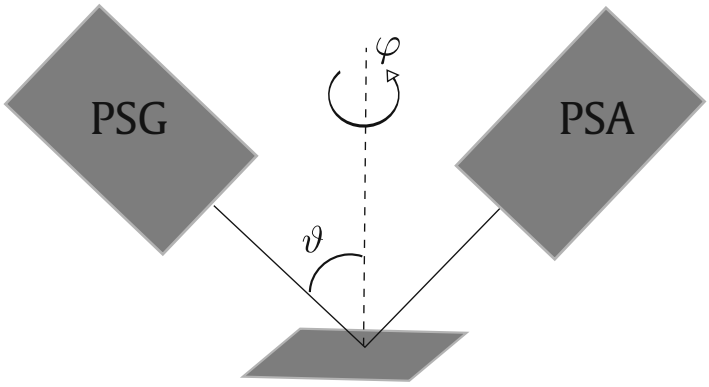

Figure 4.6.: Schematic of an ellipsometer in reflection mode. The incidence angle is indicated by ϑ and the orientation of the incidence plane by the angle φ.

4.5.1. In plane Au nanowires

In Paper 12 the optical properties of in plane Au nanowires are studied. The anisotropic Au nanopatterned surfaces were prepared in a two stage process. First ion beam sputtering (IBS) was used to prepare nanoripples on a quartz substrate. The spatial surface modulation is induced by a combination of an erosive instability and energy relaxation, dominated by diffusion and hyperthermal mobility. After the production of nanoripples, Au was evaporated onto the sample at gracing incidence. As a result of shadowing, Au nanoparticles formed on the sides facing the Au source. Along the ripples, Au nanoparticles formed nearly connected lines, whereas normal to the ripples they were more separated. A schematic view of the sample and the local geometry is shown in Figure 4.7.

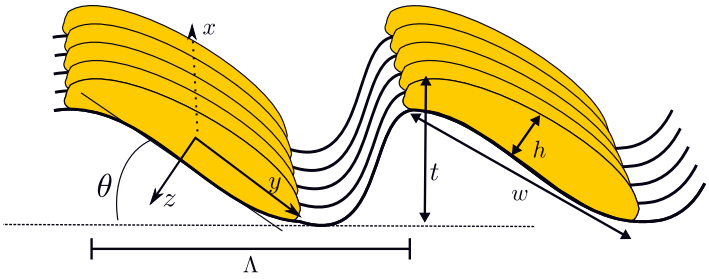

Figure 4.7.: Schematic illustration of the in plane Au nanowire sample. The local coordinate system is illustrated, along with the relevant dimensions. The figure is from Paper 12.

The sample was measured for incidence angles 50° to 75°, and for a 360° rotation of the incidence plane. Figure 4.8 shows the measured spectroscopic Mueller matrix at 50° incidence for all incidence planes. The incidence plane has been mapped to the polar angle, while the wavelength has been mapped to the radial direction. The measured Mueller matrix data show a strong asymmetry in all elements. It is particularly interesting that the block off-diagonal elements, in particular the $m_{14/41}$ element, show a different symmetry

originating from the biaxial form, induced by the tilt angle of the nanoparticles (visualized by the tilt angle θ in Figure 4.7).

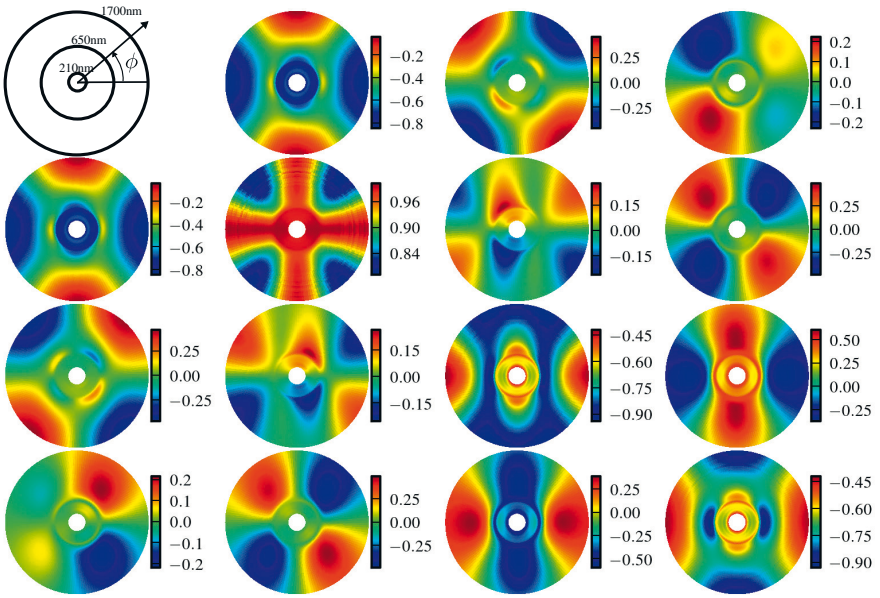

Figure 4.8.: Polar color map of the experimental spectroscopic Mueller matrix measured at 50° incidence for the Au nanowire sample. The figure is from Paper 12.

An optical model, that was used to fit the complete data set, was developed by parametrizing an effective spectroscopic dielectric tensor for the film. The dielectric tensor elements are plotted in Figure 4.9, where the coordinates refer to the local coordinate system indicated in Figure 4.7. Localized surface plasmon resonances were found for all three axes. The tensor was parametrized using 9 oscillators. By fitting the Euler rotations of the tensor, the tilt angle (θ in Figure 4.7) was found to be 12.8°, which was found to be in good agreement with an AFM analysis.

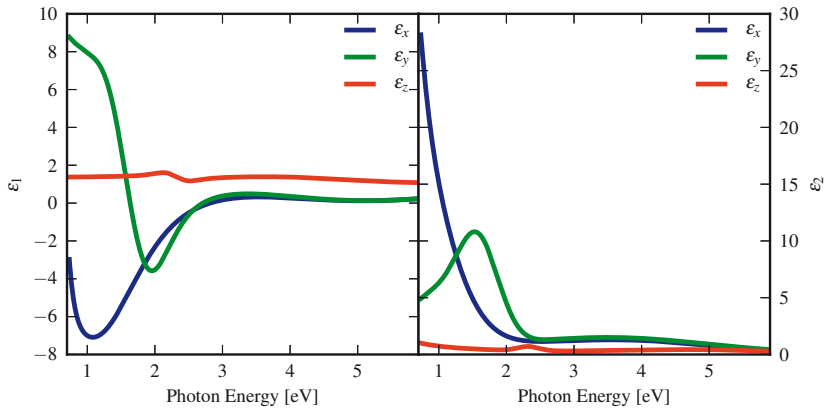

Figure 4.9.: The parameterized complex dielectric tensor. The figure is from Paper 12.

4.5.2. Plasmonic resonant Cu in mixed oxide nanopillars

In Paper 13, plasmon resonances for Cu nanoparticles embedded in a mixed oxide nanopillar film are studied by spectroscopic Mueller matrix ellipsometry. The oxide nanopillars were fabricated by low energy IBS of a sol-gel film of copper oxide and silica. By varying the ion energy and the substrate temperature, different pillar populations can be manufactured. Cohin *et al.* [111] showed, by transmission electron microscopy (TEM) that metallic copper nanoparticles form on the top and inside shorter nanowires. On longer nanowires, the metallic copper formed on the sides, as illustrated in Figure 4.10. As the mixed nanopatterned film of Cu and oxide had an irregular structure, the current approach for analyzing the data is mostly phenomenological.

By inspecting the spectroscopic Mueller matrix, oscillations were observed in all Mueller matrix elements. Figure 4.11 shows generalized ellipsometric parameters for the measurement at 65° incidence. The ellipsometric parameters were found by fitting the measured Mueller matrix to the Mueller-Jones matrix in Equation (4.7). It was found that the fringes in Ψ could not originate from interference, but were rather different plasmon modes. In particular, in Figure 4.11, it was found that the maximum and minimum in Ψ originated from s-polarized and p-polarized modes respectively. The splitting of modes

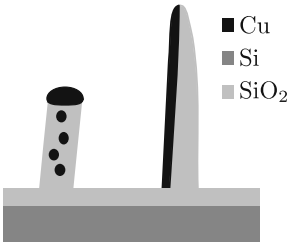

Figure 4.10.: A sketch of the oxide nanopillars with copper particles on the top, inside and on the side of the nanopillars [111].

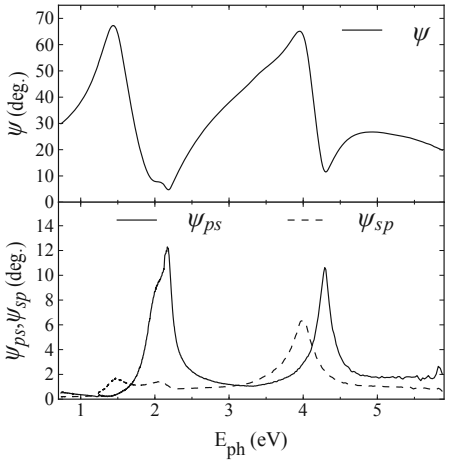

Figure 4.11.: Generalized ellipsometric parameters generated from the measured Mueller matrix.

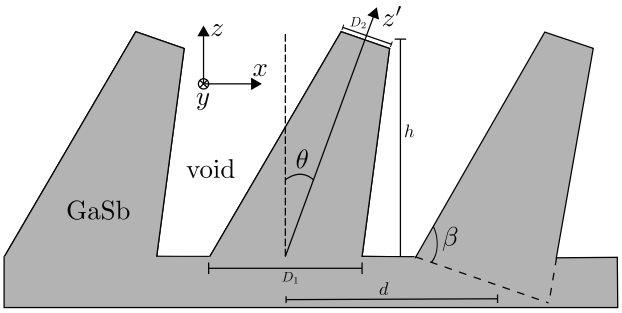

Figure 4.12.: A sketch of the GaSb nanopillar geometry. The figure is from Paper 11.

Figure 4.11, it was found that the maximum and minimum in Ψ originated from s-polarized and p-polarized modes respectively. The splitting of modes can in terms of effective medium theory be explained by the shape of the Cu nanoparticles. Disk like Cu particles (similar to what was observed in TEM on top of the shorter wires) correspond to low energy s-polarized and high energy p-polarized modes. Needle shaped Cu particles (which was observed on the side of long nanowires) correspond to p-polarized resonances at low energies and s-polarized resonances at higher energies.

4.5.3. Determination of small tilt angles of GaSb nanopillars

Paper 10 describes the determination of small tilt angles of GaSb nanopillars. In Paper 11, the ellipsometric results are partially confirmed through grazing incidence small angle x-ray scattering (GISAXS). GaSb nanopillars have previously been studied extensively by Nerbø *et al.* [22, 25, 112–115], using a Mueller matrix ellipsometer with a spectral range limited to the visible. In the current work, it is demonstrated that by including ultra violet light, the sensitivity to the tilt angle is strongly enhanced. Two samples, made under the same conditions, were studied. The samples were produced by low energy IBS of a clean GaSb substrate, where the growth is driven by the difference in diffusion velocity and sputtering yield of the two components of the semiconductor [116]. As Sb has a higher sputtering yield, there will be an excess of Ga on the surface. The Ga atoms form droplets which act as sputtering masks for

In order to model the spectroscopic data, a 50 layer anisotropic Bruggeman effective medium model was used (Equation (4.35)). Each layer was modeled as a cylinder, *i.e.* using a depolarization factor of $L_{x,y} = 0.5$ for the x and y direction, and $L_z = 0$ for the z direction. By geometrical considerations, the GaSb fill factors of each layer were calculated as a function of the cylinder radius. The height of the pillars of the two samples were found to be 39.3 nm and 37.0 nm. While the tilt angles were found to be 4.78° and 2.82°. A tilt angle accuracy of 0.25° was estimated by comparing the results for two different radius models.

Further, GISAXS was used to confirm the film anisotropy induced by the nanopillar tilt and to find the average nanopillar separation. The latter allowed the average local geometry to be estimated.

5. Conclusions

Mueller matrix polarimeters based on ferroelectric liquid crystals (FLC) and liquid crystal variable retarders (LCVR) were designed and realized. Optimal broadband polarimeter designs were found by optimizing the condition numbers of the polarization state generator and analyzer. As the optimization search space has numerous local optima, a genetic algorithm (GA) was selected to solve the challenging optimization problem. The resulting polarimeters show good performance over large spectral ranges. GA optimized FLC and LCVR based polarimeters were subsequently implemented in measurement setups. The eigenvalue calibration method for Mueller matrix polarimeters was adapted to overdetermined polarimeters and used to calibrate the instruments.

An imaging FLC based Mueller matrix polarimeter was implemented and used for several applications. In particular, retardance imaging was applied to strain mapping in multi-crystalline silicon, directional mapping of collagen fibers in biological tissue, and structural characterization of domains in synthetic clay.

Spectroscopic Mueller matrix ellipsometry was used to characterize anisotropic nanostructured samples of GaSb, in plane plasmonic Au nanowires and mixed films of plasmonic Cu particles and oxide nanowires. By using a multilayer anisotropic Bruggeman effective medium model, it was demonstrated that ultraviolet to near infrared Mueller matrix ellipsometry is sensitive to small tilt angles of GaSb nanopillars. By combining Mueller matrix ellipsometry with gracing incidence small angle x-ray scattering, the local average geometry of the nanopillars was found.

The optical properties of in plane Au nanowires fabricated on a nanostructured quartz substrate was investigated with Mueller matrix ellipsometry. It was found that the spectroscopic effective dielectric tensor was biaxial with localized plasmon resonances both along and normal to the wires. A local nanowire tilt coincided with the Euler angle rotations of the dielectric tensor.

Plasmon resonant Cu nanoparticles embedded on the top, the inside and the side of oxide nanowires were detected by spectroscopic Mueller matrix

ellipsometry. The plasmon resonances were found to split in two sets of s- and p-polarized modes due to the shape of the Cu nanoparticles.

5.1. Suggested future work

The results in this thesis opens for new applications and venues of Mueller matrix polarimetry. It was shown that FLC based polarimeters are fast and allow for Mueller matrix sample rates of more than 100 Hz. Many dynamic and fast changing phenomenas have properties which can be measured by a polarimeter. One example is the alignment of clay particles in a magnetic field.

If the Mueller matrix imaging instrument was adapted to a microscope setup, higher resolution could be obtained. Applying a hyper spectral camera would also be interesting. As the penetration depth in many absorbing materials are wavelength dependent one could envisage polarimetric depth profiling in *e.g.* biological tissue.

Strain is currently an important topic in the silicon solar cell community. Imaging of strain has a large potential to supply input to numerical models and simulations for improved solidification. In-line strain characterization during production can also be envisaged.

For the in plane plasmonic Au nanowires, the location of the plasmon resonance along the nanowires is uncertain. Using mid infrared Mueller matrix ellipsometry, the location of the plasmon could be determined.

And finally, the spectroscopic Mueller matrix measurement of Cu nanoparticles in mixed oxide nanopillars was not modelled. A model where a combination of scattering from the localized plasmons and the reflection from substrate could in the future be envisaged. Whenever a model is developed, the growth mechanisms of the fabrication process could be studied by real-time *in-situ* investigations.

Bibliography

[1] L. M. S. Aas, P. G. Ellingsen, M. Kildemo, and M. Lindgren, "Dynamic Response of a fast near infra-red Mueller matrix ellipsometer," J. Mod. Optic. **57**, 1603–1610 (2010).

[2] P. A. Letnes, I. S. Nerbø, L. M. S. Aas, P. G. Ellingsen, and M. Kildemo, "Fast and optimal broad-band Stokes/Mueller polarimeter design by the use of a genetic algorithm," Opt. Express **18**, 23095–23103 (2010).

[3] L. M. S. Aas, P. G. Ellingsen, B. E. Fladmark, P. A. Letnes, and M. Kildemo, "Overdetermined broadband spectroscopic Mueller matrix polarimeter designed by genetic algorithms," Opt. Express **21**, 8753 (2013).

[4] L. M. S. Aas, D. G. Skåre, P. G. Ellingsen, P. A. Letnes, and M. Kildemo, "Design, optimization and realization of FLC based Stokes polarimeters and Mueller matrix ellipsometer using a genetic algorithm," Preprint, subm. to Thin Solid Films (2013).

[5] L. M. S. Aas, P. G. Ellingsen, and M. Kildemo, "Near infra-red Mueller matrix imaging system and application to retardance imaging of strain," Thin Solid Films **519**, 2737–2741 (2010).

[6] L. M. S. Aas, I. S. Nerbø, M. Kildemo, D. Chiappe, C. Martella, and F. Buatier de Mongeot, "Mueller matrix imaging of plasmonic polarizers on nanopatterned surface," Proc. SPIE **8082**, 80822W (2011).

[7] P. G. Ellingsen, M. B. Lilledahl, L. M. S. Aas, C. d. L. Davies, and M. Kildemo, "Quantitative characterization of articular cartilage using Mueller matrix imaging and multiphoton microscopy," J. Biomed. Opt. **16**, 116002 (2011).

[8] P. G. Ellingsen, L. M. S. Aas, V. S. Hagen, R. Kumar, M. B. Lilledahl, and M. Kildemo, "Mueller matrix 3D directional imaging of collagen fibers," Preprint, subm. to J. Biomed. Opt. (2013).

[9] M. Kildemo, L. M. S. Aas, P. G. Ellingsen, H. Hemmen, E. L. Hansen, and J. O. Fossum, "Mueller matrix imaging of nematic textures in colloidal dispersions of Na-fluorohectorite synthetic clay," Proc. SPIE **8082**, 808221 (2011).

[10] L. M. S. Aas, M. Kildemo, Y. Cohin, and E. Søndergård, "Determination of small tilt angles of short GaSb nanopillars using UV–visible Mueller matrix ellipsometry," Thin Solid Films **541**, 97–101 (2013).

[11] K. Høydalsvik, L. M. S. Aas, E. Døli, E. Søndergård, M. Kildemo, and D. W. Breiby, "Combining surface X-ray scattering and ellipsometry for non-destructive area-averaged characterisation of ion beam-induced GaSb surface nanostructures," Accepted for publication in Thin Solid Films (2013).

[12] L. M. S. Aas, , M. Kildemo, C. Martella, M. C. Giordano, D. Chiappe, and F. Buatier de Mongeot, "Optical properties of biaxial nanopatterned gold plasmonic nanowired grid polarizer," Preprint, subm. to Opt. Express (2013).

[13] Z. Ghadyani, M. Kildemo, L. M. S. Aas, Y. Cohin, and E. Søndergård, "Spectroscopic Mueller matrix ellipsometry of plasmonic resonant Cu in mixed oxide nanopillars," Preprint, subm. to Opt. Express (2013).

[14] M. Kildemo, J. Maria, P. G. Ellingsen, and L. M. S. Aas, "Parametric model of the Mueller matrix of a Spectralon white reflectance standard deduced by polar decomposition techniques," Opt. Express **21**, 18509 (2013).

[15] J. Maria, L. M. S. Aas, and M. Kildemo, "In and out of incidence plane Mueller matrix scattering ellipsometry of rough mc-Si," Preprint, subm. to Thin Solid Films (2013).

[16] O. Svensen, J. J. Stamnes, M. Kildemo, L. M. S. Aas, S. R. Erga, and O. Frette, "Mueller matrix measurements of algae with different shape and size distributions," Appl. Opt. **50**, 5149–5157 (2011).

[17] P. A. Letnes, I. S. Nerbø, L. M. S. Aas, P. G. Ellingsen, and M. Kildemo, "Genetic invention of fast and optimal broad-band stokes/mueller polarimeter designs," in "Proceedings of the 13th annual conference companion on Genetic and evolutionary computation," (2011), pp. 237–238.

[18] S. Zollner, "Spectroscopic ellipsometry for inline process control in the semiconductor industry," in "Ellipsometry at the Nanoscale," , M. Losurdo and K. Hingerl, eds. (Springer Berlin Heidelberg, 2013), pp. 607–627.

[19] R. M. A. Azzam and N. M. Bashara, *Ellipsometry and Polarized light* (North-Holland, 1977).

[20] M. Schubert, "Generalized ellipsometry and complex optical systems," Thin Solid Films **313-314**, 323–332 (1998).

[21] M. Losurdo, "Applications of ellipsometry in nanoscale science: Needs, status, achievements and future challenges," Thin Solid Films **519**, 2575–2583 (2011).

[22] I. Nerbø, "Real-time study of the formation of gasb nanopillars by spectroscopic mueller matrix ellipsometry," Ph.D. thesis, NTNU (2011).

[23] D. Schmidt, "Generalized ellipsometry on sculptured thin films made by glancing angle deposition," Ph.D. thesis, University of Nebraska (2010).

[24] D. Schmidt, E. Schubert, and M. Schubert, "Generalized ellipsometry determination of non-reciprocity in chiral silicon sculptured thin films," Phys. Stat. Sol. (a) **205**, 748–751 (2008).

[25] M. Kildemo, I. S. Nerbø, E. Søndergård, L. Holt, I. Simonsen, and M. Stchakovsky, "Optical response of nanostructured GaSb," Phys. Stat. Sol. (c) **5**, 1382–1385 (2008).

[26] W. M. Duncan and S. A. Henck, "Insitu spectral ellipsometry for real-time measurement and control," Appl. Surf. Sci. **63**, 9 – 16 (1993).

[27] R. Collins, I. An, H. Fujiwara, J. Lee, Y. Lu, J. Koh, and P. Rovira, "Advances in multichannel spectroscopic ellipsometry," Thin Solid Films **313-314**, 18–32 (1998).

[28] S. A. Mayer, *Plasmonics, Fundamentals and Applications* (Springer, 2007).

[29] M. Kauranen and A. Zayats, "Nonlinear plasmonics," Nat. Photon. **6**, 737–748 (2012).

[30] A. Belardini, M. C. Larciprete, M. Centini, E. Fazio, C. Sibilia, M. Bertolotti, A. Toma, D. Chiappe, and F. Buatier de Mongeot, "Tailored second harmonic generation from self-organized metal nano-wires arrays." Opt. Express **17**, 3603–9 (2009).

[31] K. a. Willets and R. P. Van Duyne, "Localized surface plasmon resonance spectroscopy and sensing." Annu. Rev. Phys. Chem. **58**, 267–97 (2007).

[32] T. Oates, H. Wormeester, and H. Arwin, "Characterization of plasmonic effects in thin films and metamaterials using spectroscopic ellipsometry," Prog. Surf. Sci. **86**, 328–376 (2011).

[33] H. a. Atwater and A. Polman, "Plasmonics for improved photovoltaic devices." Nat. Mater. **9**, 205–213 (2010).

[34] T. W. H. Oates, M. Ranjan, S. Facsko, and H. Arwin, "Highly anisotropic effective dielectric functions of silver nanoparticle arrays." Opt. Express **19**, 2014–2028 (2011).

[35] T. Oates, L. Ryves, and M. Bilek, "Dynamic spectroscopic ellipsometry determination of nanostructural changes in plasmonic silver films." Opt. Express **15**, 15987–98 (2007).

[36] D. Smith and D. Schurig, "Electromagnetic Wave Propagation in Media with Indefinite Permittivity and Permeability Tensors," Phys. Rev. Lett. **90**, 077405 (2003).

[37] A. Belardini, F. Pannone, and G. Leahu, "Asymmetric transmission and anomalous refraction in metal nanowires metasurface," J. Europ. Opt. Soc. Rap. Public. **7**, 12051 (2012).

[38] M. Anastasiadou, A. De Martino, D. Clement, F. Liège, B. Laude-Boulesteix, N. Quang, J. Dreyfuss, B. Huynh, A. Nazac, L. Schwartz, and Others, "Polarimetric imaging for the diagnosis of cervical cancer," Phys. Stat. Sol. (c) **5**, 1423–1426 (2008).

[39] T. Novikova, A. Pierangelo, A. De Martino, A. Benali, and P. Validire, "Polarimetric imaging for cancer diagnosis and staging," Opt. Photon. News **23**, 26–33 (2012).

[40] T. Novikova, A. Pierangelo, S. Manhas, A. Benali, P. Validire, B. Gayet, and A. De Martino, "The origins of polarimetric image contrast between healthy and cancerous human colon tissue," Appl. Phys. Lett. **102**, 241103 (2013).

[41] M. Dubreuil, P. Babilotte, L. Martin, D. Sevrain, S. Rivet, Y. Le Grand, G. Le Brun, B. Turlin, and B. Le Jeune, "Mueller matrix polarimetry for improved liver fibrosis diagnosis." Opt. Lett. **37**, 1061–3 (2012).

[42] G. Anna, H. Sauer, F. Goudail, and D. Dolfi, "Fully tunable active polarization imager for contrast enhancement and partial polarimetry." Appl. Opt. **51**, 5302–9 (2012).

[43] F. Goudail and G. Anna, "On the optimization of polarimetric imaging systems for target detection," Proc. SPIE **8160** (2011).

[44] H. Arwin, R. Magnusson, J. Landin, and K. Järrendahl, "Chirality-induced polarization effects in the cuticle of scarab beetles: 100 years after Michelson," Philos. Mag. **92**, 1583–1599 (2012).

[45] W. B. Sparks, J. Hough, T. a. Germer, F. Chen, S. DasSarma, P. DasSarma, F. T. Robb, N. Manset, L. Kolokolova, N. Reid, F. D. Macchetto, and W. Martin, "Detection of circular polarization in light scattered from photosynthetic microbes." P. Natl. Acad. Sci. **106**, 7816–21 (2009).

[46] G. Horváth, A. Barta, I. Pomozi, B. Suhai, R. Hegedüs, S. Å kesson, B. Meyer-Rochow, and R. Wehner, "On the trail of Vikings with polarized skylight: experimental study of the atmospheric optical prerequisites allowing polarimetric navigation by Viking seafarers," Proc. R. Soc. B **366**, 772–782 (2011).

[47] a. Le Floch, G. Ropars, J. Lucas, S. Wright, T. Davenport, M. Corfield, and M. Harrisson, "The sixteenth century Alderney crystal: a calcite as an efficient reference optical compass?" Proc. R. Soc. A **469**, 20120651–20120651 (2013).

[48] C. H. Bennett, G. Brassard, S. Breidbard, and S. Wiesner, "Quantum cryptography, or unforgeable subway tokens," in "Advances in Cryptology: Proceedings of CRYPTO '82," (Plenum, 1982), pp. 267–275.

[49] P. Hauge, "Conventions and formulas for using the Mueller-Stokes calculus in ellipsometry," Surf. Sci. **96**, 81–107 (1980).

[50] J. J. Gil and E. Bernabeu, "Depolarization and polarization indices of an optical system," Optica Acta **33**, 185–189 (1986).

[51] R. Barakat, "Theory of the coherency matrix for light of arbitrary spectral bandwidth," J. Opt. Soc. Am **53**, 317–322 (1963).

[52] R. A. Chipman, "Depolarization index and the average degree of polarization," Appl. Opt. **44**, 2490–2495 (2005).

[53] S. R. Cloude, *Polarisation : Applications in Remote Sensing* (OUP Oxford, 2009).

[54] S. Y. Lu and R. A. Chipman, "Interpretation of Mueller matrices based on polar decomposition," J. Opt. Soc. Am. A **13**, 1106–1113 (1996).

[55] J. Morio and F. Goudail, "Influence of the order of diattenuator, retarder, and polarizer in polar decomposition of Mueller matrices." Opt. Lett. **29**, 2234–6 (2004).

[56] R. Ossikovski, A. De Martino, and S. Guyot, "Forward and reverse product decompositions of depolarizing Mueller matrices," Opt. Lett. **32**, 689–691 (2007).

[57] R. Ossikovski, "Analysis of depolarizing Mueller matrices through a symmetric decomposition." J. Opt. Soc. Am. A **26**, 1109–1118 (2009).

[58] R. Ossikovski, "Canonical forms of depolarizing Mueller matrices." J. Opt. Soc. Am. A **27**, 123–30 (2010).

[59] R. Sridhar and R. Simon, "Normal form for Mueller Matrices in Polarization Optics," J. Mod. Optic. **41**, 1903–1915 (1994).

[60] S. Manhas, M. K. Swami, P. Buddhiwant, N. Ghosh, P. K. Gupta, and K. Singh, "Mueller matrix approach for determination of optical rotation in chiral turbid media in backscattering geometry," Opt. Express **14**, 190–202 (2006).

[61] R. Ossikovski, "Differential matrix formalism for depolarizing anisotropic media." Opt. Lett. **36**, 2330–2 (2011).

[62] S. Kumar, H. Purwar, R. Ossikovski, I. A. Vitkin, and N. Ghosh, "Comparative study of differential matrix and extended polar decomposition formalisms for polarimetric characterization of complex tissue-like turbid media." J. Biomed. opt. **17**, 105006 (2012).

[63] H. D. Noble, S. C. McClain, and R. A. Chipman, "Mueller matrix roots depolarization parameters," Appl. Optics **51**, 735–744 (2012).

[64] H. D. Noble and R. A. Chipman, "Mueller matrix roots algorithm and computational considerations." Opt. Express **20**, 17–31 (2012).

[65] J. J. Gil, "Characteristic properties of Mueller matrices." J. Opt. Soc. Am. A **17**, 328–34 (2000).

[66] S. R. Cloude, "Conditions for physical realizability of matrix operators in polarimetry," Proc. SPIE **1166**, 177–185 (1989).

[67] R. Simon, "The connection between Mueller and Jones matrices of polarization optics," Opt. Commun. **42**, 293–297 (1982).

[68] J. M. Bennett, "A critical evaluation of rhomb-type quarterwave retarders." Appl. Opt. **9**, 2123–9 (1970).

[69] R. W. Collins and J. Koh, "Dual rotating-compensator multichannel ellipsometer: instrument design for real-time Mueller matrix spectroscopy of surfaces and films," J. Opt. Soc. Am. A **16**, 1997 (1999).

[70] D. S. Sabatke, M. R. Descour, E. L. Dereniak, W. C. Sweatt, S. A. Kemme, and G. S. Phipps, "Optimization of retardance for a complete Stokes polarimeter," Opt. Lett. **25**, 802–804 (2000).

[71] F. Stabo-Eeg, M. Kildemo, E. Garcia-Caurel, and M. Lindgren, "Design and characterization of achromatic 132 retarders in CaF 2 and fused silica," J. Mod. Opt. **55**, 2203–2214 (2008).

[72] D. Sabatke, M. Descour, E. Dereniak, W. Sweatt, S. Kemme, and G. Phipps, "Optimization of retardance for a complete Stokes polarimeter," Opt. Lett. **25**, 802–804 (2000).

[73] F. Stabo-Eeg, M. Kildemo, I. S. Nerbø, and M. Lindgren, "Well-conditioned multiple laser Mueller matrix ellipsometer," Opt. Eng. **47**, 073604 (2008).

[74] W. H. Press, S. A. Teukolsky, W. T. Vetterling, and B. P. Flannery, *Numerical Recipes: The Art of Scientific Computing* (Cambridge University Press, 2007).

[75] J. S. Tyo, "Noise equalization in Stokes parameter images obtained by use of variable-retardance polarimeters," Opt. Lett. **25**, 1198–1200 (2000).

[76] R. Hagen, S. Roch, and B. Silbermann, *C* Algebras Numerical Analysis* (Marcel Dekker, 2001).

[77] J. Ladstein, F. Stabo-Eeg, E. Garcia-Caurel, and M. Kildemo, "Fast near-infra-red spectroscopic Mueller matrix ellipsometer based on ferroelectric liquid crystal retarders," Phys. Stat. Sol. (c) **5**, 1097–1100 (2008).

[78] S. Tomczyk, R. Casini, A. G. de Wijn, and P. G. Nelson, "Wavelength-diverse polarization modulators for Stokes polarimetry." Appl. Opt. **49**, 3580–6 (2010).

[79] J. H. Holland, "Genetic algorithms," Sci. Am. **267**, 44–50 (1992).

[80] D.-K. Yang and S.-T. Wu, *Fundamentals of liquid crystal devices* (Wiley, 2006).

[81] E. Compain, S. Poirier, and B. Drevillon, "General and self-consistent method for the calibration of polarization modulators, polarimeters, and mueller-matrix ellipsometers." Appl. Opt. **38**, 3490–3502 (1999).

[82] M. Suezawa, K. Sumino, and I. Yonenaga, "Dislocation dynamics in the plastic deformation of silicon crystals. ii. theoretical analysis of experimental results," Phys. Stat. Sol. (a) **51**, 217–226 (1979).

[83] T. Narasimhamurty, *Photoelastic and electro-optic properties of crystals* (Plenum Press, New York :, 1981).

[84] J.-S. Chung and G. E. Ice, "Automated indexing for texture and strain measurement with broad-bandpass x-ray microbeams," J. Appl. Phys. **86**, 5249 (1999).

[85] M. Hÿtch, J. Putaux, and J. Pénisson, "Measurement of the displacement field of dislocations to 0.03 Åby electron microscopy," Nature **423**, 270–273 (2003).

[86] M. Kildemo, O. Hunderi, and B. Drévillon, "Approximation of reflection coefficients for rapid real-time calculation of inhomogeneous films," J. Opt. Soc. Am. A **14**, 931–939 (1997).

[87] G. E. Jellison and F. a. Modine, "Two-modulator generalized ellipsometry: theory." Appl. Opt. **36**, 8190–8 (1997).

[88] J. D. Jackson, *Classical Electrodynamics Third Edition* (Wiley, 1998), 3rd ed.

[89] H. Fujiwara, ed., *Spectroscopic Ellipsometry Principles and Applications* (Wiley, 2007).

[90] G. E. Jellison and F. A. Modine, "Parameterization of the optical functions of amorphous materials in the interband region," Appl. Phys. Lett. **69**, 371–373 (1996).

[91] A. Forouhi and I. Bloomer, "Optical dispersion relations for amorphous semiconductors and amorphous dielectrics," Phys. Rev. B **34** (1986).

[92] M. Schubert, *Infrared Ellipsometry on Semiconductor Layer Structures* (Springer, 2010).

[93] H. Goldstein, C. P. Poole, and J. L. Safko, *Classical Mechanics* (Addison Wesley, 2001).

[94] A. Sihvola, *Electromagnetic Mixing Formulas and Applications* (IET, 1999).

[95] D. E. Aspnes, "Local-field effects and effective-medium theory: A microscopic perspective," Am. J. Phys. **50**, 704–709 (1982).

[96] D. A. G. Bruggeman, "Berechnung verschiedener physikalischer Konstanten von heterogenen Substanzen. I. Dielektrizitätskonstanten und Leitfähigkeiten der Mischkörper aus isotropen Substanzen," Ann. Phys. **416**, 636–664 (1935).

[97] C. F. Bohren and D. R. Huffman, *Absorption and Scattering of Light by Small Particles* (Wiley-VCH, 2004).

[98] G. A. Niklasson and C. G. Granqvist, "Optical properties and solar selectivity of coevaporated Co-Al2O3 composite films," J. Appl. Phys. **55**, 3382 (1984).

[99] C. Granqvist and O. Hunderi, "Optical properties of Ag-SiO_2 Cermet films: A comparison of effective-medium theories," Phys. Rev. B **18**, 2897 (1978).

[100] G. Smith, "Effective medium theory and angular dispersion of optical constants in films with oblique columnar structure," Opt. Commun. **71**, 279–284 (1989).

[101] J. Spanier and I. Herman, "Use of hybrid phenomenological and statistical effective-medium theories of dielectric functions to model the infrared reflectance of porous SiC films," Phys. Rev. B **61**, 10437–10450 (2000).

[102] T. Yamaguchi, S. Yoshida, and a. Kinbara, "Optical effect of the substrate on the anomalous absorption of aggregated silver films," Thin Solid Films **21**, 173–187 (1974).

[103] T. Yamaguchi, H. Takahashi, and A. Sudoh, "Optical behavior of a metal island film," J. Opt. Soc. Am. **68**, 1039 (1978).

[104] C. Granqvist and O. Hunderi, "Optical properties of ultrafine gold particles," Phys. Rev. B **16** (1977).

[105] I. Simonsen, R. Lazzari, J. Jupille, and S. Roux, "Numerical modeling of the optical response of supported metallic particles," Phys. Rev. B **61**, 7722–7733 (2000).

[106] P. A. Letnes, I. Simonsen, and D. L. Mills, "Substrate influence on the plasmonic response of clusters of spherical nanoparticles," Phys. Rev. B **83**, 075426 (2011).

[107] M. Schubert, *Handbook of Ellipsometry* (William Andrew, 2006), chap. Theory and Applications of Generalized Ellipsometry.

[108] W. Xu, L. Wood, and T. Golding, "Optical degeneracies in anisotropic layered media: treatment of singularities in a 4 4 matrix formalism," Phys. Rev. B **61**, 1740–1743 (2000).

[109] D. W. Berreman, "Optics in Stratified and Anisotropic Media: 4 X 4-Matrix Formulation," J. Opt. Soc. Am. **62**, 502–510 (1972).

[110] H. Wöhler, G. Haas, M. Fritsch, and D. Mlynski, "Faster 4 4 matrix method for uniaxial inhomogeneous media," J. Opt. Soc. Am. A **5**, 1554–1557 (1988).

[111] Y. Cohin, E. Barthel, N. Brun, C. Goldman, S. Le Roy, and E. Søndergård, "Spontaneous formation of copper-silica nanostructures by ion abrasion," Adv. Mater. (Submitted).

[112] I. Nerbø, S. L. Roy, M. Foldyna, E. Søndergård, and M. Kildemo, "Real-time in situ Mueller matrix ellipsometry of GaSb nanopillars: observation of anisotropic local alignment," Opt. Express **19**, 571–575 (2011).

[113] I. S. Nerbø, S. Le Roy, M. Kildemo, and E. Søndergard, "Real-time in situ spectroscopic ellipsometry of GaSb nanostructures during sputtering," Appl. Phys. Lett. **94**, 213105 (2009).

[114] I. S. Nerbo, S. Le Roy, M. Foldyna, M. Kildemo, and E. Søndergård, "Characterization of inclined GaSb nanopillars by Mueller matrix ellipsometry," J. Appl. Phys. **108**, 014307 (2010).

[115] M. Kildemo, I. Nerbø, S. Hagen, S. Leroy, and E. Søndergård, "Spectroscopic ellipsometry of nanostructured GaSb surfaces consisting of densely

packed 80–230nm long cones," Mat. Sci. Eng. B-Solid. **165**, 217–220 (2009).

[116] S. Le Roy, E. Søndergård, I. S. Nerbø, M. Kildemo, and M. Plapp, "Diffuse-interface model for nanopatterning induced by self-sustained ion-etch masking," Phys. Rev. B **81**, 161401 (2010).

A. Papers

L. M. S. Aas, P. G. Ellingsen, M. Kildemo, and M. Lindgren, Dynamic Response of a fast near infra-red Mueller matrix ellipsometer, J. Mod. Optic. **57**, 1603–1610 (2010)

Paper 1

Journal of Modern Optics
Vol. 57, No. 17, 10 October 2010, 1603–1610

Taylor & Francis
Taylor & Francis Group

Dynamic response of a fast near infra-red Mueller matrix ellipsometer

Lars M.S. Aas*, Pål G. Ellingsen, Morten Kildemo and Mikael Lindgren

Department of Physics, Norwegian University of Science and Technology (NTNU), N-7491 Trondheim, Norway

(*Received 8 June 2010; final version received 26 July 2010*)

The dynamic response of a near infra-red ferroelectric liquid crystal-based Mueller matrix ellipsometer (NIR FLC-MME) is presented. A time-dependent simulation model, using the measured time response of the individual FLCs, is used to describe the measured temporal response. Furthermore, the impulse response of the detector and the pre-amplifier is characterized and included in the simulation model. The measured time-dependent intensity response of the MME is reproduced in simulations, and it is concluded that the switching time of the FLCs is the limiting factor for the Mueller matrix measurement time of the FLC-based MME. Based on measurements and simulations, our FLC-based NIR-MME system is estimated to operate at the maximum speed of approximately 16 ms per Mueller matrix measurement. The FLC-MME may be operated several times faster, since the switching time of the crystals depends on the individual crystal being switched, and to what state it is switched. As a demonstration, the measured temporal response of the Mueller matrix and the retardance of a thick liquid crystal variable retarder upon changing state is demonstrated.

Keywords: Mueller matrix; ellipsometer; polarimeter; near infra-red; FLC

1. Introduction

Fast Mueller matrix ellipsometers (MME) may have a wide range of applications in biology, medicine, and various monitoring and control systems, supplying additional polarimetric information in imaging and spectroscopic applications. A variety of high performance MMEs has been reported [1–8], but they are usually of considerable complexity or not suitable for use with CCD or CMOS stripe-spectrographs and imaging sensors. We are also considering the limit of non-reversible processes not covered by, for example, the pump-probe techniques used for ultrafast birefringence or dichroism measurements. Some authors have reported on fast Mueller matrix measurements [1–2,9,10]. A typical solution uses a division of amplitude polarimeter and four detectors to work as the polarimeter or polarization state analyzer (PSA). The modulation may be performed with a fast electro-optic [1,3] or photo-elastic modulator [2]. However, such systems require a considerable increased complexity in instrumentation and signal processing. A recent development is the Snapshot Mueller matrix polarimeter based on spectral polarization coding, which enables Mueller matrix measurements within a microsecond [9,10]. However, this system does not allow for spectroscopic measurements, as the technique requires small spectral variations in the Mueller matrix of the sample. A rotating Fresnel prism retarder with a retardation of 132° across a wide spectral range (including UV) is probably the most optimal conditioned system around [5,11]. However, the latter system is inherently slow due to the mechanical rotation of the retarders, thus making it less suitable for fast MME purposes.

Liquid crystal (LC) spatial light modulators have been developed over the past decades for a variety of applications. The LCs are of course most widely used in display applications where the amplitude mode of operation is desired, but phase control can be used in, for example, beam-steering and shaping [12–13], adaptive optics [14], optical tweezers [15], to mention a few. The ferroelectric LCs are fast and allow for a rapid determination of the Mueller matrix. Several FLC-based MME designs have been proposed, although the first proposal of a polarimeter system similar to the one reported on here, appears to have been by Gandorfer and co-workers [16]. However, as shown here, the FLCs are still the limiting factor for the switching speeds, contrary to the findings reported recently [17,18]. The main disadvantage of liquid crystals, and in particular the current FLCs, is the well known degradation of the crystals upon ultraviolet radiation [19]. Applications of this technology in MME are currently thus limited to the visible and the infra-red. In this paper we investigate the dynamic response of a novel NIR-MME operating from 700

*Corresponding author. Email: lars.aas@ntnu.no

ISSN 0950–0340 print/ISSN 1362–3044 online

DOI: 10.1080/09500340.2010.515750
http://www.informaworld.com

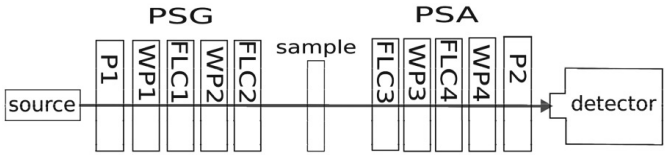

Figure 1. Layout of the FLC-based NIR-MME studied in this paper. The source is either a tungsten halogen white incoherent source or a 980 nm diode laser source. The FLC switching, timing and the signal acquisition are controlled through a computer. The optical components are ordered as a polarizer (P1), quartz waveplate (WP1), ferroelectric liquid crystal 1 (FLC1), waveplate (WP2), sample (e.g. air), FLC3, waveplate (WP3), FLC4 and waveplate (WP4). The details of the optical components are given in Table 1.

to 1600 nm. In a follow up paper we report on the features and applications of a FLC-based NIR-MME imaging system based around the same design.

A key issue when designing a Mueller matrix ellipsometer is optimization of the modulation or analyzer matrix of a polarization state generator (PSG) or a PSA in terms of their matrix condition number [5,11–12]. In this respect, the variable liquid crystal retarder (VLCR) based Mueller matrix ellipsometer can be truly optimal, but only for a single wavelength at a time. Furthermore, the switching of a VLCR is slow compared with the FLC variant. In fact, the dynamic possibilities of the fast near infra-red ferroelectric liquid crystal-based MME are here demonstrated by characterization of the dynamic Mueller matrix of a VLCR during the switching.

2. Experimental details

The NIR-MME reported on here can be operated in spectroscopic mode from 750 nm to 1800 nm, using a grating monochromator and a single detector. A tungsten-halogen lamp (100 W) with a stabilized power supply was used for incoherent illumination. The system is alternatively operated by using a stable laser diode operating at 980 nm, with maximum output power of 300 mW (found particularly useful for high speed measurements with short integration time).

A purpose-built (by Elektron Manufaktur Mahlsdorf) extended InGaAs detector with a built-in pre-amplifier, having an overall well-designed flat frequency response and cut-off frequency at 150 kHz, was used in the spectroscopic mode.

A multifunctional NI-DAQ card with a maximum sampling rate of 1.25 Ms/s (mega samples per second), is both used to acquire measurements and to control the FLCs. The MME is operated with in-house made Labview-based software. The initial FLC-based MME design was chosen based on the design by Gandorfer and co-workers [16], and similar designs have later been reported elsewhere [7,18]. In particular, Gandorfer and co-workers proposed a sequence of components such that the PSG and the PSA are composed of a polarizer – fixed waveplate (WP1) – ferroelectric liquid crystal (FLC1) – WP2 – FLC2. The remaining problem is then to determine the retardances and orientations of the waveplates and FLCs in order to optimize the condition number over the design spectral region. The PSA is, in this initial design, simply chosen with identical components in reverse order. Figure 1 shows a schematic drawing of the design.

The optical components in our design consist of a high contrast dichroic NIR polarizer, followed by a fixed 'true zero-order' quarter-wave retarder at 465 nm, a half-wave FLC at 510 nm, a fixed half-wave retarder at 1008 nm, and finally a half-wave FLC at 1020 nm. The true zero-order waveplates were manufactured in quartz, while the FLCs were custom-made versions of commercially available crystals (Displaytech Inc). The FLCs at 510 nm were the only elements fixed in the optimization, and originally chosen simply from cost considerations, while the fitted thicknesses of the remaining waveplates are the results of an optimization with respect to the condition number across the design spectral range.

The calibration samples were chosen as two NIR polarizers (similar to above) with azimuth orientation 0° and 90° relative to the first polarizer, and a zero-order waveplate at 1310 nm with azimuth orientation of the fast axis at 60° [18].

All the components were characterized individually, including retardance and azimuth orientation. The measurements were performed with collimated light and normal incidence to the optical polarization components. Simulation of the optical response of the full FLC-based Mueller matrix ellipsometer was compared to the measured response, using the characteristic properties of each characterized component.

Measurements were performed on air, and on a custom-made version of a commercially available VLCR (Meadowlark Inc.). The VLCR was designed to be a half-wave retarder at 2200 nm.

3. Mueller matrix theory for FLC-based MME

The MME is constructed by considering the Mueller matrix measurement theory proposed by Compain and colleagues [2,20,22–23]. In particular, the intensity matrix (**B**), which contains the 16 measured intensities, is given by the matrix product of the modulation matrix (**W**), the sample Mueller matrix (**M**) and the analyzer matrix (**A**)

$$\mathbf{B} = \mathbf{AMW}. \tag{1}$$

From the measured **B** matrix, and the known **W** and **A** matrices, the Mueller matrix can readily be calculated by matrix multiplication

$$\mathbf{M} = \mathbf{A}^{-1}\mathbf{B}\mathbf{W}^{-1}. \tag{2}$$

It is evident from basic matrix theory that **W** and **A**, for minimal error propagation, need to be as invertible as possible, i.e. as far from singular as possible. Specifically, it has been shown that the error in the intensity measurements, the calibration errors on **A** and **W**, are summed into the errors in the resulting Mueller matrix as follows [5]

$$\frac{\|\Delta\mathbf{M}\|}{\|\mathbf{M}\|} \le \kappa_{\mathbf{A}}\frac{\|\Delta\mathbf{A}\|}{\|\mathbf{A}\|} + \kappa_{\mathbf{W}}\frac{\|\Delta\mathbf{W}\|}{\|\mathbf{W}\|} + \kappa_{\mathbf{A}}\kappa_{\mathbf{W}}\frac{\|\Delta\mathbf{B}\|}{\|\mathbf{B}\|}, \tag{3}$$

where $\kappa_{\mathbf{A}}$ and $\kappa_{\mathbf{W}}$ are the condition numbers of **A** and **W**, defined in our work by the L_2 norm. This particular design method was originally proposed by Tyo [21], and later implemented and further developed by Compain and colleagues [1]. Compain and colleagues suggested an efficient and robust calibration technique (denoted the Eigenvalue Calibration Method) [20], which is also implemented here in order to determine the matrices **A** and **W**.

The modulation matrix **W** is constructed by defining each column vector as a unique Stokes vector generated by switching the two FLCs to one of their four different states. Let

$$\begin{aligned}\widehat{\theta} = \{&\theta_{1,\mathrm{FLC1}}, \theta_{2,\mathrm{FLC1}}, \theta_{1,\mathrm{FLC2}}, \theta_{2,\mathrm{FLC2}},\\ &\theta_{1,\mathrm{FLC3}}, \theta_{2,\mathrm{FLC3}}, \theta_{1,\mathrm{FLC4}}, \theta_{2,\mathrm{FLC4}}\}\end{aligned} \tag{4}$$

describe the set of azimuth angles of the FLCs. The two stable states $\{\theta_{1,j}, \theta_{2,j}\}$ of crystal j, are nominally separated by 45° in this work. The modulation matrix is then given by

$$\mathbf{W} = [\,\vec{S}_1 \quad \vec{S}_2 \quad \vec{S}_3 \quad \vec{S}_4\,], \tag{5}$$

where each stokes vector $\vec{S}_k$ is generated as:

$$\begin{aligned}\vec{S}_k &= \vec{S}(\lambda, \hat{\theta})\\ &= \mathbf{M}_{ret}(\theta_{i,\mathrm{FLC2}}, \delta_{\mathrm{FLC2}}(\lambda), T_{f,s})\mathbf{M}_{ret}(\theta_{\mathrm{WP2}}, \delta_{\mathrm{WP2}}(\lambda), T_{f,s})\\ &\quad\times \mathbf{M}_{ret}(\theta_{j,\mathrm{FLC1}}, \delta_{\mathrm{FLC1}}(\lambda), T_{f,s})\\ &\quad\times \mathbf{M}_{ret}(\theta_{\mathrm{WP1}}, \delta_{\mathrm{WP1}}(\lambda), T_{f,s})\mathbf{M}_{pol}\big[\,1 \quad 0 \quad 0 \quad 0\,\big]^t\end{aligned} \tag{6}$$

where $\mathbf{M}_{ret}$ are the Mueller matrices of the retarders, oriented at a given angle θ with respect to the first polarizer (here used as a laboratory axis reference) with retardance δ. $\mathbf{M}_{pol}$ is the matrix of the polarizer horizontally aligned in our system. The index i denotes the state of FLC2, and j denotes the state of FLC1.

Similarly, the analyzer matrix is composed of the discrete analyser states

$$\mathbf{A} = [\,\vec{A}_1 \quad \vec{A}_2 \quad \vec{A}_3 \quad \vec{A}_4\,]^T. \tag{7}$$

Each analyzer state is then calculated as above, taking into account the reverse order of the optical components, resulting in

$$\begin{aligned}\vec{A}_k = \vec{A}(\lambda, \hat{\theta}) = &\big[\,1 \quad 0 \quad 0 \quad 0\,\big]^t\mathbf{M}_{pol}\mathbf{M}_{ret}(\theta_{i,FLC4}, \delta_{FLC4}(\lambda))\\ &\times \mathbf{M}_{ret}(\theta_{WP4}, \delta_{WP4}(\lambda))\mathbf{M}_{ret}(\theta_{j,FLC3,}, \delta_{FLC3}(\lambda))\\ &\times \mathbf{M}_{ret}(\theta_{WP3}, \delta_{WP3}(\lambda)).\end{aligned} \tag{8}$$

The index i denotes the two stable states of FLC3, while j denotes the two stable states of FLC4.

4. Results and discussion

4.1. Static polarization properties of the optical components and the MME system

The current version of our NIR-MME system has the characteristics summarized in Table 1, where all orientations of the polarizers, waveplates and the FLCs were individually determined by separate Mueller matrix measurements in a commercial FLC-based visible MME instrument (Horiba Jobin Yvon). The analysis was performed by an implementation of the Lu–Chipman polar decomposition approach [24–26]. The dispersive retardances of each component in the NIR spectral region were determined by a simple crossed polarizer set-up, as no commercial spectroscopic NIR-MME was available. Similarly, the transmittances of the fast and slow axes of the fixed wave-plates and the FLCs were determined by transmission measurements, by orienting the fast or the slow axis of these components with the transmission axis of the polarizers. The details of the measured dispersive retardances and transmission coefficients have been reported elsewhere [17]. For completeness, some of the results are summarized here. The dispersive retardances were modeled by the following dispersion formula:

$$\Delta nd \approx \frac{A_{UV}\lambda}{\left(\lambda^2 - \lambda_{UV}^2\right)^{\frac{1}{2}}} - \frac{A_{IR}\lambda}{\left(\lambda_{IR}^2 - \lambda^2\right)^{\frac{1}{2}}} \tag{9}$$

where the retardances are given in nm at the wavelength λ. The constants A_{UV}, A_{IR}, λ_{UV} and λ_{IR} were determined by best fits to the data sets (Table 1).

Table 1. Static properties of polarization components in the order corresponding to Figure 1. The retardance is reported at a single wavelength, i.e. for WP1 then $\Delta nd = 116.25$ nm at $\lambda = 465$ nm. The wavelength dependent retardance is calculated from the fitted parameters A_{IR}, A_{UV}, λ_{IR} and λ_{UV}. All azimuth orientations (θ) of the fast axis of the stable state (denoted by '–'), are given with respect to the polarizers. Positive rotation of the azimuth axis is defined by anticlockwise rotation upon looking into the source [27].

	Retardance	θ (deg)	$\Delta\theta_{FLC}$	A_{UV}	λ_{UV} [nm]	A_{IR}	λ_{UV} [μm]
Polarizer		0					
WP1	λ/4@465 nm	129.2		110	134	50	11.16
FLC1	λ/2@510 nm	66.7(−)	44.0	202	280	0	
		110.7(+)					
WP2	λ/2@1008 nm	164.0		520	134	257	11.16
FLC2	λ/2@1020 nm	55.5(−)	45.4	505	283	0	
		100.9(+)					
FLC3	λ/2@1020 nm	55.1 (−)	44.2	505	283	0	
		99.3 (+)					
WP3	λ/2@1008 nm	163.1		520	134	257	11.16
FLC4	λ/2@510 nm	68.5(−)	42.2	202	280	0	
		110.7(+)					
WP4	λ/4@465 nm	129.4		110	134	50	11.16
Analyzer		0					

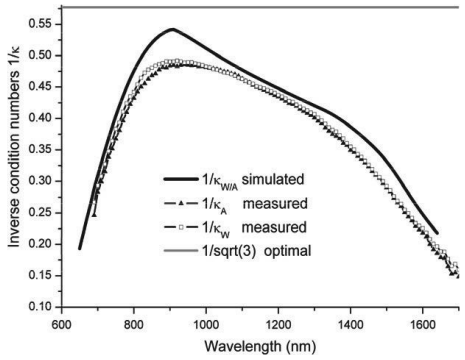

Figure 2. Simulated, measured and optimal inverse condition numbers for the polarization state generator and analyzer, of the FLC-based Mueller matrix system, with the components tabulated in Table 1, and the setup in Figure 1.

The real static dispersive response of the MME may be quantified through the measurement of the condition number of the PSA and the PSG. The simulated response of the MME, using the values in Table 1, can be used to calculate the theoretical condition number. Figure 2 shows both the measured and the simulated condition number of the PSG and the PSA. The system is in good correspondence with the simulations.

4.2. Temporal optical response model for the fast FLC-based MME

The deviation from a step-like temporal response of the recorded intensities in the measured **B** matrix arises as the system cannot switch immediately from one state to another, and that the photo-detector unit and its preamplifier might have a finite frequency response. Many future real-time applications of a MME could require the temporal characteristics of a certain polarization changing phenomenon. Moving objects, phase transitions, growth of a film or nanostructures, or variable orientation of molecules as in a liquid crystal are mentioned as a few examples.

Consider as an example a linear mechanical rotation of a waveplate (instead of using a FLC) by 45°, and the resulting intensity recorded by the detector as the waveplate is rotating. The switching of a FLC takes time, as the molecules in the LC need to be moved to their new orientations, which causes a nonlinear response of the recorded intensity as a function of the average angle of orientation. Furthermore, it is typical to drive such liquid crystals by an initial voltage spike, in order to enhance the switching frequency. As this involves a collective movement of the molecules making up the liquid crystals, the exact effect of the temporal response of the crystals in terms of its optical properties is uncertain.

To study the limitations in terms of the speed of a FLC-based MME, the formalism in Section 3 (Equations (3)–(7)) was modified to include both the temporal characteristics of the rotating waveplates and the detector response. The results can readily be generalized to other discrete-state MME designs, e.g. one based on electro-optic crystals. The measured temporal response can be compared to simulations, which can increase the understanding of the temporal characteristics of such systems, as will be exemplified below.

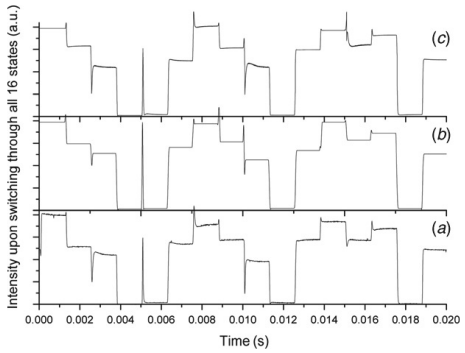

Figure 3. Measured and simulated temporal response of the recorded intensity upon switching through all 16 states of the FLCs: (*a*) shows the measured intensity upon switching through all 16 states; (*b*) shows the simulated intensity assuming a linear precession of the molecular director axis; (*c*) shows the simulated intensity using the time dependent angular rotation from Figure 4. In both simulations the impulse response of the detector is included, and the switching times given by t_{up} and t_{down} in Table 2 are used.

The generated Stokes vectors were modified in order to allow for the temporal characteristics of the time-dependent angle of orientation between two stable states of the FLC, i.e. $\hat{\theta}(t)$, giving

$$\vec{S}_k = \vec{S}(\lambda, \hat{\theta}(t)). \tag{10}$$

By switching the system through the 16 states i.e. 4×4 different stable states of the FLCs, the recorded intensities are stored in the wavelength and time dependent, intensity matrix

$$\mathbf{B}(t, \lambda) = \mathbf{A}(t, \lambda)\mathbf{M}(\lambda)\mathbf{W}(t, \lambda).$$

If the temporal response of the sample Mueller matrix **M** is to be determined, it is evidently of utter importance that the time constants involved in the **A** and **W** matrices are much shorter than the ones involved in the sample Mueller matrix.

Figure 3(*a*) shows the temporal measured intensity response of the NIR-MME system. To keep the signal level high, the 980 nm diode laser source was used in these experiments. The sample was air, modeled as the identity matrix. It is a peculiar intensity response, with overshoots and undershoots before going to the stable states.

The FLCs are nominally reported to switch in 55 µs, and first it was investigated to what extent the overshoots could be due to the detector (and preamplifier) performance. This issue can easily be introduced into the simulations by introducing the impulse response of the preamplifier of the detector

$$\mathbf{B}(t, \lambda) = h(t) \otimes \mathbf{A}(t, \lambda)\mathbf{M}(\lambda)\mathbf{W}(t, \lambda), \tag{11}$$

were $h(t)$ is the detector impulse response, and $\otimes$ denotes the convolution. The detector pre-amplifier response was therefore characterized using the frequency modulation option of the diode laser and a lock-in amplifier. The frequency response analysis showed a flat response with an 80 dB/decade fall above 151 kHz. The results were fitted to the transfer function $H(s) = (1 + sT)^{-4}$, where the time constant $T = 1.05$ µs/rad, giving the impulse response in the time domain of $h(t) = t^3(6Te^{t/T})^{-1}$. Although systematically included in the simulations below, the detector–preamplifier combination is many orders faster than the observed overshoots, and can be neglected in the analysis for Mueller matrix measurement frequencies (i.e. 16 switches) below approximately 2.5 kHz. However, for even faster systems, the detector response will evidently affect the maximal Mueller matrix measurement frequency.

4.2.1. Dynamic response of the FLCs

The FLCs can be regarded as waveplates with nominally two stable states, each separated by a rotation of the waveplate by 45°. In a more accurate model the switching between the stable states is obtained by rotating the molecular director axis of the molecules in the FLC by 180° in a cone around the normal axis of the molecular layer [19]. In order to understand the temporal limitations of the FLC-based MME it is most important to understand the collective dynamic response of the director axis. For simplicity, it is sufficient for our purposes to consider the approximation of crystal switching by assuming a simple rotation of a waveplate from the most stable state 1, to the second excited stable state 2. Let us denote 'up-switching' when switching from the more stable to the excited state ($\theta_{1,j} \rightarrow \theta_{2,j}$), and 'down-switching' when switching from the excited state to the more stable state ($\theta_{2,j} \rightarrow \theta_{1,j}$).

Since no fast Mueller matrix ellipsometer was available to measure the dynamic response of the switching of the crystals, a simple crossed polarizer setup was used. The FLCs were positioned with their fast axis at −20° with respect to the input polarizer. The measurements were performed at 980 nm, using the flat response InGaAs detector-preamplifier and the intensity was measured as a function of time. The estimated FLC orientation angle was solved by assuming the constant static retardance using Table 1, with the following equation:

$$I(t) = 1 - \cos^2 2\theta(t) - \cos\delta \sin^2 2\theta(t). \tag{12}$$

Figure 4 shows the dynamic response of the crystals used in this study, using the latter method. The more correct model for the switching is obtained by

precessing the tip of the molecular director in a cone around its axis of rotation. Then $\chi(t) = 0 \ldots \pi$ is related to the azimuth orientation angle by $\tan\theta(t) = \tan\varphi \cdot \cos\chi(t)$, with a fixed tilt angle of $\varphi(t) = \pi/8$. The latter precessing will also introduce a time-varying retardance. However, this model mainly modifies the centre of the switching curve, which is observed to be inaccurately determined in a crossed polarizer setup (see the discontinuous region around 22.5° in Figure 4). The details of the switching response obtained from Figure 4 are tabulated in Table 2, giving the transition times (t_{up} and t_{down}) to the intensity first crossing the level of stable state, for up and down switching, respectively. The transition times to steady state are given by t_{ss-up} and $t_{ss\text{-}down}$, for up and down switching, respectively. A detailed inspection of the insets in Figure 4, shows that that the azimuth angle of the crystals appears to pass the stable state before settling, resulting in an overshoot, which typically ranges from $\Delta\theta = 0.5$–1°, corresponding to a precession overshoot of $d\chi = 12$–18°. The switching times are found to vary from crystal to crystal, and the thicker crystals appear to have a 25% longer switching time when going up and a 35% longer switching time when going down, compared with the thinner FLCs.

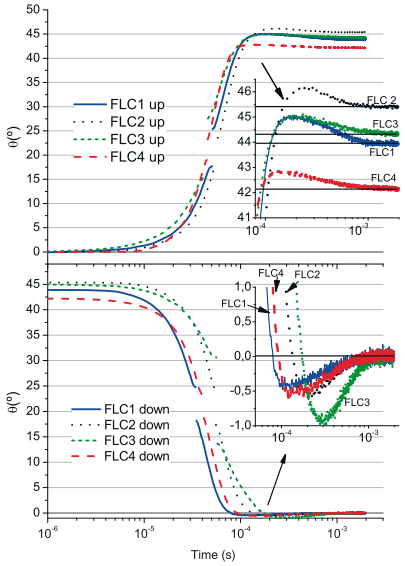

Figure 4. Measured temporal response of the azimuth angle $\theta(t)$ of the FLCs used in this study. The upper figure shows the up-switching of the crystals (more stable to less stable state), while the bottom figure shows the down-switching (less stable to more stable state). The temporal characteristics, such as t_{up} (first crossover with steady state) and t_{ss} (time to reach steady state) and the overshoot are tabulated in Table 2. (The color version of this figure is included in the online version of the journal.)

4.2.2. *Simulation of the dynamic response of the FLC-based MME*

The model for the optical intensities stored in **B** was used to simulate a system that was, as far as possible, similar to the experimental set-up. In the first simulation, the crystals were imagined to switch semi-instantaneously between the states. It was observed that there were no overshoots, and the results were only slightly filtered by the response of the detector.

In a more realistic simulation, the crystals were linearly switched between the two stable states, using the measured up and down switching times tabulated in Table 2. The director axis was modeled to precess linearly in a cone towards the second state, i.e. by letting $\chi(t) = \pi t/t_{up,down}$. The retardance and the azimuth orientation were determined by using the standard Euler rotation of the dielectric tensor, which was assumed uniaxial with the extraordinary axis along the molecular director axis. Figure 3(*b*) shows the resulting simulated intensity response of the full MME upon switching through all the stable states. It is observed that the large overshoots and undershoots are well reproduced in the simulation, and we conclude that these are simply due to the time-varying intensity illuminating the detector upon changing the Stokes vector as a function of time. A simple linear rotation of the azimuth angle $\theta(t)$ does not considerably modify the response. The simulated dynamic intensity response using the most advanced model for linear switching between the two states, Figure 3(*b*), is not fully

Table 2. Temporal switching characteristics of the FLCs used in the fast MME. The up switching and down switching times were used in the simulation in Figure 3.

	t_{up} (μs)	$t_{ss\text{-}up}$ (μs)	Overshoot (°)	t_{down} (μs)	$t_{ss\text{-}down}$ (μs)	Overshoot (°)
FLC1 (thin)	113	800	1.00	78	850	0.44
FLC2 (thick)	149	950	0.72	133	1050	0.57
FLC3 (thick)	120	1000	0.54	173	1072	1.00
FLC4 (thin)	91	756	0.68	92	920	0.62

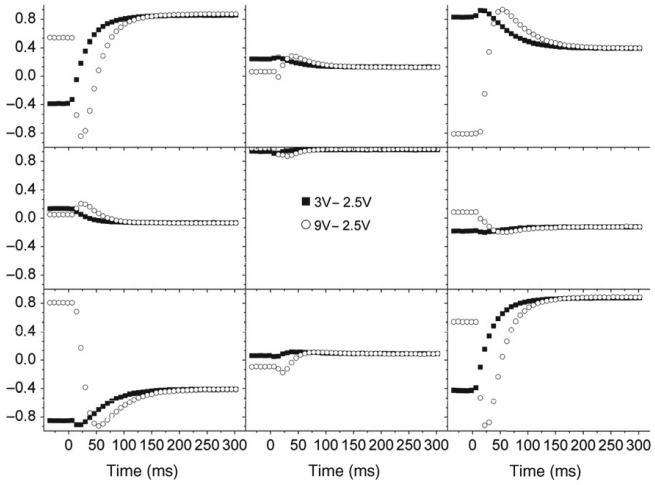

Figure 5. Temporal sub Mueller matrix ($\hat{m}_R(t)$) of a thick VLCR upon switching from 304° to 25° (circle) and 116° to 25° (square). The system was operated at 8 ms per Mueller matrix.

coincident with the measured response shown in Figure 3(*a*). The crystals clearly have a more complex response of the average azimuth angle, as was already demonstrated by the overshoots in the switching measurements of the FLCs in Figure 4. In the final simulation, the measured switching response of each crystal was therefore carefully introduced into the simulation in an identical manner to the system. The resulting simulated intensity obtained upon switching through the 16 states is shown in Figure 3(*c*). It is observed that the simulation reproduces the measured response very well, and that the overall system response and its limitations may now be fully understood.

4.3. *Application example: dynamic characterization of a thick pneumatic variable liquid crystal retarder*

As a demonstration of the operation of the fast FLC based NIR-MME, we have studied the temporal response of the Mueller matrix and the retardance of a thick variable liquid crystal retarder (VLCR), as a function of the switching time, at 980 nm. The full Mueller matrix was measured for each time sample. Since the transition between states occurs very quickly, the system was operated by sampling a Mueller matrix every 8 ms. For visualization purposes the measured Mueller matrix is approximated by

$$\mathbf{M}(t) = \begin{bmatrix} 1 & \overrightarrow{0}^T \\ \overrightarrow{0} & \hat{m}_R(t) \end{bmatrix},$$

where $\hat{m}_R(t)$ is the measured time dependent (3×3) retardance sub-matrix and $\overrightarrow{0} = [0, 0, 0]^T$ is the null vector. The resulting temporal retardance sub-matrix is shown in Figure 5. Figure 5 shows both $\hat{m}_R(t)$ observed by switching the VLCR by 277° (9 V to 2.5 V, $\Delta V = 6.5$ V) and by 90° (3 V to 2.5 V, $\Delta V = 0.5$ V). The azimuth orientation of the fast axis was −50°. The VLCR is observed to typically switch to its steady state in approximately 200 ms, independent of ΔV. At maximum velocity, the VLCR switches with 8.6° per ms, the under-sampling will thus cause some errors in the measurements. The Lu–Chipman polar decomposition of the matrix gives the temporal evolution of the retardance, which is shown in Figure 6.

5. Summary and conclusion

The dynamic response of a FLC-based Mueller matrix Ellipsometer operating in the near infra-red has been measured and accurately modelled. The dynamic response of the intensity recorded on the detector is a function of the time-dependent collective rotation of the molecular director axis and the impulse response of the detector. The simulations correspond well with the measurements, and it is concluded that using a flat and high-frequency cut-off preamplifier and InGaAs detector does not limit the response, while the dynamic response of the LC molecules rotating towards steady state is the limiting factor for switching speed.

The switching of the crystals from one state to another results in an optical driving signal that may

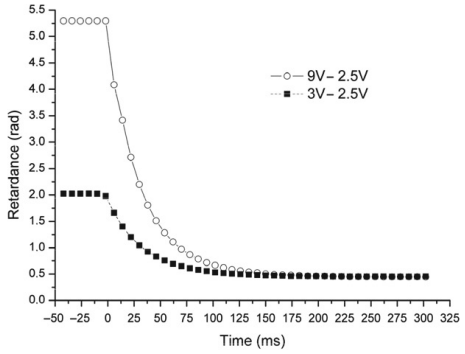

Figure 6. Dynamic response of the retardance (in radians) of a thick VLCR upon switching from 9 V to 2.5 V (circles), and 3V to 2.5 Volts (squares). The MME system was operated at 8 ms per Mueller matrix.

take various forms, and in the worst case has nearly the form of a delta-function. We have shown above, that this is a simple optical phenomenon that may be easily modelled by including a fast linear precession of the director axis of the molecules in the FLCs. Similar issues will be present in any fast operating MME. This response put certain requirements on the detector and preamplifier. However, the detector preamplifier designed for the current setup should be able to handle up to 2.5 kHz repetition rates of Mueller matrix measurements. It is therefore the transient response of the switching of the FLCs that is the critical issue in the FLC-based MME. For accurate measurements, the steady-state response requires a minimum complete Mueller matrix measurement time of 15 ms. A further margin for data acquisition may also be required in order to obtain a good signal-to-noise ratio, resulting in 16 ms as a typical minimum requirement. The system may be operated faster, e.g. by only waiting for the t_{up} and t_{down}, and allowing the additional measurement errors due to the overshoot. The system may then optimally be operated at a minimum measurement time of 2 ms in addition to acquisition times for each Mueller matrix.

As a demonstration, the system has been successfully used to study the dynamic Mueller matrix during switching of a custom-made thick variable liquid crystal, with a sampling of 8 ms per Mueller matrix.

References

[1] Compain, E.; Drevillon, B. *Rev. Sci. Instrum.* **1997,** *68,* 2671–2680.
[2] Compain, E.; Drevillon, B. *Rev. Sci. Instrum.* **1998,** *69,* 1574–1580.
[3] Lara, D.; Dainty, C. *Opt. Lett.* **2005,** *30,* 2879–2881.
[4] Lee, J.; Koh, J.; Collins, R.W. *Rev. Sci. Instrum.* **2001,** *72,* 1742–1754.
[5] Stabo-Eeg, F.; Kildemo, M.; Nerbo, I.S.; Lindgren, M. *Opt. Eng.* **2008,** *47,* 073604.
[6] Collins, R.W.; Koh, J.J. *Opt. Soc. Am. A* **1999,** *16,* 1997–2006.
[7] Garcia-Caurel, E.; De Martino, A.; Drevillon, B. *Thin Solid Films* **2004,** *455-56,* 120–123.
[8] De Martino, A.; Kim, Y.K.; Garcia-Caurel, E.; Laude, B.; Drevillon, B. *Opt. Lett.* **2003,** *28,* 616–618.
[9] Dubreuil, M.; Rivet, S.; Le Jeune, B.; Cariou, J. *Opt. Express* **2007,** *15,* 13660–13668.
[10] Dubreuil, M.; Rivet, S.; Le Jeune, B.; Cariou, J. *Appl. Opt.* **2009,** *48,* 6501–6505.
[11] Stabo-Eeg, F.; Kildemo, M.; Garcia-Caurel, E.; Lindgren, M. *J. Mod. Opt.* **2008,** *55,* 2203–2214.
[12] Hallstig, E.; Stigwall, J.; Martin, T.; Sjoqvist, L.; Lindgren, M. *J. Mod. Opt.* **2004,** *51,* 1233–1247.
[13] Hallstig, E.; Martin, T.; Sjoqvist, L.; Lindgren, M. *J. Opt. Soc. Am. A* **2005,** *22,* 177–184.
[14] Shirai, T. *Appl. Opt.* **2002,** *41,* 4013–4023.
[15] Curtis, J.E.; Koss, B.A.; Grier, D.G. *Opt. Commun.* **2002,** *207,* 169–175.
[16] Gandorfer, A.M. *Opt. Eng.* **1999,** *38,* 1402–1408.
[17] Ladstein, J.; Kildemo, M.; Svendsen, G.K.; Nerbo, I.S.; Stabo-Eeg, F. *Proc. SPIE* **2007,** *6587,* 65870D.
[18] Ladstein, J.; Stabo-Eeg, F.; Garcia-Caurel, E.; Kildemo, M. *Phys. Status Solidi C* **2008,** *5,* 1097–1100.
[19] Gu, C.; Yeh, P. *Optics of Liquid Crystal Displays*; Wiley: New York, 1999.
[20] Compain, E.; Poirier, S.; Drevillon, B. *Appl. Opt.* **1999,** *38,* 3490–3502.
[21] Tyo, J.S. *Opt. Lett.* **2000,** *25,* 1198–1200.
[22] Compain, E.; Drevillon, B. *Appl. Opt.* **1998,** *37,* 5938–5944.
[23] Compain, E.; Drevillon, B.; Huc, J.; Parey, J.Y.; Bouree, J.E. *Thin Solid Films* **1998,** *313,* 47–52.
[24] Ossikovski, R.; Anastasiadou, M.; Ben Hatit, S.; Garcia-Caurel, E.; De Martino, A. *Phys. Status Solidi A* **2008,** *205,* 720–727.
[25] Swami, M.K.; Manhas, S.; Buddhiwant, P.; Ghosh, N.; Uppal, A.; Gupta, P.K. *Opt. Express* **2006,** *14,* 9324–9337.
[26] Lu, S.Y.; Chipman, R.A. *J. Opt. Soc. Am. A* **1996,** *13,* 1106–1113.
[27] Hauge, P.S.; Muller, R.H.; Smith, C.G. *Surf. Sci.* **1980,** *96,* 81–107.

P. A. Letnes, I. S. Nerbø, L. M. S. Aas, P. G. Ellingsen, and M. Kildemo, Fast and optimal broad-band Stokes/Mueller polarimeter design by the use of a genetic algorithm, Opt. Express **18**, 23095–23103 (2010)

Paper 2

Fast and optimal broad-band Stokes/Mueller polarimeter design by the use of a genetic algorithm

Paul Anton Letnes,* Ingar Stian Nerbø, Lars Martin Sandvik Aas, Pål Gunnar Ellingsen, and Morten Kildemo

Department of Physics, The Norwegian University of Science and Technology (NTNU), N-7491 Trondheim, Norway

**paul.anton.letnes@gmail.com*

Abstract: A fast multichannel Stokes/Mueller polarimeter with no mechanically moving parts has been designed to have close to optimal performance from 430 – 2000 nm by applying a genetic algorithm. Stokes (Mueller) polarimeters are characterized by their ability to analyze the full Stokes (Mueller) vector (matrix) of the incident light (sample). This ability is characterized by the condition number, κ, which directly influences the measurement noise in polarimetric measurements. Due to the spectral dependence of the retardance in birefringent materials, it is not trivial to design a polarimeter using dispersive components. We present here both a method to do this optimization using a genetic algorithm, as well as simulation results. Our results include fast, broad-band polarimeter designs for spectrographic use, based on 2 and 3 Ferroelectric Liquid Crystals, whose material properties are taken from measured values. The results promise to reduce the measurement noise significantly over previous designs, up to a factor of 4.5 for a Mueller polarimeter, in addition to extending the spectral range.

OCIS codes: (120.2130) Ellipsometry and polarimetery; (120.4570) Optical design of instruments; (300.0300) Spectroscopy.

References and links

1. A. M. Gandorfer, "Ferroelectric retarders as an alternative to piezoelastic modulators for use in solar Stokes vector polarimetry," Opt. Eng. **38**, 1402–1408 (1999).
2. P. Collins, R. Redfern, and B. Sheehan, "Design, construction and calibration of the Galway astronomical Stokes polarimeter (GASP)," in *AIP Conference Proceedings,* D. Phelan, O. Ryan, and A. Shearer, eds. (AIP, Edinburgh (Scotland), 2008), vol. 984, p. 241.
3. A. Alvarez-Herrero, V. Martínez-Pillet, J. del Toro Iniesta, and V. Domingo, "The IMaX polarimeter for the solar telescope SUNRISE of the NASA long duration balloon program," in *Proceedings of API'09,* E. Garcia-Caurel, ed. (EPJ Web of Conferences, 2010), vol. 5, p. 05002.
4. J. D. Howe, M. A. Miller, R. V. Blumer, T. E. Petty, M. A. Stevens, D. M. Teale, and M. H. Smith, "Polarization sensing for target acquisition and mine detection," in *Polarization Analysis, Measurement, and Remote Sensing III,* D. B. Chenault, M. J. Duggin, W. G. Egan, and D. H. Goldstein, eds., Proc. SPIE **4133**, 202–213 (2000).
5. M. H. Smith, P. D. Burke, A. Lompado, E. A. Tanner, and L. W. Hillman, "Mueller matrix imaging polarimetry in dermatology," in *Biomedical Diagnostic, Guidance, and Surgical-Assist Systems II,* T. Vo-Dinh, W. S. Grundfest, and D. A. Benaron, eds., Proc. SPIE **3911**, 210–216 (2000).
6. R. N. Weinreb, S. Shakiba, and L. Zangwill, "Scanning laser polarimetry to measure the nerve fiber layer of normal and glaucomatous eyes," Am. J. Ophthalmol. **119**, 627–636 (1995).

#134880 - $15.00 USD Received 9 Sep 2010; revised 5 Oct 2010; accepted 5 Oct 2010; published 18 Oct 2010

7. M. Foldyna, A. D. Martino, R. Ossikovski, E. Garcia-Caurel, and C. Licitra, "Characterization of grating structures by Mueller polarimetry in presence of strong depolarization due to finite spot size," Opt. Commun. **282**, 735–741 (2009).
8. I. S. Nerbø, S. Le Roy, M. Foldyna, M. Kildemo, and E. Søndergård, "Characterization of inclined GaSb nanopillars by Mueller matrix ellipsometry," J. Appl. Phys. **108**, 014307 (2010).
9. L. Jin, M. Kasahara, B. Gelloz, and K. Takizawa, "Polarization properties of scattered light from macrorough surfaces," Opt. Lett. **35**, 595–597 (2010).
10. T. A. Germer, "Polarized light scattering by microroughness and small defects in dielectric layers." J. Opt. Soc. Am. A **18**, 1279–1288 (2001).
11. T. Germer, "Measurement of roughness of two interfaces of a dielectric film by scattering ellipsometry," Phys. Rev. Lett. **85**, 349–352 (2000).
12. F. Stabo-Eeg, M. Kildemo, I. Nerbø, and M. Lindgren, "Well-conditioned multiple laser Mueller matrix ellipsometer," Opt. Eng. **47**, 073604 (2008).
13. J. S. Tyo, "Noise equalization in Stokes parameter images obtained by use of variable-retardance polarimeters," Opt. Lett. **25**, 1198–1200 (2000).
14. D. S. Sabatke, M. R. Descour, E. L. Dereniak, W. C. Sweatt, S. A. Kemme, and G. S. Phipps, "Optimization of retardance for a complete Stokes polarimeter," Opt. Lett. **25**, 802–804 (2000).
15. R. M. A. Azzam and A. De, "Optimal beam splitters for the division-of-amplitude photopolarimeter," J. Opt. Soc. Am. A **20**, 955–958 (2003).
16. R. M. A. Azzam, "Photopolarimetric measurement of the Mueller matrix by Fourier analysis of a single detected signal," Opt. Lett. **2**, 148 (1978).
17. J. M. Bueno, "Polarimetry using liquid-crystal variable retarders: theory and calibration," J. Opt. A: Pure Appl. Opt. **2**, 216–222 (2000).
18. E. Garcia-Caurel, A. D. Martino, and B. Drévillon, "Spectroscopic Mueller polarimeter based on liquid crystal devices," Thin Solid Films **455-456**, 120–123 (2004).
19. J. Ladstein, M. Kildemo, G. Svendsen, I. Nerbø, and F. Stabo-Eeg, "Characterisation of liquid crystals for broadband optimal design of Mueller matrix ellipsometers," in *Liquid Crystals and Applications in Optics,* M. Glogarova, P. Palffy-Muhoray, and M. Copic, eds. Proc. SPIE **6587**, 65870D (2007).
20. L. M. S. Aas, P. G. Ellingsen, M. Kildemo, and M. Lindgren, "Dynamic Response of a fast near infra-red Mueller matrix ellipsometer," J. Mod. Opt. **(accepted)** (2010).
21. D. Cattelan, E. Garcia-Caurel, A. De Martino, and B. Drevillon, "Device and method for taking spectroscopic polarimetric measurements in the visible and near-infrared ranges," Patent application 2937732, France (2010).
22. J. H. Holland, "Genetic algorithms," Scientific American **267**, 44–50 (1992).
23. D. Floreano and C. Mattiussi, *Bio-Inspired Artificial Intelligence: Theories, Methods, and Technologies* (The MIT Press, 2008).
24. A. Kudla, "Application of the genetic algorithms in spectroscopic ellipsometry," Thin Solid Films **455-456**, 804–808 (2004).
25. G. Cormier and R. Boudreau, "Genetic algorithm for ellipsometric data inversion of absorbing layers," J. Opt. Soc. Am. A **17**, 129–134 (2000).
26. V. R. Fernandes, C. M. S. Vicente, N. Wada, P. S. André, and R. A. S. Ferreira, "Multi-objective genetic algorithm applied to spectroscopic ellipsometry of organic-inorganic hybrid planar waveguides," Opt. Express **18**, 16580–16586 (2010).
27. F. Stabo-Eeg, M. Kildemo, E. Garcia-Caurel, and M. Lindgren, "Design and characterization of achromatic 132° retarders in CaF_2 and fused silica," J. Mod. Opt. **55**, 2203–2214 (2008).
28. W. H. Press, S. A. Teukolsky, W. T. Vetterling, and B. P. Flannery, *Numerical Recipes: The Art of Scientific Computing* (Cambridge University Press, 2007).
29. E. Compain, S. Poirier, and B. Drevillon, "General and self-consistent method for the calibration of polarization modulators, polarimeters, and Mueller-matrix ellipsometers," Appl. Opt. **38**, 3490–3502 (1999).
30. J. Ladstein, F. Stabo-Eeg, E. Garcia-Caurel, and M. Kildemo, "Fast near-infra-red spectroscopic Mueller matrix ellipsometer based on ferroelectric liquid crystal retarders," Phys. Status Solidi C **5**, 1097–1100 (2008).

1. Introduction

Polarimeters are applied in a wide range of fields, from astronomy [1–3], remote sensing [4] and medical diagnostics [5, 6] to applications in ellipsometry such as characterizing gratings [7], nanostructures [8] and rough surfaces [9–11]. As all polarimeters are based on inverting so-called system matrices, it is well known that the measurement error from independent Gaussian noise is minimized when the condition number (κ) of these system matrices is minimized [12, 13]. It has been shown that $\kappa = \sqrt{3}$ is the best condition number that can be achieved for such a system, and that this optimal condition number can be achieved by several different

#134880 - $15.00 USD Received 9 Sep 2010; revised 5 Oct 2010; accepted 5 Oct 2010; published 18 Oct 2010

approaches using various optical components (*e.g.* rotating retarders [14], division of amplitude [15, 16], and liquid-crystal variable retarders [17]). In many applications it is necessary to perform fast spectroscopic measurements (*e.g.* by using a Charge-Coupled Device (CCD) based spectrograph) [18]. In that case, the wavelength dependence of the optical elements will cause the polarimeter not to be optimally conditioned over the full range simultaneously. A system based on two Ferroelectric Liquid Crystals (FLC) has been reported to be fast and reasonably well conditioned over the visible or near infrared spectral range [18–20]. By introducing a third FLC a similar system has been proposed to have an acceptable condition number from the visible to the near infra-red ($430-1700$ nm) [21]. The design of a system having the best possible condition number over a broad spectrum is a challenging optimization problem due to the large number of parameters; many optimization algorithms are prone to return local optimums, and a direct search is too time consuming. To avoid this time-consuming exhaustive search, we decided to employ the Genetic Algorithm (GA). A GA simulates evolution on a population of individuals in order to find an optimal solution to the problem at hand. Genetic Algorithms were pioneered by Holland [22], and are discussed in detail in *e.g.* Ref. [23]. GAs have previously been applied in ellipsometry to solve the inversion problem for the thickness and dielectric function of multiple thin layers, see *e.g.* Ref. [24–26].

2. Overdetermined polarimetry

A Stokes polarimeter consists of a polarization state analyzer (PSA) capable of measuring the Stokes vector of a polarization state, see Fig. 1. The PSA is based on performing at least 4 different measurements along different projection states. A measured Stokes vector $\mathbf{S}$ can then be expressed as $\mathbf{S} = \mathbf{A}^{-1}\mathbf{b}$, where $\mathbf{A}$ is a system matrix describing the PSA and $\mathbf{b}$ is a vector containing the intensity measurements. $\mathbf{A}^{-1}$ denotes the matrix inverse of $\mathbf{A}$, which in the case of overdetermined polarimetry with more than 4 projection states will denote the Moore–Penrose *pseudoinverse*. The analyzing matrix $\mathbf{A}$ is constructed from the first rows of the Mueller matrices of the PSA for the different states. The noise in the measurements of $\mathbf{b}$ will be amplified by the condition number of $\mathbf{A}$, $\kappa_{\mathbf{A}}$, in the inversion to find $\mathbf{S}$. Therefore $\kappa_{\mathbf{A}}$ should be as small as possible, which correspond to do as independent measurements as possible (*i.e.* to use projection states that are as orthogonal as possible).

A Mueller matrix $\mathbf{M}$ describes how an interaction changes the polarization state of light, by transforming an incoming Stokes vector $\mathbf{S}_{\text{in}}$ to the outgoing Stokes vector $\mathbf{S}_{\text{out}} = \mathbf{M}\mathbf{S}_{\text{in}}$. To measure the Mueller matrix of a sample it is necessary to generate at least 4 different polarization states by a polarization state generator (PSG) and measure the outgoing Stokes vector by at least 4 measurements for each generated state. The measured intensities can then be arranged in a matrix $\mathbf{B} = \mathbf{AMW}$, where the system matrix $\mathbf{W}$ of the PSG contains the generated Stokes vectors as its columns. These generated Stokes vectors are found simply as the first column of the Mueller matrix of the PSG in the respective states. $\mathbf{M}$ can then be found by inversion as $\mathbf{M} = \mathbf{A}^{-1}\mathbf{B}\mathbf{W}^{-1}$. The error $\Delta\mathbf{M}$ in $\mathbf{M}$ is then bounded by the condition numbers according to [27]

$$\frac{\|\Delta\mathbf{M}\|}{\|\mathbf{M}\|} \lesssim \kappa_{\mathbf{W}}\kappa_{\mathbf{A}}\frac{\|\Delta\mathbf{B}\|}{\|\mathbf{B}\|} + \kappa_{\mathbf{A}}\frac{\|\Delta\mathbf{A}\|}{\|\mathbf{A}\|} + \kappa_{\mathbf{W}}\frac{\|\Delta\mathbf{W}\|}{\|\mathbf{W}\|}. \tag{1}$$

The condition number is given as $\kappa_{\mathbf{A}} = \|\mathbf{A}\|\|\mathbf{A}^{-1}\|$, which for the the 2-norm can be calculated from the ratio of the largest to the smallest singular value [28]. $\Delta\mathbf{A}$ and $\Delta\mathbf{W}$ are calibration errors, which increase with κ when calibration methods using matrix inversion are applied. The PSG can be constructed from the same optical elements as the PSA, placed in the reverse order, which would give $\kappa_{\mathbf{A}} = \kappa_{\mathbf{W}} \equiv \kappa$. As the error in Mueller matrix measurements is proportional

#134880 - $15.00 USD Received 9 Sep 2010; revised 5 Oct 2010; accepted 5 Oct 2010; published 18 Oct 2010

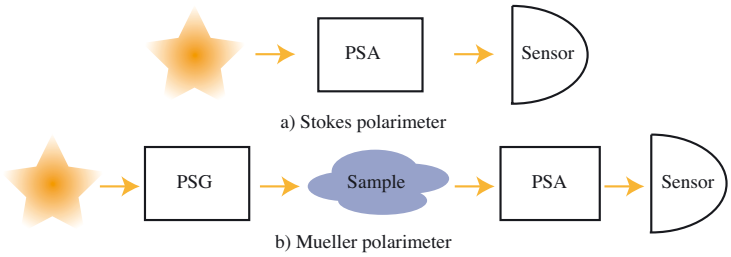

Fig. 1. (a) A Stokes polarimeter measures the polarization state of an arbitrary light source using a Polarization State Analyzer (PSA). (b) A Mueller polarimeter measures how the polarization state of light, generated by with a Polarization State Generator (PSG), is changed by a sample.

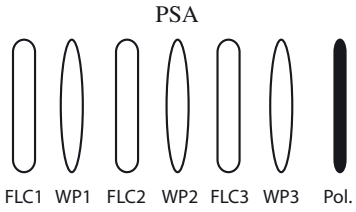

Fig. 2. Sketch of a PSA consisting of 3 FLC's, 3 waveplates (WP), each with a retardance δ and an orientation θ relative to the transmission axis of a polarizer.

to κ^2, it is very important to keep this value as low as possible.

If 4 optimal states can be achieved (giving $\kappa = \sqrt{3}$), no advantage is found by doing a larger number of measurements with different states, compared to repeated measurements with the 4 optimal states [14]. If, however, these optimal states can not be produced ($\kappa > \sqrt{3}$), the condition number, and hence the error, can be reduced by performing more than 4 measurements. For a FLC based polarimeter this can be done by using 3 FLCs followed by a polarizer as PSA, with up to 3 waveplates (WP) between the FLCs to increase the condition number (see Fig. 2). A PSG can be constructed with the same elements in the reverse order. Since each FLC can be switched between two states (this switching can be described as a rotation of the fast axis of a retarder by $+45°$), $2^3 = 8$ different states can be analyzed (generated) by the PSA (PSG). To accurately measure the Stokes vector, the system matrix **A** needs to be well known. For a Mueller polarimeter generating and analyzing 4 states in the PSG and PSA, the eigenvalue calibration method (ECM) [29] can be applied. The ECM allows the measuring of the actual produced states by the PSA and PSG (**A** and **W**), without relying on exact knowledge or modeling of the optical components. However, the ECM is based on the inversion of a product of measured intensity matrices **B** for measurements on a set of calibration samples. This product becomes singular for a system analyzing and generating more than four states. A workaround of this problem is to choose the subset of 4 out of 8 states which gives the lowest κ value, and build a **B** matrix of those states to find 4 of the 8 rows (columns) of **A** (**W**). More rows (columns) of **A** (**W**) can then be found by calibrating on a different subset of the 8 states, giving the second lowest κ value, and so on. By repeating the calibration on different subsets of states, all the 8 rows (columns) of **A** (**W**) can be found with low relative error $\|\Delta\mathbf{A}\|/\|\mathbf{A}\|$ ($\|\Delta\mathbf{W}\|/\|\mathbf{W}\|$).

#134880 - $15.00 USD Received 9 Sep 2010; revised 5 Oct 2010; accepted 5 Oct 2010; published 18 Oct 2010

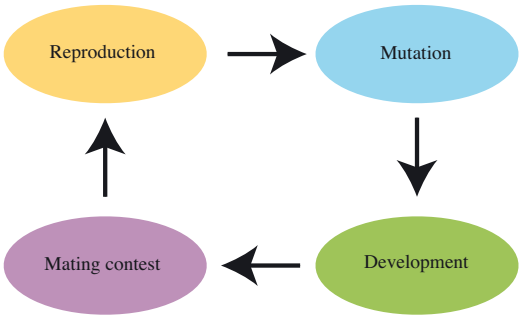

Fig. 3. The four essential processes in a genetic algorithm are shown above. Sexual reproduction is performed by multi-point genetic crossover, giving rise to the next generation of individuals. Mutation can be simulated with simple bit negation (*e.g.* $0 \rightarrow 1$ and *vice versa*). Development is the process where a genotype is interpreted into its phenotype, *i.e.* the binary genome is interpreted as a polarimeter design. In the mating contest, one evaluates the fitness of each individual's phenotype, and let the more fit individuals reproduce with higher probability than the less fit individuals.

3. Genetic optimization

In order to optimize $\kappa(\lambda)$, one can conceivably employ a variety of optimization algorithms, from simple brute-force exhaustive search to more advanced algorithms, such as *e.g.* Levenberg–Marquardt, simulated annealing, and particle swarm optimization. Our group has previously performed optimization of a polarimeter design based on fixed components, namely, two FLCs and two waveplates. In this case, the optimization problem reduces to searching the space of 4 orientation angles. With a resolution of 1° per angle, this gives a search space consisting of $180^4 \approx 10^9$ states to evaluate; on modern computer hardware, this direct search can be performed. In order to optimize the retardances of the components as well, the total number of states increases to about $\left(10^9\right)^2 = 10^{18}$. Obviously, brute force exhaustive search is unfeasible for such large search spaces.

A GA performs optimization by simulating evolution in a population of individuals (here: simulated polarimeters). The three pillars of evolution are variation, heritability, and selection. Our initial population must have some initial genetic variation between the individuals; hence, we initialize our population by generating random individuals. Heritability means that the children have to carry on some of the traits of their parents. We simulate this by either cloning parents into children (asexual reproduction) or by performing genetic crossover (sexual reproduction) in a manner that leave children with some combination of the traits of their parents. Finally, selection is done by giving more fit individuals a larger probability of survival. For this purpose, we used the tournament selection protocol, described in Ref. [23]. For a sketch of the essential processes involved in a GA, see Fig. 3.

Our GA builds directly on the description given by Holland [22], using a binary genome as the genetic representation. In this representation, a string of 0s and 1s represent the genome of the individual. To simulate mutation in our genetic algorithm, we employ logical bit negation; *i.e.* $0 \rightarrow 1$ or vice versa. Sexual reproduction is simulated by using multi-point crossover, *i.e.* simply cutting and pasting two genomes together, as described by Holland [22].

The interpretation of the genome into a phenotype (development), in this case a polarimeter design, is done in a straightforward way. For each variable in the polarimeter's configuration,

#134880 - $15.00 USD Received 9 Sep 2010; revised 5 Oct 2010; accepted 5 Oct 2010; published 18 Oct 2010

i.e. for each orientation angle and each retardance, we select m bits in the genome (typically, $m = 8$) and interpret this number as an integer in the range from 1 to 2^m. The integer is subsequently interpreted as a real number in a predefined range, *e.g.*, $\theta \in [0°, 180°]$. In order to avoid excessively large jumps in the search space due to mutations, we chose to implement the interpretation of bits into integers by using the Gray code, also known as the reflected binary code. The most important parameter values in our GA are shown in Table 2. Making good choices for each of these parameters is often essential in order to ensure good convergence.

After determining the phenotype, we must assign to each simulated polarimeter individual a fitness function (also known as the objective function). In order to do this, we first calculate $\kappa(\lambda)$. As discussed, $\kappa^{-1}(\lambda)$ maximally takes on the value $1/\sqrt{3}$. Hence, we define an error function, e, as

$$e = \frac{1}{N_\lambda} \sum_{n=1}^{N_\lambda} \left(\kappa^{-1}(\lambda_n) - 1/\sqrt{3} \right)^4. \tag{2}$$

In Eq. (2), $\lambda_n = \lambda_{\min} + (n-1)\Delta\lambda$, with $n = 1, 2, \ldots, N_\lambda$ and $\Delta\lambda = 5$ nm. $\lambda_{\min}$ and N_λ are determined by the wavelength range we are interested in. The choice of taking the difference between $\kappa^{-1}(\lambda)$ and the optimal value to power 4 is done in order to "punish" peaks in the condition number more severely. As GAs conventionally seek to maximize the fitness function, we define an individual's fitness as

$$f = \frac{1}{e}. \tag{3}$$

This definition is convenient because f takes on real and positive values where higher values represents more optimal polarimeter designs.

4. Results

For the case of a polarimeter based on 3 FLCs and 3 WPs, we have minimized $\kappa(\lambda)$ by varying the orientation angle, θ, and the retardance, δ, of all the elements. This yields a 12-dimensional search space, *i.e.*, 6 retardances and 6 orientation angles. θ is the angle between the fast axis of the retarder (WP or FLC) and the transmission axis of the polarizer (see Fig. 2), taken to be in the range $\theta \in [0°, 180°]$. The retardance, δ, is modeled using a modified Sellmeier equation,

$$\delta \approx 2\pi L \left[\frac{A_{UV}}{(\lambda^2 - \lambda_{UV}^2)^{1/2}} - \frac{A_{IR}}{(\lambda_{IR}^2 - \lambda^2)^{1/2}} \right], \tag{4}$$

where A_{UV}, A_{IR}, λ_{UV}, and λ_{IR} are experimentally determined parameters for an FLC ($\lambda/2$@510 nm, Displaytech Inc.) and a Quartz zero order waveplate ($\lambda/4$@465 nm) taken directly from Refs. [19] (for the FLCs, $A_{IR} = 0$). L is a normalized thickness, with $L = 1$ corresponding to a retardance of $\lambda/2$@510 nm for the FLCs and $\lambda/4$@465 nm for the waveplates. Each L and θ are represented by 8 bits each in the genome. We use experimental values to ensure that our design is based on as realistic components as possible.

The 3-FLC polarimeter design scoring the highest fitness function is shown in Table 1. The wavelength range for which we optimized the polarimeter was from 430 to 2000 nm. To visualize the performance of this design, we show a plot of $\kappa^{-1}(\lambda)$ in Fig. 4. The inverse condition number, κ^{-1}, is larger than 0.5 over most parts of the spectrum, which is close to the optimal inverse condition number ($\kappa^{-1} = 1/\sqrt{3} = 0.577$). This is a great improvement compared to the earlier reported 3-FLC design [21], which oscillates around $\kappa^{-1} \approx 0.33$. The new design promise a decrease in noise amplification by up to a factor of 2.1 for a Stokes polarimeter, and up to factor of 4.5 for a Mueller polarimeter. In addition the upper spectral limit is extended

#134880 - $15.00 USD Received 9 Sep 2010; revised 5 Oct 2010; accepted 5 Oct 2010; published 18 Oct 2010

Table 1. Orientation angles, θ, and normalized thicknesses L, of the components of the best 3-FLC polarimeter. (WP = (fixed) waveplate)

Component	θ[°]	L
FLC1	56.5	2.44
WP1	172.9	1.10
FLC2	143.3	1.20
WP2	127.1	1.66
FLC3	169.4	1.42
WP3	110.1	4.40

from 1700 nm to 2000 nm. Shorter wavelengths than 430 nm were not considered as the FLC material will be degraded by exposure to UV light. Previous designs often suffer from $\kappa^{-1}(\lambda)$ oscillating as a function of wavelength, whereas our solution is more uniform over the wavelength range we are interested in. This uniformity in $\kappa(\lambda)$ will, according to Eq. (1), give a more uniform noise distribution over the spectrum.

To give some idea of how fast the GA converges, a plot of f [see Eq. (3)] as a function of the generation number is shown in Fig. 5. The mean population fitness (μ) and standard deviation (σ) is also shown. As so often happens with genetic algorithms, we see that the maximal and average fitness increases dramatically in the first few generations. Following this fast initial progress, evolution slows down considerably, before it finally converges after 600 generations. The parameters used in our GA to obtain these results are shown in Table 2.

A design using fewer components, in particular 2 FLCs and 2 waveplates, does have advantages. These advantages include increased transmission of light, as well as reduced cost and complexity with respect to building and maintaining the instrument. In addition some applications have weight and volume restrictions [3]. For these reasons, we have performed genetic optimization of the 2-FLC design. In Fig. 6, we show the performance of two polarimeter designs for the wavelength ranges 430 – 1100 nm (compatible with an Si detector) and 800 – 1700 nm. Both of these polarimeter designs show condition numbers which are considerably better

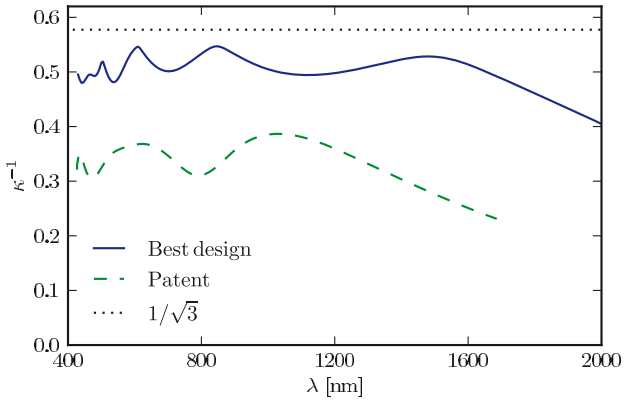

Fig. 4. Inverse condition number for the best GA-generated 3-FLC design. For comparison, we show the inverse condition number of the patented 3-FLC design [21].

#134880 - $15.00 USD Received 9 Sep 2010; revised 5 Oct 2010; accepted 5 Oct 2010; published 18 Oct 2010

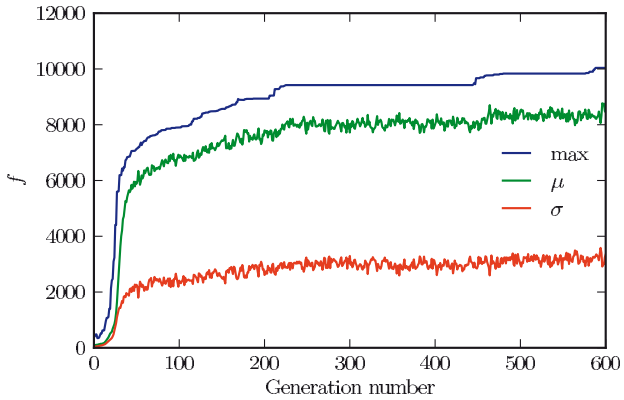

Fig. 5. Convergence of fitness as a function of generation number. μ and σ refer to the average and standard deviation of the population's fitness, respectively. The best result from this simulation is the one shown in Fig. 4.

Table 2. Genetic Algorithm parameters. The "crossover rate" is the probability for two parents to undergo sexual reproduction (the alternative being asexual reproduction). The parameter "crossover points" refer to the number of points where we cut the genome during crossover (sexual reproduction). "Mutation rate" is the probability for any given individual to undergo one or several bit flip mutations in one generation

Parameter	Value
Crossover rate	0.7
Crossover points	2
Mutation rate	0.2
Population size	500

Table 3. Orientation angle, θ, and normalized thickness, L, of the 2-FLC polarimeters shown in Fig. 6

	Visible design		NIR design	
Component	θ[°]	L	θ[°]	L
FLC 1	90.4	1.17	177.9	2.60
WP 1	3.5	3.58	112.9	2.94
FLC 2	92.5	1.02	74.8	1.75
WP 2	19.8	3.52	163.1	4.71

than previously reported designs. The numerical parameters of the two designs based on 2 FLCs are shown in Table 3.

Our optimization algorithm can, with little effort, be applied to a wider range of polarimeter design. Any optical component can be included into our GA; for example, one can include fixed waveplates of different materials, prisms, mirrors, and other types of liquid crystal devices. The material of each component could also be a variable, which could help alleviate the dispersion problem. The only requirement is that the retardance of the component in question must be

#134880 - $15.00 USD Received 9 Sep 2010; revised 5 Oct 2010; accepted 5 Oct 2010; published 18 Oct 2010

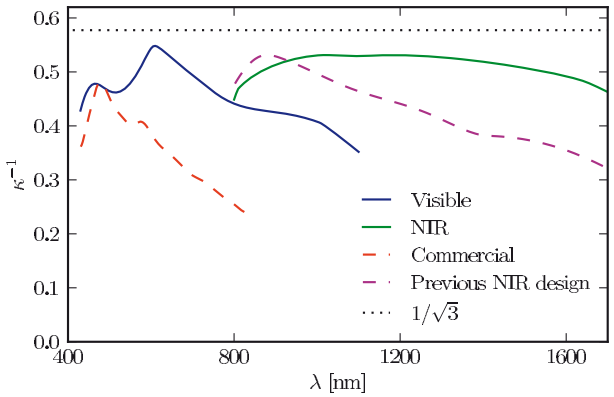

Fig. 6. Condition number for two designs using 2 FLC retarders and 2 waveplates. By optimizing $\kappa(\lambda)$ over a narrower part of the spectrum, we can design good polarimeters with fewer components. The polarimeter designs labeled "Visible" and "IR" show our two designs, optimized for 430 nm $< \lambda <$ 1100 nm and 800 nm $< \lambda <$ 1700 nm, respectively. For comparison with our "NIR" design, we show the previous simulated design from Ref. [30]. The curve labeled "Commercial" shows the measured condition number of a commercial instrument (MM16, Horiba, 2006) based on the same (FLC) technology.

possible to either model theoretically or measure experimentally. It is possible to optimize a polarimeter for a different wavelength range, simply by changing program inputs. Focusing on a wavelength range which is as narrow as possible typically results in higher condition numbers than reported here. Evaluating different technologies, materials and components for polarimetry should thus be relatively straightforward. The task is not computationally formidable: we have used ordinary desktop computers in all our calculations.

5. Conclusion

In conclusion, we have used genetic algorithms to optimize the design of a fast multichannel spectroscopic Stokes/Mueller polarimeter, using fast switching ferroelectric liquid crystals. We have presented three polarimeter designs which promise significant improvement with respect to previous work in terms of noise reduction and spectral range. Our approach requires relatively little computational effort. One can easily generate new designs if one should wish to use other components and materials, or if one wishes to focus on a different part of the optical spectrum. We hope that our designs will make polarimetry in general, and ellipsometry in particular, a less noisy and more efficient measurement technique.

Acknowledgements

The authors would like to thank professor Keith Downing at the Department of Computer and Information Science at NTNU for helpful discussions regarding genetic algorithms and their implementation.

#134880 - $15.00 USD Received 9 Sep 2010; revised 5 Oct 2010; accepted 5 Oct 2010; published 18 Oct 2010

L. M. S. Aas, P. G. Ellingsen, B. E. Fladmark, P. A. Letnes, and M. Kildemo, Overdetermined broadband spectroscopic Mueller matrix polarimeter designed by genetic algorithms, Opt. Express **21**, 8753 (2013)

Paper 3

Overdetermined broadband spectroscopic Mueller matrix polarimeter designed by genetic algorithms

Lars Martin Sandvik Aas,* Pål Gunnar Ellingsen, Bent Even Fladmark, Paul Anton Letnes, and Morten Kildemo

Department of Physics, The Norwegian University of Science and Technology (NTNU), N-7491 Trondheim, Norway

**lars.martin.aas@gmail.com*

Abstract: This paper reports on the design and implementation of a liquid crystal variable retarder based overdetermined spectroscopic Mueller matrix polarimeter, with parallel processing of all wavelengths. The system was designed using a modified version of a recently developed genetic algorithm [Letnes et al. Opt. Express **18**, 22, 23095 (2010)]. A generalization of the eigenvalue calibration method is reported that allows the calibration of such overdetermined polarimetric systems. Out of several possible designs, one of the designs was experimentally implemented and calibrated. It is reported that the instrument demonstrated good performance, with a measurement accuracy in the range of 0.1% for the measurement of air.

OCIS codes: (120.2130) Ellipsometry and polarimetry; (120.4570) Optical design of instruments; (300.0300) Spectroscopy.

References and links

1. P. G. Ellingsen, M. B. Lilledahl, L. M. S. Aas, C. d. L. Davies, and M. Kildemo, "Quantitative characterization of articular cartilage using Mueller matrix imaging and multiphoton microscopy," J. Biomed. Opt. **16**, 116002 (2011).
2. M. H. Smith, P. D. Burke, A. Lompado, E. A. Tanner, and L. W. Hillman, "Mueller matrix imaging polarimetry in dermatology," Proc. SPIE **3911**, 210–216 (2000).
3. R. N. Weinreb, S. Shakiba, and L. Zangwill, "Scanning laser polarimetry to measure the nerve fiber layer of normal and glaucomatous eyes," Am. J. Ophthalmol. **119**, 627–636 (1995).
4. J. D. Howe, M. A. Miller, R. V. Blumer, T. E. Petty, M. A. Stevens, D. M. Teale, and M. H. Smith, "Polarization sensing for target acquisition and mine detection," Proc. SPIE **4133**, 202–213 (2000).
5. A. Alvarez-Herrero, V. Martínez-Pillet, J. del Toro Iniesta, and V. Domingo, "The IMaX polarimeter for the solar telescope SUNRISE of the NASA long duration balloon program," in *API'09*, (2010), pp. 05002.
6. R. Azzam and N. Bashara, *Ellipsometry and Polarized light* (North-Holland, 1977).
7. H. Fujiwara, *Spectroscopic Ellipsometry: Principles and Applications* (John Wiley & Sons, Chichester, England; Hoboken, NJ, 2007).
8. H. Tompkins and E. A. Irene, *Handbook of Ellipsometry* (William Andrew, 2005).
9. M. Foldyna, A. D. Martino, R. Ossikovski, E. Garcia-Caurel, and C. Licitra, "Characterization of grating structures by Mueller polarimetry in presence of strong depolarization due to finite spot size," Opt. Commun. **282**, 735–741 (2009).
10. D. Schmidt, A. C. Kjerstad, T. Hofmann, R. Skomski, E. Schubert, and M. Schubert, "Optical, structural, and magnetic properties of cobalt nanostructure thin films," J. Appl. Phys. **105**, 113508 (2009).
11. L. M. S. Aas, M. Kildemo, Y. Cohin, and E. Søndergård, "Determination of small tilt angles of short gasb nanopillars using uv-visible mueller matrix ellipsometry," Thin Solid Films (2012).

#185039 - $15.00 USD Received 8 Feb 2013; revised 15 Mar 2013; accepted 19 Mar 2013; published 2 Apr 2013

12. I. S. Nerbø, S. Le Roy, M. Foldyna, M. Kildemo, and E. Søndergård, "Characterization of inclined GaSb nanopillars by Mueller matrix ellipsometry," J. Appl. Phys. **108**, 014307 (2010).
13. T. Oates, H. Wormeester, and H. Arwin, "Characterization of plasmonic effects in thin films and metamaterials using spectroscopic ellipsometry," Prog. Surf. Sci. **86**, 328–376 (2011).
14. B. Gallas, K. Robbie, R. Abdeddaïm, G. Guida, J. Yang, J. Rivory, and a. Priou, "Silver square nanospirals mimic optical properties of U-shaped metamaterials." Opt. Express **18**, 16335–16344 (2010).
15. T. A. Germer, "Polarized light scattering by microroughness and small defects in dielectric layers." J. Opt. Soc. Am. A **18**, 1279–1288 (2001).
16. T. Germer, "Measurement of roughness of two interfaces of a dielectric film by scattering ellipsometry," Phys. Rev. Lett. **85**, 349–352 (2000).
17. Ø. Svensen, M. Kildemo, J. Maria, J. J. Stamnes, and O. Frette, "Mueller matrix measurements and modeling pertaining to Spectralon white reflectance standards." Opt. Express **20**, 15045–15053 (2012).
18. J. M. Bennet, R. Chipman, and R. M. A. Azzam, "Polarized light," in *Handbook of Optics*, M. Bass and V. Mahajan, eds. (McGraw-Hill, Inc., 2010), pp. 12.3–16.21.
19. F. Stabo-Eeg, M. Kildemo, I. Nerbø, and M. Lindgren, "Well-conditioned multiple laser Mueller matrix ellipsometer," Opt. Eng. **47**, 073604 (2008).
20. E. Compain and B. Drevillon, "Complete high-frequency measurement of Mueller matrices based on a new coupled-phase modulator," Rev. Sci. Instrum. **68**, 2671 (1997).
21. O. Arteaga, J. Freudenthal, B. Wang, and B. Kahr, "Mueller matrix polarimetry with four photoelastic modulators: theory and calibration." Appl. Optics **51**, 6805–6817 (2012).
22. G. E. Jellison and F. a. Modine, "Two-channel polarization modulation ellipsometer." Appl. Optics **29**, 959–974 (1990).
23. E. Garcia-Caurel, A. D. Martino, and B. Drevillon, "Spectroscopic Mueller polarimeter based on liquid crystal devices," Thin Solid Films **455**, 120–123 (2004).
24. L. Aas, P. Ellingsen, and M. Kildemo, "Near infra-red Mueller matrix imaging system and application to retardance imaging of strain," Thin Solid Films **519**, 2737–2741 (2010).
25. P. Letnes, I. Nerbø, L. Aas, P. Ellingsen, and M. Kildemo, "Fast and optimal broad-band Stokes/Mueller polarimeter design by the use of a genetic algorithm," Opt. Express **18**, 23095–23103 (2010).
26. J. H. Holland, "Genetic algorithms," Sci. Am. **267**, 44–50 (1992).
27. D. Floreano and C. Mattiussi, *Bio-Inspired Artificial Intelligence: Theories, Methods, and Technologies* (The MIT Press, 2008).
28. E. Compain, S. Poirier, and B. Drevillon, "General and self-consistent method for the calibration of polarization modulators, polarimeters, and mueller-matrix ellipsometers." Appl. Optics **38**, 3490–3502 (1999).
29. S. B. Hatit, M. Foldyna, A. De Martino, and B. Drévillon, "Angle-resolved Mueller polarimeter using a microscope objective," Phys. Stat. Sol. (a) **205**, 743–747 (2008).
30. A. Ben-Israel and T. N. E. Greville, *Generalized Inverses: Theory and Applications* (Springer-Verlag, 2003).
31. R. Hagen, S. Roch, and B. Silbermann, *C* Algebras Numerical Analysis* (Marcel Dekker, 2001).
32. L. Aas, P. Ellingsen, M. Kildemo, and M. Lindgren, "Dynamic Response of a fast near infra-red Mueller matrix ellipsometer," J. Mod. Opt. **57**, 1603–1610 (2010).
33. C. S. Perone, "Pyevolve," `http://pyevolve.sourceforge.net/`.

1. Introduction

Polarimeters measure the polarization state of electromagnetic waves. Methods based on polarimetry are thus non-invasive and have the possibility for remote sensing applications, which makes them attractive in many fields of science. In the range of optical frequencies, polarimetry has proven to be useful and promising in e.g. biomedical diagnostics [1–3], remote sensing [4] and astronomy [5]. The sample measuring polarimeter (ellipsometer) is a key characterization technique for thin films [6–8], with recent applications to e.g. gratings [9], nanostructures [10–12], plasmonics [13], metamaterials [14] and scattering from rough surfaces [15–17].

A Mueller matrix ellipsometer/polarimeter consists of a complete polarization state generator (PSG) and polarization state analyzer (PSA), which determines all the polarization altering properties of a sample both in reflection and in transmission. A Stokes polarimeter consist only of a PSA and is used to determine the complete polarization state of partially polarized light.

A PSA/PSG generally consists of a diattenuating polarizer and an active birefringent optical component either modulated by azimuthal rotation or by an externally applied electric field [18]. Typical examples are rotating (wave-plate/bi-prism) retarders [6, 19], electro-optical modulation [20], photoelastic modulators [21, 22], and liquid crystal retarders [23, 24]. Disper-

#185039 - $15.00 USD Received 8 Feb 2013; revised 15 Mar 2013; accepted 19 Mar 2013; published 2 Apr 2013

sion in the optical components is usually limiting the wavelengths range of the polarimeters, but novel system designs may overcome this problem for at least a limited spectral range [23].

Certain wide band achromatic polarimeters (from the ultraviolet to the infrared) may be constructed using near non-dispersive retarders, by exploiting the total internal reflection from Fresnel prisms [19]. These retarders do commonly have a small aperture, are sensitive to alignment and require mechanical azimuth rotation for operation, and are thus not really suitable for imaging and space applications. On the other hand, liquid crystal retarders have no moving parts and can easily be made with large apertures, but they are strongly dispersive and a liquid crystal based wide band polarimeter requires a more advanced design.

A common way of designing polarimeters with dispersive components, is to first choose components based on a previous design or use a qualified guess. Secondly, the orientations of the components and the electrically controlled states are estimated by a local exhaustive or a gradient search. Due to a large search space, these latter search methods are computationally expensive and require particularly good starting guesses in order not to converge to a local minimum. Furthermore, for liquid crystal based wide spectral range multichannel polarimeters, it is necessary to add more modulating components [25], or states in the original components, in order to improve the conditioning of the system. The polarization state measurement is then said to be overdetermined. This makes the system design even more complex, due to the addition of more dimensions to the search space, hence requiring an efficient design algorithm [25].

Evolutionary algorithms are inspired by how nature evolves and how natural selection occurs. Genetic algorithms [26] are a subcategory of these and are based on the use of a genome, commonly a series of binary numbers, to evaluate, breed and compare different solutions. Genetic algorithms have proven to be effective at solving certain types of problems and are especially effective in large search spaces with a number of local minima. However, it is important to note that the algorithm does not search every solution and it cannot be guaranteed that the global optimum is found, though with well configured parameters it should be a good one [27].

Advantages of overdetermined polarimeters and the use of genetic algorithms to design them, was proven theoretically for a broadband system based on ferroelectric liquid crystal components in [25]. The genetic algorithm was generically implemented in order to create designs using any polarization modulating component with known dispersive properties. We here report for the first time an experimental implementation and testing of a genetic algorithm designed wide-band liquid crystal variable retarder Mueller matrix polarimeter.

2. Theory

Let us first briefly review the theory and notation used to describe the measurement of Stokes vectors and Mueller matrices using a PSA and a PSG, both for determined and overdetermined systems. The calibration of overdetermined Mueller matrix polarimeters is thereafter explained using a generalization of the eigenvalue calibration method (ECM) [28].

The polarization state of light, can generally be represented in vector form by the four element Stokes vector defined by

$$\mathbf{S} = \begin{bmatrix} s_1 \\ s_2 \\ s_3 \\ s_4 \end{bmatrix} = \begin{bmatrix} \langle E_x(t)^2 \rangle + \langle E_y(t)^2 \rangle \\ \langle E_x(t)^2 \rangle - \langle E_y(t)^2 \rangle \\ 2\langle E_x(t)E_y(t)\cos\delta(t) \rangle \\ 2\langle E_x(t)E_y(t)\sin\delta(t) \rangle \end{bmatrix},$$

where $E_x(t)$ and $E_y(t)$ are time dependent, electric field amplitudes of the $x-$ and $y-$components, of an electric field propagating in the $z-$direction. $\langle\cdot\rangle$ denotes time averages and $\delta(t)$ is the time dependent phase difference between the $x-$ and $y-$components of the

#185039 - $15.00 USD Received 8 Feb 2013; revised 15 Mar 2013; accepted 19 Mar 2013; published 2 Apr 2013

electric field. Note that the averaging of time varying amplitudes and phases, results in a reduced degree of polarization.

The Mueller matrix is a 4×4 transfer matrix transforming an initial Stokes vector to the final by $\mathbf{S}_{\text{final}} = \mathbf{M}_{\text{sample}}\mathbf{S}_{\text{initial}}$. A Mueller matrix can describe all changes in the polarization state of light upon the interaction with a sample, with quantifiable effects, like for instance polarizance, diattenuation, retardance and depolarization [18].

In order to measure $\mathbf{M}$, one needs at least four probing Stokes vectors [18]. Consequently these Stokes vectors need to be measured by a polarimeter/PSA. A polarimeter/PSA projects the incoming intensity to at least four carefully selected polarization states. These states are the Stokes vectors in the PSA, organized into the rows of the PSA matrix $\mathbf{A}$. The intensity vector, $\mathbf{b} = \mathbf{AS}$, for an incoming Stokes vector can then be measured, and the Stokes vector found by inversion; $\mathbf{S} = \mathbf{A}^{-1}\mathbf{b}$. Similarly, for the PSG in the Mueller matrix polarimeter/ellipsometer, the generated Stokes vectors are organized as columns in the $\mathbf{W}$ matrix. The product $\mathbf{MW}$ gives the Stokes vectors for the PSA to analyze, yielding the total intensity measurement matrix $\mathbf{B} = \mathbf{AMW}$. As a result, the Mueller matrix can then, in principle, readily be calculated by inversion of $\mathbf{A}$ and $\mathbf{W}$, $\mathbf{M} = \mathbf{A}^{-1}\mathbf{B}\mathbf{W}^{-1}$. There are several ways of finding $\mathbf{A}$ and $\mathbf{W}$ for a system, but a common method is the robust and increasingly popular ECM [28]. It uses the measurement of a set of calibration samples to account for all systematic errors, such as alignment errors and time/temperature dependent variations in components of the system [23,24,29]. Prior knowledge is only required for the form of the reference sample Mueller matrix (i.e. if it is a polarizer or retarder) and an initial qualified guess of the azimuth orientation, for solving the system with the ECM. In our case, $\mathbf{A}$ and $\mathbf{W}$ result from six states in the PSA and PSG, corresponding to 12 specific Stokes vectors $\mathbf{S}_{W1-6}$ and $\mathbf{S}_{A1-6}$

$$\mathbf{W} = [\mathbf{S}_{W1}, \mathbf{S}_{W2}, \mathbf{S}_{W3}, \mathbf{S}_{W4}, \mathbf{S}_{W5}, \mathbf{S}_{W6}],$$
$$\mathbf{A} = [\mathbf{S}_{A1}, \mathbf{S}_{A2}, \mathbf{S}_{A3}, \mathbf{S}_{A4}, \mathbf{S}_{A5}, \mathbf{S}_{A6}]^T.$$

The ECM is explained in the original paper [28] for systems using four Stokes vectors in the PSG and PSA. Here we present the generalization needed to calibrate a system with n Stokes vectors in the PSA and m Stokes vectors in the PSG. We start with a set of reference Mueller matrices, $\{\mathbf{M}\}$, corresponding to a set of intensity measurements, $\{\mathbf{B}\}$. $\mathbf{B}_i$ is of size $n \times m$ and is given by

$$\mathbf{B}_i = \mathbf{AM}_i\mathbf{W}.$$

For convenience, reference sample $\mathbf{M}_0$ is chosen to be air, such that $\mathbf{B}_0 = \mathbf{AW}$. Next, two sets of matrices, $\{\mathbf{C}\}$ and $\{\mathbf{C}'\}$, are constructed using

$$\mathbf{C}_i = \mathbf{B}_0^{\dagger}\mathbf{B}_i = \mathbf{W}^{\dagger}\mathbf{M}_i\mathbf{W} \qquad \text{and} \qquad \mathbf{C}'_i = \mathbf{B}_i\mathbf{B}_0^{\dagger} = \mathbf{AM}_i\mathbf{A}^{\dagger}, \tag{1}$$

where † denotes the Moore-Penrose pseudoinverse, which is the common way of defining the inverse of a non-square matrix with noise [30]. In the case where $\mathbf{B}_i$ is of size four by four, the sets $\{\mathbf{C}\}$ and $\{\mathbf{C}'\}$ have the same eigenvalues as the set of Mueller matrices $\{\mathbf{M}\}$. As $\mathbf{C}_i$ is independent of $\mathbf{A}$, and $\mathbf{C}'_i$ is independent of $\mathbf{W}$, $\mathbf{A}$ and $\mathbf{W}$ may be found independently, and $\{\mathbf{M}\}$ may be found both from $\{\mathbf{C}\}$ and $\{\mathbf{C}'\}$ independently.

In an overdetermined system $\mathbf{C}_i$ and $\mathbf{C}'_i$ holds more eigenvalues than the corresponding Mueller matrix $\mathbf{M}_i$. One way of finding which of the eigenvalues that correspond to the Mueller matrix $\mathbf{M}_i$, is to do a search in the eigenvalues of $\mathbf{C}_i$ and $\mathbf{C}'_i$ and compare them with expected values. However, in a real measurement including noise, the latter approach did in our experience not appear robust. The noise is related to the relative error in $\mathbf{M}$, shown by Stabo-Eeg et

#185039 - $15.00 USD Received 8 Feb 2013; revised 15 Mar 2013; accepted 19 Mar 2013; published 2 Apr 2013

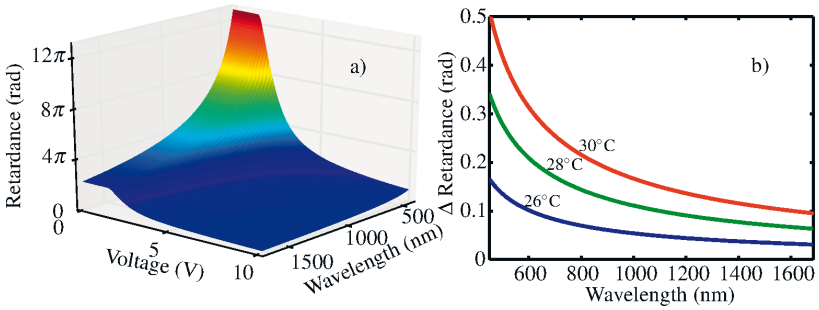

Fig. 1. (a) The measured retardance of a LCVR as a function of wavelength and the voltage applied. (b) The retardance of the LCVR measured at 0 V with the temperature stabilized at 26°C, 28°C and 30°C. The figure shows the relative difference to the LCVR retardance at 24°C.

al. [19] to be

$$\frac{\|\Delta\mathbf{M}\|}{\|\mathbf{M}\|} \lesssim \kappa_{\mathbf{W}}\kappa_{\mathbf{A}}\frac{\|\Delta\mathbf{B}\|}{\|\mathbf{B}\|} + \kappa_{\mathbf{A}}\frac{\|\Delta\mathbf{A}\|}{\|\mathbf{A}\|} + \kappa_{\mathbf{W}}\frac{\|\Delta\mathbf{W}\|}{\|\mathbf{W}\|}, \tag{2}$$

where $\kappa_{\mathbf{W}}$ and $\kappa_{\mathbf{A}}$ are the condition numbers of $\mathbf{W}$ and $\mathbf{A}$ respectively. For a square non-singular matrix the condition number is defined as $\kappa_{\mathbf{A}} = \|\mathbf{A}\|\|\mathbf{A}^{-1}\|$, while for a non-square matrix the generalized condition number is given by $\kappa_{\mathbf{A}} = \|A\|\|A^{\dagger}\|$ [31], where $\|\cdot\|$ denotes the second norm of the matrix. From Eq. (2) it is seen that in order to minimise the noise in $\mathbf{M}$, it is necessary to reduce the condition numbers of $\mathbf{A}$ and $\mathbf{W}$.

A robust solution to finding the correct eigenvalues of $\{\mathbf{M}\}$ from $\{\mathbf{C}\}$ and $\{\mathbf{C}'\}$, is to (at each wavelength) reduce $\mathbf{B}_0$ and $\mathbf{B}_i$ in Eq. (1) to the 4×4 subset of $\mathbf{B}_0$ and $\mathbf{B}_i$ resulting in the lowest condition number for the reduced $\mathbf{B}_0$. When inverting $\mathbf{B}_0$, this ensures minimal noise propagation into $\mathbf{C}_i$ and to the eigenvalues of $\mathbf{M}_i$. After finding the eigenvalues of $\{\mathbf{M}\}$, the remainder of the calibration procedure follows the original paper by Compain et al. [28], using the non reduced $\{\mathbf{B}\}$.

Also worth noting is that the noise equation, Eq. (2), is the basis for the genetic optimisation, which tries to maximise the inverse condition number.

3. Experimental

The essential optical components in the Mueller matrix polarimeter presented here, are polarizers and liquid crystal variable retarders (LCVR). In the calibration, a polarizer and a waveplate was used. We used a high extinction ratio near infra-red polarizer (*LPNIR*) from *Thorlabs* and a true zero-order quarter waveplate at 1310 nm from *Casix*. The LCVRs were custom made for the near infrared from *Meadowlark Optics*.

LCVRs are wave retarders having the retardance as a function of applied voltage. Compared to ferroelectric liquid crystal retarders (previously proposed overdetermined polarimeter design [25]) which have only one fixed retardance, but with two stable azimuth orientations, they typically have much longer transition times between two states [32], but have the advantage of allowing the selection of all retardation values between a maximum and minimum value.

In order to design the optimal polarimeter, the retardance as a function of voltage and wavelength needs to be known with reasonable precision. Although the calibration routine handles small deviations in dispersive optical properties, high accuracy of the Mueller matrix elements

#185039 - $15.00 USD Received 8 Feb 2013; revised 15 Mar 2013; accepted 19 Mar 2013; published 2 Apr 2013

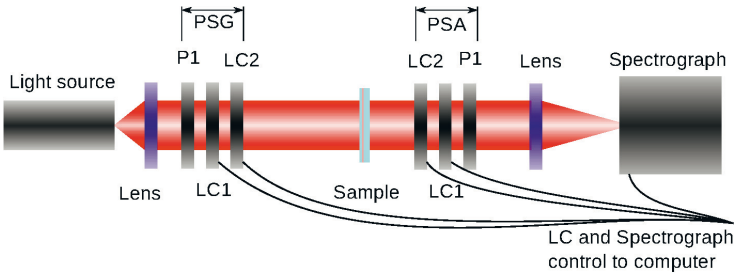

Fig. 2. Schematic drawing of a typical spectroscopic Mueller matrix polarimeter using liquid crystal variable retarders (LCVR), a broad band light source and spectrometer.

is only insured as long as the condition number is not strongly degraded with respect to the design. In the instrument reported here, it was also found that there were, due to manufacturing uncertainties, differences in thickness between the individual crystals. The crystals were therefore characterized individually in the range of 450 – 1680 nm using a commercial available Mueller matrix polarimeter *RC2* from *J.A. Woollam Co.*. Figure 1(a) shows as an example, a surface plot of the resulting retardance as a function of voltage and wavelength for one of the LCVRs. It is noted that for lower voltages the retardance reaches a threshold at the critical voltage 1.5 V, while it approaches a low residual retardance for high voltages. The large retardance in the visible insures the possibility for a reasonable retardance variation in the longer wavelengths of the NIR spectrum.

It was found that the retardance was reduced significantly with the increased ambient temperature. Figure 1(b) shows the deviation in the wavelength dependent retardance for 26°C, 28°C and 30°C, relative to the retardance at 24°C at 0 V. Thus, for reproducible and accurate measurements, the LCVRs must be operated in an environment with a stable temperature.

Figure 2 shows a schematic drawing of a typical LCVR Mueller matrix polarimeter system design, based on a broadband white light source, a spectrograph and four temperature controlled LCVRs. The polarizer and the two crystals on the left side of the sample makes up the PSG, while the components in the opposite order on the right side of the sample makes up the PSA (i.e. a Stokes polarimeter).

The system design was done using a genetic algorithm based on the *Pyevolve* library [33]. The algorithm tries to maximize a fitness function, which was defined as

$$f = \frac{1}{e},$$

where e is the error function defined as

$$e = \sum_{n=1}^{N_\lambda} \left(\frac{1}{\sqrt{3}} - \frac{1}{\kappa(\lambda_n)} \right)^4.$$

Here N_λ is the total number of wavelengths and $\kappa(\lambda_n)$ is the generalized condition number of $\mathbf{A}$ or $\mathbf{W}$ for a given wavelength λ_n. This fitness function is similar to the one previously defined in [25] and incorporates experimentally measured optical properties of the components using the Mueller formalism to calculate the generalized condition number of $\mathbf{A}$ or $\mathbf{W}$. As for the previous fitness function, it punishes inverse condition numbers far away from the theoretical maximum inverse condition number $\left(1/\sqrt{3}\right)$, by taking the difference to the fourth power. Fi-

#185039 - $15.00 USD Received 8 Feb 2013; revised 15 Mar 2013; accepted 19 Mar 2013; published 2 Apr 2013

nally, it is noted that since the genetic algorithm is based on bit strings, the conversion from bits to numbers will not always yield a voltage, or wavelength where the LCVRs were experimentally characterized, in these cases the closest measured retardance value was used.

The genetic optimization was performed using the settings given in Table 1. 8 bits was considered sufficient to represent the voltage and the rotation angle, i.e. a step size of 0.04 V and 0.7°. The wavelength range was selected to be 900 – 1700 nm, the range of a typical indium gallium arsenide (InGaAs) near infrared detector. In particular, we used the *NirQuest512* spectrograph from *Ocean Optics*. The number of generations, population size and mutation rate were found by trial and error, by encouraging diversity and avoiding formation of large groups of individuals focused around one minimum. Elitism (copying of the best individual from one generation to the next), two point crossover and tournament were also used.

Table 1. General settings for the genetic optimization

Property	**Values**
Voltage bits per LCVR	8
Rotation bits per LCVR	8
Wavelength range	$850-1700$ nm in 200 equal steps
Number of generations	500
Population size	200
Crossover method	Two point crossover
Crossover rate	70%
Selection method	Tournament with 4 individuals
Elitism	The best individual
Mutation rate	4%

4. Results and discussion

Several Mueller matrix polarimeters were optimized in order to cover the near infrared spectral range. By using two LCVRs in both the PSG and the PSA, one may in principle generate a large number of states. However, a system that approaches the theoretically optimal inverse condition number $1/\sqrt{3}$ will need 16 states for every measured wavelength, as long as a retardance of $\pi/2$ is available. For a large number of wavelengths (typically > 500), such a system results in an unreasonable high total measurement time. Therefore, several Mueller matrix polarimeters were designed and evaluated with only a limited number of states in the PSG and the PSA, in order to keep the measurement time low. Three Mueller matrix polarimeter designs were optimized and evaluated. All designs used an equal number of states in the PSG and the PSA. The first design used two states in each of the LCVRs, totaling 4 (2×2) states for the PSA or the PSG, and 16 (4^2) states for the complete system. The second design had two states in the first LCVR and three in the second LCVR, totaling 6 (2×3) states for the PSA/PSG and 36 (6^2) in the complete system. Similarly the last design had two states in the first and four in the second LCVR, resulting in a total of 8 (2×4) states for the PSA/PSG, and 64 (8^2) for the complete polarimeter. For simplicity, these three designs will from now on be denoted as 2×2, 2×3 and 2×4. The resulting designs are summarized in Table 2, whereas the resulting inverse condition numbers are shown in Fig. 3. It is evident that by going from a 2×2 to a 2×3 design the condition number is increased on the two edges of the spectrum. By moving to 2×4 states, the condition number increases over the whole spectrum. It is clear that there will be a trade-off between the measurement time and the gain in the increased condition number, and hence the

#185039 - $15.00 USD Received 8 Feb 2013; revised 15 Mar 2013; accepted 19 Mar 2013; published 2 Apr 2013

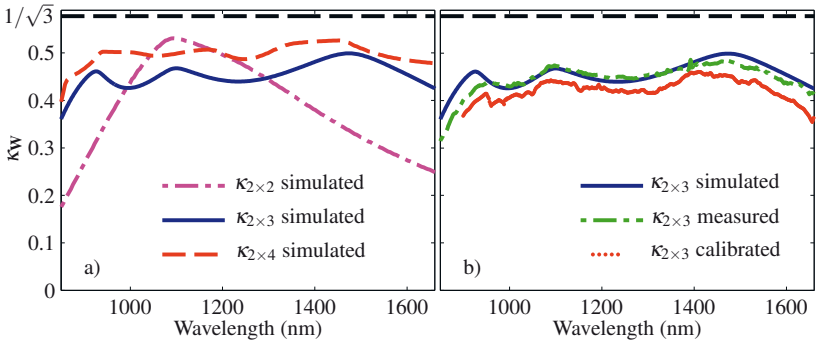

Fig. 3. The inverse of the generalized condition number of **W** as a function of wavelength. Figure (a) shows the comparison between the best designs for a 2×2, 2×3 and 2×4 states system, where the systems are presented in terms of the number of retardance (voltage) states for each of the two LCVRs making up the PSG or the PSA. Figure (b) shows both the simulated, measured and calibrated inverse condition number of the experimentally realized polarimeter with 2×3 states.

noise reduction at the edges of the spectrum. As a compromise, we found it practical to use the 2×3 design for the experimental realization of the Mueller matrix polarimeter.

Table 2. Configuration of the optimal polarimeters

	Polarimeter type		
Component property	2×2	2×3	2×4
Orientation of LCVR1 (°)	135.5	40.9	60.7
Orientation of LCVR2 (°)	112.9	105.7	101.6
Voltages of LCVR1 (V)	3.6, 9.7	3.8, 9.9, 2.8	3.7, 1.6, 2.6, 2.1
Voltages of LCVR2 (V)	2.6, 6.8	2.9, 8.8	8.5, 2.7

In comparison to previously reported ferroelectric liquid crystal (FLC) designs [25] obtained using a similar genetic algorithm, the 2×3 LCVR design has a much narrower wavelength range and a slightly lower inverse condition number. This is as expected, since the design using three FLCs has three compensating wave-plates in addition to the liquid crystals, giving extra degrees of freedom. Specifically, these degrees of freedom arise from the fact that both the thickness (birefringence) and the azimuthal orientation of each component can be selected, and as a result one would expect an overall higher inverse generalized condition number. However, more optical components reduce the transmitted intensity, which in some cases results in a greatly reduced signal to noise ratio. A high signal to noise ratio is particularly important for applications with a limited flux, for example a large field of view imaging or space applications.

The 2×3 design was mounted in custom made temperature controlled holders, one for the PSG and one for the PSA. These were then separately mounted in the beam-path of the RC2, and by switching through all the 2×3 states of the LCVRs, the Stokes vectors of the **W** and **A** matrix was determined in the range 350 – 1680 nm, by selecting the first column of the measured Mueller matrix. The resulting inverse generalized condition number is shown in Fig. 3(b) (in green stippled lines), together with the simulated inverse generalized condition number

#185039 - $15.00 USD Received 8 Feb 2013; revised 15 Mar 2013; accepted 19 Mar 2013; published 2 Apr 2013

resulting from the design obtained by the genetic algorithm (solid line). As seen, the correspondence between the experimental and simulated inverse generalized condition numbers is excellent. This demonstrates the power of such a system design and implementation, utilizing genetic algorithms and re-characterization of the optical components after arrival. The PSG and the PSA were then mounted in the transmission geometry shown in Fig. 2, making up the complete LCVR based Mueller matrix polarimeter. **A** and **W** were found using the ECM, as discussed in section 2. The generalized condition number of the calibrated **W** matrix is plotted in Fig. 3(b). It is observed from the figure that the general spectral features in the optimized condition number are reproduced in the experimental version, although it suffers from small offsets in some parts of the spectrum. The latter offsets are possible due to that the components of the PSA/PSG were slightly realigned between the measurement using the commercial Mueller matrix ellipsometer compared to the final implementation of the LCVR Mueller matrix polarimeter. On the other hand, it shows that the modified ECM automatically compensates for alignment errors during assembly, and the final system calibrate correctly with only minor changes in the propagation of noise.

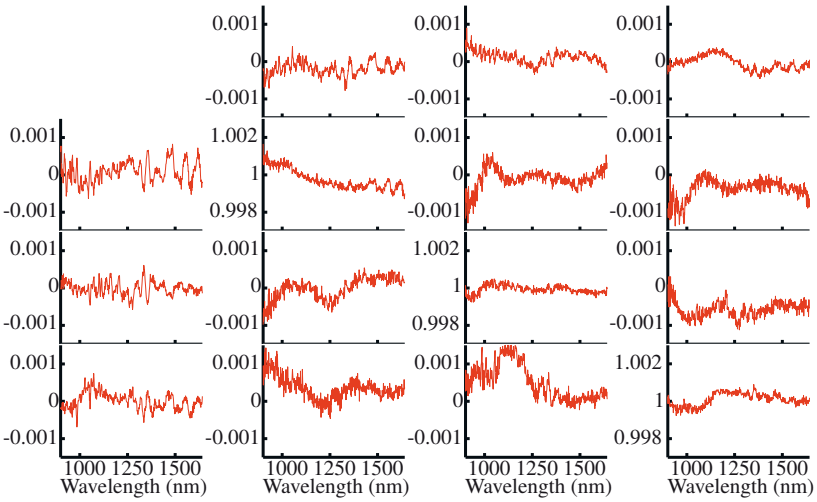

Fig. 4. The measured spectroscopic Mueller matrix of air normalized to the m_{11} element.

An important measure of the Mueller matrix polarimeter accuracy is the measurement of air, whose Mueller matrix is simply the 4×4 identity matrix. Figure 4 shows the spectroscopic Mueller matrix measurement of air (normalized to the m_{11} element). The deviation from the identity matrix is small, since the error is less than 0.1% over most of the spectrum, and is never more than 0.17%.

It is recalled that the wide band LVCR design uses few components and thereby has small reflection losses from the optical interfaces. Hence, the designed Mueller matrix polarimeter should also be well suited for a fast imaging setup with low loss of light, compared to a FLC based setup, while insuring small measurement errors across the spectral range of operation, even suitable for hyperspectral imaging. The reduction in number of components also enables a more compact design. Another advantage of the setup will be the possibility to redesign the spectral characteristics without having to rotate the components, since the voltage of the LCVRs

#185039 - $15.00 USD Received 8 Feb 2013; revised 15 Mar 2013; accepted 19 Mar 2013; published 2 Apr 2013

is software controlled. By using the genetic algorithm, it is possible to fix the rotation angles and only optimize on the LVCR voltage in order to fulfill other system specifications. Finally, one may envisage a system that can improve itself by self-characterization and intelligent design by implementing an in-line version of the genetic algorithm.

5. Conclusion

Genetic algorithms have been used to design multichannel Mueller matrix polarimeters based on liquid crystal variable retarders for the near infrared with 2×2, 2×3 or 2×4 voltage states for the polarization state generator and analyzer. The design using 2×3 states was experimentally realized and calibrated, based on its advantageous trade-off between total measurement time and overall performance with respect to error propagation (optimized inverse condition number). The resulting Mueller matrix polarimeter demonstrated here, shows good performance in the design wavelength range (900-1700 nm) with less than 0.1% error on the Mueller matrix of air, making it suitable in for example hyperspectral or multispectral imaging applications.

Acknowledgment

L.M.S.A acknowledges support from The Norwegian Research Center for Solar Cell Technology (project num. 193829).

#185039 - $15.00 USD Received 8 Feb 2013; revised 15 Mar 2013; accepted 19 Mar 2013; published 2 Apr 2013

L. M. S. Aas, D. G. Skåre, P. G. Ellingsen, P. A. Letnes, and M. Kildemo, Design, optimization and realization of FLC based Stokes polarimeters and Mueller matrix ellipsometer using a genetic algorithm, Preprint, subm. to Thin Solid Films (2013)

Paper 4

Design, optimization and realization of a ferroelectric liquid crystal based Mueller matrix ellipsometer using a genetic algorithm

Lars Martin S. Aas, Daniel G. Skåre, Pål G. Ellingsen, Paul Anton Letnes, Morten Kildemo

Department of Physics, The Norwegian University of Science and Technology (NTNU), N-7491 Trondheim, Norway

Abstract

The design of complete broadband polarimeters with high performance is challenging due to the wavelength dependence of optical components. An efficient genetic algorithm computer code was recently developed in order to design and re-optimize complete broadband Stokes polarimeters and Mueller matrix ellipsometers. Our results are improvements of previous patented designs based on two and three ferroelectric liquid crystals (FLC). FLC based polarimeters are suited for broadband hyperspectral imaging, or multichannel spectroscopy applications. We have realized and implemented one design using two FLCs and compare the spectral range and precision with previous designs.

Keywords: Mueller matrix Ellipsometer, Optical Design, Ellipsometry, Polarimetry

1. Introduction

A polarimeter is an instrument that measures the polarization state of light to gain information about light sources, or materials interacting with polarized light. By measuring how the polarization of light is altered after being reflected from a smooth surface, the technique is often referred to as ellipsometry.

The need for fast broadband Mueller matrix ellipsometers and Stokes polarimeters result in challenging design problems when using active polarization modulators which are intrinsically strongly dispersive. Although designs based on *e.g.* the Fresnel rhomb and alike are nearly achromatic, these are not well suited for neither imaging nor high speed applications. In the case of polarimeters and Mueller matrix ellipsometers based on liquid crystal modulators, the direct search space may become huge [1] and standard optimization methods can evidently result in local minima far away from the optimum. An efficient Genetic Algorithm (GA) computer code was recently developed in order to design and re-optimize complete broadband Stokes polarimeters and Mueller matrix ellipsometers (MME) [1]. This code is here used to search systems generating and analyzing optimally selected polarization states, in order to reduce the propagation of noise from the intensity measurements to the Mueller matrix elements. Although the GA code was initially motivated by the challenging task of searching the components, states and azimuthal orientations for optimally conditioned broadband liquid crystal based polarimeters [1, 2], the software is written in a versatile manner in order to handle general polarimeters based on any polarization changing components. For small scale production, we propose that the GA algorithm can be used to re-optimize the design due to imperfect polarization components, *e.g.* due to small deviations in the specifications of the optical components. Any addition of "non-conventional" polarization altering components in the polarimeter, such as mirrors and prisms can be included in the GA algorithm, given that the dispersive properties of such components are known.

A classical GA [3, 4] was chosen to optimize the polarimeters based on Ferroelectric Liquid Crystals (FLC). FLC based polarimeters were first proposed by Gandorfer [5], and Jensen and Peterson [6]. They have the advantage of being fast [7] and having no moving parts, which is an advantage for imaging applications. A commercial FLC multichannel spectroscopic (430-850 nm) Mueller matrix ellipsometer [16] is available from *Horiba Yvon Jobin*. The FLC system is based on optical components with known properties [7, 8]. Its overall performance depends on the components in a complex manner. Traditional optimization methods are hampered by local minima in the large search space. A genetic optimization algorithm is more robust and will normally move out of local minima. Resulting in a polarimeter design with less noise amplification on a broader spectral range.

In this work, a new design for the commercial FLC based MM16 system has been implemented. Furthermore, we demonstrate how the GA algorithm may be used in small scale production, where we may simply re-optimize the design in the case of an off-specification component.

2. Theory

The complete polarization state of light, including partially polarized states, can be expressed concisely using the Stokes vector. It completely describes the polarization state with four

Email address: lars.martin.aas@gmail.com (Lars Martin S. Aas)

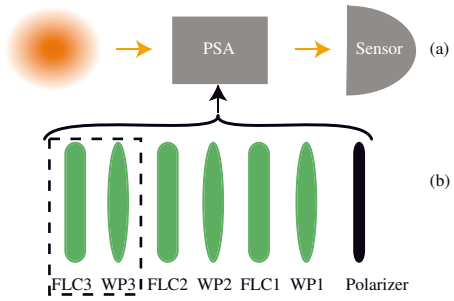

Figure 1: A schematic drawing of a polarimeter, (a) shows a general polarimeter where the polarization state of incident light is analyzed by the Polarization State Analyzer and a light intensity detector. In (b) the components of a Polarization State Analyzer is exemplified through a combination of two or three FLCs and waveplates (WP) and a linear polarizer.

real elements [9]

$$\boldsymbol{S} = \begin{bmatrix} I \\ Q \\ U \\ V \end{bmatrix} = \begin{bmatrix} \langle E_{0,x}(t)^2 \rangle + \langle E_{0,y}(t)^2 \rangle \\ \langle E_{0,x}(t)^2 \rangle - \langle E_{0,y}(t)^2 \rangle \\ 2\langle E_{0,x}(t) E_{0,y}(t) \cos\delta(t) \rangle \\ 2\langle E_{0,x}(t) E_{0,y}(t) \sin\delta(t) \rangle \end{bmatrix},$$

where $\langle \cdots \rangle$ denotes time average over, the in general, quadratic time dependent orthogonal electric field components ($E_{0,x}(t)$ and $E_{0,y}(t)$) and phase ($\delta(t)$).

The change of a polarization state can be described by a 4×4 real-valued transformation matrix called a Mueller matrix, $\mathbf{M}$, connecting an incoming Stokes vector $\mathbf{S}_{\text{in}}$ to an outgoing Stokes vector

$$\mathbf{S}_{\text{out}} = \mathbf{M}\mathbf{S}_{\text{in}}. \tag{1}$$

Any linear interaction of light can be described by the Mueller matrix. A Mueller matrix can describe a range of polarization effect, such as diattenuation (different amplitude transmittance or reflectance for different polarization modes), retardance (*i.e.* changing δ), and depolarization (which increases the random component of the electric field).

A Stokes polarimeter consists of a polarization state analyzer (PSA) capable of determining the Stokes vector by performing at least four intensity measurements. For a given state (i), the polarization altering properties of the PSA can be described by its Mueller matrix $\mathbf{M}^{\text{PSA}}(i)$, which can be found as the matrix product of the Mueller matrices of all the optical components in the PSA. These components are a linear polarizer, and a number of phase retarders (*e.g.* FLCs and waveplates), see Figure 1. An FLC is a phase retarder which can be electronically switched between two states. The difference between the states corresponds ideally to a rotation of the fast axis by 45° ($\theta(0) = \theta_0$ and $\theta(1) = \theta_0 + 45°$). By using a linear polarizer and two FLCs as a PSA, one can generate $2^2 = 4$ different projection states, by using three FLCs one can generate $2^3 = 8$ states, *etc*.

If an unknown polarization state with Stokes vector $\mathbf{S}$ passes through the PSA, for a state i, the detector will measure an intensity I depending only on the first row of $\mathbf{M}^{\text{PSA}}(i)$

$$I = \sum_{j=1}^{4} \mathbf{M}^{\text{PSA}}_{1,j}(i)\mathbf{S}_j.$$

The intensity can be considered to be the projection of $\mathbf{S}$ along a Stokes vector equal to $\mathbf{M}^{\text{PSA}\ T}_{1,1..4}$, where T denotes the transpose. These Stokes vectors are organized as rows in the system matrix $\mathbf{A}$. When operating on a Stokes vector the result is

$$\mathbf{b} = \mathbf{A}\mathbf{S}.$$

Here $\mathbf{b}$ is a vector composed by the intensity measurements at the different projection states. An unknown Stokes vector can then be found by $\mathbf{S} = \mathbf{A}^{-1}\mathbf{b}$. The noise in $\mathbf{S}$ comes from the measurement noise in $\mathbf{b}$ but is amplified by the condition number (κ) of $\mathbf{A}$ [10]. Therefore κ of a polarimeter should be as small as possible [11]. A low κ indicates that the probing polarization states are close to orthogonal. The condition number of $\mathbf{A}$ is given as $\kappa = \|\mathbf{A}\|\|\mathbf{A}^{-1}\|$, which for the 2-norm is equal to the ratio of the largest to the smallest singular value of the matrix [10]. Theoretically the best condition number that can be achieved for a polarimeter is $\kappa = \sqrt{3}$ [11]. If four optimal states can be achieved, no advantage is found by doing a larger number of measurements with different states, compared to repeated measurements with the four optimal states [12]. If, however, these optimal states can not be produced ($\kappa > \sqrt{3}$), the condition number, and hence the error, can be reduced by measuring more than four states. For an FLC based polarimeter this is accomplished by using three FLCs in the PSA, with up to three waveplates (WP) coupled to the FLCs to reduce the condition number (see Figure 1), or components with more than two states, such as liquid crystal variable retarders (LCVR). In this case $\mathbf{A}$ will not be a square matrix, and the *Moore-Penrose pseudoinverse* is then used to invert $\mathbf{A}$ [2].

To measure the Mueller matrix of a sample, it is necessary to illuminate the sample with at least four different polarization states. The Stokes vectors of these states can be organized as columns in a polarization state generator (PSG) system matrix $\mathbf{W}$. After interaction with the sample the product $\mathbf{MW}$ gives the resulting four Stokes vectors. They are then measured by the PSA, yielding the intensity matrix $\mathbf{B} = \mathbf{AMW}$. The Mueller matrix can then be found by multiplying the expression by $\mathbf{A}^{-1}$ and $\mathbf{W}^{-1}$ from each side, $\mathbf{M} = \mathbf{A}^{-1}\mathbf{B}\mathbf{W}^{-1}$. The PSG may be constructed from the same optical components as the PSA.

3. Fitness evaluation

It has already been established that κ should be as small as possible in order to reduce noise in the polarimetric measurements. It is a fairly trivial exercise to optimize κ for a single wavelength. However, there are two sources of wavelength dependence of the optical properties of the components.

One of these is the explicit wavelength dependence of the

retardance Δ_R, which can be calculated as [13]

$$\Delta_R = \frac{2\pi l(\Delta n)}{\lambda_0}, \tag{2}$$

where l is the physical thickness of the component (*e.g.* waveplate or FLC), λ_0 is the vacuum wavelength of the light, and Δn is the birefringence of the material. Birefringence is the difference in refractive index between the fast axis (index of refraction n_f) and the slow axis (n_s), *i.e.* $\Delta n = |n_\mathrm{f} - n_\mathrm{s}|$ [13]. There is an explicit wavelength dependence in Eq. (2), which complicates the design of the PSA. A weaker, but still important, effect is the wavelength dependence of the birefringence, *i.e.* $\Delta n = \Delta n(\lambda)$. Both of these effects are taken into account by using experimental data for the retardance [2, 14].

To evaluate the performance of a polarimeter design, we compare the inverse condition number ($\kappa^{-1}(\lambda)$) to the theoretically optimal value ($1/\sqrt{3}$). The argument for using κ^{-1} rather than κ is that $\sqrt{3} < \kappa < \infty$ while $0 < \kappa^{-1} < 1/\sqrt{3}$, which is more numerically convenient. In detail, we define an "error function" (e)

$$e = \frac{1}{N_\lambda} \sum_{n=1}^{N_\lambda} \left(\kappa^{-1}(\lambda_n) - 1/\sqrt{3}\right)^4. \tag{3}$$

In the above equation, we typically use $\lambda_n = \lambda_\mathrm{min} + (n-1)\Delta\lambda$, with $n = 1, 2, \ldots, N_\lambda$ and $\Delta\lambda = 5$ nm. It is, of course, possible to choose other discretization schemes for λ: for some applications, one can *e.g.* be interested in optimal performance near a few spectral lines (wavelengths). We take $\left(\kappa^{-1} - 1/\sqrt{3}\right)$ to the power of four to punish unwanted peaks in κ more severely. As GAs conventionally seek to maximize the fitness function, the fitness function is defined as

$$f = \frac{1}{e}. \tag{4}$$

As e will never be zero in practice, there is no need to add a constant term in the denominator. The fitness function does not carry any physical significance on its own; it is simply an overall measure of how well the polarimeter can measure along orthogonal polarization states for the chosen wavelengths.

4. Genetic algorithm

The GA was based on the open Python library Pyevolve [15], and was written to handle any kind of optical components. We have, however, so far concentrated our efforts on systems based on liquid crystals (here in particular FLCs) as polarization modulators, with fixed waveplates "sandwiched" between them. An achromatic design is enabled by the coupling of waveplates and FLCs. Both polarimeter designs based on three and two FLC retarders were optimized. Each FLC has two variables, the normalized thickness L (normalized to a reference component) and its azimuthal orientation angle θ. The same is true for the fixed waveplates. For three and two FLC system, this yields 12- and 8-dimensional search spaces: six and four components with two variables each.

In the GA, "polarimeter designs" are represented using a traditional binary genome. Each component is assigned a number of bits for θ and a number of bits for L. θ is the simplest case, as its possible values are limited: the best achievable alignment accuracy is estimated to $\Delta\theta \approx 0.5°$. With the range of θ being from 0° to 180°, 8 bits were found sufficient to represent the azimuth orientation of the components. For L, one should choose a minimum and a maximum value according to which components can be realistically purchased. Here, too, is the experimental resolution somewhat coarse, such that a large number of bits is not required for its representation (8-10 bits is sufficient). After determining L and θ for each of the six or four components, we proceed by determining the full transfer matrix of the PSA, $\mathbf{M}^\mathrm{PSA}(\lambda, i)$ for each discrete wavelength λ_n and each projection state i. As described in Section 2, one can determine the condition number $\kappa(\lambda)$ for $\mathbf{A}$ from the transfer matrices $\mathbf{M}^\mathrm{PSA}(\lambda, i)$. The first generation of polarimeters was initialized by generating genomes with the bits chosen randomly with a uniform distribution.

Initially, the component ordering was a variable in the genome. In that case, the first few bits of the genome determines the ordering of the components. This was done by interpreting these bits as the index in a list of components. However, the best results from initial simulation runs almost always had the same component ordering as older "non-genetic" designs [7, 14, 16]. Hence, we removed this feature to speed up convergence.

The genetic operators that were used are the well known ones for binary genomes [3, 4]. For mutation, the simple bit-flip operator was used; *i.e.* flipping $0 \rightarrow 1$ or vice versa. The mutation rate per individual was typically set to 0.2 per generation. Crossover was performed by multi-point crossover. Experience indicates that two crossover points combined with a crossover rate of 0.7 gives the best convergence performance. The selection protocol we used was tournament selection with $K = 4$ individuals in the tournament pool and $\varepsilon = 0.3$ probability of an "underdog" selection. The elitism rate was set to 1 individual per generation. It should be noted that depending on the number of components and, hence, the genome length, the exact rates may have to be adjusted somewhat for optimal performance.

In the final simulations a population of 500 individuals evolved over 600 generation. Several equivalent simulation runs were performed with different initializations of the random number generator. As the theoretically optimal performance for realistic materials is not known, no other convergence criteria than the maximum number of generations was used. Decent results can, however, be achieved more quickly with smaller population sizes and a lower number of generations.

5. Results

While the GA can handle components with arbitrary dispersion relations, our discussion is limited to components whose wavelength-dependent retardance can be fitted to the following

modified Sellmaier equation

$$\Delta(\lambda) \approx 2\pi L \left[\frac{A_{UV}}{(\lambda^2 - \lambda_{UV}^2)^{1/2}} - \frac{A_{IR}}{(\lambda_{IR}^2 - \lambda^2)^{1/2}} \right]. \quad (5)$$

Here, L is the normalized thickness of the component, which is proportional to the component's physical thickness. $L = 1$ correspond to an FLC with $\lambda/2$ at 510 nm. The parameters A_{UV}, A_{IR}, λ_{UV}, and λ_{IR} can be found by fitting experimental data to this model. Initially, for the results presented in this paper, numerical values from quartz waveplates and FLCs were used [14]. FLCs were manufactured according to the specifications of the initial optimization. Waveplates were manufactured after re-optimizing, using measured values for the thicknesses of the FLCs. Finally the orientation of all components were optimized after all the waveplates were characterized. As a result, the PSA and the PSG are not equal, due to differences in the individual optical components.

As the typical upper wavelength limit of a silicon spectrograph is 1000 nm, the range was set from 430 nm to 1000 nm. It is noted that the commercial system ranges from 430 nm to 850 nm. We also aimed at a better condition number for the whole spectral range.

The resulting condition number for the polarimeter using two FLCs is shown in Figure 2. It is noted that the system design was somewhat limited by the fact that thin FLCs could not be manufactured. Only a quasi-optimal system within the manufacturer limitations was designed. The results from the PSG and the PSA are plotted separately.

All new designs show a better condition number than the commercial instrument, and allow for measurements of the Mueller matrix across a broader spectral range. The final measured condition number is slightly poorer compared to the simulated. As the components were not covered with anti-reflective coatings, the oscillations appearing in the spectrum may originate from multiple reflections. Another source of errors are the mounting accuracy of the optical components. It has previously been shown that the FLC rotation angle is not always 45°, but varies with a few degrees between individual components [7]. One could envisage to include such individual switching angles and possibly also a higher weight on stable solutions into the fitness function.

We briefly recall that we have recently reported systems designed using three FLCs in the PSG and PSA for an extended wavelength range from 430 nm to 2000 nm [1]. Here, the power of the GA design algorithm becomes even more evident, which is clearly seen by the polarimeter design shown in Figure 3. The design parameters of the polarimeters, *i.e.* the θ and L values, for both the three and two FLC design are shown in Table 1. For comparison with previous designs, a recently patented design [19] is plotted for comparison with the GA generated one. The GA generated design is based on three FLCs and three waveplates, while the previous patented design is based on three FLCs and one waveplate. A disadvantage of using additional waveplates is the reduced transmittance with more reflective surfaces. The new design is useful over a broader spectral range (here defined as the parts of the spectrum where $\kappa^{-1} \gtrsim 0.2$) and

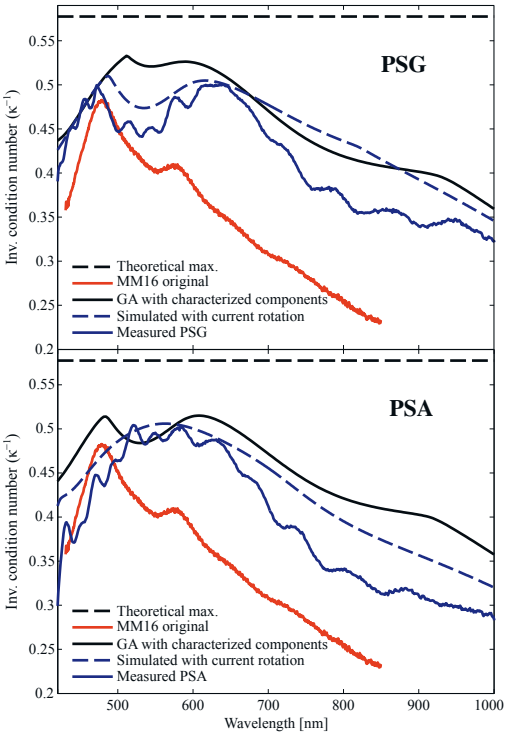

Figure 2: Inverse condition number for polarimeter designs based on two FLCs and two waveplates. Results are shown for an older design in the visible [18]. We also show GA generated designs that cover a wider spectral range with a better condition number for optimal theoretical design (solid black), best design after characterization (dashed blue) and best achieved design after mounting and calibration (solid blue).

has an overall lower noise amplification due to a lower condition number (higher inverse condition number). It should be noted that the FLC technology is limited downwards in wavelength to 430 nm, due to material degradation when exposed to ultra violet light.

One can get an impression of how complex the fitness landscape is from Figure 4. Here, a plot of $f(\theta_1, \theta_2)$ is shown, where θ_1 is the orientation angle of FLC3 and θ_2 is the orientation angle of WP3, the two first components in Figure 1. All other parameters, *i.e.* θ and L values for the other components, were set to the optimal value as given in Table 1. Note that $f(\theta_1, \theta_2)$ is periodic in both variables with a period of 180°. Due to the enormous number of local minima, even in only 2 of the 12 search dimensions, a clever optimization algorithm is required.

The Mueller matrix ellipsometer based on two FLCs in the PSG and the PSA (Figure 2) were inserted into the MM16 instrument from Horiba and calibrated the normal way using the eigenvalue calibration method [20] implemented in the software DeltaPsi 2. To verify the precision of the instrument, ten measurements of air were made, these are plotted in Figure 5 together with a measurement using the old design (red curve).

Table 1: Orientation angle, θ, and normalized thickness, L, for all components of the best polarimeter based on three and two FLCs, as shown in Figures 3 and 2. For comparison, the wavelength where the retardance is $\lambda/4$ is also included(for some components, for $\lambda/2$) for our design as well as the patented design with three FLCs. The notation WP1, FLC1 *etc.* is explained in Figure 1. Note that the previous patented design uses only one fixed waveplate, while our design uses three.

	Three FLC design			Three FLC Patent		2 FLC Visible design		
Component	θ[°]	L	$\lambda/4$ @	θ[°]	$\lambda/4$ @	θ[°]	L	$\lambda/4$ @
FLC1	56.5	2.44	1991 nm	46.0	1150 nm	100.6	1.06	894 nm
WP1	172.9	1.10	493 nm			10.2	3.37	1404 nm
FLC2	143.3	1.20	1009 nm	−5.0	1050 nm	89.9	1.05	901 nm
WP2	127.1	1.66	722 nm	92.0	$\lambda/2$ (Achromatic)	18.5	3.75	1552 nm
FLC3	169.4	1.42	1181 nm	72.0	600 nm			
WP3	110.1	4.40	1798 nm					

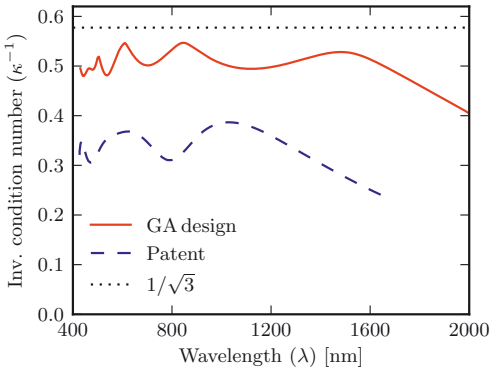

Figure 3: Inverse condition number ($\kappa^{-1}(\lambda)$) for a GA-generated and a previously patented design [19]. The GA-generated design is based on three FLCs and three waveplates, while the previous patented design is based on three FLCs and one waveplate.

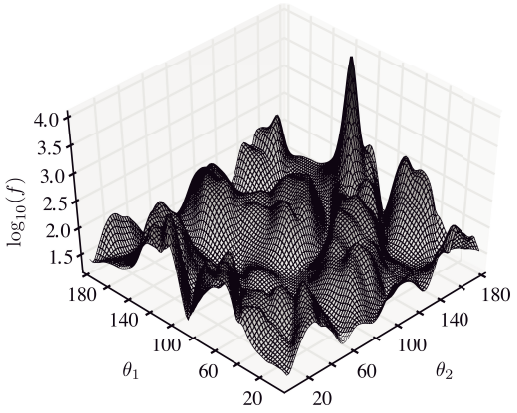

Figure 4: A two-dimensional "cut" of the fitness landscape around the optimal value for the GA-generated design with three FLCs shown in Figure 3. θ_1 is the orientation angle of FLC3 and θ_2 is the orientation angle of WP3, as shown in Figure 1. The other θ and L parameters were set to the optimal values.

The mean of the ten measurements are plotted with a dark blue curve and the standard deviation is plotted as the light blue area around the curve. There is no evident difference in accuracy or precision between the measurements using the two different designs. Both designs have a maximum error of approximately one per cent. The obvious improvement is the increased spectral range.

An important application of FLC based polarimeters are in addition to the spectroscopic ellipsometry the Mueller matrix imaging [21–23]. The increased bandwidth allows for a multipurpose instrument with multiple wavelengths.

6. Conclusion

Genetic Algorithms (GA) are able to generate optimized designs of Stokes polarimeters and Mueller matrix ellipsometers covering a broader spectral range with reduced noise amplification (lower system matrix condition numbers). Compared to previous optimization techniques used for this purpose, often based on direct or gradient searches in small parts of the search space, the GA outperforms these methods when having multidimensional search spaces with many local minima. An instrument based on ferroelectric liquid crystal retarders optimized using the GA was assembled and characterized showing system properties as expected from the simulations, with extended spectral range.

Acknowledgements

LMSA acknowledges financial support from The Norwegian Research Center for Solar Cell Technology (project num. 193829). The authors are grateful to Denis Catelan, Horiba for assisting and advising on the mechanical parts, and the extension of the spectrograph range of the MM16.

References

[1] P. A. Letnes, I. S. Nerbø, L. M. S. Aas, P. G. Ellingsen, M. Kildemo, Opt. Express 18 (2010) 23095–23103.

[2] L. M. S. Aas, P. l. G. Ellingsen, B. E. Fladmark, P. A. Letnes, M. Kildemo, Opt. Express 21 (2013) 8753.

[3] D. E. Goldberg, Genetic algorithms in search, optimization, and machine learning, Addison-Wesley, Reading, Mass., 1989.

[4] J. H. Holland, Adaptation in natural and artificial systems: an introductory analysis with applications to biology, control, and artificial intelligence, MIT Press, Cambridge, Mass., 1992.

[5] A. M. Gandorfer, Opt. Eng. 38 (1999) 1402–1408.

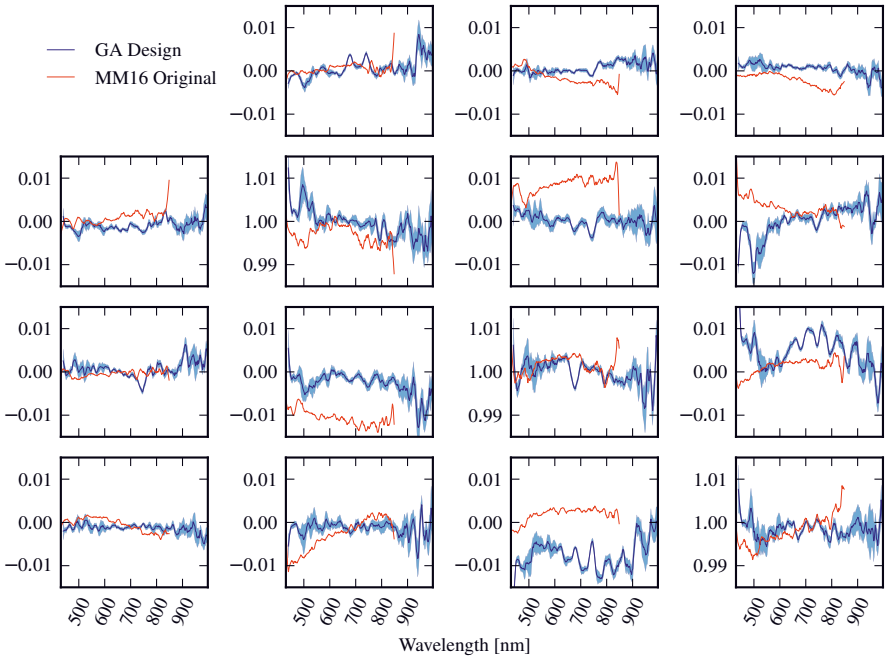

Figure 5: Mueller matrix measurement of air (identity matrix) including the measurement using the original vis-design (red) and the measurement using the new design (blue), the light blue area shows the standard deviation of 10 measurements. The new design allows the wavelength range to be extended to 1000 nm, while the precision of the new and old design appears to be similar.

[6] G. L. Jensen, J. Q. Peterson, Proc. SPIE 3437 (1998) 42–51.
[7] L. Aas, P. Ellingsen, M. Kildemo, M. Lindgren, J. Mod. Optic. 57 (2010) 1603–1610.
[8] J. Ladstein, F. Stabo-Eeg, E. Garcia-Caurel, M. Kildemo, Phys. Status Solidi (C) 5 (2008) 1097–1100.
[9] P. Hauge, Surf. Sci. 96 (1980) 81–107.
[10] W. H. Press, S. A. Teukolsky, W. T. Vetterling, B. P. Flannery, Numerical Recipes: The Art of Scientific Computing, Cambridge University Press, 2007.
[11] J. S. Tyo, Opt. Lett. 25 (2000) 1198–1200.
[12] D. S. Sabatke, M. R. Descour, E. L. Dereniak, W. C. Sweatt, S. A. Kemme, G. S. Phipps, Opt. Lett. 25 (2000) 802–804.
[13] E. Hecht, Optics, Addison-Wesley, Glenview, Il., 2002.
[14] J. Ladstein, M. Kildemo, G. K. Svendsen, I. S. Nerbø, F. Stabo-Eeg, Proc. SPIE 6587 (2007).
[15] C. S. Perone, Pyevolve, `http://pyevolve.sourceforge.net/`, 2013.
[16] E. Garcia-Caurel, A. D. Martino, B. Drévillon, Thin Solid Films 455-456 (2004) 120 – 123.
[17] Citizen Finetech Miyota Co., `http://cfm.citizen.co.jp`, 2013.
[18] As measured for the commercial instrument MM16, Horiba Jobin Yvon, 2010.
[19] D. Cattelan, E. Garcia-Caurel, A. de Martino, B. Drevillon, Patent application 2937732 (2010).
[20] E. Compain, S. Poirier, B. Drevillon, Appl. Opt. 38 (1999) 3490–3502.
[21] S. B. Hatit, M. Foldyna, A. De Martino, B. Drévillon, Phys. Status Solidi (a) 205 (2008) 743–747.
[22] P. G. Ellingsen, M. B. Lilledahl, L. M. S. Aas, C. d. L. Davies, M. Kildemo, J. Biomed. Opt. 16 (2011) 116002.
[23] L. Aas, P. Ellingsen, M. Kildemo, Thin Solid Films 519 (2010) 2737–2741.

L. M. S. Aas, P. G. Ellingsen, and M. Kildemo, Near infra-red Mueller matrix imaging system and application to retardance imaging of strain, Thin Solid Films **519**, 2737–2741 (2010)

Paper 5

Thin Solid Films 519 (2011) 2737–2741

Contents lists available at ScienceDirect

Thin Solid Films

journal homepage: www.elsevier.com/locate/tsf

Near infra-red Mueller matrix imaging system and application to retardance imaging of strain

Lars Martin Sandvik Aas *, Pål Gunnar Ellingsen, Morten Kildemo

Department of Physics, Norwegian University of Science and Technology, Norway

ARTICLE INFO

Article history:
Received 1 September 2010
Received in revised form 4 November 2010
Accepted 9 December 2010
Available online 31 December 2010

Keywords:
Mueller matrix
Imaging
Strain imaging
Polarimetry
Ellipsometry
Silicon wafer

ABSTRACT

We report on the design and performance of a near infra-red Mueller matrix imaging ellipsometer, and apply the instrument to retardance imaging of strain in near infra-red transparent solids. Particularly, we show that the instrument can be used to investigate complex strain domains in multi-crystalline silicon wafers.

1. Introduction

In this paper the near infra-red (NIR) ferroelectric liquid crystal (FLC) based Mueller matrix ellipsometer (MME) design reported recently [1], is modified to an imaging set-up, and used to demonstrate the application to retardance imaging of strain in transparent crystals. Neither a NIR imaging MME system nor an FLC based imaging MME has to our knowledge been previously reported.

Several non-scanning imaging MME systems based on Variable Liquid Crystal Retarders (VLCR) have recently been reported [2,3]. These systems have so far only been operated in the visible range, and will generally be many orders slower than an FLC based system [1]. Using such systems, it has been reported that imaging MME is an interesting tool in both bio-applications [3–6], and strain imaging [7]. Recent non-imaging Mueller matrix ellipsometric studies of bio-tissue demonstrate the usefulness of the Mueller matrix in combination with polar decomposition techniques [8–11].

The advantage of the complete Mueller matrix measurement relies on the possibility to use polar decomposition techniques [11–15] and that the Eigenvalue Calibration Method (ECM) may be used for the calibration of the system [16,17]. Furthermore, the Mueller matrix will not suffer from unexpected properties initially believed not to be part of the sample properties, such as polarization dependent scattering or depolarization, different types of diattenuation, and both circular and linear birefringence components.

Several FLC based designs have been proposed, although the first proposed system similar to the one reported here, appears to be by Gandorfer *et al.* [18]. FLC based MMEs are appealing since they involve no moving parts, and supply a highly stable beam. They are both suitable for direct imaging applications (hyper-spectral and monochrome), or in conjunction with for example stripe CCD spectrographs commonly used in spectroscopy. Furthermore, FLCs modulate rapidly for a fast determination of the Mueller matrix. The disadvantage of liquid crystals, and in particular the current FLCs is the well known degradation upon UV-radiation. Applications of liquid crystal technology in MME are so far limited to the visible and the infra-red.

Reducing material costs is a great concern for the silicon solar cell industry. One approach is to reduce the wafer thickness. A factor making the latter difficult, is the internal residual strain, which is often induced in the process of casting. To control and verify a successful wafer production with lower strain, effective instruments are needed to measure the residual strain. In addition to a report of the system instrumentation, we demonstrate the application of the FLC based NIR MME imaging system to make a map of two dimensional projections of strain fields in multi-crystalline silicon wafers. The strain fields are proportional to the retardance, when neglecting multiple reflections in the sample [24,25].

2. Experimental

2.1. Overview of the system and concept

The NIR-MME imaging setup was designed to operate both in transmission and reflection mode. The applications demonstrated in

* Corresponding author. Department of Physics, Norwegian University of Science and Technology, 7491 Trondheim, Norway. Tel.: +47 73 59 34 55.
E-mail address: lars.aas@ntnu.no (L.M.S. Aas).

0040-6090/$ – see front matter © 2011 Elsevier B.V. All rights reserved.
doi:10.1016/j.tsf.2010.12.093

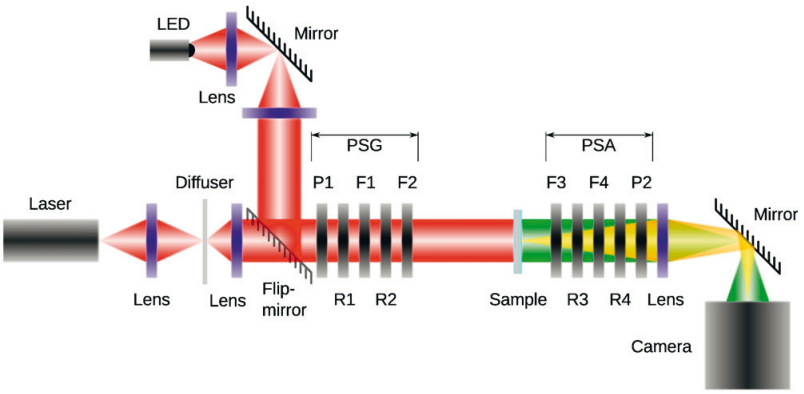

Fig. 1. (Color online) Schematic drawing of the Mueller matrix imaging system. The system consists of two sources, Polarization State Generator and Analyzer, imaging optics and a camera.

this paper are only from transmission mode measurements. The system was designed to operate in the range 700–1600 nm [1,19]. A schematic drawing of the setup is shown in Fig. 1. In particular, the Polarization State Analyzer (PSA) and the Polarization State Generator (PSG) are both composed of a NIR dichroic polarizer (P1/P2), a zero order quarter wave-plate at 465 nm (R1/R4), a half wave-plate at 1020 nm (R2/R3), an FLC half wave retarder at 510 nm (F1/F4) and an FLC half wave retarder at 1020 nm (F2/F3). The FLCs have fixed retardances and can switch between two orientations of the fast axis. A suitable combination of wave-plates and FLCs ensures that the PSG generates four sub-optimal Stokes vectors for all wavelengths in the design range. These four Stokes vectors define the column vectors of the PSG matrix (**W**). The four analyzer states of the PSA define the rows of the analyzer matrix (**A**). A Mueller matrix measurement is carried out by measuring the 16 intensities obtained when switching through all possible FLC combinations. The measurement and the calibration process is similar to the one proposed for the LCVR systems [20], and the rotating compensator systems [21]. The 16 measured intensities form a matrix **B**, which correspond to the matrix product of **A**, the sample Mueller matrix (**M**) and **W**

$$\mathbf{B} = \mathbf{WMA}. \tag{1}$$

M can then be found by multiplying **B** by the inverse of **W** and **A** from each side

$$\mathbf{M} = \mathbf{W}^{-1}\mathbf{B}\mathbf{A}^{-1}. \tag{2}$$

It is evident from linear algebra that for Eq. (2) to be solvable, **A** and **W** need to be non-singular. Specifically, it has been shown that the error in the intensity measurements (**B**) and the calibration errors of **A** and **W** are amplified into the errors of a measured Mueller matrix as [21]

$$\frac{||\Delta\mathbf{M}||}{||\mathbf{M}||} \lesssim \kappa_{\mathbf{A}} \frac{||\Delta\mathbf{A}||}{||\mathbf{A}||} + \kappa_{\mathbf{W}} \frac{||\Delta\mathbf{W}||}{||\mathbf{W}||} + \kappa_{\mathbf{W}}\kappa_{\mathbf{A}} \frac{||\Delta\mathbf{B}||}{||\mathbf{B}||}, \tag{3}$$

where $\kappa_{\mathbf{W}} = ||\mathbf{W}||||\mathbf{W}^{-1}||$ and $\kappa_{\mathbf{A}}$ are the matrix condition numbers of **A** and **W**, where we use the L_2 norm which is the ratio of the largest to the smallest singular value [22].

In order to find **W** and **A**, an implementation of the ECM is used. The method allows **W** and **A** to be calculated without exact knowledge of the Mueller matrix of the calibration samples. More details about the FLC MME system and its calibration are reported elsewhere [1,19].

2.1.1. Light sources and detectors

The system is operated with three different light sources. For spectroscopic, and for measurement of weakly scattering samples, a tungsten halogen white light source (150 W) is used in combination with a grating monochromator or band pass filters. For samples with more absorption or scattering, higher intensity was needed and a 980 nm diode laser (max 300 mW) source or a LED array with centre wavelength at 1300 nm (110 mW) was used. In all cases, the light is collimated before entering the PSG. In the case of the diode laser, a rotating diffuser was used to reduce speckle.

The digital camera was a Xenics Xeva camera operating at 15 Hz, consisting of a 14-bit InGaAs FPA detector with 640×512 pixels and sensitive to the spectral band 0.9–1.7 μm. In addition, due to less thermal noise and dead pixels, a silicon camera from Hamamatsu was used in combination with the 980 nm laser. The field of view of the system is 1 cm×1 cm with a diffraction limited resolution of 12.5 μm.

2.2. Analysis of the Mueller matrix

The polarimetric information in a measured Mueller matrix can in many cases be extracted using polar decomposition techniques. Several decomposition techniques have been proposed [12–14]. In particular, the forward polar decomposition technique, described in details elsewhere [8,10–12,14], was applied to all measurements presented here. The basic principle of the forward decomposition is to assume that the polarizing properties of the measured Mueller matrix (**M**) is taking place in the following order, diattenuation ($\mathbf{M}_D$), retardation ($\mathbf{M}_R$) and depolarization ($\mathbf{M}_\Delta$), which gives

$$\mathbf{M} = \mathbf{M}_\Delta\mathbf{M}_R\mathbf{M}_D. \tag{4}$$

It is further convenient to calculate a numeric quantity for the polarimetric properties, in this paper only the retardance and the orientation of the slow axis are explicitly used.

Due to detector noise, the measured Mueller matrix will always have an error. The error may result in a slightly unphysical Mueller matrix. By putting appropriate physical constraints on the measured matrices, a measure of the matrix physicality can be found. It is further possible to calculate the closest physical matrix of an unphysical matrix. In particular, the constraints proposed by Cloude [23] was applied in this work.

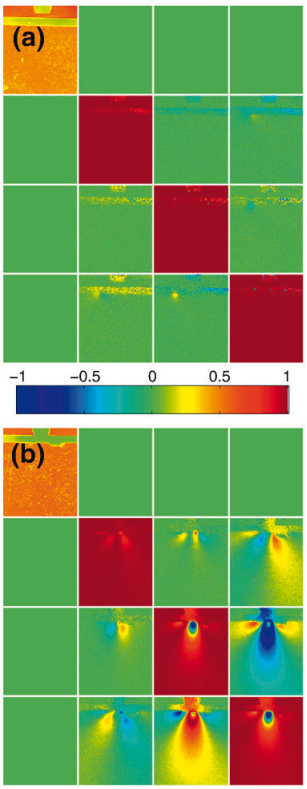

Fig. 2. (Color online) Mueller matrix images of non stressed (a) and stressed (b) calcium fluoride crystals. The elements are normalized to $m_{1,1}$, except from the $m_{1,1}$ image which shows the transmission intensity image. In (a) the crystal is found isotropic, i.e. no strain induced birefringence is observed in the crystal, while in (b) the crystal is found with a graded anisotropy due to the non uniform applied stress.

3. System performance, results and discussion

3.1. Validation of calibration of the NIR MME imaging system

For an image the average inverse condition number of **A** and **W** is 0.46. An estimate of the accuracy of the Mueller matrix imaging system can be made by considering a measurement of the well defined Mueller matrix of air (the identity matrix). The mean matrix of a measured Mueller matrix image was

$$\begin{bmatrix} 1.000\pm0.00 & -0.004\pm0.01 & -0.003\pm0.01 & 0.006\pm0.01 \\ 0.000\pm0.01 & 1.002\pm0.02 & -0.001\pm0.02 & -0.002\pm0.02 \\ 0.001\pm0.01 & -0.002\pm0.02 & 1.006\pm0.03 & -0.003\pm0.02 \\ 0.001\pm0.01 & 0.002\pm0.02 & 0.007\pm0.02 & 0.998\pm0.03 \end{bmatrix},$$

with the standard deviation from the mean value given as the ±. The error in the mean matrix is in the third decimal, while the standard deviation from the mean is in the second. The variations found over the pixels may have many sources, but is most likely due to detector noise. The mean noise (fidelity) found from Cloude filtering is −23.7 dB with standard deviation of 0.8 dB. The non-uniformity and error is found to be satisfactory.

3.2. Polarimetric images and strain mapping

Polarimetric imaging can be used to investigate strain fields in transparent crystals. An isotropic material which experiences a non-isotropic stress, becomes, as described by the photoelastic theory [24,25], anisotropic (birefringent) due to the induced internal strain. Polarimetry is very sensitive to changes in the retardance

$$\delta = \Delta n \cdot d = (n_{\text{slow}} - n_{\text{fast}}) \cdot d, \tag{5}$$

which is proportional to the birefringence (difference in refractive index from slow to fast axis, Δn) and the thickness of the sample (d). The refractive index will increase in the direction of the positive strain (compression). Hence the direction of the slow axis will give the direction of the positive strain. The retardance will be a projection of the strain in real space to the xy-image plane. A quantitative calculation of the strain using the photoelastic properties and known crystal orientation [24,25], is out of the scope of the current proof of concept report.

3.2.1. Retardance imaging of strain in stressed CaF_2

The capability of the MME system to image strain patterns was investigated by inducing a direct force onto a crystalline CaF_2 prism, which is isotropic and transparent from the UV to the infrared. The prism was placed on a platform in the image plane of the system, and stress was applied through a metal plug. The upper edge of the prism was opaque, such that the interface region between the metal plug and the crystal could not be examined. Fig. 2 shows Mueller matrix images of the prism without and with applied stress. It is evident from the non stressed image that the crystal is isotropic, and has no

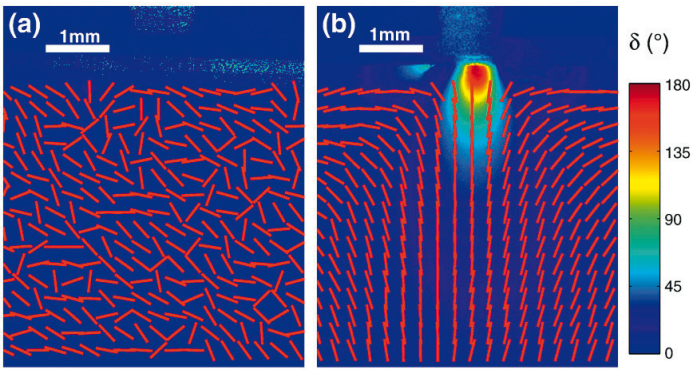

Fig. 3. (Color online) Calculated retardance from the Mueller matrix image in Fig. 2. (a) shows the retardance map when no stress is applied, and (b) when stress is applied. The lines show the direction of the slow axis, while the color-map indicates the retardance in degrees with wavelength of 980 nm.

retardance or diattenuation. After the stress is applied, the crystal becomes anisotropic, seen by the appearance of the non diagonal lower right 3×3 matrix. The magnitude of the retardance and the orientation of the slow axis are then calculated from the measured Mueller matrix.

The corresponding retardance plots for the two Mueller matrix images in Fig. 2 are shown in Fig. 3. It is evident that when no stress is applied, there is no slow axis, and the calculated direction is therefore random, as a result of noise. When stress is applied, the direction of the slow axis corresponds to the direction of the positive strain.

Evidently, this sample could have been studied with any visual MME imaging system. However, in case of more rough surfaces or a low band-gap crystal, the use of near infra-red light becomes imminent.

3.2.2. Retardance imaging of strain in a multi-crystalline silicon wafer

The band-gap of Si makes the material transparent for photons with lower energy than 1.1 eV, which means that a visible MME cannot perform bulk strain measurements in transmission.

In this experiment the sample was initially a 150 μm thick multi-crystalline wafer, with a surface of about 4 cm×2.5 cm and a trapezoidal shape (see Fig. 4). Crystalline silicon is isotropic with a diamond cubic lattice structure. In multi-crystalline wafers the grains are through-going and the grain boundaries go straight through the wafer, eliminating the problem of shading grains. In order to avoid large losses of intensity and to obtain a good signal to noise ratio, the wafer was polished on both sides, down to a thickness of approximately 100 μm. The wafer was placed in an assembly consisting of two bars with slits, keeping the wafer vertically stable and in position (see Fig. 4). Stress was then applied to the wafer by buckling [26], which is a well known method for material strength tests. The strain is induced when the bars are forced towards each other such that the wafer bends by the control of a fine threaded screw.

In order to map the whole wafer, the assembly is mounted on a translation stage which automatically moves to the next position after each Mueller matrix image acquisition. For simplicity and proof of concept, only one of the images is considered here, the location of this area on the wafer is indicated by the red square in Fig. 4.

Fig. 5 shows the calculated retardance and the orientation of the slow axis of the selected area on the strained wafer. The crystal grains show contrast in both the orientation of slow axis and the retardance maps, which indicates that both different magnitude and orientation of strain can be found. The two areas (1 and 2) indicated by the red squares in Fig. 5(a) are enlarged and shown in Figs. 6 and 7.

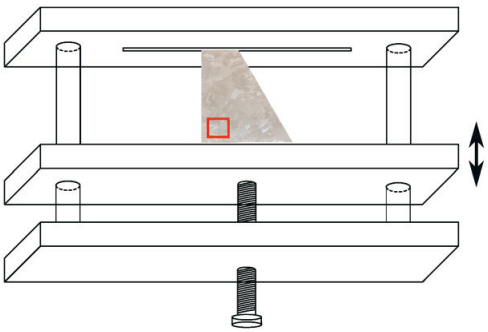

Fig. 4. The assembly made for the buckling of the wafer. The wafer is placed between a fixed and a non fixed bracket, which then can be translated by a fine threaded screw.

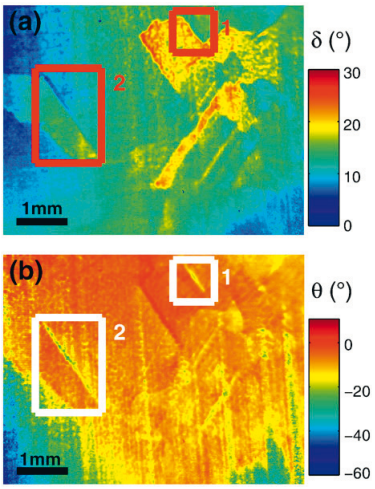

Fig. 5. Figure (a) shows the calculated retardance map of the area indicated by the red square in Fig. 4, with applied strain, while figure (b) shows the orientations of the slow axes for the area in interest. Areas 1 and 2 indicate the two areas that are described in more detail within the text.

The retardance image of area 1 (Fig. 6) shows a grain boundary where the retardance is higher for the grain located in the lower part of the image, compared to the upper grain. Various domains of lower and higher retardance can also be observed inside the two grains. Fig. 6(a) shows that at the grain boundary there appears to be domains with lower retardance than the surrounding grains. It is

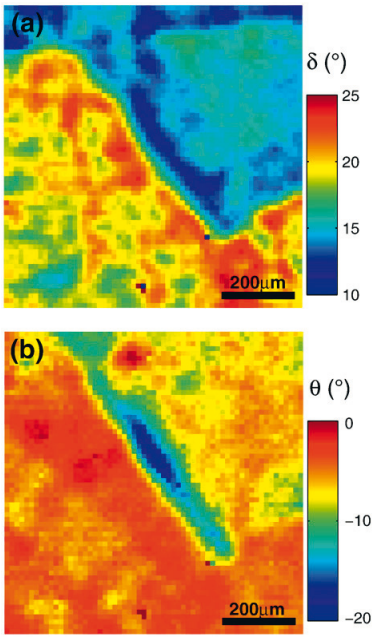

Fig. 6. (Color online) Figure (a) shows the calculated retardance map of area 1, with applied strain. There is good contrast at the grain boundary, also interesting is the low retardance domain along the grain boundary, which may be induced due to a relaxation of strain at the boundary. Figure (b) shows the calculated orientation of the slow axis.

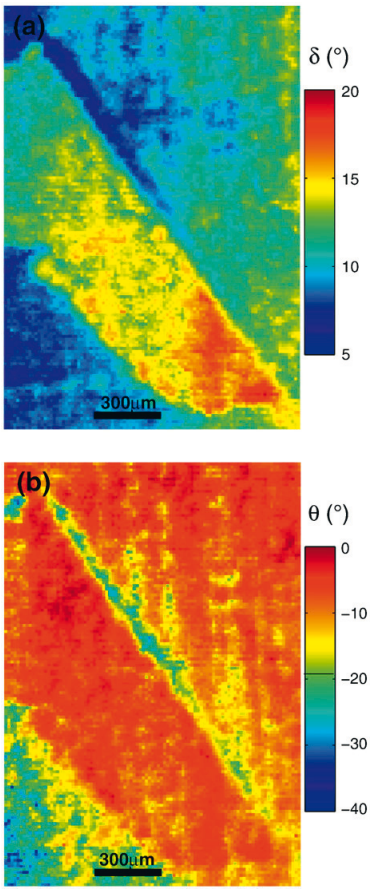

Fig. 7. (Color online) Figure (a) shows the calculated retardance map of area 2, with applied strain. Figure (b) shows the corresponding orientation of slow axis. In this area of the wafer we also see that there is a domain along the grain boundary where the retardance is lower than in the two adjacent grains. Also the slow axis has a different orientation in this domain.

observed from Fig. 6(b), that the orientation of the strain is very different in this particular domain. These observations may possibly be due to a relaxation of strain at the grain boundary.

In area 2 (Fig. 7) the grain is observed to have a higher retardance than the adjacent grains. One may expect that the whole grain experienced the same retardance, but in this case a higher retardance is found in the lower part of the grain. This observation can possibly be explained by the low retardance on the grain boundary around the upper part of the grain, where a relaxation may have occurred. The corresponding orientation of the slow axis (Fig. 7(b)) shows a different strain orientation than the surrounding grains. The details of the structures within the domains can without great difficulty be studied in a lab set-up. A production line equipment can be evisaged in order to inspect strain over large areas, or strain above a particular threshold level. Polarimetric imaging may also be useful in several other occasions e.g. to characterize the polarization dependent optical properties of optical components, such as lenses, wherever these have to be taken into account.

Surface roughness, multiple reflections and depolarization, and its effect on the measured retardance, are important effects, and will together with quantitative analysis of strain be addressed in future work.

4. Conclusions

In conclusion, we have constructed a near infra-red (NIR) Mueller matrix imaging ellipsometer based on ferroelectric liquid crystal retarders. The system has been demonstrated to be a valuable tool in the characterization of strain in NIR transparent solids, and in particular multi-crystalline silicon. Through the use of Mueller matrix analysis tools, a detailed analysis of strain field domains can be made, which in the future can be quantified and used as input to numerical models.

Acknowledgements

The authors acknowledge Håkon Ottar Nordhagen and Stéphane Dumoulin from the Department of Applied Mechanics and Corrosion at SINTEF for collaboration and useful discussions on strain in multi-crystalline silicon.

The authors are also gratefull to Hallvard Skjerping, Frantz Stabo-Eeg, Ingar Stian Nerbø and Mikael Lindgren for help and discussions on the MME imaging system.

The work was performed within “The Norwegian Research Centre for Solar Cell Technology” project number 193829), a Centre for Environment-friendly Energy Research co-sponsored by the Norwegian Research Council and research and industry partners in Norway.

References

[1] Lars Martin Sandvik Aas, Paal Gunnar Ellingsen, Morten Kildemo, Mikael Lindgren, J. Mod. Opt. 57 (17) (2010) 1603.
[2] Blandine Laude-Boulesteix, Antonello De Martino, Bernard Drévillon, Laurent Schwartz, Appl. Opt. 43 (14) (May 2004) 2824.
[3] J.M. Bueno, P. Artal, Opt. Lett. 24 (1) (1999) 64.
[4] J.R. Chung, J.S. Baba, A.H. DeLaughter, G.L. Cote, Proceedings of SPIE, vol. 4613, 2002, p. 111.
[5] A.M. Baldwin, J.R. Chung, J.S. Baba, C.H. Spiegelman, M.S., 25th Proceedings of IEEE, 2003, p. 1027.
[6] D. Lara-Saucedo, C. Dainty, Investig. Ophtalmol. Vis. Sci. 44 (5) (2003) 3627.
[7] Michael Richert, Xavier Orlik, Antonello De Martino, Opt. Express 17 (16) (August 2009) 14199.
[8] Nirmalya Ghosh, Michael F.G. Wood, I. Alex Vitkin, J. Biomed. Opt. 13 (4) (2010) 044036.
[9] M.K. Swami, S. Manhas, P. Buddhiwant, N. Ghosh, A. Uppal, P.K. Gupta, Opt. Express 14 (2006) 9324.
[10] S. Manhas, M.K. Swami, P. Buddhiwant, N. Ghosh, P.K. Gupta, K. Singh, Opt. Express 14 (2006) 190.
[11] Nirmalya Ghosh, Michael F.G. Wood, Shu-hong Li, Richard D. Weisel, Brian C. Wilson, Ren-Ke Li, I. Alex Vitkin, J. Biophotonics 2 (3) (March 2009) 145.
[12] S.Y. Lu, R.A. Chipman, J. Opt. Soc. Am. A 13 (5) (1996) 1106.
[13] Razvigor Ossikovski, J. Opt. Soc. Am. A Opt. Image Sci. Vis. 26 (5) (May 2009) 1109.
[14] R. Ossikovski, A. De Martino, S. Guyot, Opt. Lett. 32 (6) (2007) 689.
[15] R. Ossikovski, M. Anastasiadou, S.B. Hatit, E. Garcia-Caurel, A. De Martino, Phys. Status Solidi (A) 205 (4) (2008) 720.
[16] E. Compain, S. Poirier, B. Drevillon, Appl. Opt. 38 (16) (June 1999) 3490.
[17] E. Garcia-Caurel, Thin Solid Films 455–456 (2004) 120.
[18] A.M. Gandorfer, Opt. Eng. 38 (8) (1999) 1402.
[19] T.S. Narasimhamurty, Photoelastic and electro-optic properties of crystals, Plenum Press, New York, 1981.
[20] D.F. Nelson, M. Lax, Phys. Rev. B 3 (8) (1971) 2778.
[21] J. Ladstein, F. Stabo-Eeg, E. Garcia-Caurel, M. Kildemo, Phys. Status Solidi (c) 5 (5) (May 2008) 1097.
[22] J.M. Bueno, J. Opt. A: Pure Appl. Opt. 2 (3) (2000) 216.
[23] F. Stabo-Eeg, M. Kildemo, I.S. Nerbø, M. Lindgren, Opt. Eng. 47 (2008) 073604.
[24] J.S. Tyo, Opt. Lett. 25 (16) (2000) 1198.
[25] S.R. Cloude, Proc Soc Photo Opt Instrum Eng, vol. 1166, 1989, p. 177.
[26] Don Orr Brush, Buckling of bars, plates and shells, McGraw-Hill, 1975.

L. M. S. Aas, I. S. Nerbø, M. Kildemo, D. Chiappe, C. Martella, and F. Buatier de Mongeot, Mueller matrix imaging of plasmonic polarizers on nanopatterned surface, Proc. SPIE **8082**, 80822W (2011)

Paper 6

Mueller matrix imaging of plasmonic polarizers on nanopatterned surface

Lars Martin S. Aas[a], Ingar Stian Nerbø[a], Morten Kildemo[a], Daniele Chiappe[b], Christian Martella[b] and Francesco Buatier de Mongeot[b]

[a]Department of Physics, Norwegian University of Science and Technology, 7491 Trondheim, Norway;
[b]Dipartimento di Fisica, Università di Genova, and CNISM, Via Dodecaneso, 33, 16146 Genova, Italy

ABSTRACT

We present the application of a near infra red Mueller matrix imaging ellipsometer to the characterization of plasmonic polarizers. The samples are prepared by evaporation of Au onto SiO_2 ripples. The nanostructured ripple surface has been produced by ion beam sputtering at an off normal angle of incidence. Au was thereafter evaporated onto the surface at an grazing angle. As a result, thin lines of nearly connected Au nanoparticles form along the illuminated side of the ripples, resulting in a large in-plane anisotropy of the structure. Mueller matrix imaging is used to determine the lateral uniformity of the optical signal in correlation to the real space topography of the sample, and to determine to what degree the nanoparticles tend to form a connected wire, or whether there are well separated Au particles. The success of this method in order to produce polarizers, lies in controlling the process to allow well connected lines of Au particles along the ripples, with a high degree of homogeneity. Mueller Matrix images of the sample recorded at normal incidence are shown, and the information that can be extracted from such images is discussed.

Keywords: Mueller matrix, imaging, plasmonics, ellipsometry, polarimetry

1. INTRODUCTION

Standard Spectroscopic Ellipsometry (SE) has for a long time, and recently also spectroscopic Mueller Matrix Ellipsometry (MME), been the technique of choice for the inspection of surfaces, thin films and recently also nanostructured surfaces, due to the enhanced phase sensitivity introduced by the measurement of the phase difference between p and s polarized light.[1] Most semiconductor processing factories will perform a large number of ellipsometric measurements during the production. A fundamental problem of SE has been the standard spot size, which traditionally has been on the order of 1-4 mm in diameter. Such a large spot size is often incompatible with research quality samples, and also for in-line monitoring of the homogeneity of a process. Such an issue becomes further important, when the process is a low cost fabrication method which requires even more strict attention to homogeneity issues. The standard ellipsometer may partially recover some of its deficits by aiming at a micro-spot, which will typically be on the order of 100 μm in diameter, at the cost of much reduced flux due to the lack of commercially available incoherent sources with a high radiance. The use of laser sources could allow a true microspot ellipsometer. But still, a complete overview of the sample will require a complete spatial mapping, where the mapping time scales with the spot size. The imaging ellipsometer, and in particular the imaging MME, may be the response to many of these issues, allowing better process control.

There are several advantages of measuring the complete Mueller matrix compared to traditional ellipsometric measurements, among them are the possibility to use polar decomposition techniques,[2–6] and the Eigenvalue calibration Method (ECM)[7] for instrument calibration.

In this work, a near infra red Mueller Matrix Imaging Ellipsometer (MMIE) is applied to the characterization of nano patterned plasmonic polarizers. The samples are prepared by evaporation of Au onto SiO_2 ripples. The

Further author information: (Send correspondence to L.M.S.A.)
L.M.S.A: E-mail: lars.aas@ntnu.no, Telephone: +47 73 59 34 55

Optical Measurement Systems for Industrial Inspection VII, edited by Peter H. Lehmann, Wolfgang Osten, Kay Gastinger, Proc. of SPIE Vol. 8082, 80822W · © 2011 SPIE
CCC code: 0277-786X/11/$18 · doi: 10.1117/12.889585

nanostructured ripple surface has been produced by ion beam sputtering at a grazing angle of incidence. Au was thereafter evaporated onto the surface at an inclined angle. As a result, thin lines of nearly connected Au nanoparticles form along the illuminated side of the ripples, giving large in-plane anisotropy of the structure. Figure 1 shows AFM images of the surface showing a clear anisotropy. Several studies have recently been reported on aligned metal nanoparticles, exhibiting an anisotropic plasmon resonance.[8–12] This anisotropy is usually examined by studying the transmission of linearly polarized light. In this work we will explore the advantages of performing spatially resolved full Muller matrix measurements on such samples.

2. MUELLER-STOKES THEORY

For a monochromatic plane wave the polarization state is elegantly described by the Jones calculus, however in many cases the wave can have a random component making the orthogonal amplitude and phase components time dependent. The electromagnetic wave is then said to be partially polarized and can no longer be described by the time independent Jones vector. By describing the polarization state in terms of intensities or time averages in stead of complex fields, the complete polarization state, including partially polarized and non-polarized light, can be expressed concisely using the four real elements in the Stokes vector

$$\boldsymbol{S} = \begin{bmatrix} I \\ Q \\ U \\ V \end{bmatrix} = \begin{bmatrix} \langle E_{0,x}(t)^2 \rangle + \langle E_{0,y}(t)^2 \rangle \\ \langle E_{0,x}(t)^2 \rangle - \langle E_{0,y}(t)^2 \rangle \\ 2\langle E_{0,x}(t) E_{0,y}(t) \cos\delta(t) \rangle \\ 2\langle E_{0,x}(t) E_{0,y}(t) \sin\delta(t) \rangle \end{bmatrix},$$

where the notation $\langle \cdots \rangle$ denotes time average of time dependent electric field component amplitudes ($E_{0,x}(t)$ and $E_{0,y}(t)$) and phase difference ($\delta(t)$) for light propagating along the z-axis. The first element (I) is a measure of the total light intensity, while the three others describe the relative intensity of polarized light. Specifically Q is the difference between the components of linearly x and y polarized light, U the difference between the components of linearly $\pm 45^\circ$ polarized light and V the difference between the left and right handed circular polarization components.

The linear transformation of polarized light is elegantly described by the Mueller matrix ($\mathbf{M}$), connecting an incoming ($\mathbf{S}_{in}$) to an outgoing Stokes vector ($\mathbf{S}_{out}$),

$$\mathbf{S}_{\text{out}} = \mathbf{M}\mathbf{S}_{\text{in}}.$$

The Mueller matrix completely describe any polarization interaction of light such as polarizance, diattenuation, retardance and depolarization.

2.1 Stokes vector and Mueller matrix measurement

Stokes vectors are measured with a polarimeter or polarization state analyzer (PSA) projecting the incoming polarization state to at least four well chosen Stokes vectors and measure the intensities of those states. The four Stokes vectors are organized as the rows in the PSA matrix $\mathbf{A}$. The intensity of each projected state is measured in an intensity vector $\mathbf{b} = \mathbf{AS}$. The unknown Stokes vector is then found by inverting $\mathbf{A}$,

$$\mathbf{S} = \mathbf{A}^{-1}\mathbf{b}.$$

Mueller matrices are measured by incidenting at least four well chosen Stokes vectors onto the sample and then measure the outgoing Stokes vector with the PSA, giving at least 16 intensity measurements ($\mathbf{B}$). The four polarization states made by the polarization state generator (PSG) are organized in a matrix $\mathbf{W}$. Giving $\mathbf{B} = \mathbf{AMW}$ for the intensity measurements. $\mathbf{M}$ is then found by multiplying by the inverse of $\mathbf{A}$ and $\mathbf{W}$ from each side,

$$\mathbf{M} = \mathbf{A}^{-1}\mathbf{B}\mathbf{W}^{-1}.$$

The relative error propagating into $\mathbf{M}$ is related to the choice of Stokes vectors in $\mathbf{A}$ and $\mathbf{W}$, and it has been shown that the relative error scales with the condition number of $\mathbf{A}$ and $\mathbf{W}$.[13,14] Optimizing the Stokes vectors in $\mathbf{A}$ and $\mathbf{W}$ is therefore an important part of the design of a Mueller matrix ellipsometer.[15]

2.2 Analysis of the Mueller matrix

The fact that Stokes vectors and Mueller matrices have always real elements make it more convenient to measure, and formalisms have been developed to make the measurement. One of the major advantages of complete Mueller matrix measurements is in many cases the possibility to easily extract polarimetric information such as diattenuation, retardance and depolarization. This can be done by direct analysis of the measured matrix and by the use of polar decomposition techniques, where it is assumed that the polarization effects are taking place in a specific order.[4,6]

A lot of information of the sample can be found by just concidering the elements of the normalized Mueller matrix

$$\mathbf{M} = \begin{bmatrix} 1 & m_{12} & m_{13} & m_{14} \\ m_{21} & m_{22} & m_{23} & m_{24} \\ m_{31} & m_{32} & m_{33} & m_{34} \\ m_{41} & m_{42} & m_{43} & m_{44} \end{bmatrix}.$$

After measurement, the matrix elements are scaled by the relative intensity of each pixel, such that general normalization is needed especially when locking at Mueller matrix images, however, the unnormalized M_{11} element may be usefull for relative transmittance or reflectance conciderations. The vector $\vec{D} = [m_{12}, m_{13}, m_{14}]^T$ determine the diattenuation of the sample, describing how much the sample attenuate different polarization states, while polarizance vector $\vec{P} = [m_{21}, m_{31}, m_{41}]^T$ describes the outgoing polarization if the incoming light was unpolarized. The polarizance is the length of this vector, and specifically the linear polarizance is $P = \sqrt{m_{21}^2 + m_{31}^2}$ with orientation $\theta_P = \frac{1}{2}\arctan(m_{31}/m_{21})$. For a sample that gives depolarization the degree of polarization is reduced after interaction with the sample. The depolarization index P_d of a Mueller matrix is calculated by the diagonal elements of the Mueller matrix[16]

$$P_d = \sqrt{\frac{\sum_{i,j=1}^{4} m_{i,j}^2 - 1}{3}}.$$

In the so called forward polar decomposition technique the ordering is diattenuation ($\mathbf{M}_D$), retardation ($\mathbf{M}_R$) and depolarization ($\mathbf{M}_\Delta$) giving the Mueller matrix

$$\mathbf{M} = \mathbf{M}_\Delta \mathbf{M}_R \mathbf{M}_D.$$

From the pure retarding matrix is it further useful to find the retardance vector

$$\mathbf{r} = \begin{bmatrix} r_1 \\ r_2 \\ r_3 \end{bmatrix} = \frac{R}{2\sin R} \begin{bmatrix} m_{R_{34}} - m_{R_{43}} \\ m_{R_{42}} - m_{R_{24}} \\ m_{R_{23}} - m_{R_{32}} \end{bmatrix},$$

where R is the total retardance and the length of $\mathbf{r}$, $R = \arccos((\mathrm{Tr}(\mathbf{M}_R) - 1)/2)$, and $m_{R_{ij}}$ are the elements of $\mathbf{M}_R$. Linear retardance (δ) is found by

$$\delta = 2\arccos\sqrt{r_3^2(1 - \cos^2(R/2)) + \cos^2(R/2)}$$

The orientation of linear retardance also refered to as slow axis (θ_δ) is found similar to the orientation of polarizance.[17] Decomposition algoritms have also been proposed for different ordering of the polarization effects.[2,5]

3. EXPERIMENTAL

3.1 Sample preparation

The samples are prepared recurring to a two step approach which combines defocused ion beam sputtering (IBS) of a SiO_2 substrate to form a ripple undulation orthogonal to the ion beam projection, followed by a subsequent deposition of Au at grazing angle of incidence.[10]

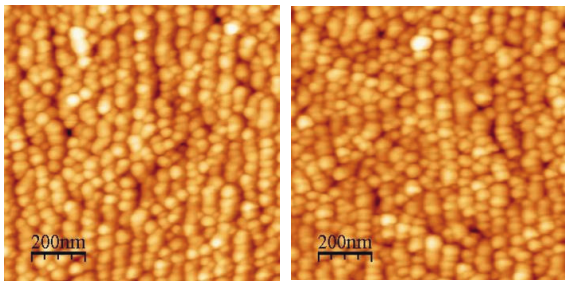

Figure 1. (Color online) AFM images of Au nanoparticles on ripples, on two different areas of the sample

IBS is a simple and low cost nanofabrication technique capable of patterning metallic and dielectric substrates. In this process the competition between an erosive instability, due to sputtering action of the ion beam, and relaxation mechanisms, dominated by thermally activated diffusion and by hyperthermal ion induced mobility, lead to the selection of a preferential spatial modulation of the surface profile. This corresponds to the formation of a self-organized periodic ripple pattern onto the substrate surface.[11,18–20] Depending on the nature of the substrate material and on the irradiation parameters (ion beam energy, incidence angle, gas species, substrate temperature) different morphological features can be enhanced.[18,21] In our case, irradiation of the SiO_2 substrates is performed in an UHV system at an off normal sputtering angle ($\theta = 45^o$) using a gridded multi aperture Ar+ source at an ion energy of 800 eV and a constant flux of 4.0×10^{15}ions/cm^2 s. A well defined rippled pattern oriented orthogonal to the ion beam projection is obtained on the surface after irradiation doses in the range of 3×10^{19}ions/cm^2. After IBS, the patterned SiO_2 substrate is used as a template to induce the lateral confinement of the Au nanoparticles recurring to grazing angle deposition in the same UHV system. The deposition is performed by thermal evaporation from an alumina crucible at an angle of 80^o from the surface normal while the constant flux is monitored by means of a quartz microbalance until a deposited gold thickness of 10nm is reached (thickness value evaluated with respect to a flat compact film). The spatial distribution of the metal atoms onto the corrugated template is now modulated by shadowing effects so that higher local fluxes are recorded at the top of the illuminated ridges where preferential nucleation of metal cluster takes place; on the contrary, the glass regions in the troughs of the ripple not illuminated by the atom beam remain uncovered by gold. This leads to the formation and agglomeration of metal clusters which coalesce until connected Au nanowires are formed as the thickness of the metal film increases. Along the direction orthogonal to the ripple axis, the nanowires are instead well disconnected. In Figure 1 the AFM images of the surface show very clearly the presence of a morphological anisotropy on a micrometer lateral scale. The morphological anisotropy is reflected in the optical response of the nanowire arrays, as revealed by far field optical transmission spectra of the samples when illuminated with different linear polarized light. The measurements reveal the excitation of localized plasmon resonances when light is polarized orthogonally to the nanowires.[10]

3.2 Measurement

The Mueller matrix imager is based on a polarizer, two waveplates and two ferroelectric liquid crystals (FLC) in the PSG, and similarly (but in reverse order) in the PSA.[22–24] The Mueller matrix images presented in this work is recored with an illumination wavelength of 980 nm. The instrument is, however, designed to be spectroscopic in the wavelength range of 800-1700 nm. Figure 2 shows a sketch of the Mueller matrix imaging system. The instrument were equipped with a 8 bit silicon CMOS camera from Edmund optics. The FLCs and camera are controlled and synchronized through LabView software, while post processing is done in Matlab.

4. RESULTS AND DISCUSSION

A full Mueller matrix image of the plasmonic polarizer, consisting of aligned Au nanoparticles on a patterned SiO_2 surface, is presented in Figure 3. The image is recorded at normal incidence and shows an area of about 1×1 cm^2. An imperfect sample was deliberately chosen, to demonstrate the advantages of Mueller matrix imaging as an

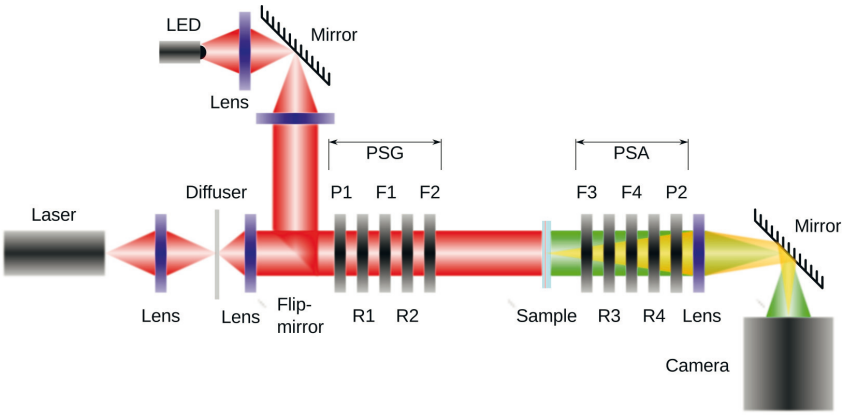

Figure 2. (Color online) The PSG and PSA consist of the modulating components ferroelectric liquid crystals (F1-4), zero order waveplates (R1-4) and polarizers (P1-2). As illumination either a 980 nm diode laser or a 1300 nm LED source is used, in both cases the source is collimated before entering the PSG. The sample is placed in the image plane of the camera optics.

inhomogeneity and imperfection discovery tool. The surface is clearly imperfect, with small scratches and spots with pollution scattered across the surface. The spatial resolution of the Mueller matrix image allows extracting the polarizing properties of the sample at the undamaged areas. In addition, the microscopic structure of the Au nanoparticles gradually changes over the surface, leading to different optical properties. A typical polarimetric measurement without spatial resolution would result in an average measurement over a relatively large area of the sample (depending on spot size), including damaged parts, leading to depolarization and errors.

In the Mueller matrix image the sample is aligned approximately with the ripples parallel to the vertical axis (y-axis). Since the Au dots are aligned along ripples, the surface will have a higher absorption for light polarized along this direction than normal to the ripples, leading to positive values in element m_{12} and m_{21}. The

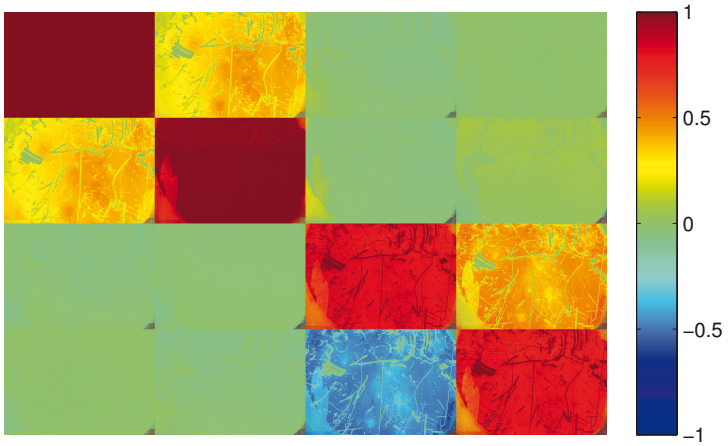

Figure 3. (Color online) Normal incidence transmission Mueller matrix image of aligned Au nanoparticles deposited on a patterned SiO_2 surface. All elements have been normalized by M_{11}

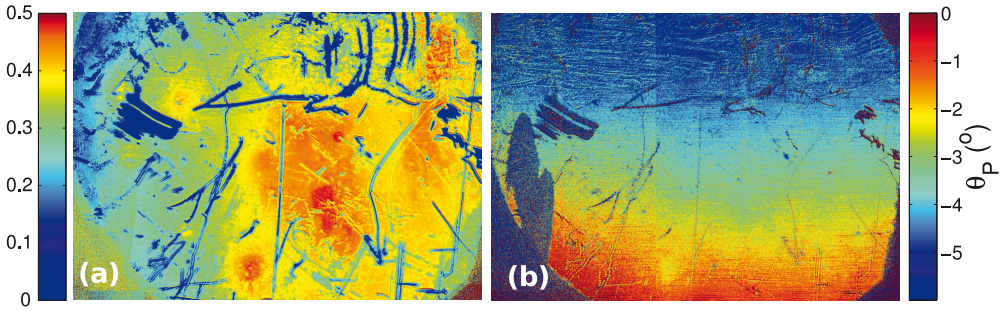

Figure 4. (Color online) Linear polarizance (a) and orientation of polarizance (b) found from decomposition of the Mueller matrix image in figure 3

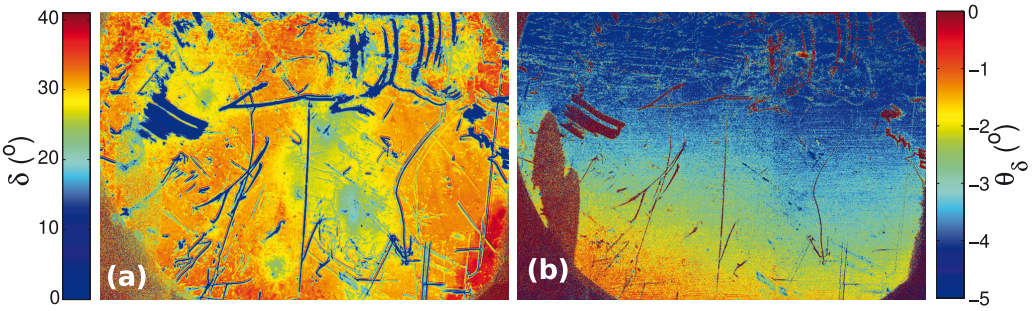

Figure 5. (Color online) Retardance found from decomposition of the Mueller matrix image in figure 3

four elements in the bottom right of the matrix show that the sample is retarding, revealing a difference in the effective refractive index parallel and normal to the ripples. The Mueller matrix is close to being block-diagonal, with the 2×2 upper right and 2×2 lower left elements being close to zero. This indicates that the principal axes of the effective dielectric function of the sample approximately corresponds to the experimental coordinate system. By decomposing the Mueller matrix the exact eigenpolarization states can be found. An image of the linear polarizance (P) is presented in Figure 4 (a) together with the orientation of the transmission axis (Figure 4 (b)). Similarly the retardance and its orientation is presented in Figure 5, the intensity (M_{11}) image is presented in Figure 6 (a) and the polarization index in Figure 6 (b).

By decomposing the Mueller matrix, different types of defects in the surface can be observed. Shallow scratches that have removed the Au nanoparticles, but not damaged the surface bellow, is clearly visible in the polarizance (Figure 4) and retardance (Figure 5) images. In these areas the surface have lost its anisotropic properties, and does not work as a polarizer. The area without nanostructures shows no retardance, indicating that there is no significant strain in the glass substrate. Deeper scratches can be seen from the depolarization index images, such as the blue part in the left of Figure 6 (b), which is a deep scratch made to mark the direction of the ripples. In the upper part of the depolarization index image, an inhomogeneous area with some depolarization can be observed. This part still have intact nanostructures on the front surface, the depolarization is caused by scratches on the backside of the glass substrate. From the intensity image (M_{11}, Figure 6 (a)) one can see some spots of contamination (probably glue left from sample handling) on the backside of the sample. These spots mainly change the total intensity,but not the polarization, and is not visible in the normalized Mueller elements.

From the linear polarizance image presented in Figure 4, we see that the undamaged parts of the surface behaves as a partial polarizer, with a polarizance gradually varying between 0.5 to 0.3. The direction of the

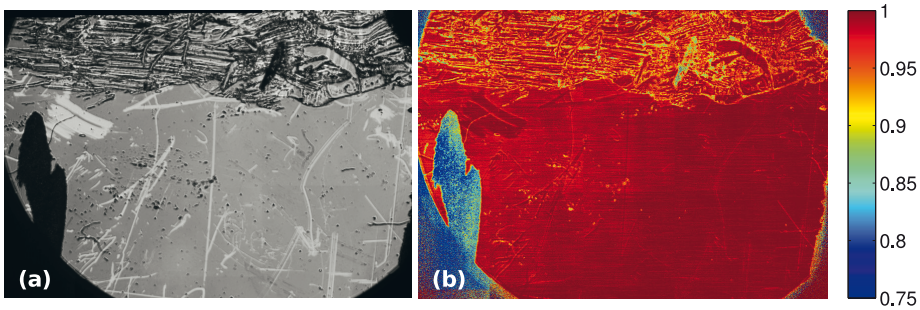

Figure 6. (Color online) Intensity image (a) and degree of polarization index image calculated from the Mueller matrix in Figure 3

transmission axis varies by as much as 5° from the top to the bottom of the sample, and does not seem to be directly connected to values of the polarizance. The polarizing properties of the surface is attributed to the Au nanoparticles being aligned along the direction of the ripples, creating long partially connected chains. The structure will then have optical properties similar to a metal for an electric field parallel to the ripples, resulting in high absorption. The various values of polarizance observed is likely to be caused by an unevenly distribution of Au on the surface. From the intensity image (proportional to M_{11}) it is observed that the areas with high polarizance also have the highest intensity. This indicates that there is probably too much Au deposited on the areas with low polarizance, making the nanoparticles partially connected also in the direction normal to the ripples.

The retardance image (Figure 5) shows that there is less retardance in the areas with high polarizance. If the structure is represented by an effective dielectric function, this means that the difference in refractive index times the thickness ($\Delta n \cdot d$) is less in these areas compared to the areas with a lower polarizance. The orientation of the slow axis of the retardance is approximatly equal to the orientation of the transmission axis for the polarizance, meaning that the real and imaginary part of the index of refraction share the same principal coordinate system.

5. CONCLUSION

A spatially inhomogeneous plasmonic partial polarizer have been characterized by near infra red Mueller matrix imaging. The plasmonic polarizer was prepared by evaporating Au on a rippled SiO_2 substrate at grazing incidence, resulting in nanoparticles aligned along the ripple ridges. The sample was found to have different kinds of defects, such as scratches and contaminations, and these defects could be distinguished from the Mueller matrix image. The spatial resolution allowed to find the polarization altering properties of the nanostructure at the undamaged areas of the sample. The polarizability of the undamaged areas was found to vary from 0.3 to 0.5, and was attributed to a variation in the difference in the the nanoparticle connectivity along and orthogonal to the ripples. From the total transmission image it is concluded that the areas with low polarizability probably correspond to ares with too much Au, resulting in some contact between particles across the ripples.

Acknowledgments

This work has been partly supported by Fondazione Carige, by MAE under program Italia-Polonia, by MIUR under Project No.PRIN 2008J858Y7, and by ENEA under contract MSE.

REFERENCES

[1] Tompkins, H. and Haber, E. A., [*Handbook of Ellipsometry (Materials Science and Process Technology)*], William Andrew (Jan. 2006).

[2] Ossikovski, R., De Martino, A., and Guyot, S., "Forward and reverse product decompositions of depolarizing Mueller matrices," *Optics letters* **32**(6), 689–691 (2007).

[3] Ghosh, N., Wood, M. F. G., Li, S.-h., Weisel, R. D., Wilson, B. C., Li, R.-K., and Vitkin, I. A., "Mueller matrix decomposition for polarized light assessment of biological tissues.," *Journal of biophotonics* **2**, 145–56 (Mar. 2009).

[4] Lu, S. and Chipman, R., "Interpretation of Mueller matrices based on polar decomposition," *Journal of the Optical Society of America A* **13**(5), 1106–1113 (1996).

[5] Ossikovski, R., "Analysis of depolarizing Mueller matrices through a symmetric decomposition.," *Journal of the Optical Society of America. A, Optics, image science, and vision* **26**, 1109–18 (May 2009).

[6] Ossikovski, R., Anastasiadou, M., Hatit, S., Garcia-Caurel, E., and De Martino, A., "Depolarizing Mueller matrices: how to decompose them?," *Physica Status Solidi (A)* **205**(4), 720–727 (2008).

[7] Compain, E., Poirier, S., and Drevillon, B., "General and self-consistent method for the calibration of polarization modulators, polarimeters, and mueller-matrix ellipsometers.," *Applied optics* **38**, 3490–502 (June 1999).

[8] Camelio, S., Babonneau, D., Lantiat, D., Simonot, L., and Pailloux, F., "Anisotropic optical properties of silver nanoparticle arrays on rippled dielectric surfaces produced by low-energy ion erosion," *Physical Review B* **80**, 1–10 (Oct. 2009).

[9] Ranjan, M., Oates, T. W. H., Facsko, S., and Möller, W., "Optical properties of silver nanowire arrays with 35 nm periodicity.," *Optics letters* **35**, 2576–8 (Aug. 2010).

[10] Toma, a., Chiappe, D., Massabo, D., Boragno, C., and Buatier de Mongeot, F., "Self-organized metal nanowire arrays with tunable optical anisotropy," *Applied Physics Letters* **93**(16), 163104 (2008).

[11] Toma, A., Chiappe, D., Boragno, C., and Buatier De Mongeot, F., "Self-organized ion-beam synthesis of nanowires with broadband plasmonic functionality," in [*Physical Review B*], **81** (Apr. 2010).

[12] Oates, T. W. H., Keller, A., Facsko, S., and Mücklich, A., "Aligned Silver Nanoparticles on Rippled Silicon Templates Exhibiting Anisotropic Plasmon Absorption," *Plasmonics* **2**, 47–50 (Mar. 2007).

[13] Tyo, J. S., "Design of optimal polarimeters: Maximization of signal-to-noise ratio and minimization of systematic error," *Appl. Opt* **41**(4), 619–630 (2002).

[14] Stabo-Eeg, F., Kildemo, M., Nerbø, I., and Lindgren, M., "Well-conditioned multiple laser Mueller matrix ellipsometer," *Optical Engineering* **47**(July), 073604 (2008).

[15] Letnes, P., Nerbø, I., Aas, L., and Ellingsen, P., "Fast and optimal broad-band Stokes/Mueller polarimeter design by the use of a genetic algorithm," *Optics express* **18**(22), 23095–23103 (2010).

[16] Gil, J. J. and Bernabeu, E., "Depolarization and polarization indices of an optical system," *Optica Acta* **33**(2), 185–189 (1986).

[17] Manhas, S., Swami, M., Buddhiwant, P., Ghosh, N., Gupta, P., and Singh, K., "Mueller matrix approach for determination of optical rotation in chiral turbid media in backscattering geometry," *Opt. Express* **14**, 190–202 (2006).

[18] Valbusa, U., "Nanostructuring by ion beam," *Materials Science and Engineering: C* **23**, 201–209 (Jan. 2003).

[19] Chiappe, D., Toma, a., Zhang, Z., Boragno, C., and Buatier de Mongeot, F., "Amplified nanopatterning by self-organized shadow mask ion lithography," *Applied Physics Letters* **97**(5), 053102 (2010).

[20] Toma, A., Buatier de Mongeot, F., Buzio, R., Firpo, G., Bhattacharyya, S., Boragno, C., and Valbusa, U., "Ion beam erosion of amorphous materials: evolution of surface morphology," *Nuclear Instruments and Methods in Physics Research Section B: Beam Interactions with Materials and Atoms* **230**, 551–554 (Apr. 2005).

[21] de Mongeot, F., Toma, A., Molle, A., Lizzit, S., Petaccia, L., and Baraldi, A., "Carbon Monoxide Dissociation on Rh Nanopyramids," *Physical Review Letters* **97**, 56103 (Aug. 2006).

[22] Aas, L. S., Ellingsen, P., and Kildemo, M., "Dynamic Response of a fast near infra-red Mueller matrix ellipsometer," *Journal of Modern Optics* **57**(17), 1603–1610 (2010).

[23] Aas, L., Ellingsen, P., and Kildemo, M., "Near infra-red Mueller matrix imaging system and application to retardance imaging of strain," *Thin Solid Films* **519**, 2737–2741 (Dec. 2010).

[24] Ladstein, J., Kildemo, M., Svendsen, G., Nerbø, I., and Stabo-Eeg, F., "Characterisation of liquid crystals for broadband optimal design ofMueller matrix ellipsometers," in [*Proceedings of SPIE*], **6587**, 65870D, Spie (2007).

P. G. Ellingsen, M. B. Lilledahl, L. M. S. Aas, C. d. L. Davies, and M. Kildemo, Quantitative characterization of articular cartilage using Mueller matrix imaging and multiphoton microscopy, J. Biomed. Opt. **16**, 116002 (2011)

Paper 7

Journal of Biomedical Optics 16(11), 116002 (November 2011)

Quantitative characterization of articular cartilage using Mueller matrix imaging and multiphoton microscopy

Pål Gunnar Ellingsen, Magnus Borstad Lilledahl, Lars Martin Sandvik Aas, Catharina de Lange Davies, and Morten Kildemo
Norwegian University of Science and Technology, Department of Physics, Faculty of Natural Sciences and Technology,
Institutt for Fysikk, 7491 Trondheim, Norway

Abstract. The collagen meshwork in articular cartilage of chicken knee is characterized using Mueller matrix imaging and multiphoton microscopy. Direction and degree of dispersion of the collagen fibers in the superficial layer are found using a Fourier transform image-analysis technique of the second-harmonic generated image. Mueller matrix images are used to acquire structural data from the intermediate layer of articular cartilage where the collagen fibers are too small to be resolved by optical microscopy, providing a powerful multimodal measurement technique. Furthermore, we show that Mueller matrix imaging provides more information about the tissue compared to standard polarization microscopy. The combination of these techniques can find use in improved diagnosis of diseases in articular cartilage, improved histopathology, and additional information for accurate biomechanical modeling of cartilage. [DOI: 10.1117/1.3643721]

Keywords: Mueller matrix imaging; multiphoton microscopy; collagen; cartilage.

Paper 11303R received Jan. 15, 2011; revised manuscript received Aug. 18, 2011; accepted for publication Sep. 6, 2011; published online Oct. 26, 2011.

1 Introduction

Articular cartilage covers and protects the bones in joints, and its integrity is essential for normal function. It imparts two important properties to a joint. First, it provides a low-friction surface for smooth articulation of the joint; second, it provides a cushioning layer to distribute loads and protect the underlying bone. The structure of articular cartilage is typically divided into three distinct morphological zones: (i) The superficial layer with a dense collagen network and the collagen fibers oriented primarily tangential to the articulating surface, (ii) the intermediate layer, where the fibers are more randomly distributed, and (iii) the radial layer, where the fibers are oriented perpendicular to the bone surface. The collagen fibers are cross-linked with proteoglycans in a fluid-saturated gel of glycosaminoglycans and proteoglycans. Scattered throughout the cartilage are chondrocytes that reside in lacunae and are responsible for the formation of new cartilage.[1]

Osteoarthritis is a disease in articular cartilage symptomized by pain and reduced joint function, affected by a variety of factors (genetic, traumatic, age, excessive loading).[2] It is the leading cause of disability in the U.S. and will likely see an increased incidence in the future due to an aging and more obese population.[3] Osteoarthritis is characterized by structural changes in the cartilage, accompanied by a loss of proper function. The loss of function will lead to changed loading conditions in the knee and, therefore, further changes in the microscopic structure. In order to predict the outcome of this biological cascade, it is necessary to have methods to characterize the current tissue structure. Osteoarthritis is usually diagnosed based on clinical findings, sometimes with the addition of radiographic imaging. However, in a significant fraction of symptomatic patients, no radiographic changes are found.[4] Magnetic resonance imaging may be used for further stratification, but the association between clinical symptoms and findings from images is not always strong.[5] Therefore, a more detailed investigation using novel imaging techniques, is necessary to enhance diagnosis.

Bright-field light microscopy of haematoxylin-eosin–stained sections is the standard method to assess the microscopic structure of cartilage, even though it is not possible to see the structure of the collagen network. Polarization microscopy is sometimes used but can only provide qualitative information on the direction of collagen fibers due to the complex nature of the polarization properties of tissue. Novel methods to study the microscopic structure of cartilage will provide more details on the current pathological status and perhaps differentiate between conditions that cannot be distinguished with standard techniques.

Multiphoton microscopy (MPM) is a nonlinear optical process used to acquire images of biological specimens.[6] Because of the nonlinearity of the signals, the technique is intrinsically confocal (no need for confocal optics), and many biological molecules exhibit specific intrinsic nonlinear signatures such that no staining is required. The second-harmonic generation (SHG) signal can be used to image the collagen type II fibers present in cartilage.[7,8] *In vivo* imaging is possible and yields high-resolution, three dimensional images.[9] *In vivo* MPM would be a valuable complementary technique to standard arthroscopy. Methods have been developed to generate quantitative measures of the structure of the collagen fabric[10] and its optical properties.[11] The drawback of MPM is that high-resolution imaging of macroscopic volumes is time consuming. Furthermore, in the intermediate and radial layers, the collagen fibers are below the resolution limit of optical microscopy, such that individual fibers cannot be resolved.

Address all correspondence to: Morten Kildemo, Norwegian University of a Science and Technology, Department of Physics, Faculty of Natural Sciences and Technology, 7491 Trondheim, Norway; Tel: +0047 73593211; E-mail: morten.kildemo@ntnu.no.

1083-3668/2011/16(11)/116002/6/$25.00 © 2011 SPIE

Mueller matrix imaging (MMI) provides a complementary technique to MPM and extracts the full Mueller matrix for every pixel in the image of a sample.[12] Because the resolution is adjustable (but usually worse than MPM by a factor of around 10), and camera-based imaging is used instead of point scanning, larger areas are scanned faster compared to MPM. Because MMI also is an optical technique, it cannot resolve the small collagen fibers in the middle layer. However, the advantage of MMI is that it is based on the rich polarization information contained in the full Mueller matrix, such that the directionality of the fibers may be derived, as well as the optical rotation and depolarization of the sample, by using forward polar decomposition.[13,14] The use of decomposed Mueller matrix measurements to characterize tissue phantoms and biological samples has been described,[15,16] but to our knowledge never on samples of cartilage. Compared to other polarimetric imaging systems that only measure some of the components of the Mueller matrix[17–19] and require significant prior knowledge of the sample and the desired measurements, the Mueller matrix imaging system is much more flexible, enabling the characterization of more complex and unexplored samples with the possibility to fully characterize the polarization properties of the sample. Here, we show that the combination of MPM and MMI provide more detailed information about the articular cartilage structure compared to conventional methods and potentially a better understanding of the progression of osteoarthritis.

2 Materials and Methods

2.1 *Materials*

The medial femoral condyle of chicken cartilage ($n = 2$) was cut in 100-μm-thick sections to a depth of 2 mm using a vibratome (Leica VT-1000). After sectioning, the samples were transferred to microscope slides and a cover glass placed on top. The edges were sealed with Vaseline to avoid dehydration. Sections were cut in the transversal plane. The sections were kept at 4°C between measurements.

2.2 *Multiphoton Microscopy*

The MPM images where acquired using a commercial system (Zeiss LSM 510), equipped with a Ti:sapphire laser pumped by a 5-W solid state laser (Coherent Mira and Verdi, respectively). The Ti:sapphire laser was tuned to 800 nm for excitation of the SHG signal. A dichroic short-pass filter at 650 nm was used to collect the backscattered light. A second dichroic at 475 nm and a bandpass filter at 390–425 nm were used to separate the SHG from the fluorescence. All images were acquired in the epi configuration.

Images were acquired with a 10×, 0.6 numerical aperture (NA) objective. For samples larger than the field of view, several images were juxtaposed automatically using the microscopy control system. Images were acquired at four to eight different depths, with an interval of 10 μm, depending on the quality of the signal in the deeper sections.

On the basis of an image-analysis algorithm described in detail elsewhere,[10] we derived the primary direction and anisotropy of the fibers at every pixel in the image. Briefly, the algorithm calculates the two-dimensional discrete Fourier transform of a small subframe around a given pixel. Typically, the strongest Fourier components will tend to lie on a line perpendicular to the fibers in the image. The direction of this line was found by minimizing the sum of angles, weighted by the Fourier power spectrum relative to this line. The anisotropy is extracted as a measure of how close the strongest frequency components are clustered around this line.

2.3 *Mueller Matrix Imaging*

The near-infrared Mueller matrix imaging (NIR MMI) system used here is described in greater detail elsewhere.[12] Note that the light source used here is the 980-nm laser diode and that the numerical aperture of the system is 0.04. It uses two ferroelectric liquid crystals (FLCs) together with a polarizer and two wave plates to generate four orthogonal Stokes vectors in what is know as a polarization-state generator (PSG), which then are used to probe the sample. After passing through the sample, the resulting polarization-state is analyzed by a polarization state analyzer (PSA), consisting of the same components as the PSG, in reverse order. Sixteen intensity images are acquired using different settings of the PSG and PSA. The Muller matrix $\mathbf{M}$ is then calculated from the configurations of the PSG and PSA using the eigenvalue calibration method.[20] Repeating this for every pixel in the images results in a Mueller matrix image, $\mathbf{M}_{\mathrm{im}}$. The Mueller matrix is normalized, meaning that all of the elements in the matrix is divided by the M_{11} element.

The measured $\mathbf{M}$ is decomposed into depolarization, ($\mathbf{M}_{\Delta}$), retardation, ($\mathbf{M}_{\mathrm{R}}$), and diattenuation, ($\mathbf{M}_{\mathrm{D}}$), matrices using forward polar decomposition, $\mathbf{M} = \mathbf{M}_{\Delta}\mathbf{M}_{\mathrm{R}}\mathbf{M}_{\mathrm{D}}$, first described by Lu and Chipman[13] and applied by Manhas et al.[14] to tissue characterization.

From $\mathbf{M}_{\mathrm{R}}$, it is further possible to find the linear retardance, direction of the slow axis (perpendicular to the fast axis), and the optical rotation (see Manhas et al.[14]). We assume that the collagen fibers can be modeled using the Bruggeman effective medium theory,[21] and thus assign the slow optical axis to the long axis of the fibers.

3 Results

3.1 *Multiphoton Microscopy*

SHG images of the superficial layer show a distinct collagen structure, which is illustrated in Fig. 1(a). By employing the direction analysis method described in Sec. 2.2, we derived the primary direction and degree of anisotropy of the fibers, which is shown in Figure 1(b). The direction is coded according to color using the provided legend and the anisotropy is mapped to the intensity of the color. Figure 2(a) shows a sample where both the superficial and intermediate layers can be seen. The center region, which belongs to the superficial zone, exhibits clear fibrillar structure, whereas in the intermediate layer, shown in the lower right part of Fig. 2(a), no collagen fibers can be discerned. Only the lacunae can be seen as dark voids, embedded in a smooth SHG signal. Figure 2(b) shows that the analysis picks up the direction in the superficial region but that in the intermediate layer where no structure can be discerned, the anisotropy is very low, corresponding to low intensity in the color image.

3.2 *Mueller Matrix Imaging*

MMI images were acquired from the same samples as imaged with MPM. The MMI images were first Cloude filtered[22] and

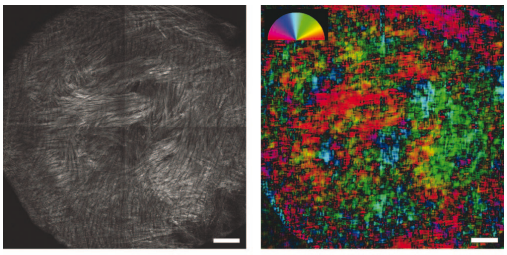

(a) (b)

Fig. 1 (a) SHG intensity image of a transverse section of cartilage in the superficial layer (100 μm below the surface), where the collagen fibers are clearly visible. This image is the result of four images tiled together. (b) Result of the directional analysis. The calculated direction of the fibers is color coded according to the semicircle legend. The intensity of the color has been scaled to the calculated anisotropy value. Scale bar is 200 μm.

then decomposed using the forward polar decomposition described in Sec. 2.3. An example of the full Mueller matrix for a cartilage sample is illustrated in Fig. 3. The M_{11} element has been substituted by the intensity image, because this element would be equal to 1 as a result of the normalization. The values of the diattenuation matrix $\mathbf{M}_D$ were found to be very small and are not included here.

After the decomposition, the direction of the slow axis is found from the retardance matrix $\mathbf{M}_R$.[14] The corresponding image of the directions is illustrated in Fig. 4. Because the long axis of the collagen fibers corresponds to the optical slow axis, the directional image shows the collagen fiber direction and can be compared to the MPM image of the same sample, as shown in Fig. 5.

The forward polar decomposition enables in addition to the direction of the slow axis, the calculation of the amount of double refraction in the sample known as the linear retardance (which is seen in Fig. 6), the amount of left or right circular polarization induced by the sample, known as the optical rotation (shown in Fig. 7), and the depolarization index (as seen in Fig. 8). The

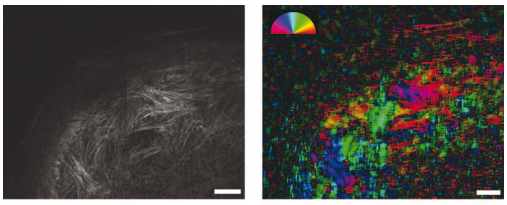

(a) (b)

Fig. 2 (a) SHG intensity image of a transverse section of cartilage from slightly below the superficial layer (500 μm below the surface). The central part of the image belongs to the superficial region, and here, the fibers are clearly visible. The lower right part belongs to the intermediate layer. No clear structure of fibers can be seen in this region, only the lacunae are distinguishable as dark voids. (b) Result of directional analysis. The calculated direction of the fibers is color coded according to the semicircle legend. The intensity of the color has been scaled by the calculated anisotropy value. In the intermediate layer, only a weak random direction is picked up. Scale bar is 200 μm.

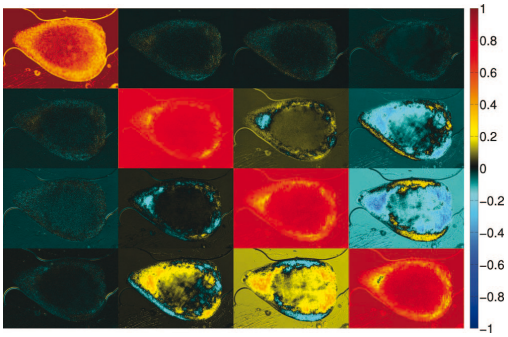

Fig. 3 Full Cloude-filtered Mueller matrix image for a sample of cartilage, from a transversal section at a depth of 500 μm, with the intensity image overlaid the M_{11} element. The central dark area in M_{11} is the intermediate layer, and the surrounding bright area is the superficial layer.

depolarization index shows how much of the incoming polarized light is converted into partially polarized light.

The intermediate zone of the cartilage (center of Figs. 4 and 6) exhibits more variation and features in the MMI images compared to what can be seen in the MPM images. In this intermediate zone, the direction and retardance images show regions with differing structure.

4 Discussion

The Mueller matrix was decomposed into three polarization properties of which only the retardation and depolarization were used directly in this study. The retardance (circular, linear, and direction of fast axis) will, in terms of effective medium theory, yield results from features smaller than the resolution in the image. The latter property is useful, beacuse it can be used to characterize collagen fibers from the intermediate and radial zone of the cartilage, where the collagen fibrils are below the resolution limit of MPM.

Because the collagen fibers have a higher refractive index than the surrounding medium,[23] they will have the slow axis

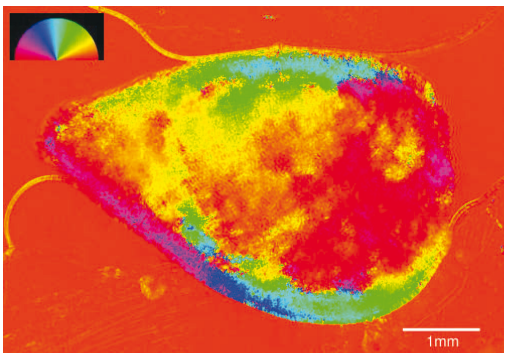

Fig. 4 Visualization of the direction of the slow axis found from $\mathbf{M}_R$.

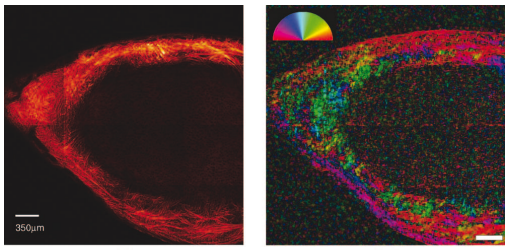

Fig. 5 (a) SHG images from the same area as the MMI images and (b) calculated directions of image in (a).

along the long axis. The difference in the refractive index of the slow and fast axes can be calculated using the simple linear dispersion relation for a birefringent medium

$$\Delta n = \frac{\lambda\delta}{2\pi L},$$

where λ is the wavelength (here, 980 nm), δ the linear retardance (in radians), and L the thickness of the sample (here, 100 μm). Using a representative value of $\delta = 50$ deg for the edges of the sample, as seen in Fig. 6, and $\delta = 15$ deg for the intermediate region, results in an apparent birefringence $\Delta n = 1.4 \times 10^{-3}$ for the edges, similar to previously reported values,[24] and $\Delta n = 0.4 \times 10^{-3}$ from intermediate regions. As Fig 6 shows, there are large differences in the linear retardance across the sample, resulting in large differences in Δn, such that care should be taken when reporting birefringence measurements of collagen in turbid media.

The slow axis found from the decomposed Mueller matrix is the projection of the three-dimensional slow axis into the imaging plane. In addition, since directions found from the Mueller matrix measurement are from a volume, the directions seen in Fig. 4, will be an average of the collagen fibers through the sample as opposed to the MPM images, which are acquired at a certain depth (Fig. 5). Even when taking the latter into consideration, the directions in the sample correspond well to the direction in the corresponding MPM image, indicating that the direction of the collagen fibers are mostly homogeneous through the sections. However, when characterizing the samples using MPM some variation in the direction with respect to the depth was observed, which would result in a intermediate direction in the MMI image and correspondingly different calculated values for the directional parameter.

In the intermediate layer (center of Fig. 6), where the MPM images cannot resolve individual collagen fibrils that are smaller than the imaging resolution limit, the MMI directional image shows structure variations and, thus, the ability to characterize the subresolution structures in this area of cartilage.

The collagen fibers in the cartilage scatter the incoming light, contributing to the depolarization (see Fig. 8). The depolarization will increase with the density and size of the collagen fibers, and could thus be useful for extracting more information about the collagen structure. By comparing the depolarization image (shown in Fig. 8) to the retardance image (shown in Fig. 6), one can see that the areas with a high depolarization index are mostly the same areas as the ones with high retardance, indicating a higher concentration or larger size of the collagen fibers, resulting in the higher depolarization. The reason the retardance is small in some areas of high depolarization could be attributed

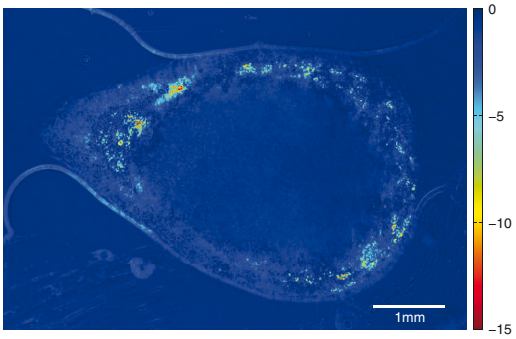

Fig. 7 Optical rotation in degrees.

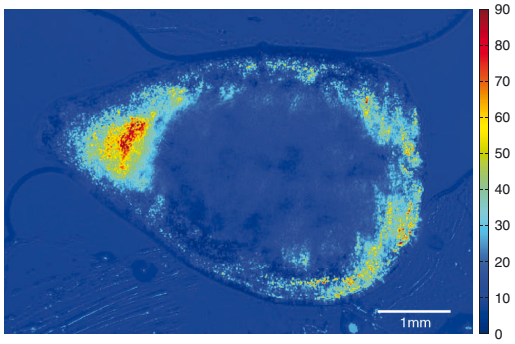

Fig. 6 Retardance image, showing the absolute value of the linear retardance. Color bar is in degrees.

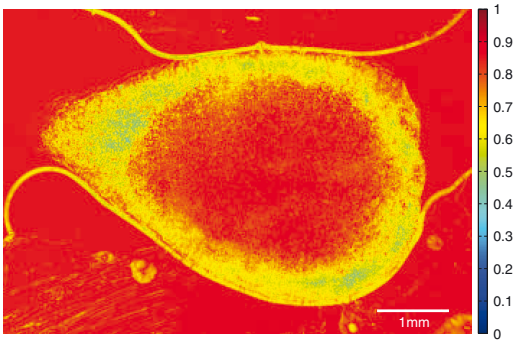

Fig. 8 Depolarization index, where 1 is fully polarized and 0 fully depolarized.

Table 1 Specific rotation for hyaluronic acid (HA), keratane sulfate (KS), and chondroitin sulfate (CS) in a water solution (Ref. 28). In addition, the specific rotation of collagen in 0.5M $CaCl_2$ is given (Ref. 27). The temperature at which the specific rotation is measured is given, when given in the source. The concentration of the chemical compounds in human femoral head cartilage from ages 3 to 19 are also given (Ref. 29). Total wet volume of tissue per unit weight of collagen (d_c^{-1}) is 4.96 ± 0.041 ml/g (Ref. 29).

Chemical substance	Specific rotation $[\alpha]_{589}$	Wet tissue weight percentage w
HA	−68.2 deg at 27°C	0.16
KS	4.5 deg	0.83 ± 0.095
CS type A	−25 deg	2.86 ± 0.10
Collagen	−360 deg at 8°C	18.5 ± 1.4

to the collagen fibers in that area being aligned at an angle to the image plane, reducing the measured linear retardance.

An interesting observation is that the optical rotation (see Fig. 7) appears large compared to commonly reported values from solution. However, such large values may be justified by considering the triple helix[25] structure of the collagen together with proteoglycans. The left-handed collagen helix will induce optical rotation to the incoming polarized light. The amount of induced optical rotation is dependent on the orientation of the collagen fiber, with little contribution from out-of-plane fibers. Cartilage consists of proteoglycans, which contain[26] hyaluronic acid (HA), keratane sulfate (KS), and chondroitin sulfate (CS), all of which are optical active. The optical activity of these components are given in Table 1, together with their concentrations in femoral head cartilage. On the basis of these values, the expected optical rotation from a 100-μm-thick solution of cartilage is calculated using

$$\phi = [\alpha_c]_{583}\, Ld, \tag{1}$$

where ϕ is the expected optical rotation, $[\alpha_c]_{583}$ the specific rotation in Table 1 for the given compound, L the thickness of the sample in decimeter (here, 10^{-3} dm), and d the density in (grams per milliliter), given here by $d = d_c w_s / w_c$, where d_c is the collagen density, w_s the substance weight percentage, and w_c the collagen weight percentage. Using (1) and values from Table 1 gives an optical rotation due to proteoglycans of -8.6×10^{-4} deg, and due to collagen of -0.07 deg at 583 nm, assuming that a 0.5 M $CaCl_2$ solution has the same optical rotation as water. The proteoglycan contribution to the optical rotation is thus negligible. The measurements of the optical rotation here were done at 980 nm, which is expected to give lower optical rotation due to the two-term Drude equation.[27] The optical rotation of the collagen fibers depends on their orientation. Hence, one would expect the ordered collagen fibers in the cartilage to have a higher optical rotation compared to randomly ordered collagen fibers in solution. This corresponds well to the observed values of optical rotation. Figure 7 shows structural variation across the image plane, believed to be caused by changes in the fibril direction relative to the image plane. However the variation in signal across the sample is different compared to the retardance and depolarization images, indicating that additional information is stored in this image.

The comparison between the direction found from the MPM images and from the MMI images showed that they overall agreed quite well. Discrepancies could be seen toward the edges and at some isolated interior regions. Toward the edges, the Fourier analysis technique used in the MPM analysis will exhibit some artifacts as it picks up the edge of the sample as a strong frequency component (interpreted as a fiber) running tangential to the edge. If the fibers run perpendicularly to the edge, then this will be picked up by MMI and large discrepancies are expected. Other sources of discrepancies could be due to small collagen fibers not resolved by MPM and/or changes in the collagen direction through the sample (MPM could not image completely through the thickness of the sample). The tiling of the microscope images to create images of larger regions is evident in Figs. 1(a) and 2(a), which is due to uneven excitation over the imaging plane, probably due to movement of the beam at the back aperture of the objective. However, it appears that the transition between images is quite well filtered out during image analysis.

MMI will be unable to differentiate between collagen fibers running parallel to the sample surface and fibers that are at an angle to the surface. One way to distinguish these two cases would be to rotate the sample in the beam such that the Mueller matrix is extracted with the collagen fibers rotated at different angles to the incoming beams. By having enough different directions, it should be possible to extract a three-dimensional average direction of the fibers.

The structure of the collagen fibers as seen in the MPM images could be useful in the diagnosis and assessment of osteoarthritis. In this study, the MMI was performed in transmission mode; however the technique can also be applied in reflection mode, which would make it applicable for *in vivo* use. MMI can also be used in conjunction with high NA objectives to achieve even higher resolution images of the polarization properties. In the current setting, however, it is perhaps its ability to image large regions relatively fast that is its main advantage. Histopathology is another field where MMI could be very valuable. Its ability to generate more detailed polarization properties could make it valuable for better assessing the structure of diseased cartilage in histopathology studies. For example, the depolarization index and differences in linear and circular retardation are not picked up by regular polarization microscopes. The detailed structure that is possible to extract with these two imaging techniques could also have important applications in the study of the biomechanics of cartilage.

5 Conclusion

By applying an image-analysis technique based on the Fourier transform on the MPM images, we were able to quantify the direction of the fibers in the superficial layer. Combining this with Mueller matrix imaging proved to be a powerful combination, allowing for the extraction of directional parameters from the intermediate layer. The structure in the intermediate layer is usually assumed to be isotropic, but the retardance images clearly show that there is structural inhomogeneities in the connective tissue in these areas as well. In conclusion, the combination of

MMI and MPM provides a powerful technique in the study of osteoarthritis and other cartilage diseases.

Acknowledgments

We acknowledge Linh Hoang, at the Department of pathology, Children and Women's Health at NTNU, for help in preparing the cartilage samples.

References

1. W. C. Mow, W. Y. Gu, and F. H. Chen, *Structure and Function of Articular cartilage and Meniscus*, 3rd ed., pp. 181–258, Lippincott, Williams and Wilkins, Philadelphia (2005).
2. D. J. Hunter and D. T. Felson, "Osteoarthritis," *BMJ* **332**(7542), 639–642 (2006).
3. "National health interview survey," Tech. Rep., Center for Disease Control and Prevention (2009).
4. M. B. Kinds, P. M. J. Welsing, E. P. Vignon, J. W. J. Bijlsma, M. A. Viergever, A. C. A. Marijnissen, and F. P. J. G. Lafeber, "A systematic review of the association between radiographic and clinical osteoarthritis of hip and knee," *Osteoarth Cartilage* **19**(7), 768–778 (2011).
5. E. Yusuf, M. C. Kortekaas, I. Watt, T. W. J. Huizinga, and M. Kloppenburg, "Do knee abnormalities visualised on mri explain knee pain in knee osteoarthritis? a systematic review," *Ann. Rheum. Dis.* **70**(1), 60–67 (2011).
6. W. Denk, "Two-photon laser scanning fluorescence microscopy," *Science* **248**(4951), 73–76 (1990).
7. A. T. Yeh, M. J. Hammer-Wilson, D. C. Van Sickle, H. P. Benton, A. Zoumi, B. J. Tromberg, and G. M. Peavy, "Nonlinear optical microscopy of articular cartilage," *Osteoarth Cartilage* **13**(4), 345–352 (2005).
8. J. C. Mansfield, C. P. Winlove, J. Moger, and S. J. Matcher, "Collagen fiber arrangement in normal and diseased cartilage studied by polarization sensitive nonlinear microscopy," *J. Biomed. Opt.* **13**(4), 044020 (2008).
9. M. J. Levene, D. A. Dombeck, K. A. Kasischke, R. P. Molloy, and W. W. Webb, "*In vivo* multiphoton microscopy of deep brain tissue," *J. Neurophysiol.* **91**(4), 1908–1912 (2004).
10. M. B. Lilledahl, D. M. Pierce, T. Ricken, G. A. Holzapfel, and C. d. L. Davies, "Structural analysis of articular cartilage using multiphoton microscopy: input for biomechanical modelling," *IEEE Trans. Med. Imaging* (in press).
11. A. Erikson, J. Ortegren, T. Hompland, C. de Lange Davies, and M. Lindgren, "Quantification of the second-order nonlinear susceptibility of collagen I using a laser scanning microscope," *J. Biomed. Opt.* **12**(4), 044002 (2007).
12. L. M. S. Aas, P. G. Ellingsen, and M. Kildemo, "Near infra-red Mueller matrix imaging system and application to retardance imaging of strain," *Thin Solid Films* **519**, 2737–2741 (2011).
13. S. Y. Lu and R. A. Chipman, "Interpretation of Mueller matrices based on polar decomposition," *J. Opt. Soc. Am. A* **13**(5), 1106–1113 (1996).
14. S. Manhas, M. K. Swami, P. Buddhiwant, N. Ghosh, P. K. Gupta, and K. Singh, "Mueller matrix approach for determination of optical rotation in chiral turbid media in backscattering geometry," *Opt. Express* **14**(1), 190–202 (2006).
15. N. Ghosh, M. F.G. Wood, and I. A. Vitkin, "Mueller matrix decomposition for extraction of individual polarization parameters from complex turbid media exhibiting multiple scattering, optical activity, and linear birefringence," *J. Biomed. Opt.* **13**(4), 044036 (2008).
16. N. Ghosh, M. F. G. Wood, S. Li, R. D. Weisel, B. C. Wilson, R. Li, and I. A. Vitkin, "Mueller matrix decomposition for polarized light assessment of biological tissues," *J. Biopho.* **2**(3), 145–56 (2009).
17. L.-W. Jin, K. A. Claborn, M. Kurimoto, M. A. Geday, I. Maezawa, F. Sohraby, M. Estrada, W. Kaminksy, and B. Kahr, "Imaging linear birefringence and dichroism in cerebral amyloid pathologies," *Proc. Natl. Acad. Sci.* **100**, 15294–15298 (2003).
18. M. Shribak and R. Oldenbourg, "Techniques for fast and sensitive measurements of two-dimensional birefringence distributions," *Appl. Opt.* **42**(16), 3009–3017 (2003).
19. W. Kaminksy, L.-W. Jin, S. Powell, I. Maezawa, K. Claborn, C. Branham, and B. Kahr, "Polarimetric imaging of amyloid," *Micron (Oxford, England: 1993)* **37**, 324–338 (2006).
20. E. Compain, S. Poirier, and B. Drevillon, "General and self-consistent method for the calibration of polarization modulators, polarimeters, and mueller-matrix ellipsometers," *App. Opt.* **38**, 3490–3502 (1999).
21. H. G. Tompkins and E. A. Irene, *Handbook of Ellipsometry*, Vol. 1, William Andrew Publishing/Noyes, Norwich, NY (2005).
22. S. R. Cloude, "Conditions for the physical realisability of matrix operations in polarimetry," *Proc. SPIE* **1166**, 177–185 (1989).
23. V. V. Tuchin, L. V. Wang, and D. A. Zimnyakov, *Optical Polarization in Biomedical Applications*, Springer-Verlag, Berlin (2006).
24. N. Ugryumova and S. J. Matcher, "Variable angle-of-incidence polarization-sensitive optical coherence tomography: its use to study the 3D collagen structure of equine articular cartilage," *Proc. SPIE* **6079**, 60792C (2006).
25. B. Brodsky and J. Ramshaw, "The collagen triple-helix structure," *Matrix Biol.* **15**, 545–554 (1997).
26. D. Heinegård and I. Axelsson, "Distribution of keratan sulfate in cartilage proteoglycan," *J. Bio. Chem.* **252**, 1971–1979 (1977).
27. P. H. Vonhippel and K. Y. Wong, "The collagen gelatin phase transition. II. shape of the melting curves and effect of chain length," *Biochemistry* **2**(6), 1399–1413 (1963).
28. Combined Chemical Dictionary Online Version 14.2," Taylor & Francis, Boca Raton, FL (2011).
29. A. Maroudas, M. T. Bayliss, and M. F. Venn, "Further studies on the composition of human femoral head cartilage," *Ann. Rheum. Dis.* **39**(5), 514–523 (1980).

P. G. Ellingsen, L. M. S. Aas, V. S. Hagen, R. Kumar, M. B. Lilledahl, and M. Kildemo, Mueller matrix 3D directional imaging of collagen fibers, Preprint, subm. to J. Biomed. Opt. (2013)

Paper 8

Mueller matrix 3D directional imaging of collagen fibers

Pål Gunnar Ellingsen, Lars Martin Sandvik Aas, Vegard Stenhjem Hagen, Rajesh Kumar, Magnus Borstad Lilledahl and Morten Kildemo

Department of Physics, Faculty of Natural Sciences and Technology, Norwegian University of Science and Technology, Trondheim, Norway

Abstract. A method for measuring the 3D direction images of collagen fibers in biological tissue is presented. Images of the 3D directions are derived from the measured transmission Mueller matrix images, acquired at different incidence angles, by taking advantage of the form birefringence of the collagen fibers. By comparing the 3D direction images with images of the collagen fibers from second harmonic generation microscopy, a good agreement is found. The Mueller matrix images are decomposed using the newly developed differential decomposition, which is more suited to biological tissue samples than the common polar decomposition method.

Keywords: Mueller matrix imaging, collagen, directional imaging, SHG

1 INTRODUCTION

Biomedical research is experiencing a revolution due to the development of systems for spectral and spatial characterisation. In addition, pulsed lasers are readily available for nonlinear optical applications. Recently polarisation sensitive techniques, known from the thin film community, have been developed for biomedical applications. In the thin film community, the polarisation sensitive technique spectroscopic ellipsometry has been successfully used to characterise material properties of many kinds for several decades.[1] As a consequence, ellipsometry now plays an important role in the semiconductor industry. More recently, spectroscopic Mueller matrix ellipsometry has been employed to characterise anisotropic nanostructured materials and plasmonic structures.[2–5] Due to the turbidity of biological tissue,[6] the modeling is more complicated than for more uniform samples such as thin films. In addition, partial depolarisation of light in the sample requires acquisition of the full polarisation properties, i.e. the Mueller matrix, and not only the ellipsometric parameters Ψ and Δ. Nevertheless, it has shown promise for characterisation of biological tissue.[7–12]

Currently, several setups have been developed to acquire Mueller matrix images of biological samples. Pierangelo et al.[12] demonstrated the use of a reflection imaging Mueller matrix ellipsometer to characterise and diagnose colorectal cancer. Several broadband Mueller matrix designs for imaging setups have been proposed[13] and some have been implemented.[14] Such systems are non-destructive and have the possibility to achieve a sub micrometer resolution, as well as information about the structures smaller than the diffraction limit. By carefully choosing the wavelength, it is possible to make the technique sensitive to a certain depth range in the tissue.[6] If Mueller matrix imaging is combined with hyperspectral imaging it would be possible to study depth dependent effects.

There are a range of different polarisation effects which change a Mueller matrix, the common being depolarisation, diattenuation, birefringence and optical activity. If a material possesses several of these effects, it is not always easily seen from the Mueller matrix which of the effects are responsible for a certain part of the measured data. One way of simplifying the analysis, is to decompose the measured

Send correspondence to morten.kildemo@ntnu.no

Mueller matrix. Up until recently, the most common way to decompose the matrix has been the forward polar decomposition.[15,16] Recently Ossikovski et al.[17] pointed out that polar decomposition assumes the effects to be multiplicative, which is not the case for biological media. They suggested a more suitable approach for decomposing simultaneous effects, namely the differential decomposition, originally proposed by Azzam[18] and later extended to include depolarising media by Ossikovski.[19] Differential decomposition has recently been applied on biological tissue by Kumar et al.,[11] whom in addition, showed how to calculate physical properties from the decomposed matrices.

With the decomposed Mueller matrix from biological tissue containing collagen fibers, it has been shown possible to extract the in plane direction of the fibers from their induced birefringence.[10] Our work generalises this idea to find the 3D direction of collagen fibers in biological tissue. The method is tested and validated by comparing a 3D direction image of tendon derived from Mueller matrix images, with second harmonic images of the same sample.

2 MATERIALS AND METHODS

2.1 Sample preparation

Tendon tissue was taken from medial femoral condyle of the knee of a chicken, bought fresh from the supermarket. A small section of the tissue was embedded in a mounting medium for cryo-sectioning (O.C.T., Sakura). Rapid freezing of the O.C.T. embedded tissue was completed using liquid nitrogen. These frozen section were stored in a freezer (−60 °C) until cut using a cryostat, into 50 µm thin tissue sections. The cutting plane was parallel to the collagen fibers. The thin sections were placed on standard microscope glass slides and stored in a freezer (−60 °C). Before measurements, the tissue samples were brought back to room temperature and covered with a standard cover slip. Edges of the cover slip were sealed with Vaseline to avoid dehydration. Between measurements the slides were stored at 4 °C.

2.2 SHG imaging

SHG images were collected on a Zeiss LSM 510 meta micrscope using a Coherent Mira 900 for excitation at 790 nm. Imaging was done with a 40× 1.2 NA objective. A custom built polarisation set up, which compensates for any birefringence in the optical path, was used to ensure circular polarization. The average power at the focal plane was about 8 mW.

2.3 Mueller matrix imaging setup

After the samples were imaged with SHG, they were measured in a custom built Mueller matrix imaging (MMI) ellipsometer. The system uses ferroelectric liquid crystals for the polarisation state generator and analyser. Details of the system can be found in Aas et al.[20] An improvement was made to the illumination, by replacing both the laser and rotating diffuser, with a 940 nm collimated LED. In addition, a motorised rotation stage for the sample was introduced in order to image the sample at the different projections needed to extract the 3D direction, as described below.

The system was calibrated using the eigenvalue calibration method[21] on four reference samples (air, two polarisers and a retarder), ensuring the correct measurement of the Mueller matrix. By comparing the measurement of air to the identity matrix an error estimate was made, resulting in a measure for the accuracy of the system.

2.4 Decomposition of the Mueller matrix

As the differential decomposition method is able to decompose simultaneous polarisation effects, it was chosen for the decomposition of the measured Mueller matrices presented here. Due to measurement noise, some of the measured Mueller matrices are slightly unphysical, which was compensated for by using the filtering described by Cloude[22] prior to the decomposition.

The differential decomposition results in two matrices, L_m and L_u,[19] where L_m contains the elements used to calculate the retardance and the diattenuation. Using L_u, the errors in the retardance and the diattenuation can be calculated by using the same matrix elements from L_u as originally used from L_m. Furthermore, from L_u the depolarisation can be calculated. In this study the relevant properties are the linear retardance δ, the angle of orientation of the linear retardance θ and the depolarisation* Δ.[11]

2.5 Directional calculation

From our daily life we are familiar with determining the orientation of an object just by looking at it. As our eyes are placed a distance apart, they see two different projections of the image, enabling our brain to deduce the orientation of the object we are looking at. The MMI setup can only image one projection, but it is possible to rotate the sample in two different sample rotations α, see figures 1 and 2, and then use the two resulting images to calculate the direction of the imaged birefringent structure, here the collagen framework.

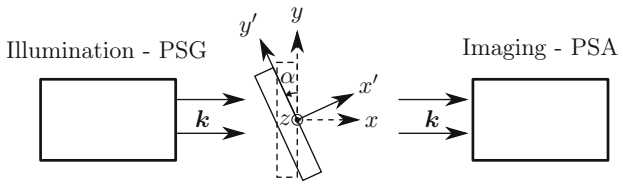

Figure 1: Rotation α of the sample seen from above the setup.

In order to derive the direction of the structure, the easiest is to start with the Euler transformations.[23] They require the definition of two coordinate systems, the laboratory frame of reference and the sample frame of reference. Let $\boldsymbol{p} = [x, y, z]$ describe a vector in the laboratory frame of reference. The frame of reference is defined in such a way that the x axis points along the direction of illumination, y axis is horizontal and z axis vertical, see figure 1. Let $\boldsymbol{p'} = [x', y', z']$ be a vector in the sample frame of reference. The sample frame of reference coincides with the laboratory frame for a rotation $\alpha = 0°$, see figure 1. The sample is only rotated around the $z = z'$ axis, see figures 1 and 2, resulting in the following Euler rotation matrix

$$\boldsymbol{R}(\alpha) = \begin{bmatrix} \cos\alpha & \sin\alpha & 0 \\ -\sin\alpha & \cos\alpha & 0 \\ 0 & 0 & 1 \end{bmatrix} \tag{1}$$

*It is here noted that the depolarisation ($\Delta^{\log -M}$, eq. 19 in the paper by Kumar et al.[11]) has the wrong signs of the exponential, it should be $\Delta^{\log -M} = 1 - (1/3)\left(e^{\alpha_1} + e^{\alpha_3} + e^{\alpha_3}\right)$ as discussed in a private correspondence with Ossikovski, one of the authors of the original paper.

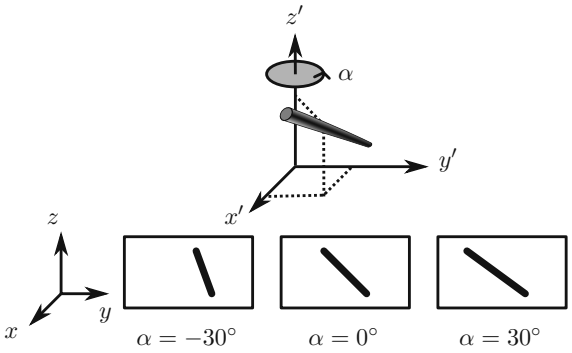

Figure 2: The coordinate systems used for the directional calculation. The laboratory frame (xyz) is identical to the sample frame of reference ($x'y'z'$) at $\alpha = 0$. The x axis points along the illumination direction towards the camera, and z is vertical. As the rotation is around z, $z' = z$ for any α. The lower row of figures show the projection of the a vector onto the imaging plane at different values of α.

By using this transformation it is possible to transform from the sample frame of reference $\boldsymbol{p}'$ to the laboratory frame of reference $\boldsymbol{p}$, by $\boldsymbol{p} = \boldsymbol{R}(-\alpha)\boldsymbol{p}'$. Applying this transformation gives the following relations

$$\begin{aligned} x &= x' \cos\alpha - y' \sin\alpha \\ y &= x' \sin\alpha + y' \cos\alpha \\ z &= z' \end{aligned} \tag{2}$$

The goal is to determine $\boldsymbol{p}'$ by measuring the Mueller matrix at two different sample rotations, α_1 and α_2, by looking at the projections into the laboratory frame of reference (the measured image), resulting in the measured (y_1, z_1) and (y_2, z_2). By choosing $\alpha_2 = -\alpha_1 = \alpha$, (in our setup $\alpha_2 < 0$ due to the direction of rotation) and solving equation (2), the components of $\boldsymbol{p}'$ results in

$$x' = \frac{y_2 - y_1}{2\sin\alpha}, \quad y' = \frac{y_1 + y_2}{2\cos\alpha}, \quad z' = z_1 = z_2 \tag{3}$$

As the MMI measurement only yields the direction of the slow axis, θ, and not the projected length (the length in the yz plane) of the fibre, it is not possible to find the absolute value (length) of the vector. In order to resolve this, we define the projected length of the fibre as

$$l = \sqrt{y^2 + z^2} = \sqrt{x'^2 \sin^2\alpha + y'^2 \cos^2\alpha + 2x'y' \sin\alpha\cos\alpha + z'^2}$$

It is now possible to define the coordinates with respect to the measured angles

$$\begin{aligned} y_1 &= l_1 \cos\theta_1, \quad z_1 = l_1 \sin\theta_1 \\ y_2 &= l_2 \cos\theta_2, \quad z_2 = l_2 \sin\theta_2 \end{aligned}$$

Using $z_1 = z_2 = z$ we find that

$$y_1 = z\cot\theta_1, \quad y_2 = z\cot\theta_2$$

which, when inserted into equation (3), gives

$$x' = \frac{z\,(\cot\theta_2 - \cot\theta_1)}{2\sin\alpha}, \qquad y' = \frac{z\,(\cot\theta_1 + \cot\theta_2)}{2\cos\alpha}, \qquad z' = z$$

These equations are dependent on the absolute length of z, however, as we are only interested in the direction of the fibre we can set $z = 1$. This limits the solution to only include positive z, which is not a problem since all solutions with negative z can be represented by the opposite vector located in the positive z space. In addition, it will not be possible to get a solution purely in the xy plane ($z = 0$). A real measurement contains some noise, both from the measurement itself and from numerical noise, ensuring that the angle is never exactly zero. In addition, the rotation around z means that it is not possible to see difference between different vectors in the xy plane if $z = 0$. The final equations are then

$$x' = \frac{\cot\theta_2 - \cot\theta_1}{2\sin\alpha}, \qquad y' = \frac{\cot\theta_1 + \cot\theta_2}{2\cos\alpha}, \qquad z' = 1 \tag{4}$$

When presenting results derived with equation (4), the vector is normalised to its length $\sqrt{x'^2 + y'^2 + z'^2}$.

Another consideration to make is that the angle of incidence is not the same as the rotation angle of the sample, due to the difference in refractive index. The tissue is sandwiched between two glass slides, but these do not effect the correction, according to Snell's law. Thus the correction for α is , $\alpha = \arcsin(\sin(\alpha_r)/n_t)$, where α_r is the angle of rotation (incidence angle on the glass) and n_t the refractive index of tissue, assumed here to be 1.4.[6]

2.6 Directional imaging

By changing the angle of incidence on the sample, obtained by rotating the sample, and using the slow axis direction found from the decomposition, it is possible to calculate and hence make an image of the 3D direction of the fibers as describe in subsection 2.5. The calculation is done using incidence angles of $\alpha_r = \pm 30°$. The resulting images are resampled, using α_r, such that the stretching due to rotation is counteracted and the pixels are square. α_r is used because the image is seen on the surface of the glass.

3 RESULTS AND DISCUSSION

3.1 Depolarisation and linear retardance

Linear retardance describes how much the polarisation in one direction is phase shifted with respect to its orthogonal polarisation. Figure 3 shows the linear retardance together with its uncertainty for the tendon sample. As has been described elsewhere,[10] the high amount of collagen results in a high retardance, mainly due to the form birefringence induced by the shape of the fibers in the effective medium. A previous study[10] looked at cartilage, which is less ordered than the tendon. Being less ordered means that the structure should be modelled as a layered effective medium (requiring a layered decomposition of the Mueller matrix) with one orientation for every layer. The larger degree of order in the tendon makes the results clearer and remove the need for considering the sample as a multilayered system.

Figure 3(b) shows the uncertainty of the linear retardance, which is seen to be above the random noise level in some areas. As the uncertainty is a result of scattering, depolarisation and measurement uncertainties it is useful for the analysis of the sample. Since the knowledge of the uncertainty has previously been limited to the measurement error known from the calibration, specifically the error

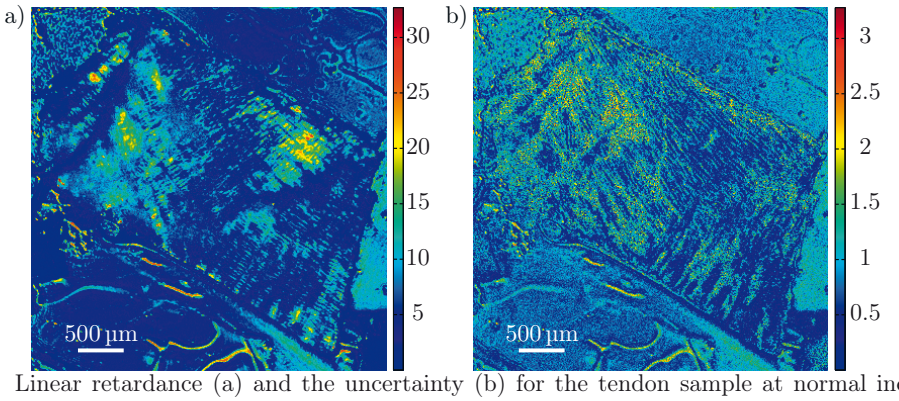

Figure 3: Linear retardance (a) and the uncertainty (b) for the tendon sample at normal incidence. Both images are in degrees.

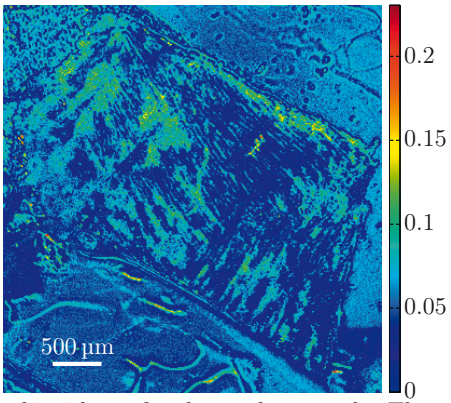

Figure 4: Depolarisation at normal incidence for the tendon sample. The color scale is from 0 for fully polarised to 1 fully depolarised.

on measuring air, this is new and potentially important information. The measurement error of the current system, provided by the calibration procedure, is on the order of a few percent. Hence most of the uncertainty seen in figure 3(b) is due to other effects. By comparing the uncertainty measurement to the depolarisation shown in figure 4, it is observed that they correlate well, indicating that the largest uncertainty in the linear retardance is due to depolarising effects such as multiple scattering and integration of several polarisation states in one pixel.

3.2 Directional imaging

From the retardance found in the decomposition it is not only possible to calculate the linear retardance, but also the direction of the fast axis of the birefringence. This property can, together with the correct effective medium model, be used to find the direction of collagen fibers as explained in section 2.

The directional image and the SHG image for the tendon sample are shown in figure 5. As the 3D image in figure 5(a) shows, the fibers are mostly in the plane as expected due to direction of the cryostat

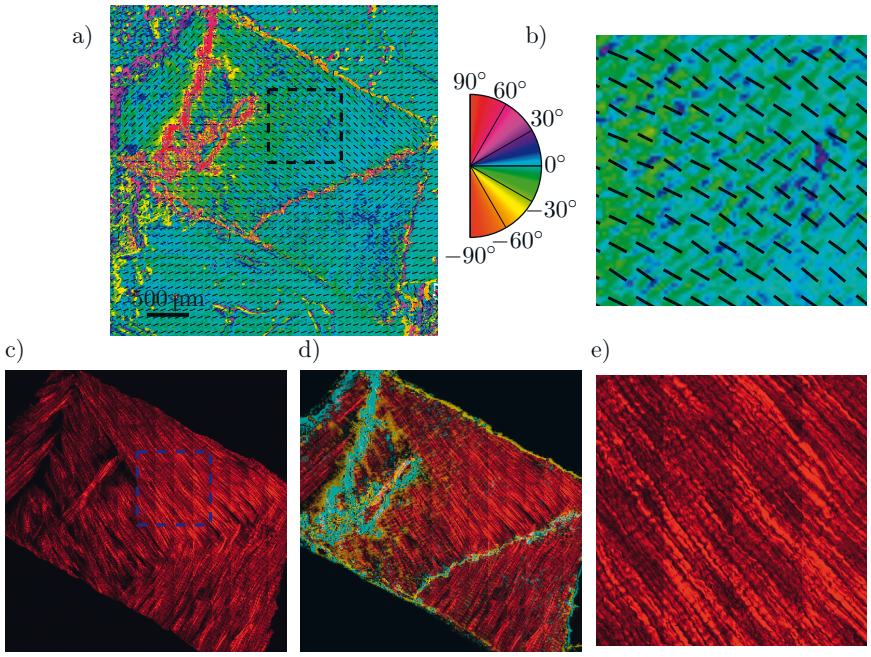

Figure 5: 3D directional image (a) with a zoomed view (b), a SHG image (c) with a zoomed in view (e) and an overlay of the SHG and the out of plane direction of the tendon (d). The colourwheel beside the directional image shows the out of plane direction in degrees, with 0° being in the image plane and ±90° normal to the image plane. +90° is the direction towards the reader (positive x). The overlay (d) (area outside of the sample masked for clarity) shows the SHG and out of plane directions overlain. The yellow colour represent the negative out of plane direction and the cyan the positive direction. No colour represents an in plane direction and increasing colour more out of plane.

cut. The calculated in plane direction (black lines in figure 5(a) and 5(b)) corresponds very well with the apparent direction in the SHG images. There are some areas that are clearly out of plane (red in the 3D image), which are either dark or show some weak structure in the SHG image. The latter can be explained by the SHG signal generation. Fiber orientations of are important, as a fiber in plane has a much larger cross section for generating SHG, compared to one out of plane. This means that the darker parts of the image in figure 5(c) probably are due to out of plane orientation of the fibers, as found in the 3D image. Figure 5(d) shows an overlay of figures 5(a) and 5(c).

The lower right of the sample shows an offset between the directional image and the SHG. There could be several reasons for this offset, one being that the size of the fibers are around the upper limit of the validity of the effective medium model. In this study it was necessary that fibers were sufficiently large to visualise with SHG, which is limited by the diffraction limit. It is expected that the Mueller matrix imaging results will be better for smaller fibers.

It is clear that the large out of plane directions correspond well with the same areas in the SHG image. Additionally, by studying the image 5(a) and the zoomed in views in figure 5(b) and figure 5(e),

it is possible to see that the oscillating structure (the oscillation between green and blue) along the fibers is visible both in the SHG image and the out of plane direction image. Both of these results confirm that the 3D directional imaging finds the correct directions. The ability to find the direction in MMI, even though the resolution is much poorer than for SHG, is one of its advantages.

4 CONCLUSION

The method for finding the 3D direction of collagen fibers embedded in biological tissue from Mueller matrix images is shown to be in good agreement for tendon when compared to SHG images. In particular, it is possible to see oscillating structures in the collagen orientation, as well as the out of plane directions of fibers. The possibility to see effects from collagen fibers below the diffraction limit could be an important input to the understanding of how the collagen framework looks. Additionally, the use of the differential decomposition instead of the, until now, most common polar decomposition, has provided a good insight into the uncertainties in the calculation of the physical properties.

Acknowledgments

The authors would like to thank Razvigor Ossikovski for correspondence on the implementation of the differential decomposition method.

References

[1] R. M. A. Azzam and N. M. Bashara, *Ellipsometry and Polarized light*, North-Holland (1977).

[2] D. Schmidt, A. C. Kjerstad, T. Hofmann, R. Skomski, E. Schubert, and M. Schubert, "Optical, structural, and magnetic properties of cobalt nanostructure thin films," *J. Appl. Phys.* **105**(11), 113508 (2009).

[3] I. Nerbø, S. L. Roy, M. Foldyna, E. Søndergård, and M. Kildemo, "Real-time in situ Mueller matrix ellipsometry of GaSb nanopillars: observation of anisotropic local alignment," *Opt. Express* **19**(13), 571–575 (2011).

[4] L. Aas, M. Kildemo, Y. Cohin, and E. Søndergård, "Determination of small tilt angles of short GaSb nanopillars using UV–visible Mueller matrix ellipsometry," *Thin Solid Films* **541**, 97–101 (2013).

[5] T. Oates, H. Wormeester, and H. Arwin, "Characterization of plasmonic effects in thin films and metamaterials using spectroscopic ellipsometry," *Prog. Surf. Sci.* **86**, 328–376 (2011).

[6] V. V. Tuchin, *Tissue optics: light scattering methods and instruments for medical diagnosis*, SPIE Press, 2nd ed. (2007).

[7] J. Chung, W. Jung, M. J. Hammer-Wilson, P. Wilder-Smith, and Z. Chen, "Use of polar decomposition for the diagnosis of oral precancer.," *Appl. Optics* **46**, 3038–45 (2007).

[8] N. Ghosh, M. F. G. Wood, S. Li, R. D. Weisel, B. C. Wilson, R. Li, and I. A. Vitkin, "Mueller matrix decomposition for polarized light assessment of biological tissues," *J. Biophotonics* **2**(3), 145–56 (2009).

[9] M.-R. Antonelli, A. Pierangelo, T. Novikova, P. Validire, A. Benali, B. Gayet, and A. De Martino, "Mueller matrix imaging of human colon tissue for cancer diagnostics: how Monte Carlo modeling can help in the interpretation of experimental data," *Opt. Express* **18**, 10200 (2010).

[10] P. G. Ellingsen, M. B. Lilledahl, L. M. S. Aas, C. D. L. Davies, and M. Kildemo, "Quantitative characterization of articular cartilage using Mueller matrix imaging and multiphoton microscopy," *J. Biomed. Opt.* **16**, 116002 (2011).

[11] S. Kumar, H. Purwar, R. Ossikovski, I. A. Vitkin, and N. Ghosh, "Comparative study of differential matrix and extended polar decomposition formalisms for polarimetric characterization of complex tissue-like turbid media," *J. Biomed. Opt.* **17**(10), 105006 (2012).

[12] A. Pierangelo, S. Manhas, A. Benali, C. Fallet, J.-L. Totobenazara, M.-R. Antonelli, T. Novikova, B. Gayet, A. De Martino, and P. Validire, "Multispectral Mueller polarimetric imaging detecting residual cancer and cancer regression after neoadjuvant treatment for colorectal carcinomas," *J. Biomed. Opt.* **18**(4), 046014 (2013).

[13] P. A. Letnes, I. S. Nerbø, L. M. S. Aas, P. G. Ellingsen, and M. Kildemo, "Fast and optimal broad-band Stokes/Mueller polarimeter design by the use of a genetic algorithm," *Opt. Express* **18**(22), 10 (2010).

[14] L. M. S. Aas, P. G. Ellingsen, B. E. Fladmark, P. A. Letnes, and M. Kildemo, "Overdetermined broadband spectroscopic Mueller matrix polarimeter designed by genetic algorithms," *Opt. Express* **21**(7), 8753 (2013).

[15] S.-Y. Lu and R. A. Chipman, "Interpretation of Mueller matrices based on polar decomposition," *J. Opt. Soc. Am. A* **13**(5), 1106 (1996).

[16] S. Manhas, M. K. Swami, P. Buddhiwant, N. Ghosh, P. K. Gupta, and J. Singh, "Mueller matrix approach for determination of optical rotation in chiral turbid media in backscattering geometry," *Opt. Express* **14**(1), 190 (2006).

[17] R. Ossikovski, A. De Martino, and S. Guyot, "Forward and reverse product decompositions of depolarizing Mueller matrices," *Opt. Lett.* **32**(6), 689691 (2007).

[18] R. Azzam, "Propagation of partially polarized light through anisotropic media with or without depolarization: a differential 4 x 4 matrix calculus," *J. Opt. Soc. Am.* **68**(12), 1756–1767 (1978).

[19] R. Ossikovski, "Differential matrix formalism for depolarizing anisotropic media," *Opt. Lett.* **36**(12), 2330–2 (2011).

[20] L. M. S. Aas, P. G. Ellingsen, and M. Kildemo, "Near infra-red Mueller matrix imaging system and application to retardance imaging of strain," *Thin Solid Films* **519**(9), 2737–2741 (2011).

[21] E. Compain, S. Poirier, and B. Drevillon, "General and self-consistent method for the calibration of polarization modulators, polarimeters, and mueller-matrix ellipsometers," *Appl. Optics* **38**(16), 3490–502 (1999).

[22] S. R. Cloude, "Conditions for the physical realisability of matrix operations in polarimetry," *Proc. SPIE* **1166**, 177–185 (1989).

[23] H. Goldstein, C. Poole, and J. Safko, *Classical Mechanics*, Addison Wesley, third ed. (2002).

M. Kildemo, L. M. S. Aas, P. G. Ellingsen, H. Hemmen, E. L. Hansen, and J. O. Fossum, Mueller matrix imaging of nematic textures in colloidal dispersions of Na-fluorohectorite synthetic clay, Proc. SPIE **8082**, 808221 (2011)

Paper 9

Mueller matrix imaging of nematic textures in colloidal dispersions of Na-fluorohectorite synthetic clay

Morten Kildemo*, Lars. M. S. Aas, Pål.G. Ellingsen

Experimental Optics Group, Department of Physics, Norwegian University of Science and Technology (NTNU),7491 Trondheim, Norway

Henrik Hemmen, Elisabeth L. Hansen, Jon O. Fossum

Laboratory for Soft and Complex Matter Studies, Department of Physics, Norwegian University of Science and Technology (NTNU), 7491 Trondheim, Norway

ABSTRACT

A Mueller Matrix Imaging Ellipsometer system is operated in transmission and used to study nematic textures in colloidal dispersions of synthetic Na-fluorohectorite clay platelets in solution. It is clearly observed that the anisometric particles organize into phases with strong birefringence, which results in a strong retardance. The Mueller matrix imaging technique supplies an image of the retardance matrix, even in the presence of other effects such as light scattering and diattenuation. The spatial variation of the absolute value of the retardance, the orientation of the fast axis of the retardance, the total diattenuation and the orientation of the diattenuation are presented. In particular, from knowledge of the anisotropic shape of the particles, the orientation of the particles within ordered domains, and the density of the particles within the domains are spatially determined. The experiments are based on adding synthetic clay particles into a solution contained in a thin rectangular glass container. Upon letting gravitation act on the sample, different phases appear after a few weeks. One phase contains nematic textures and we are able to determine the ordering and also estimate the density of the domains/texture within the phase, in addition to estimating the local order within a domain with an image resolution of 12 μm.

Keywords: Polarimetry, Imaging, Colloidal liquid crystals, Ellipsometry
*Morten.Kildemo@phys.ntnu.no; Tel.: +47 73593211

1. INTRODUCTION

Mueller matrix imaging is a relatively new and interesting technique that has become largely simplified in recent years, due to the appearance of a simplified formalism for the design and calibration of such an optical imaging system.[1-4] In order to perform high resolution Mueller matrix imaging, it is largely advantageous to use non-rotating or non-moving active polarization components, such as e.g. liquid crystals. For many applications, it is further interesting to enable reasonably fast imaging. We have developed a ferro electric liquid crystal (FLC) based Mueller Matrix Imager (FLC-MMI), designed to operate achromatically in the range 800-1700 nm.[5] Such a system can also be denoted a Mueller Matrix Imaging Ellipsometer, and it differs from the imaging polarimeter, in that it has a polarization state generator, which generates four optimally selected polarization states for the illumination. One of the key features of the current FLC based system is that it may be operated fast, as long as sufficient flux is available on each pixel, which requires a powerful source, a sufficiently high gain and a high frame rate camera. In the current work, collimated light from a 980 nm laser was passed through a rotating scrambler and then used for illumination. A standard silicon based CCD camera was used for

Optical Measurement Systems for Industrial Inspection VII, edited by Peter H. Lehmann, Wolfgang Osten, Kay Gastinger, Proc. of SPIE Vol. 8082, 808221 · © 2011 SPIE
CCC code: 0277-786X/11/$18 · doi: 10.1117/12.889569

detection, and since the kinetics of the process to be imaged was extremely slow, no concern with respect to acquisition time has been made.

Mueller matrix imaging is interesting due to the fact that many polarization modifying phenomena are spatially varying, and can thus supply enhanced spatial information about the sample. Typical examples of polarization altering phenomena are birefringence which induces retardance, dichroism that induces the so-called diattenuation, and light scattering that induces depolarization. All of these are spatially varying functions across a given sample, and are connected to the locally intrinsic properties of the material. The Mueller matrix effectively probes all these phenomena, although separation of each phenomenon may in certain cases be a challenging task. However, in many cases the polar decomposition technique can be used, and allows the retardance, depolarization and diattenuation to be effectively separated.[6-8] Furthermore, organic materials, strained solid state materials nanostructured materials and colloids/liquid crystals often show anisotropic optical properties as a function of e.g. anisotropic shaped particles (form birefringence), anisotropically induced strain, inherent optical anisotropy due to reduced symmetry (both birefringence and dichroism). These effects are in addition to standard effects described by Fresnel coefficients from surfaces and thin films.

In this work, we exemplify the Mueller matrix imaging technique, using a single wavelength of 980 nm, to study nematic textures in colloidal aqueous dispersions of synthetic Na-Fluorohectorite clay particles. The polydisperse particles are platelet-shaped with thicknesses in the range of 10 – 150 nm along the sheet normal, and diameters of around 1 μm. Previous work using crossed polarizers, has demonstrated that such particles in aqueous solutions have a strong birefringence.[9-11]

The strong birefringence will give a strong retardance if the particles are locally ordered. The Mueller matrix imaging technique together with the forward polar decomposition[6] is able to determine the corresponding retardance matrix, even in the presence of other effects such as light scattering and diattenuation. From the retardance matrix one determines the local orientation of the particles and the local degree of ordering. We have here studied samples similar to those that have been previously thoroughly studied by the use of crossed polarizers,[9-11] by x-ray scattering[9-13] and by magnetic resonance imaging[11, 14] As a result we show that the Mueller matrix imaging technique can directly supply high quality images, with information that would require the combined effort of both small- and/or wide-angle x-ray diffraction (using synchrotron radiation), and crossed polarizer imaging. In particular, the orientation of ordered domains of particles, and the density of such particles are spatially determined at high resolution. The experiments are based on adding synthetic clay particles into a solution contained in a thin rectangular glass container. Upon letting gravitation act on the sample, different phases appear after a few weeks. At certain concentrations, the samples show nematic textures and we are able to determine the ordering and visualize density differences of the domains/texture within the phase, in addition to estimating the local order within a domain. Similarly, we are able to separate this phase from regions of differing order. Studies on related samples are planned in the near future.

2. EXPERIMENTAL

2.1 Mueller Matrix Imager

The Mueller matrix imaging ellipsometer consists of a light source, a Polarization State Generator (PSG), the sample, a Polarization State Analyzer (PSA), an imaging lens, a plane mirror and a CCD camera. Different sources could be connected to the system, but in this work, the illumination was obtained by a 980 nm laser source collimated after passing through a rotating scrambler, as shown in Figure 1. A 980 nm bandpass filter was mounted on the camera to make the system insensitive to background illumination. The camera in this work was a Hamamatsu C4742-95 camera. The current setup (Figure 1) had a magnification close to one and a very small numerical aperture due to the apertures in the PSG and the long focal length of the imaging lens. The resolution was estimated to 12 μm. The PSG (Figure 1) consists of a high extinction ratio NIR polarizer (P1) followed by a zero order wave plate (R1), a FLC (F1), a second fixed wave plate (R2) and a second FLC (F2). A FLC is basically operating as a wave plate that is rotated by 45 degrees with an electric field applied over the cell.[1] The orientations of the FLCs and the fixed wave plates, and their retardances have been carefully selected by optimization in order to generate four Stokes vectors that span the polarization space of the Poincare sphere. The PSA basically consists of the components of the PSG in reverse order, as seen in Figure 1. Its role is to map

the Stokes vectors exiting from the sample onto four optimally spaced analysis states on the Poincare sphere. The latter measurement procedure results in an optimally conditioned system of equations that allow for minimal noise propagation upon solving for the desired 16 Mueller matrix elements, which completely describe the polarization altering properties of the sample. In order to do this conversion one uses

$$\mathbf{B} = \mathbf{AMW},$$

where $\mathbf{M}$ is the Mueller matrix of the sample, $\mathbf{B}$ is the 16 measured intensities, $\mathbf{W}$ and $\mathbf{A}$ the system matrices for the PSG and the PSA found using the eigenvalue calibration method.[4] $\mathbf{M}$ is found by multiplying the inverse of $\mathbf{A}$ and $\mathbf{W}$ from each side,

$$\mathbf{M} = \mathbf{A}^{-1}\mathbf{B}\mathbf{W}^{-1}.$$

By applying this to every pixel in the image for the 16 intensity images, the complete Mueller matrix image is found. In order to find the retardance ($\mathbf{M}_R$), the diattenuation ($\mathbf{M}_D$) and the depolarization ($\mathbf{M}_\Delta$) matrices, the forward polar decomposition was applied by defining [6]

$$\mathbf{M} = \mathbf{M}_\Delta \mathbf{M}_R \mathbf{M}_D.$$

In this work the retardance matrix and the diattenuation matrix that appears as the most interesting information carriers, while the depolarization matrix helps to control the process involved, for example rejecting spurious signals, but also localizing strongly scattering particles (which can be observed as e.g. depolarization). From the diattenuation matrix the total linear diattenuation and the orientation of the transmission axis are found, while fore the retardance matrix it is possible to find the linear retardance and the orientation of the fast axis for each pixel.[7] These scalars are represented in an image map and give an overview of the spatial variations across sample. The orientation of the fast axis is very interesting as it may in an effective medium approach for the clay particles be the normal to the clay plates (i.e. the so called form-birefringence). By plotting the fast axis, presumed normal to the plates, the orientation of the plates may in principle be spatially determined.

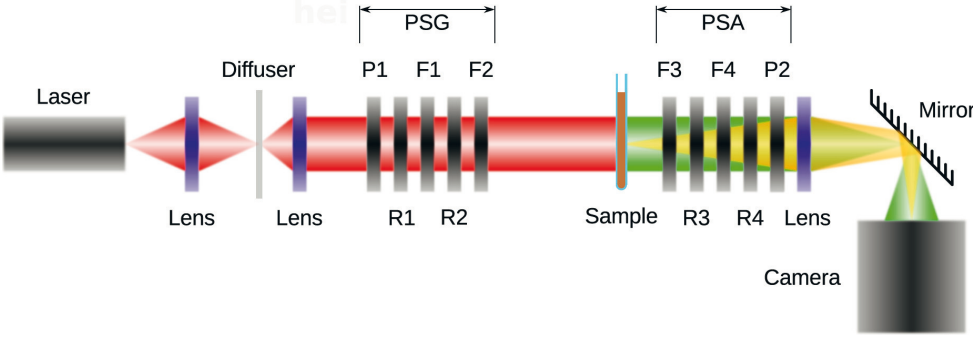

Figure 1. The setup of the Mueller matrix imager. The sample is a rectangular container filled with the nanoparticles in solution, as shown in Figure 2.

2.2 Preparation of the Colloidal dispersions of Na-fluorohectorite synthetic clay in solution

Synthetic Li-fluorohectorite clay was purchased in powder form from Corning Inc., NY and ion-exchanged to produce Na-fluorohectorite. As illustrated in Figure 1, individual Na-fluorohectorite particles are composed of around 20-100 silicate lamellae that stack by sharing Na+ ions between their basal planes. The lateral sizes of these lamellae can be as large as several μm, whereas each lamella is only 1 nm thick. Na-fluorohectorite particles carry a layer charge of 1.2e- per unit cell that originates from substitution of Li+ for Mg2+ in the atomic structure of the particles. This high layer charge causes Na-fluorohectorite lamella to remain stacked when suspended in water, in contrast to lower-charge smectites. Under the influence of gravity, aqueous

suspensions of Na-fluorohectorite particles phase-separate to form distinct regions of differing particle concentrations and order. The samples in the current study were prepared as dispersions of 0.5 g Na-fluorohectorite in 45 mL distilled water, that were centrifuged to remove particle aggregates before the samples were allowed to settle under the influence of gravity. A nematic gel region, formes over the course of a couple of days in such a sample, as ordered tactoids sediment and gradually build an extended nematic region of several domains. These domains then continue to evolve during several weeks. Figure 2d shows the sample holder used for the Mueller matrix imaging ellipsometry: a rectangular borosilicate capillary from Hilgenberg, which is 80 mm long, 4.2 mm wide, and 1.25 mm thick (1 mm inner thickness).

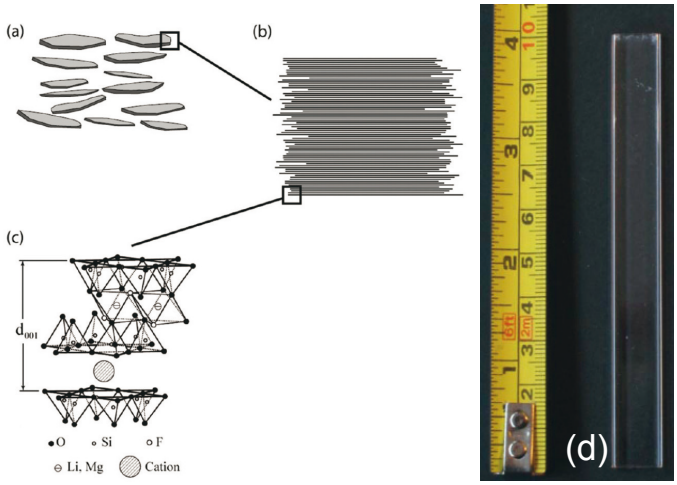

Figure 2. (a) Representation of Na-fluorohectorite particles in nematic order. In this illustration the platelets are lying on average horizontally and the platelet normals are oriented vertically. (b) Cross-section of a single clay particle, which consists of about 100 stacked crystallized lamellae. The lamellae are layered with a thickness of around 1 nm each. (c) Atomic configuration of fluorohectorite, where the intercalated cation is Na+for NaFh. Adapted from refs [11, 15]. (d) Image of the flat glass capillary used as sample cell.

2.3 Mueller matrix images of colloidal dispersions

The rectangular shaped container with the colloidal dispersions see Figure 2d, was positioned on an automatic x-y stage that allowed the full container to be observed by performing only five vertically consecutive Mueller matrix images that were numerically stitched together. The imaging process with a very high resolution (12 μm) could thus easily be performed without any micro spot optics and slow scanning. The imaging process in the current work was slowed down due to triggering issues with the reasonably old camera, using approximately 2 minutes per image. The imaging speed was simply limited by the camera, and there should be no major obstacle in order to perform each image within a few seconds. Further improvement of speed would possibly require improving the light transmission of the PSG and PSA which involves both AR-coating of components and an increase of the numerical aperture. The current FLC based Mueller matrix ellipsometer has been shown to have a lower limit of 16 ms per Mueller matrix, using a single (pixel) fast detector[1].

3. RESULTS AND DISCUSSION

Figure 3 shows the results of Mueller matrix imaging the sample, and after decomposing the measured Mueller matrix images. The figure shows from the left to the right, (a) the total retardance calculated from the retardance matrix, (b) orientation of the retardance, (c) the total diattenuation calculated from the diattenuation matrix, and

(d) the orientation of the transmission axis of the diattenuation vector. Figure (e) shows finally for completeness the degree of polarization calculated from the depolarization matrix. The color bars explaining the scale for each phenomenon is plotted below the images. In particular, the total observed retardance (Figure 3a) varies between 0 and 60 degrees, where the higher retardance gives brighter colors (dark blue means no retardance). From the retardance image, one clearly observe several regions from the top to the bottom, which we denote air, zones A, B, C and D. Between the air and zone A, there is a cap layer which gives no signal and should be regarded as an artifact (see the depolarization image). However, just below the surface, domains causing retardance is observed. This is due to partial evaporation of water from the air-water interface, increasing the particle concentration and forcing the particles to align to the interface. Zone A appears as mainly isotropic, and is thus probably an isotropic dispersion of small clay particles. There seems to be a strong phase transition from zone A to zone B, where zone B consists of domains of higher retardance. The bottom of zone B gives a gradual change to zone C, which again appears isotropic. The bottom of the container consists of a zone D with apparent layers of ordered domains with higher retardance. Such effects have basically been described previously using a simple set-up of crossed polarizers[11]. The advantage of the retardation matrix is evident in Figure (3b), which gives the orientation of the retardance. The blue colors indicate a vertical orientation of the fast axis, whereas red colors indicate that the fast axis is horizontal. If the retardance and the orientation of the retardance are viewed together, it is observed that the phase transition from zone A to zone B consists of a well-defined region of strong retardance with an orientation of the fast axis along the gravitational (vertical) axis. A close up of the latter region is shown in Figure 4, where the retardance (color-coded) and the orientation of the fast axis (lines points in the direction of the fast axis) are plotted together. It is clearly observed that the high retardance region at the phase transition has a fast axis pointing normal to phase transition (plate normals in the direction of the gravitation axis). Further into zone B, the sharp red colors in the orientation map, see Figure 3c, show that there is a larger tendency for preferential ordering of the fast axis within domains along the perpendicular to the gravitational axis. The latter may also clearly be observed from Figure 4.

Figure (3c) shows an image of the total diattenuation of the sample. In particular, the zones of high diattenuation appears correlated to the zones of higher retardance, but with a more fine grained structure than the retardance. The orientation of the diattenuation vectors, see Figure (3d), seem primarily to be in correspondence with the slow axis of the birefringence (Figure 3b), however, there are apparent large zones of deviation from the latter. Finally, the depolarization is shown to enable us principally to rule out zones of poor measurement quality, as most of the important part of the sample has a rather uniform depolarization. The zones of red colors in Figure (3e) thus define the useful part of the sample. An exception is the deep red vertical colored line at each edge of the sample, which was interpreted as a spurious specular reflection artifact from the sample container, and should not be considered in the analysis of images (a) to (d). Furthermore, there is an increased tendency for higher depolarization in the zone of strong diattenuation (zone B).

A preliminary analysis of these results in comparison with previous work,[9-14] indicate that the fast axis is indeed pointing in the direction of the normal to the clay-plates (see Figure 2). The retardance is then nominally a function of the density of particles and the number of particles ordered with their surface normal in the x,y plane in the image (here perpendicular to the probing beam). One becomes thus at normal incidence virtually blind to particles oriented with their normals along the beam direction. Since the clay particles' preferred orientation in the vicinity of a wall is homeotropic (i.e. particle normal perpendicular to the plane of the walls), we are in this sample geometry imaging only a fraction of the particles. Further experiments are planned where other container geometries and magnetic fields will be used to orient particles in such away that the retardance is maximized. However, there appears to be more information in the diattenuation image than in the retardance image, as the diattenuation appears to be enhanced rather at the edges of the domains, resulting in an apparent doubling of the number of observed lines/features in both the diattenuation and the orientation of the diattenuation vector (orientation of transmission axis). This will be further investigated in future work. In comparison with previous work on colloidal Na-fluorohectorite suspensions,[9-14] the present technique provides data on anisotropic sample properties with an excellent spatial resolution which exceeds that obtained with traditional x-ray scattering by at least one order of magnitude.

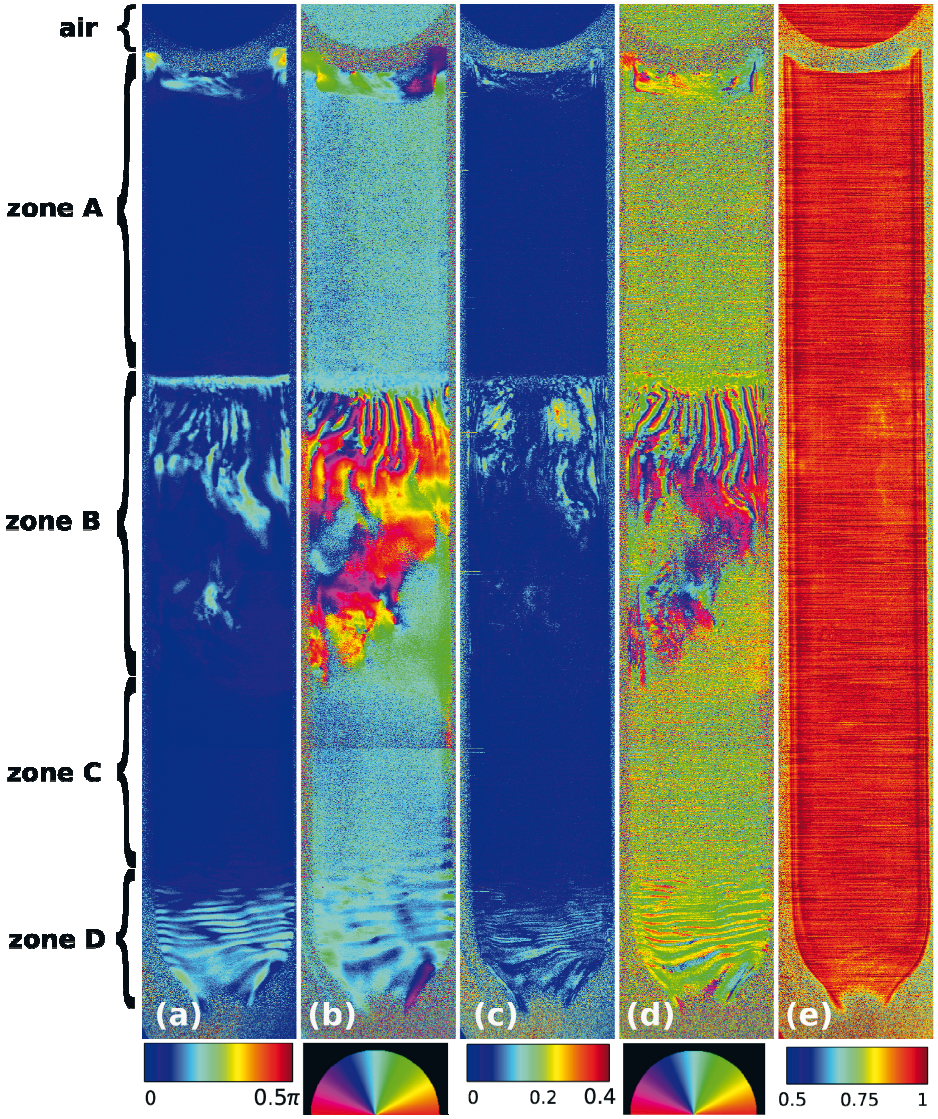

Figure 3. Result of Mueller matrix imaging of the clay-water sample. The retardance (colormap) image (a), the orientation of the fast axis (colormap) image (b), the total diattenuation (colormap) image (c), the orientation of the diattenuation vector (transmission axis) colormap image (d) and the degree of polarization (1-depolarization index) (e). The retardance is color coded between 0 and 180 degrees (see color bar). Both the orientation of the retardance and the diattenuation are color coded between 0 and 180 degrees, where the same color is given for 0 and 180 degrees. The diattenuation is color coded between 0 and 1, while the degree of polarization is color coded between 0.5 and 1.

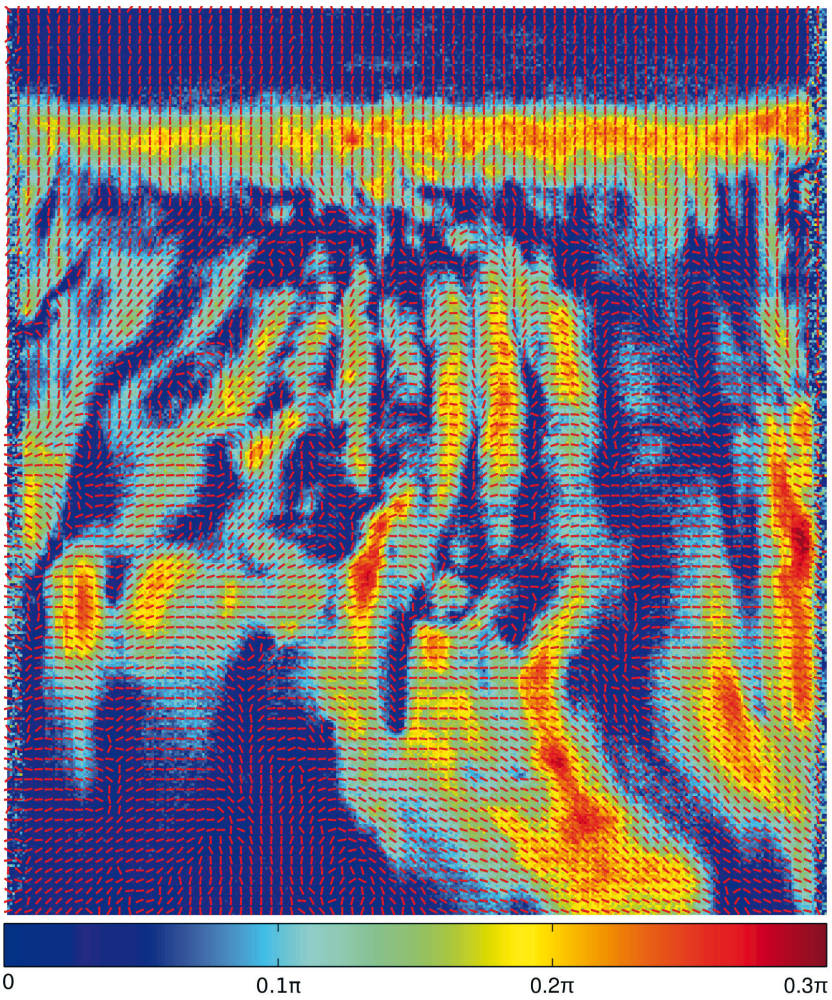

Figure 4. The retardance image (color map) and the orientation of the retardance (lines), corresponding to the transitional zone A to B in figure 3a and 3b. The direction of the lines indicates the fast axis. The number of lines have been strongly reduced in order for visibility. The horizontal color bar gives the value of the retardance.

4. CONCLUSION

The Mueller matrix imaging (MMI) ellipsometer system operating in the NIR is proven to be extremely useful for studying aggregation of anisotropic nanoparticles in solution. The combination of both retardance, orientation of the retardance, the diattenuation and the orientation of the diattenuation, and possibly also the degree of polarization, is a unique and powerful imaging tool that is particularly suitable for studying

dispersions of anisotropic nanoparticles. Furthermore, the high spatial resolution, together with the speed of acquisition makes it ideal for resolving both spatial features and dynamics. The simple and high performance calibration of the MMI makes it trivial to operate and supplies data that allows for future quantification. We have shown here that the MMI can be used for separation of the different aggregate phases and the complex nematic domain structures in colloidal dispersions of Na-fluorohectorite.

REFERENCES

[1] Aas, L. M. S., Ellingsen, P. G., and Kildemo, M., "Dynamic Response of a fast near infra-red Mueller matrix ellipsometer," Journal of Modern Optics, 57(17), 1603-1610 (2010).

[2] Aas, L. M. S., Ellingsen, P. G., and Kildemo, M., "Near infra-red Mueller matrix imaging system and application to retardance imaging of strain," Thin Solid Films, 519(9), 2737-2741 (2010).

[3] De Martino, A., Kim, Y.-K., Garcia-Caurel, E., Laude, B., and Drévillon, B., "Optimized Mueller polarimeter with liquid crystals," Optics letters, 28(8), 616-8 (2003).

[4] Compain, E., Poirier, S., and Drevillon, B., "General and self-consistent method for the calibration of polarization modulators, polarimeters, and mueller-matrix ellipsometers," Applied optics, 38(16), 3490-502 (1999).

[5] Ladstein, J., Stabo-Eeg, F., Garcia-Caurel, E., and Kildemo, M., "Fast near-infra-red spectroscopic Mueller matrix ellipsometer based on ferroelectric liquid crystal retarders," physica status solidi (c), 5(5), 1097-1100 (2008).

[6] Lu, S. Y., and Chipman, R. A., "Interpretation of Mueller matrices based on polar decomposition," Journal of the Optical Society of America A, 13(5), 1106-1113 (1996).

[7] Manhas, S., Swami, M. K., Buddhiwant, P., Ghosh, N., Gupta, P. K., and Singh, K., "Mueller matrix approach for determination of optical rotation in chiral turbid media in backscattering geometry," Opt. Express, 14, 190-202 (2006).

[8] Ossikovski, R., De Martino, A., and Guyot, S., "Forward and reverse product decompositions of depolarizing Mueller matrices," Optics letters, 32(6), 689-691 (2007).

[9] Fossum, J. O., Gudding, E., Fonseca, D. d. M., Meheust, Y., DiMasi, E., Gog, T., and Venkataraman, C., "Observations of orientational ordering in aqueous suspensions of a nano-layered silicate," Energy, 30(6), 873-883 (2005).

[10] Ringdal, N. I., Fonseca, D. M., Hansen, E. L., Hemmen, H., and Fossum, J. O., "Nematic textures in colloidal dispersions of Na-fluorohectorite synthetic clay," Physical Review E, 81(4), 1-10 (2010).

[11] Hemmen, H., Ringdal, N. I., N., E., Engelsberg, M., Hansen, E. L., Méheust, Y., Fossum, J. O., and Knudsen, K. D., "The isotropic-nematic interface in suspensions of Na-fluorohectorite synthetic clay," Langmuir : the ACS journal of surfaces and colloids, 25(21), 12507-15 (2009).

[12] DiMasi, E. d. M., Fossum, J. O., Gog, T., and Venkataraman, C., "Orientational order in gravity dispersed clay colloids: A synchrotron x-ray scattering study of Na fluorohectorite suspensions," Physical Review E, 64(6), 061704-061704 (2001).

[13] Fonseca, D. M., Méheust, Y., Fossum, J. O., Knudsen, K. D., and Parmar, K. P. S., "Phase diagram of polydisperse Na-fluorohectorite–water suspensions: A synchrotron small-angle x-ray scattering study," Physical Review E, 79(2), 021402-021402 (2009).

[14] De Azevedo, E., Engelsberg, M., Fossum, J. O., and E., R., "Anisotropic water diffusion in nematic self-assemblies of clay nanoplatelets suspended in water," Langmuir, 23(9), 5100-5105 (2007).

[15] Solin, S. A., "Clays and clay intercalation compounds: properties and physical phenomena," Annual review of materials science, 27(1), 89-115 (1997).

L. M. S. Aas, M. Kildemo, Y. Cohin, and E. Søndergård, Determination of small tilt angles of short GaSb nanopillars using UV–visible Mueller matrix ellipsometry, Thin Solid Films **541**, 97–101 (2013)

Paper 10

Thin Solid Films 541 (2013) 97–101

Contents lists available at SciVerse ScienceDirect

Thin Solid Films

journal homepage: www.elsevier.com/locate/tsf

Determination of small tilt angles of short GaSb nanopillars using UV–visible Mueller matrix ellipsometry

L.M.S. Aas [a,*], M. Kildemo [a], Y. Cohin [b], E. Søndergård [b]

[a] Department of Physics, Norwegian University of Science and Technology, 7491 Trondheim, Norway
[b] Surface du Verre et Interfaces, Unité Mixte de Recherche CNRS/Saint-Gobain, UMR 125, 39 Quai Lucien Lefranc, F-93303 Aubervilliers Cedex, France

ARTICLE INFO

Available online 21 November 2012

Keywords:
Nanomaterials
Ellipsometry and polarimetry
Subwavelength structures
Nanostructures

ABSTRACT

We demonstrate that small tilts away from the substrate normal, of short (30–40 nm high) nanopillars, may be detected and modeled by spectroscopic UV–Visible Mueller Matrix Ellipsometry (MME). The pillars were produced by sputtering a GaSb substrate with a low energy unfocused ion beam. It has previously been found that the pillars will point in the direction of the ion flux. For both samples reported here, the ion-incidence was unintentionally tilted away from the substrate normal by 2.8 and 4.8°. The MME measurements were performed using both multiple angles of incidence, and 360° rotation of the incidence plane. Graded uniaxial effective medium models were fitted to the experimental data, and through Euler angle rotations of the dielectric tensor, the tilt angle and the orientation of the pillar direction, were obtained. The UV part of the spectrum enhanced the tilt angle sensitivity down to 0.02–0.05°. A data presentation that enhances the understanding of the symmetry in the crystallographic information obtained from spectroscopic MME is proposed. The off block diagonal Mueller matrix elements are more sensitive to the in-plane anisotropy, whereas for small tilt angles m_{14} scales approximately with $\theta\sin(\phi)$.

1. Introduction

Semiconductor nanopillars are currently intensively investigated as building blocks for metamaterials and efficient light harvesting photovoltaic devices [1–4]. As such, self-organized nanopatterned GaSb is also an interesting model system in terms of developing metrology methods in order to serve both for in-situ and ex-situ monitoring and the control of the formation process. Furthermore, the formation mechanism of such GaSb nanopillars is a fascinating materials science that deserves special attention.

It has been observed that a dense pattern of nanopillars forms on GaSb [5], InP [6], InSb [7], InAs [7], and GaAs surfaces [8], upon low ion energy bombardment, i.e. through abrasion (not to be confused with sputter deposition). The idea of nanopatterning by ion beam sputtering was probably motivated by the discovery of ripple formation on glass surfaces upon low energy ion bombardment [9]. The mechanisms of the ripple formation on glass substrates are well described by the commonly accepted Bradley–Harper model [5–8,10]. However, the explanation of the formation of tall nanopillars (up to 500 nm high) of III–V semiconductors has been much disputed. In recent studies [11–16], it was demonstrated, by in-situ characterization using spectroscopic Mueller Matrix ellipsometry, that the most likely formation mechanism of the nanopillars could be described by a three stage process [11] driven by the difference in diffusion velocities and sputtering yields of the two components of the semiconductor. The initial stage is related to the removal of oxides, creation of an amorphous surface layer which finally lead to segregated Ga droplets on the surface [11]. The Ga droplets act as a self-assembled etch-mask resulting in the formation of GaSb nanopillars under the droplets. The abrasion of the Ga droplets is compensated by the diffusion of Ga atoms toward the top of the pillars, supplied by the apparent preferential sputtering of Sb. The third stage of the growth results in a steady state where the supply and abrasion of Ga reaches a dynamic equilibrium because of the limited diffusion length of Ga atoms at the surface [11].

The optical characterization (MME), both in-situ and ex-situ, in combination with Scanning Electron Microscopy (SEM), Scanning Transmission Electron Microscopy and X-ray photoemission spectroscopy proved to be crucial in order to reveal the mechanism of the formation for the GaSb nanopillars. Furthermore, through the optical characterization, it was proven that the Bradley–Harper model was insufficient to describe the formation process especially for taller pillars, and that the “diffuse interface model” [11] better matches the in-situ growth curves obtained from spectroscopic ellipsometry. In particular, the in-situ Mueller matrix spectroscopic data recorded for sputtering at different substrate temperatures revealed together with the diffuse interface model that taller cones could be formed due to the increased Ga diffusion length by resupplying the Ga etch-mask [11]. Finally, visible spectroscopic MME could reveal the formation of nanopillars pointing in the direction of the incident sputtered ions, a fact that was independently proven by destructive cross-sectional SEM [16].

* Corresponding author. Tel.: +47 73593455; fax: +47 73597710.
E-mail address: lars.aas@ntnu.no (L.M.S. Aas).

0040-6090/$ – see front matter © 2012 Elsevier B.V. All rights reserved.
http://dx.doi.org/10.1016/j.tsf.2012.10.136

2. Experimental details

In this work two samples of nanopatterned GaSb were prepared by sputtering a clean GaSb surface by low energy (300 eV) Ar^+ ions with an average flux of 2.4×10^{15} ion cm^{-2} s^{-1} at a mean temperature of 308 K. Both samples (A and B) were prepared under the same experimental conditions as the previously reported sample C in Ref. [13], resulting in a nanopillar density of 711 +/− 56 cones/μm^2, with a long range hexagonal pattern resulting in an effective lattice constant of $a_{hex}=40.4$ nm. The Voronoi tessellation technique applied to SEM images resulted in an average pillar separation of 42.2 nm with a standard deviation of 10 nm, while a similar analysis of the images from Atomic Force Microscopy (AFM) resulted in an average separation of 45 nm. Typical AFM and SEM images of such pillars are found in Refs. [12–14].

Spectroscopic MME was performed in the current work using a dual rotating compensator ellipsometer (RC2 from JA Woollam Company). Spectra were recorded from 0.73 to 5.9 eV, with simultaneous detection using InGaAs and Si based spectrographs with a total acquisition time of 20 s per spectrum. The measurements were performed using collimated light, whereas the large original beam waist diameter was reduced by an aperture down to approximately 1.5 mm before instrument calibration. The measurement accuracy was calibrated to 0.002 for the Mueller matrix elements of air. The sample surface was carefully aligned to allow for all azimuthal rotations of the sample (0° to 360° in steps of 5°). The full spectra were recorded for all of the azimuthal orientations at three incidence angles 45, 55 and 65°. The sample was realigned prior to the recording of each incidence angle.

3. Theory

A graded anisotropic Bruggeman effective medium model has been shown to appropriately model the optical response of GaSb nanostructured by ion abrasion. The model regards the cones as a stack of cylinders, see Fig. 1, whereas the anisotropy is introduced by the basic cylindrical shape. As a result, the long axis along the cones is assumed to have a depolarization factor $L_z=0$ (i.e. infinite screening factor $\sigma\to\infty$), while perpendicular to the cones, the depolarization factor is given by $L_{x,y}=0.5$ (screening factor $\sigma=2$). As a result, the depolarization factors L may be fixed for each sub-layer in the fit, which is important in order to reduce parameter correlations. The resulting effective dielectric function $\varepsilon_{||}$ parallel to the optic axis is the volume average of the dielectric function of GaSb and void $\varepsilon_{||}=f_{GaSb}\varepsilon_{GaSb}+f_v\varepsilon_v$. The effective dielectric function normal to the optic axis ($\varepsilon_\perp$) is found by the solution of $f_{GaSb}\frac{\varepsilon_{GaSb}-\varepsilon_\perp}{\varepsilon_\perp+\varepsilon_{GaSb}}+f_v\frac{\varepsilon_v-\varepsilon_\perp}{\varepsilon_\perp+\varepsilon_v}=0$, where $f_{v/GaSb}$ are the volume fill factors and $\varepsilon_{v/GaSb}$ are the dielectric functions, of void and crystalline GaSb, respectively. In the limit of very short cones, the latter approximation may be too crude since the cylinders will be strongly truncated, and one would then rather expect $0<L_z<1.0$ [17].

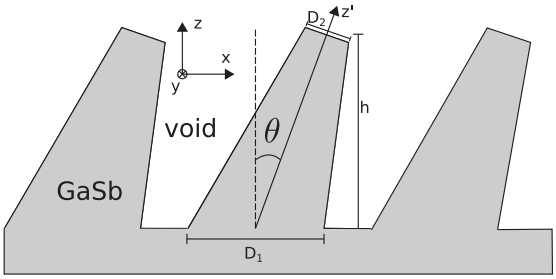

Fig. 1. Sketch of the geometry used in the optical model. The height (h) of the GaSb nanopillars, the bottom diameter D_1, the top diameter D_2, and the tilt angle θ are illustrated in the figure.

The grading was introduced by fitting for a relative diameter of the bottom of the cones (D_1), and the top of the cones (D_2). The fill factor entering into the effective medium model could thereby in an appropriate fashion introduce the fact that the pillars are distributed in a network with an average of 6 nearest neighbors (thus approximated by a hexagonal network). The fill factor for each subdivided layer was therefore modeled as follows [13]:

$$f_{GaSb}(n)=\frac{\pi}{\sqrt{12}}d^2(n),\ \text{with}\ d(n)=D_1-(n-1)\frac{D_1-D_2}{N-1},\ n=1..N, \quad (1)$$

where $d(n)$ is the diameter of each layer n and N is the total number of layers, denoted linear in d in Table 1. The dielectric function of c-GaSb used in this work was compiled data files, previously presented in Ref. [14] and references therein. An alternative grading profile was also investigated, where the assumption was a linear grading in the GaSb fill factor $f_{GaSb}(n)$. In terms of a hexagonal network, the resulting diameter of each pillar is then given by $d(n)=\sqrt{\frac{\sqrt{12}}{\pi}f_{GaSb}(n)}$. The advantage of the linear gradient in the diameter is that the conical shape of the pillars is properly modeled, and it has previously been shown to supply accurate heights for the cones, in comparison to AFM [12]. As a result, the real time monitoring of the nonlinear growth of GaSb cones has proven to be extremely valuable in order to reveal the formation process for such self-organized dense pattern of nano cones [12]. The models are in this work still simplified, since we are neglecting a layer of a-GaSb and oxide covering the pillars and are only considering a c-GaSb core of the cones together with void [13], which requires more advanced constraints to obtain physically acceptable solutions.

4. Results

Fig. 2 shows (symbols) the experimentally recorded standard ellipsometric elements, $M_{12}=N$, $M_{33}=C$ and $M_{34}=S$ elements [18] recorded at a given azimuthal orientation for the three angle of incidences 45, 55 and 65°, for sample A. Fig. 3 shows (symbols) the full Mueller matrix spectrum for three azimuthal orientations of the sample, recorded at an angle of incidence of 45°. To better understand the crystallographic problem at hand, it is here suggested to present the data as a polar color map, where the radius is the photon energy in the range 0.73–5.9 eV, and the polar angle represents the incident plane, i.e. the sample is stationary. Fig. 4 shows the measured spectroscopic Mueller matrix of sample A, for all incident planes with incidence angle 45°. Figs. 3 and 4 visualize well the increased sensitivity for the anisotropy in the sample for higher photon energies. The anisotropy increases particularly strongly for photon energies above approximately 3.0 eV. By considering the dielectric function of GaSb, which has its main critical points in the visible near UV, this increase in sensitivity may therefore be scaling with both the complex refractive index and the photon energy.

The model described in Section 3 was first fitted to the standard ellipsometric block diagonal elements ($N=m_{12}$, $C=m_{33}$ and $S=m_{34}$), where the tilt of the cones was to a first approximation neglected. Fig. 4 shows that the off-diagonal elements are small and oscillating around

Table 1
The fitted parameters in the optical model for the two different gradients as described in the text. The diameters D_1 and D_2 were constrained to be within 0 and 1.

Sample	Gradient	Height (nm)	θ (°)	D_1	D_2	MSE
A	Linear d(n)	39.3	4.78	1	0.04	4.46
A	Linear $f_{GaSb}(n)$	33.4	4.56	0.93	0.15	6.25
B	Linear d(n)	37.0	2.82	1	0.03	5.91
B	Linear $f_{GaSb}(n)$	31.9	2.67	0.94	0.10	4.84

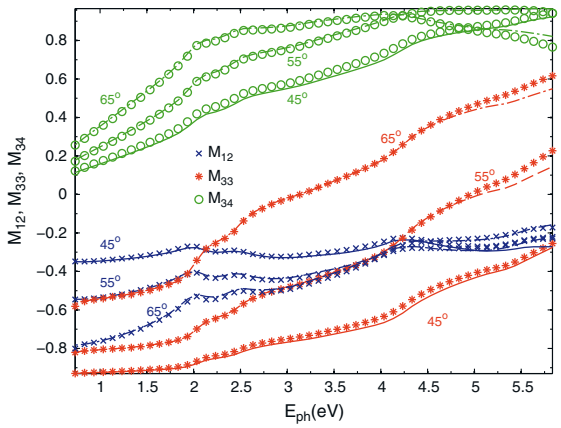

Fig. 2. Simulated (lines) and measured (symbols) spectra of M_{12}, M_{33} and M_{34} (N,C,S) at three different incidence angles, for a near block diagonal Mueller matrix (the incidence plane was found oriented 2.7° with respect to the pillar tilt axis). The experimental data are for simplicity only shown for every 0.15 eV.

zero when rotating the incidence plane, while the block diagonal elements only have small oscillations around a large value, see Figs. 2 and 3. The tilt of the cones was implemented by two Euler rotations (ϕ,θ). The tilt-angle and the relative orientation of the tilt direction with respect to the incidence plane, was determined by fitting only the off-diagonal Mueller matrix elements. The latter procedure was chosen since small modeling or systematic measurement errors result in a loss of sensitivity to the Euler rotations when fitting directly on the large block-diagonal Mueller matrix elements. An alternative approach would be to strongly modify the weights of the off-diagonal elements. The Euler angles were then fixed, and the model was re-optimized to the block diagonal elements (N, C and S). The process was repeated until convergence.

The simulated Mueller matrix elements using the fitted parameters are shown as full lines in Figs. 2 and 3, and as a polar color map in Fig. 5. It is particularly observed that the elements N, C and S are within an acceptable accuracy for all three incidence angles. The off-diagonal elements have also been fitted to a reasonable accuracy, as seen in Fig. 3, and also by comparing Figs. 4 and 5. By comparing the simulated and the experimental data for the three incidence planes plotted in Fig. 3, it is evident that the goodness of the fit varies as a function of ϕ. In particular, the MSE varies by a factor of 1.6 with 180° symmetry. The MSE variation may be due to sample inhomogeneity and the elliptical shape of the light beam on the sample. It is noted that for clarity, the experimental and simulated data has been rotated by the azimuthal angle determined from the fit, in order for the pillars to point along the horizontal axis in Figs. 4 and 5 (i.e. the condition for a diagonal Jones matrix and equivalently block diagonal Mueller matrix) and along $\phi = 0°$ in Fig. 3. The fitted parameters for the two samples A and B using the two variations of the optical model described above are summarized in Table 1. It shows that sample A has slightly taller nanopillars and higher tilt angle (θ) compared to sample B. For both samples, it is observed that the height and the tilt angle depend on the choice of gradient (nanopillar diameter profile), i.e. the linear in fill-factor or the linear in diameter. This is illustrated in Fig. 6, which shows the diameter and the fill-factor profile for sample A using these two models. Due to the very low fill factor in the top of the linear in diameter profile (i.e. D_2 is small) the correlation to the height is increased. This problem was suggested in previous work resolved by constraining

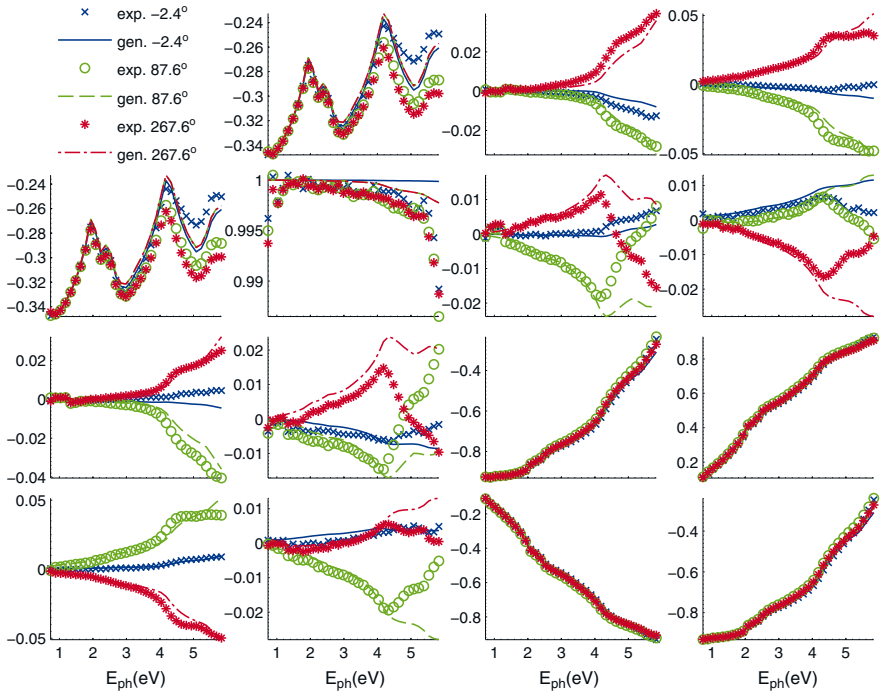

Fig. 3. Measured (symbols) and simulated (lines) Mueller matrix spectra at 45° incidence, for three different incidence plane orientations with respect to the pillar tilt axis. The experimental data are for simplicity only shown for every 0.10 eV.

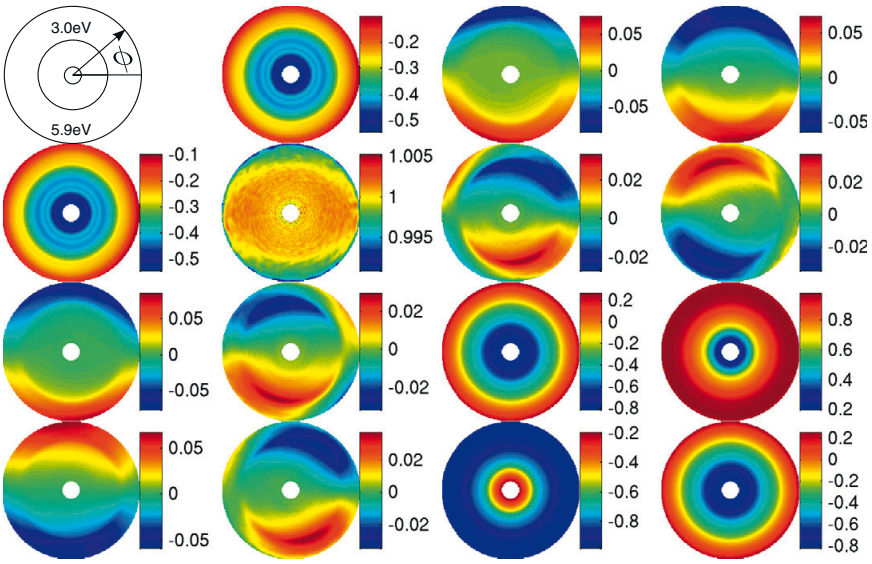

Fig. 4. The measured normalized spectroscopic Mueller matrix of sample A, at 45° incidence. The data is presented in a polar plot where the radius represents the photon energy, $r = E_{ph}$[eV], and ranges from 0.73 eV (from the white circle) to 5.9 eV (at the outer edge). The orientation of the incidence plane with respect to the pillar axis, is given by the polar angle (azimuth orientation (ϕ)), as seen from the inset. The tilt axis is here in the horizontal direction.

the top diameter D_2 to e.g. 0.1, as a layer of near unit refractive index only marginally changes the optical response of the layer [13]. On the other hand, in the linear in fill-factor gradient model, the resulting diameters are well within the constrained limits (i.e. diameters $D_1 < 1$ and $D_2 > 0$). The linear in diameter profile shows, however, a more similar diameter to the pillars observed directly by cross-section SEM [12–14], and such a profile also supplied systematically a height in better correspondence to AFM data, when fitted in the range 1.46–2.85 eV [13].

Some simple conclusions can be made by inspection of the data recorded upon azimuthal rotation of the incidence plane with respect to the sample, see Figs. 4 and 5. First of all, the simple nearly

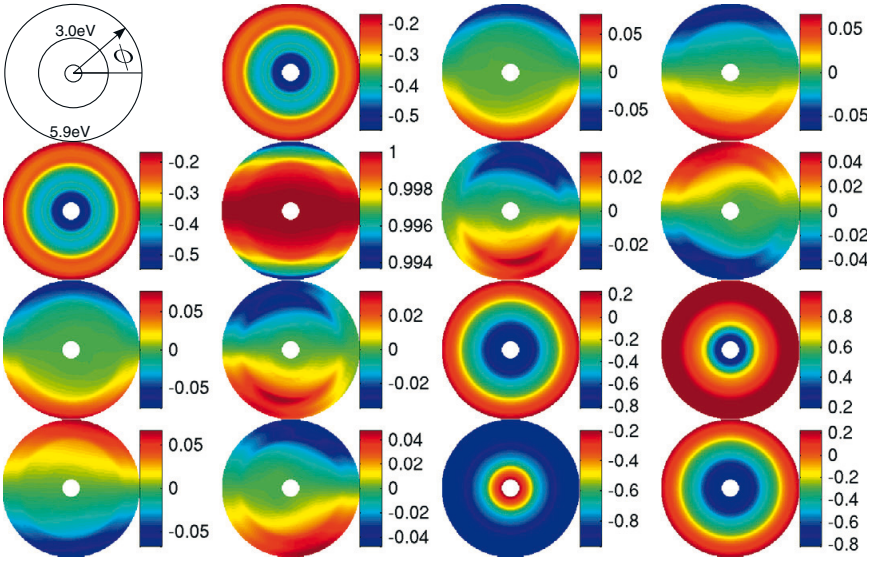

Fig. 5. The simulated spectroscopic Mueller matrix of sample A, at 45° incidence, using the fitted parameters in Table 1, and using a linear in diameter gradient. The data is presented in a polar plot where the radius represents the photon energy, $r = E_{ph}$[eV], and ranges from 0.73 eV (from the white circle) to 5.9 eV (at the outer edge). The orientation of the incidence plane with respect to the pillar axis, is given by the polar angle (azimuth orientation (ϕ)), as seen from the inset. The tilt axis is here in the horizontal direction.

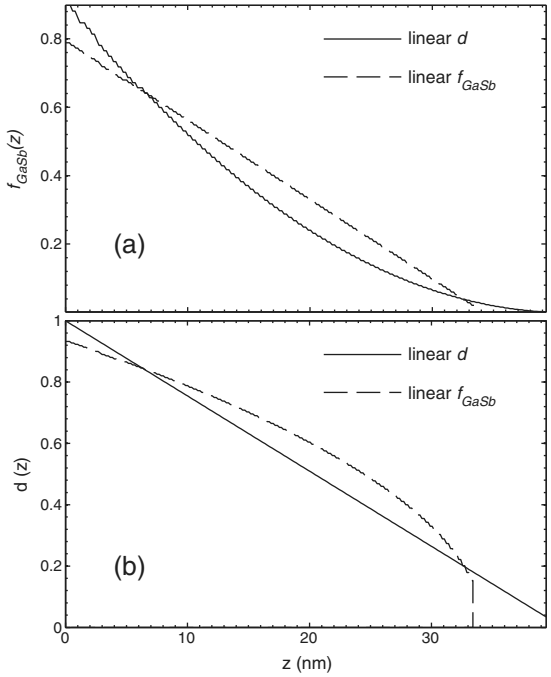

Fig. 6. The GaSb fill factor, Figure (a), and the pillar diameter, Figure (b), for the two models with a linear gradient in the diameter (solid line) and a linear gradient in GaSb fill factor (dotted line).

sinusoidal variation of the m_{14} element upon rotation of the incidence plane is striking, and makes a simple interpretation in terms of the tilt orientation (ϕ). The accuracy of ϕ was, by comparing to the noise level and systematic errors, estimated to be in the range of 0.5°. It is well known that the Mueller matrix is block diagonal (all the off-diagonal elements are zero) for no in-sample plane anisotropy, and will thus only be non-zero in the case of anisotropy in the sample plane, such as a small nanopillar tilt. Furthermore, it is observed that the amplitude of the oscillation in the m_{14} element is a factor 2–3 larger than variations in the block diagonal elements. Finally, from the fitted model, we have performed several simulations, where we inspect the change of the m_{14} element upon varying the tilt angle (θ), and have concluded that the amplitude seems to be proportional to the tilt angle. As a result, we propose that m_{14} may, for small tilt angles, be roughly approximated by $m_{14} \propto \theta \cdot \sin(\phi)$, with θ in radians. By comparing to the typical noise level of the instrument, a high sensitivity is obtained on the tilt angle θ, and we estimated the ability to detect nanopillar tilts as low as $\theta = 0.02$–$0.05°$. The tilt angle changes by 0.2° depending on gradient profile, i.e. the absolute accuracy is strongly correlated to the choice of gradient. However, for a given gradient the tilt angle was determined to the second decimal (Table 1). Previous work [12,13,16] showed that the linear in diameter grading is consistent with SEM measurements with respect to the nanopillar height, but by comparing the tilt angle from the two grading profiles it gives a realistic indication of the absolute tilt angle accuracy.

Although the amplitude of oscillation of the block diagonal elements are smaller than the off-diagonal elements, they may possibly strongly contribute to the overall solution of the problem, if it is noticed that they also oscillate around an average value upon azimuthal rotation of the sample, which will be investigated further in future work.

5. Conclusions

UV–vis spectroscopic Mueller Matrix Ellipsometry using a dual rotating compensator ellipsometer operating in the range 0.73–5.9 eV, shows that the sensitivity to anisotropy increases considerably as a function of photon energy. We observe particularly a strong increase in the anisotropy above 3 eV. A high accuracy is obtained on the tilt angle θ, for a given gradient profile, and for the two samples studied here it was determined to the 2nd decimal place. A reasonable optical model allowed to estimate the sensitivity to pillar tilts down to $\theta = 0.02$–$0.05°$. The off-diagonal Mueller matrix elements allow for a higher sensitivity to anisotropies in the sample plane.

Acknowledgments

L.M.S.A acknowledges support from “The Norwegian Research Center for Solar Cell Technology” (project num. 193829).

References

[1] J. Zhu, Z. Yu, G. Burkhard, C. Hsu, S. Connor, Y. Xu, Q. Wang, M. McGehee, S. Fan, Y. Cui, Nano Lett. 9 (1) (2009) 279.
[2] Z. Fan, H. Razavi, J.-w. Do, A. Moriwaki, O. Ergen, Y.-L. Chueh, P. Leu, J. Ho, T. Takahashi, L. Reichertz, S. Neale, K. Yu, M. Wu, J. Ager, A. Javey, Nat. Mater. 8 (2009) 648.
[3] J. Zhu, C. Hsu, Z. Yu, S. Fan, Y. Cui, Nano Lett. 10 (6) (2010) 1979.
[4] G. Mariani, P. Wong, A. Katzenmeyer, F. Leonard, J. Shapiro, D. Huffaker, Nano Lett. 11 (6) (2011) 2490.
[5] S. Facsko, T. Dekorsy, C. Koerdt, C. Trappe, H. Kurz, A. Vogt, H. Hartnagel, Science 285 (5433) (1999) 1551.
[6] Y. Yuba, S. Hazama, K. Gamo, Nucl. Instrum. Methods Phys. Res., Sect. B 206 (2003) 648.
[7] F. Frost, B. Ziberi, T. Hoche, B. Rauschenbach, Nucl. Instrum. Methods Phys. Res., Sect. B 216 (2004) 9.
[8] Y. Wang, S.F. Yoon, C.Y. Ngo, J. Ahn, Nanoscale Res. Lett. 2 (2007) 504.
[9] C.S.M. Navez, D. Chaperot, C.R. Acad. Sci. Paris 254 (1962).
[10] R. Bradley, J. Harper, J. Vac. Sci. Technol., A 6 (4) (1988) 2390.
[11] S. Le Roy, E. Søndergård, I.S. Nerbø, M. Kildemo, M. Plapp, Phys. Rev. B 81 (16) (2010) 161401.
[12] I.S. Nerbø, S. Le Roy, M. Kildemo, E. Søndergård, Appl. Phys. Lett. 94 (2009) 213105.
[13] I.S. Nerbø, M. Kildemo, S. Le Roy, I. Simonsen, E. Søndergård, L. Holt, J.C. Walmsley, Appl. Opt. 47 (2008) 5130.
[14] M. Kildemo, I.S. Nerbø, S. Hagen, S. Leroy, E. Søndergård, Mater. Sci. Eng., B 165 (3) (2009) 217.
[15] I.S. Nerbø, S.L. Roy, M. Foldyna, E. Søndergård, M. Kildemo, Opt. Express 19 (13) (2011) 12551.
[16] I.S. Nerbø, S. Le Roy, M. Foldyna, M. Kildemo, E. Søndergård, J. Appl. Phys. 108 (2010) 014307.
[17] G. Niklasson, Department of Engineering Sciences, Uppsala University, Uppsala, Sweden, Private Commun. (2011).
[18] P. Hauge, R. Muller, C. Smith, Surf. Sci. 96 (1980) 81.

K. Høydalsvik, L. M. S. Aas, E. Døli, E. Søndergård, M. Kildemo, and D. W. Breiby, Combining surface X-ray scattering and ellipsometry for non-destructive area-averaged characterisation of ion beam-induced GaSb surface nanostructures, Accepted for publication in Thin Solid Films (2013)

Paper 11

Combining surface X-ray scattering and ellipsometry for non-destructive area-averaged characterisation of ion beam-induced GaSb surface nanostructures

Kristin Høydalsvik[a], Lars Martin S. Aas[a], Ellen Døli[a], Elin Søndergård[b], Morten Kildemo[a], Dag Werner Breiby[a,]

[a]*Department of Physics, The Norwegian University of Science and Technology (NTNU), N-7491 Trondheim, Norway*
[b]*Surface du Verre et Interfaces, Unit Mixte de Recherche CNRS/Saint-Gobain, UMR 125, 39 Quai Lucien Lefranc, F-93303 Aubervilliers Cedex, France*

Abstract

Producing surfaces textured with a homogeneous pattern of nanoscale structures is increasingly important for fabrication of semiconductor devices. Although techniques exist for imaging surface nanostructures on a local scale, these techniques are often impractical for use over large areas for finding average structural information. The nanostructured surface in this study consists of densely packed cones produced by sputtering a mono-crystalline GaSb substrate with a low-energy unfocused ion beam, yielding self-organized cones that are slightly tilted away from the sample normal. Here, we devise an all-optical non-destructive characterisation scheme using Grazing-Incidence Small-Angle X-ray Scattering (GISAXS) and Spectroscopic Mueller Matrix Ellipsometry (MME) for characterising all main dimensions including average height, lateral spacing and packing motifs, and the cone top and bottom diameters. It is further shown that both MME and GISAXS are sensitive to small tilts of the nanopillar axis from the surface normal.

Keywords: Grazing-Incidence Small-Angle X-ray Scattering, GISAXS, Spectroscopic Ellipsometry, Mueller Matrix, Surface structure, Gallium antimonide, Sputtering

1. Introduction

Nanostructured surfaces of semi-conducting materials are promising for applications within optical and optoelectronic applications, such as solar cells, photodetectors and lasers. In particular, self-assembled nanostructures have raised interest in recent years due to the low cost and high effectiveness of such bottom up techniques [1–9]. Ion Beam Sputtering (IBS) of mono-crystalline GaSb surfaces leads to self-assembled nanostructures over large sample areas in a one-step procedure, yielding densely packed oriented nano-cones [1–4].

Spectroscopic Mueller Matrix Ellipsometry (MME) is a tool for investigating surfaces, based on measuring the change of polarisation state of specularly reflected light. This technique gives access to the anisotropic electronic characteristics of the material, and through mathematical models parameters like the tilt of the cones and the *relative* diameters and height of the cones can be found. Grazing-Incidence Small-Angle X-ray Scattering (GISAXS) is an X-ray technique where surface sensitivity is obtained by using a grazing incident angle of the X-rays, giving a greatly reduced scattering contribution from the substrate because of total external reflection [10]. This technique is thus especially well suited for investigating surface structures such as the GaSb nano-cones [11, 12], yielding information about the in-plane average distance between the cones and lateral structuring.

GISAXS and MME are bothcalling non-destructive and area-averaging techniques that require no special sample preparation, and the complementary nature of the two techniques makes their combined use desirable for investigation of nano-structured surfaces. In this work the nanostructured surface of a GaSb sample is investigated by using and comparing the results from the complementary methods of MME and GISAXS. We report the average height, lateral spacing and structure, the cone profile, and the small tilts of the cone axes of nano-cones.

2. Experimental

The sample investigated in this work was prepared by sputtering a clean GaSb(100) substrate by low energy (300 eV) Ar^+ ions for 10 minutes with an average flux of 2.4×10^{15} ions cm^{-2} s^{-1} at a mean temperature of 308 K. The sputter direction was intended to be normal to the sample surface, but a slight misalignment of the ion gun by up to a few degrees might have been present.

A sketch of the idealized geometry of the nano-cones with tilt angle θ, bottom diameter D_1, top diameter D_2, height h and distance between nano-cones d is shown in Figure 1.

Spectroscopic MME was performed using a dual rotating compensator ellipsometer (RC2 from JA Woollam Company). Spectra were recorded from 0.73 to 5.9 eV, with simultaneous detection using InGaAs and Si based spectrographs with a total acquisition time of 20 seconds per spectrum. The measurements were performed using collimated light with a beam waist of approximately 1.5 mm. The sample surface was carefully aligned to allow for azimuthal rotations of the sample (ϕ of 0° to 360° in steps of 5°). Full spectra were recorded for all of the azimuthal orientations at the incidence angles 45°, 55° and 65°

Email address: dag.breiby@ntnu.no (Dag Werner Breiby)

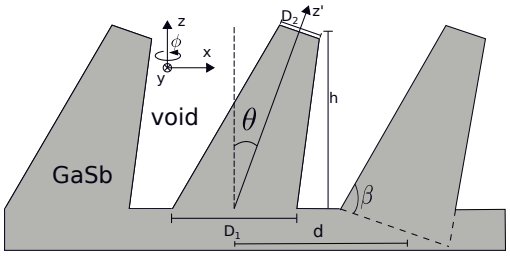

Figure 1: Sketch of the cone geometry. The height h of the GaSb nano-cones, the bottom diameter D_1, the top diameter D_2, the inter-cone distance d, the tilt angle θ and the base angle β are indicated in the figure. A Cartesian coordinate system is defined.

(defined from the surface normal). The sample was realigned prior to the recording of each incidence angle.

GISAXS measurements were performed using X-rays of wavelength 1.54 Å from a copper microfocus source with source current of 1 mA and acceleration voltage 50 kV. Optics from Xenocs and JJ X-Ray were used for collimation. For detection a Pilatus (1M) area detector from Dectris [13] positioned a distance 2112 mm from the sample was used, with an exposure time of 4 hours. Using a goniometer the grazing incident angle α_i was set to $0.23^\circ \pm 0.01^\circ$. Between each measurement the sample was realigned to ensure that the same central area of the sample was measured. Complementary Grazing-Incidence Wide-angle X-ray Scattering (GIWAXS) measurements were performed in order to investigate the crystalline structure. The experimental geometry is similar to that for GISAXS, except that the detector is moved closer to the sample (146 mm) to cover the wider scattering angles, and the CuKα radiation used was generated by a rotating anode source. The grazing incident angle was set to $0.25^\circ \pm 0.01^\circ$, and ϕ was rotated in steps of 2°. The scattered intensity is measured as a function of the scattering vector $\mathbf{Q} \equiv \mathbf{k}_f - \mathbf{k}_i$, where $\mathbf{k}_i$ and $\mathbf{k}_f$ denote the incoming and scattered wave-vectors, respectively.

3. Results and discussion

MME results are shown in Figure 2, with a polar map of the normalized spectroscopic Mueller matrix for all incidence planes. The radial direction represents a linear mapping of the photon energy from 0.73 to 5.9 eV while the angle ϕ represents the incidence plane. The sample is aligned so that the nano-cones are pointing in the direction of the incidence plane at $\phi = 0$, for this angle the block off-diagonal elements are zero and may be seen as pseudo isotropic. As the incidence plane is rotated the block off-diagonal elements exhibit one minimum and one maximum, suggesting that the material is uniaxial and tilted [14].

The ellipsometry data was modelled using a structure with a graded anisotropic Bruggeman effective medium, where the cones are represented as a stack of 50 cylinders. The Schubert algorithm [15], based on the 4×4 differential matrix formalism by Berreman [16], was used to calculate the reflection coefficients for each of these anisotropic layers. In the effective medium approximation a stack of cylinders corresponds to a depolarization factor equal to zero in the $z-$direction and 0.5 in the $x-$ and $y-$directions for each of the layers. The effective dielectric function parallel to the optical axis, $\epsilon_\parallel$, was the volume average of the dielectric function of GaSb and void, $\epsilon_\parallel = f_{\mathrm{GaSb}}\epsilon_{\mathrm{GaSb}} + f_{\mathrm{v}}\epsilon_{\mathrm{v}}$. The dielectric function normal to the axis was found by solving $f_{\mathrm{GaSb}}\frac{\epsilon_{\mathrm{GaSb}}-\epsilon_\perp}{\epsilon_\perp+\epsilon_{\mathrm{GaSb}}} + f_{\mathrm{v}}\frac{\epsilon_{\mathrm{v}}-\epsilon_\perp}{\epsilon_\perp+\epsilon_{\mathrm{v}}} = 0$. The dielectric function of crystalline GaSb, ϵ_{GaSb}, is tabulated data [17].

From previous atomic force microscopy analyses the cones were found to be distributed with six nearest neighbours [18], allowing the assumtion of a hexagonal lattice. Assuming that the radius is linearly decreasing by height, the fill factor of each layer was modelled as [14, 18, 19]

$$f_{\mathrm{GaSb}}(n) = \frac{\pi}{\sqrt{12}} d(n)^2,$$

where

$$d(n) = D_1 - (n-1)\frac{D_1 - D_2}{N-1}, \quad n = 1, 2, \ldots, N.$$

Here $d(n)$ is the cone diameter at layer n, normalised to the model restriction on the cone diameters ($D_{1,2}$) of a close-packed hexagonal lattice. The tilt angle of the nano-cones was modelled by two-angle Euler rotation of the effective dielectric tensor of each layer.

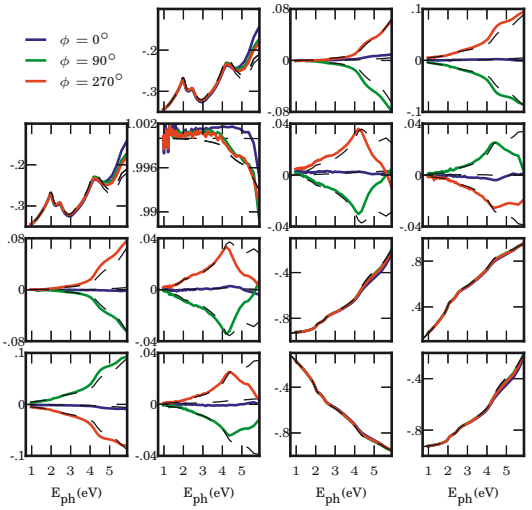

Figure 3: The measured (solid line) and simulated (dashed line) spectroscopic Mueller matrix for the incidence planes $\phi = 0^\circ$, 90° and 270°, at 45° incidence angle.

The measured data was fitted for all incidence angles and incidence planes. The height h, top diameter D_2 and bottom diameter D_1 were estimated using the $N \equiv m_{12}$, $C \equiv m_{33}$ and $S \equiv m_{34}$ parameters. Subsequently, the tilt angle was introduced and the block off-diagonal Mueller elements included, as

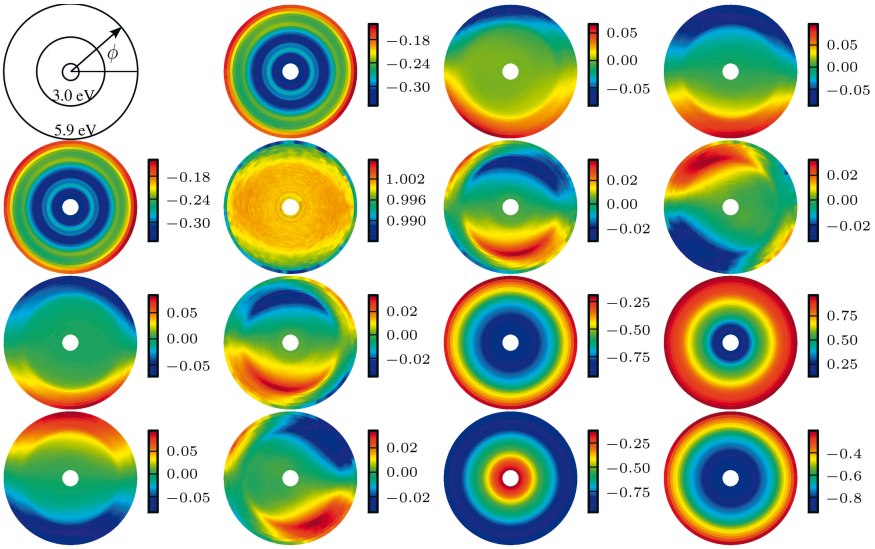

Figure 2: The measured normalized spectroscopic Mueller matrix of the sample, at 45° incidence. The data is presented in a polar plot where the radius represents the photon energy, E_{ph}, ranging from 0.73 eV (at the central white circle) to 5.9 eV (at the outer edge). The orientation of the incidence plane with respect to the cone axis is given by the azimuth orientation ϕ, as seen in the inset. The tilt axis of the cones is in the horizontal direction, towards $\phi = 0$.

they are the ones most sensitive to the optical anisotropy. The resulting best fit was found with nano-cone height 39 nm, tilt angle 4.8°, base diameter 1 (*i.e.* close-packed base) and top diameter 0.04. The experimental and simulated Mueller matrix for a selection of incidence planes are shown in Figure 3.

GISAXS patterns from four sample orientations, obtained by rotating the incidence plane (ϕ) in steps of 90°, are presented in Figure 4. An asymmetry in the scattered intensity is observed in Figures 4(a) and 4(c) for the Q_z-width of the diffraction peaks. This asymmetry is highlighted with the extracted lines shown in Figure 5. As the scattered intensity is proportional to the modulus square of the Fourier transform of the scattering objects (the "form factor"), the asymmetry in the scattered intensity patterns gives further evidence that the nano-cones are indeed slanted.

If considering the main scattering peaks as arising from the packing motif (the "structure factor") alone, a rough estimate of the mean inter-cone distances can be obtained from $d = 2\pi/Q_{xy}$, where the results for each of the four orientations are listed in table 1.

The curious "wings" above the main diffraction peaks, best visible in Figure 4(d), are another feature of interest. The "wings" also appear in the simulations (see below), and are found to originate from the form factor of the cones.

Simulations using IsGISAXS [20] were done for one of the symmetric orientation measurements (the Figure 4(d) orientation). In the simulation, the Distorted Wave Born Approximation (DWBA), including a graded interface effect, was used. The dependence between the shape and position of the cones was described using the Local Monodisperse Approximation (LMA), which assumes that the system is made of locally monodisperse domains that interfere incoherently [21]. The break down of long-range order in the lateral structure was introduced by using a 2D paracrystal model and the lateral packing of the cones was taken to be hexagonal.

Table 1: The Q_{xy} peak positions from Figure 4, and the corresponding estimated real-space distances. The distance d is longer for the symmetric orientations, (b) and (d), than for the asymmetric orientations, (a) and (c).

	Orientation	Peak position Q_{xy} [Å^{-1}]	d [nm]
Fig. 4(a)	$\mathbf{k}_i \parallel \hat{\mathbf{y}}$	0.017	37
Fig. 4(b)	$\mathbf{k}_i \parallel \hat{\mathbf{x}}$	0.015	41
Fig. 4(c)	$\mathbf{k}_i \parallel -\hat{\mathbf{y}}$	0.017	36
Fig. 4(d)	$\mathbf{k}_i \parallel -\hat{\mathbf{x}}$	0.014	44

The IsGISAXS simulations themselves do not give reliable information about the cone-height, base diameter and base angle of the cones, as it proved possible to find multiple combinations of these parameters that fit the experimental results similarly well. On the other hand, neither of these parameters correlate significantly with the cone spacing, thus facilitating extracting the inter-cone distance d from the GISAXS measurements.

The average cone separation was found from the IsGISAXS simulations to be $d = 40$ nm using a Gaussian probability distribution in the paracrystal model with standard deviation $\sigma_d = 11$ nm. Combining the cone-spacing from GISAXS with the *relative* diameters of the cones from MME, the *absolute* diameters, $D_1 = 40$ nm and $D_2 = 1.6$ nm were readily obtained. Ge-

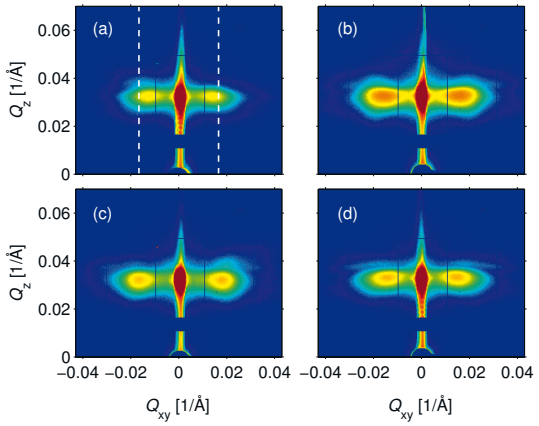

Figure 4: Experimental GISAXS patterns. The most intense peak in the centre is the specular reflection from the sample surface, whilst the peaks at each side originates from scattering by the nano-cones. In (a) the wave vector is parallel to the positive y-direction ($\mathbf{k}_i \parallel \hat{\mathbf{y}}$), in (b) parallel to the positive $x-$direction ($\mathbf{k}_i \parallel \hat{\mathbf{x}}$), in (c) parallel to the negative $y-$direction ($\mathbf{k}_i \parallel -\hat{\mathbf{y}}$) and in (d) parallel to the negative $x-$direction ($\mathbf{k}_i \parallel -\hat{\mathbf{x}}$). Note the asymmetry about the Q_z-axis as seen in (a) and (c), consistent with a tilt of the GaSb cones. The white broken lines indicate where the data in Figure 5 were taken. The intensity scale is logarithmic and the glitches with missing data-points are due to insensitive detector areas.

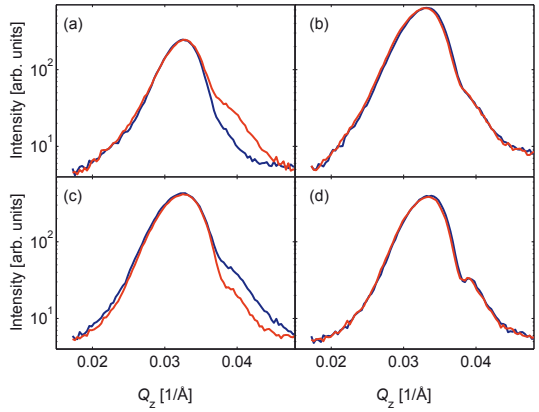

Figure 5: Extracted lines of intensity from the data shown in Figure 4, $Q_{xy} = -0.017$ Å^{-1} (red) and $Q_{xy} = +0.017$ Å^{-1} (blue). The panels (a)-(d) correspond to (a)-(d) in Figure 4. Note the full symmetry seen in (b) and (d), as opposed to (a) and (c). The intensity distribution is consistent with tilted nano-cones.

ometry then gives the value of the base angle, $\beta \approx 64°$. An IsGISAXS simulation with these parameters is presented in Figure 6, being in good qualitative agreement with the experimental data. Exploiting the sensitivity of GISAXS to in-plane structures, and the structural model parameters from MME, thus facilitate establishing a rather detailed model for the GaSb nanostructured surface, *cf.* Table 2. We emphasise that the structural information, giving an averaged model representative of an area of several mm^2 on the sample, is obtained fully by gentle physical optics methods.

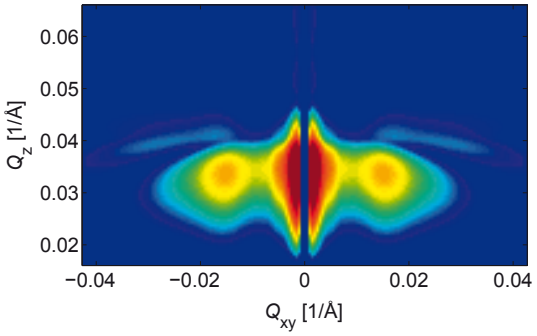

Figure 6: Simulation of GaSb nano-cones made by IsGISAXS assuming base angle $\beta = 64°$, base radius $R = 20$ nm ($\sigma_R = 3$ nm), height $h = 39$ nm ($\sigma_h = 4$ nm) and average cone separation $d = 40$ nm ($\sigma_d = 11$ nm). See text for details. The vertical line along Q_{xy} is an artefact of the simulation for $Q_{xy} \approx 0$. The simulation is in good qualitative agreement with the experimental data, *cf.* Figure 4(d).

Table 2: Parameter values from MME and GISAXS simulations.

	MME	GISAXS	Combining GISAXS & MME
h	~ 39 nm	-	~ 39 nm
θ	$\sim 5°$	-	$\sim 5°$
D_1	$1 \cdot d$	-	40 nm
D_2	$0.04 \cdot d$	-	1.6 nm
d	-	(40 ± 2) nm	(40 ± 2) nm
β	-	-	$64°$

As presented in Figure 7, the GIWAXS measurements [22] show that the sample is predominantly mono-crystalline GaSb, but with some un-oriented domains. Although a layer of surface-oxides could be anticipated on the surface, it was not observed with neither GIWAXS nor with ellipsometry.

4. Conclusion

We have demonstrated that by using the complementary techniques of MME and GISAXS large-area ($\sim$ mm^2) self-assembled nanostructured surfaces can be characterised in a non-destructive way. In this work, GaSb nano-cones produced by ion beam sputtering have been studied, finding the average structural measures of the nano-cones; height h, tilt angle θ, base diameter D_1, top diameter D_2, inter-cone distance d and base angle β as summarised in table 2.

Acknowledgements

The Research Council of Norway (SYNKROTRON programme; INFRASTRUKTUR project RECX) and The Norwegian Research Center for Solar Cell Technology (project num. 193829) are greatly acknowledged for financial support.

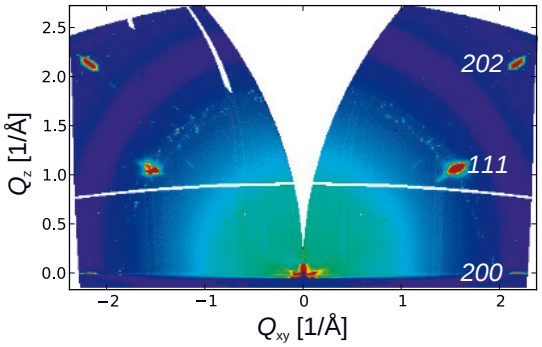

Figure 7: GIWAXS pattern obtained for GaSb nano-cones, integrated over a range of 132° in ϕ. The pattern is transformed to rectilinear reciprocal space coordinates (Q_{xy},Q_z). The *200*, *111* and *202* reflections from mono-crystalline GaSb are well-defined and intense corresponding to an oriented single crystal, whilst the faint powder-rings going through the main reflections correspond to un-oriented crystalline domains.

References

[1] S. Facsko, T. Dekorsy, C. Koerdt, C. Trappe, H. Kurz, A. Vogt, H. Hartnagel, Science 285 (1999) 1551–1553.

[2] I. S. Nerbø, S. Le Roy, M. Kildemo, E. Søndergård, Appl. Phys. Lett. 94 (2009) 213105.

[3] I. Nerbø, S. Le Roy, M. Foldyna, E. Søndergård, M. Kildemo, Opt. Express 19 (2011) 12551–12561.

[4] S. Le Roy, E. Søndergård, I. S. Nerbø, M. Kildemo, M. Plapp, Phys. Rev. B 81 (2010) 161401.

[5] D. W. Breiby, E. J. Samuelsen, O. Konovalov, B. Struth, Langmuir 20 (2004) 4116–4123.

[6] D. W. Breiby, O. Bunk, W. Pisula, T. I. Solling, A. Tracz, T. Pakula, K. Mullen, M. M. Nielsen, J. Am. Chem. Soc. 127 (2005) 11288–11293.

[7] M. H. Yan, M. J. Henderson, A. Gibaud, Appl. Phys. Lett. 91 (2007) 023104.

[8] M. Yan, A. Gibaud, J. Appl. Crystallogr. 40 (2007) 1050–1055.

[9] S. Cooil, F. Song, G. Williams, O. Roberts, D. Langstaff, B. Jørgensen, K. Høydalsvik, D. Breiby, E. Wahlström, D. Evans, J. Wells, Carbon 50 (2012) 5099–5105.

[10] L. G. Parratt, Phys. Rev. 95 (1954) 359–369.

[11] O. Plantevin, R. Gago, L. Vazquez, A. Biermanns, T. Metzger, Appl. Phys. Lett. 91 (2007) 113105.

[12] A. Keller, A. Biermanns, G. Carbone, J. Grenzer, S. Facsko, O. Plantevin, R. Gago, T. Metzger, Appl. Phys. Lett. 94 (2009) 193103.

[13] P. Kraft, A. Bergamaschi, C. Bronnimann, R. Dinapoli, E. F. Eikenberry, H. Graafsma, B. Henrich, I. Johnson, M. Kobas, A. Mozzanica, C. A. Schleputz, B. Schmitt, IEEE T. Nucl. Sci. 56 (2009) 758–764.

[14] L. Aas, M. Kildemo, Y. Cohin, E. Søndergård, Thin Solid Films (2012).

[15] M. Schubert, Phys. Rev. B 53 (1996) 4265–4274.

[16] D. W. Berreman, J. Opt. Soc. Am. 62 (1972) 502–510.

[17] M. Kildemo, I. Nerbø, S. Hagen, S. Leroy, E. Søndergård, Mat. Sci. Eng. B-Solid. 165 (2009) 217–220.

[18] I. Nerbø, M. Kildemo, S. Le Roy, I. Simonsen, E. Søndergård, L. Holt, J. Walmsley, Appl. Opt. 47 (2008) 5130–5139.

[19] I. Nerbø, S. Le Roy, M. Foldyna, M. Kildemo, E. Søndergård, J. Appl. Phys. 108 (2010).

[20] R. Lazzari, J. Appl. Crystallogr. 35 (2002) 406–421.

[21] R. Lazzari, X-ray and neutron reflectivity: principles and applications, Springer, Berlin, 2009.

[22] D. W. Breiby, O. Bunk, J. W. Andreasen, H. T. Lemke, M. M. Nielsen, J. Appl. Crystallogr. 41 (2008) 262–271.

L. M. S. Aas, , M. Kildemo, C. Martella, M. C. Giordano, D. Chiappe, and F. Buatier de Mongeot, Optical properties of biaxial nanopatterned gold plasmonic nanowired grid polarizer, Preprint, subm. to Opt. Express (2013)

Paper 12

Optical properties of biaxial nanopatterned gold plasmonic nanowired grid polarizer

Lars Martin Sandvik Aas,[1,*] Morten Kildemo,[1] Christian Martella,[2] Maria Caterina Giordano,[2] Daniele Chiappe,[2] and Francesco Buatier de Mongeot[2]

[1] *Deparment of Physics, The Norwegian University of Science and Technology (NTNU), N-7491 Trondheim, Norway*

[2] *Dipartimento di Fisica, Universita di Genova, and CNISM, Via Dodecaneso, 33, 16146 Genova, Italy*

[*] *lars.martin.aas@gmail.com*

Abstract: Gold nanoparticles deposited on self-organized nano-rippled quartz substrates have been studied by spectroscopic Mueller matrix ellipsometry. The surface was found to have biaxial anisotropic optical properties. For electric field components normal to the ripples the periodic and disconnected nature of the in plane nanowires gives rise to an optical response dominated by the localized plasmon resonance. In the direction parallel to the ripples the gold nanoparticles are aligned closely leading to localized plasmon resonances in the infrared. As Au was deposited at an angle oblique to the surface normal, the gold nanoparticles were formed on the side of the ripples facing the incoming evaporation flux. This makes the gold particles slightly inclined, correspondingly the principal coordinate system of the biaxial dielectric tensor results tilted. The anisotropic plasmonic optical response results in a strong polarizing effect, making it suitable as a plasmonic nanowired grid polarizer.

OCIS codes: (260.2130) Ellipsometry and polarimetry; (160.1190) Anisotropic optical materials; (160.3918) Metamaterials; (160.4236) Nanomaterials (250.5403) Plasmonics.

References and links

1. F. Wagner, S. Haslbeck, and L. Stievano, "Before striking gold in gold-ruby glass," Nature **407**, 691–692 (2000).
2. P. A. Letnes, I. Simonsen, and D. L. Mills, "Substrate influence on the plasmonic response of clusters of spherical nanoparticles," Phys. Rev. B **83**, 075426 (2011).
3. H. A. Atwater and A. Polman, "Plasmonics for improved photovoltaic devices." Nat. Mater. **9**, 205–213 (2010).
4. D. Smith and D. Schurig, "Electromagnetic Wave Propagation in Media with Indefinite Permittivity and Permeability Tensors," Phys. Rev. Lett. **90**, 077405 (2003).
5. A. Belardini, M. C. Larciprete, M. Centini, E. Fazio, C. Sibilia, M. Bertolotti, A. Toma, D. Chiappe, and F. Buatier de Mongeot, "Tailored second harmonic generation from self-organized metal nano-wires arrays." Opt. Express **17**, 3603–9 (2009).
6. A. Belardini, M. C. Larciprete, M. Centini, E. Fazio, C. Sibilia, D. Chiappe, C. Martella, A. Toma, M. Giordano, and F. Buatier de Mongeot, "Circular Dichroism in the Optical Second-Harmonic Emission of Curved Gold Metal Nanowires," Phys. Rev. Lett. **107**, 257401 (2011).
7. V. Robbiano, M. Giordano, C. Martella, F. D. Stasio, D. Chiappe, F. B. de Mongeot, and D. Comoretto, "Hybrid Plasmonic–Photonic Nanostructures: Gold Nanocrescents Over Opals," Adv. Opt. Mat. **1**, 389–396 (2013).
8. T. Oates, H. Wormeester, and H. Arwin, "Characterization of plasmonic effects in thin films and metamaterials using spectroscopic ellipsometry," Prog. Surf. Sci. **86**, 328–376 (2011).

9. T. W. H. Oates, A. Keller, S. Facsko, and A. Mücklich, "Aligned Silver Nanoparticles on Rippled Silicon Templates Exhibiting Anisotropic Plasmon Absorption," Plasmonics **2**, 47–50 (2007).
10. T. W. H. Oates, M. Ranjan, S. Facsko, and H. Arwin, "Highly anisotropic effective dielectric functions of silver nanoparticle arrays," Opt. Express **19**, 2014–2028 (2011).
11. S. Camelio, D. Babonneau, D. Lantiat, L. Simonot, and F. Pailloux, "Anisotropic optical properties of silver nanoparticle arrays on rippled dielectric surfaces produced by low-energy ion erosion," Phys. Rev. B **80**, 1–10 (2009).
12. M. Lončarić, J. Sancho-Parramon, and H. Zorc, "Optical properties of gold island films—a spectroscopic ellipsometry study," Thin Solid Films **519**, 2946–2950 (2011).
13. A. J. de Vries, E. S. Kooij, H. Wormeester, A. Mewe, and B. Poelsema, "Ellipsometric study of percolation in electroless deposited silver films," J. Appl. Phys. **101**, 053703 (2007).
14. E. Hecht, *Optics* (Addison Wesley, 2002).
15. A. Toma, D. Chiappe, D. Massabò, C. Boragno, and F. Buatier de Mongeot, "Self-organized metal nanowire arrays with tunable optical anisotropy," Appl. Phys. Lett. **93**, 163104 (2008).
16. L. Anghinolfi, R. Moroni, L. Mattera, M. Canepa, and F. Bisio, "Flexible Tuning of Shape and Arrangement of Au Nanoparticles in 2-Dimensional Self-Organized Arrays: Morphology and Plasmonic Response," J. Phys. Chem. C **115**, 14036–14043 (2011).
17. A. Toma, D. Chiappe, C. Boragno, and F. Buatier de Mongeot, "Self-organized ion-beam synthesis of nanowires with broadband plasmonic functionality," Phys. Rev. B **81** (2010).
18. L. M. S. Aas, I. S. Nerbø, M. Kildemo, D. Chiappe, C. Martella, and F. Buatier de Mongeot, "Mueller matrix imaging of plasmonic polarizers on nanopatterned surface," Proc. SPIE **8082**, 80822W (2011).
19. A. Toma, F. Buatier de Mongeot, R. Buzio, G. Firpo, S. Bhattacharyya, C. Boragno, and U. Valbusa, "Ion beam erosion of amorphous materials: evolution of surface morphology," Nucl. Instrum. Methods **230**, 551–554 (2005).
20. D. Chiappe, A. Toma, and F. Buatier de Mongeot, "Tailoring resisitivity anisotropy of nanorippled metal films: Electrons surfing on gold waves," Phys. Rev. B **86**, 045414 (2012).
21. R. M. Bradley and J. M. E. Harper, "Theory of ripple topography induced by ion bombardment," J. Vac Sci. Technol. A **6**, 2390–2395 (1988).
22. W. L. Chan and E. Chason, "Making waves: Kinetic processes controlling surface evolution during low energy ion sputtering," J. Appl. Phys. **101**, 121301 (2007).
23. U. Valbusa, C. Boragno, and F. Buatier de Mongeot, "Nanostructuring by ion beam," Mater. Sci. Eng. C **23**, 201–209 (2003).
24. I. Nerbø, S. L. Roy, M. Foldyna, E. Søndergård, and M. Kildemo, "Real-time in situ Mueller matrix ellipsometry of GaSb nanopillars: observation of anisotropic local alignment," Opt. Express **19**, 571–575 (2011).
25. M. Schubert, "Generalized ellipsometry and complex optical systems," Thin Solid Films **313-314**, 323–332 (1998).
26. D. Schmidt, B. Booso, T. Hofmann, E. Schubert, A. Sarangan, and M. Schubert, "Generalized ellipsometry for monoclinic absorbing materials: determination of optical constants of Cr columnar thin films." Opt. Lett. **34**, 992–4 (2009).
27. R. Azzam and N. Bashara, *Ellipsometry and Polarized light* (North-Holland, 1977).
28. T. Yamaguchi, S. Yoshida, and a. Kinbara, "Optical effect of the substrate on the anomalous absorption of aggregated silver films," Thin Solid Films **21**, 173–187 (1974).
29. T. Yamaguchi, H. Takahashi, and A. Sudoh, "Optical behavior of a metal island film," J. Opt. Soc. Am. **68**, 1039 (1978).
30. J. Spanier and I. Herman, "Use of hybrid phenomenological and statistical effective-medium theories of dielectric functions to model the infrared reflectance of porous SiC films," Phys. Rev. B **61**, 10437–10450 (2000).
31. G. A. Niklasson and C. G. Granqvist, "Optical properties and solar selectivity of coevaporated Co-Al2O3 composite films," J. Appl. Phys. **55**, 3382 (1984).
32. R. Lazzari and I. Simonsen, "GranFilm: a software for calculating thin-layer dielectric properties and Fresnel coefficients," Thin Solid Films **419**, 124–136 (2002).
33. I. Simonsen, R. Lazzari, J. Jupille, and S. Roux, "Numerical modeling of the optical response of supported metallic particles," Phys. Rev. B **61**, 7722–7733 (2000).
34. S. A. Mayer, *Plasmonics, Fundamentals and Applications* (Springer, 2007).
35. D. De Sousa Meneses, G. Gruener, M. Malki, and P. Echegut, "Causal Voigt profile for modeling reflectivity spectra of glasses," J. Non-Cryst. Solids **351**, 124–129 (2005).
36. E. D. Palik, *Handbook of Optical Constants of Solids I* (Academic, 1985).
37. M. Honkanen, V. Kettunen, M. Kuittinen, J. Lautanen, J. Turunen, B. Schnabel, and F. Wyrowski, "Inverse metal-stripe polarizers," Appl. Phys. B **68**, 81–85 (1999).
38. A. Drauschke, B. Schnabel, and F. Wyrowski, "Comment on the inverse polarization effect in metal-stripe polarizers," J. Opt. A **3**, 67–71 (2001).
39. S. Lu and R. Chipman, "Interpretation of Mueller matrices based on polar decomposition," J. Opt. Soc. Am. A **13**, 1106–1113 (1996).

1. Introduction

The optical excitation of collective oscillations of free electrons from noble metal nanoparticles, known as localized surface plasmon resonances, are known to have spectroscopic properties resulting in *e.g.* various color effects. One example is the well known "Lycurgus cup" [1], in which silver nanoparticles distributed in glass provides a different color to it depending if illumination is performed in transmission or in reflection. It is known that nanoparticle size, spacing and substrate, affects the plasmonic resonance frequency [2], and is an effective way to design selective optical properties. A recent wave of interest in plasmonics is motivated by the proven increase in photon absorption and thus in efficiency of photovoltaic devices [3] caused by the strong localization of the electric field and by enhanced scattering from the metal nanoparticles. On the fundamental level the strongly anisotropic plasmonic nanostructures are used to form metamaterials [4] with possible applications to e.g. negative refractive materials in the visible [4] or in non-linear applications [5–7].

The anisotropic optical response of plasmonic nanoparticles and metamaterials can favourably be studied by spectroscopic generalized ellipsometry, as recently reviewed by Oates *et al.* [8]. In particular, several studies of the optical properties of in plane silver nanowires on various substrates have been reported [9–11], where in particular the effective dielectric tensor of silver nanoparticle arrays on a silicon substrate was determined with spectroscopic Mueller Matrix Ellipsometry [10]. Also ellipsometric studies of isotropic and anisotropic silver and gold island films have been reported [12, 13].

In this work, we are exploring the enhanced sensitivity of Mueller matrix spectroscopic ellipsometry from the ultra violet to the near-infrared, combined with azimuthal rotation of the sample around the sample normal, using multiple angles of incidence, in order to determine the complex biaxial properties of a plasmonic layer of gold nanoparticles supported on a nano-patterned quartz substrate. Such nano-patterned plasmonic wires have many similarities to the standard infrared wire grid polarizer [14]. However, due to the localized plasmons, an inverse polarizing effect can be observed in the visible spectral range using polarized transmission spectroscopy at normal incidence [5, 15]. It has been observed that the anisotropic localized surface plasmonic properties change the polarizing properties of the sample from transverse electric (TE) to transverse magnetic (TM) [16], but the details of the dielectric tensor for such a complex plasmonic system based on aligned and partially connected gold nanoparticles have so far not been reported. The development of systematic optical methods to reveal the dielectric function of such gold based nanoplasmonic samples is further of fundamental interest due to the common use of gold nanoparticles in applications of plasmonics and metamaterials.

The samples studied in this paper was prepared by shadow deposition of gold at grazing incidence onto a quartz self-organized nano-rippled surface produced by ion beam sputtering [15], similar to samples in [17, 18].

2. Experimental

The anisotropic gold nanopatterned surfaces were prepared in a two stage process combining self-organized ion beam sputtering (IBS) to produce ripples on the surface of the quartz substrate, and gold deposition by thermal evaporation. IBS is a low cost nano-fabrication process used to pattern a range of materials from metallic to dielectric [19, 20]. A spatial modulation of the surface profile is induced by a combination of an erosive instability induced by the ion beam and energy relaxation dominated by the thermally activated diffusion and hyperthermal mobility induced by the ion beam [21, 22]. Variations of the surface morphology is made possible by changing the irradiation parameters such as ion energy, incidence angle, gas species, and sample temperature [23]. A clean quartz substrate was irradiated by Ar^+ ions in an ultra high vacuum (UHV) system at an incidence angle of 45°. The ions are ejected from a gridded multi

aperture source having an energy of 800 eV at a constant flux of 4.0×10^{15} ions/cm^{2}s. The IBS process results in a surface having well defined rippled pattern, facing the ion beam. An atomic force microscope (AFM) micrograph of such a surface is shown in Fig. 1(a). The ripples have a period of approximately $\Lambda = 70 \pm 5$ nm and an amplitude around 6 nm.

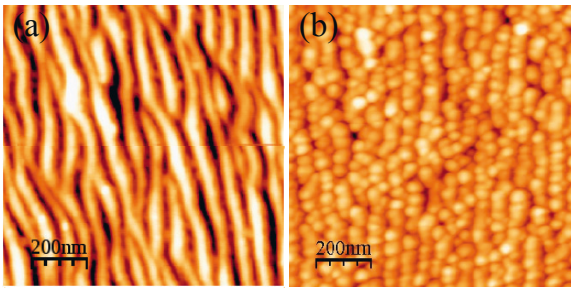

Fig. 1. (a) shows the AFM image of the glass substrate after patterning but prior to deposition of Au. (b) shows the AFM image of the surface after deposition of Au.

Gold was evaporated in the same UHV system onto the surface at a gracing incidence angle (80°), forming nanoparticles on the surface. The spatial distribution of the nanoparticles is locally modulated by the shadowing of the nanoripple ridges, such that more material is deposited onto the facing ridges. The shadowed ridge is then mainly uncovered by Au. During the deposition the distribution of particles are limited in the direction normal to the ripples. In the direction along the ripples, the particles are partially connected, forming in some cases elongated planar nanowires. Figure 1(b) shows an AFM micrograph of the nanopatterned surface.

A schematic of the cross-section of the sample system is shown in Fig. 2, where the coordinate system is aligned with the $x-$axis in the long direction of the nanowires, and the $y-z$ plane rotated by an angle θ so that the $y-$axis is in the plane of the gold nanoparticle-substrate interface. θ is in the following regarded as the tilt angle of the biaxial system. Cross-section electron microscope micrographs were not easily obtained due to the charging of the dielectric substrate. A geometrical model of the nanowires based on the AFM topographies and on the deposited amount of gold, allows to estimate the local height of the Au nanowires ($h = 29.5$ nm) measured along the z-axis and their width ($w = 72$ nm), measured along the y-axis.

For the optical characterization a variable angle multichannel dual rotating compensator Mueller matrix ellipsometer (RC2) from JA Woollam Company was used. The instrument has a collimated 150 W Xe source and operates in the spectral range from 210 nm (5.9 eV) to 1700 nm (0.73 eV), using a combination of silicon and indium gallium arsenide spectrographs having a resolution of 1 nm below 1000 nm and 2.5 nm above. The initial collimated beam has a waist of approximately 3 mm, but in the present work focusing and collection lenses with a focal length of 80 mm were applied, allowing a normal incidence spot size of 150 µm. This spot size allowed us to study a reasonably spatially homogeneous region of the sample [18].

The spectroscopic Mueller matrix was measured for the incidence angles 50° to 75° in steps of 5°. Full azimuthal rotation of the sample (360°) in steps of 5° was performed for each angle of incidence in order to fully map the anisotropy of the sample. When using focusing optics the sample alignment upon rotation is very sensitive, and was therefore adjusted prior to the measurement of each incidence angle. The same instrument was also used to measure the spectroscopic transmission Mueller matrix of the sample.

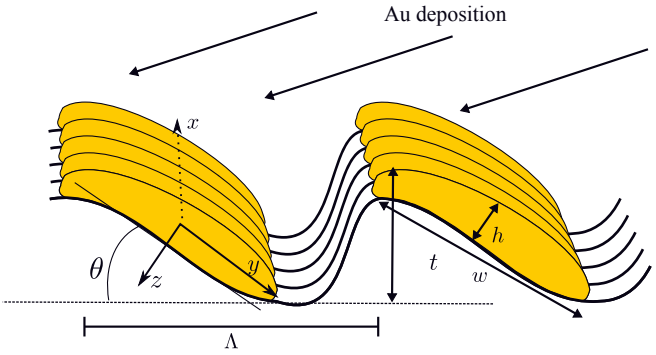

Fig. 2. The gold nanoparticles are preferentially deposited along the ridges of the quartz nanoripples. Where nucleation and agglomeration take place. Optical model based on a biaxial cartesian coordinate system where the optical axes are indicated to be aligned along the nanowires ($x-$axis), along the slope of the ripples, and normal to the ripple edge. The tilt angle θ is indicated as the local slope. The thickness of the effective layer is h.

3. Theory

With ellipsometry, the polarization nature of light is used to indirectly measure extrinsic and intrinsic properties of *e.g.* thin films, nanostructures or bulk materials [24–26]. In specific, the change of polarization state of monochromatic light upon reflection from a smooth surface can be formulated by the 2×2 complex Jones matrix transforming the incoming polarization state to the reflected by the Fresnel coefficients (r_{pp}, r_{ps}, etc.) by [27]

$$\begin{bmatrix} E_p \\ E_s \end{bmatrix}^{\text{refl.}} = \begin{bmatrix} r_{pp} & r_{ps} \\ r_{sp} & r_{ss} \end{bmatrix} \begin{bmatrix} E_p \\ E_s \end{bmatrix}^{\text{inc.}} \tag{1}$$

E_p and E_s are orthogonal plane wave electric field components, where E_p is parallel and E_s perpendicular to the incidence plane. In practical applications, in Mueller matrix polarimetry and ellipsometry in particular, the polarization state is commonly described using the four element Stokes vector

$$S = \begin{bmatrix} s_0 \\ s_1 \\ s_2 \\ s_3 \end{bmatrix} = \begin{bmatrix} I_p + I_s \\ I_p - I_s \\ I_{+45^\circ} - I_{-45^\circ} \\ I_R - I_L \end{bmatrix} = \begin{bmatrix} \langle E_{p0}(t)^2 \rangle + \langle E_{s0}(t)^2 \rangle \\ \langle E_{p0}(t)^2 \rangle - \langle E_{s0}(t)^2 \rangle \\ 2\langle E_{p0}(t) E_{s0}(t) \cos\delta(t) \rangle \\ 2\langle E_{p0}(t) E_{s0}(t) \sin\delta(t) \rangle \end{bmatrix}. \tag{2}$$

Where the elements s_0, s_1, s_2 and s_3 are time averages over electric field components resulting in the total intensity (s_0), the intensity difference between p and s polarized light (s_1), $+45^\circ$ and -45° linearly polarized light (s_2), and the right and left polarized part of the light (s_3).

The change of polarization upon interaction with a sample using the Stokes vector is described using the 4×4 element Mueller matrix. For reflection measurements of an isotropic

surface the Mueller matrix is

$$\mathbf{M}_{\text{iso}} = \begin{bmatrix} 1 & -\cos 2\Psi & 0 & 0 \\ \cos 2\Psi & 1 & 0 & 0 \\ 0 & 0 & \sin 2\Psi \cos\Delta & \sin 2\Psi \sin\Delta \\ 0 & 0 & -\sin 2\Psi \sin\Delta & \sin 2\Psi \cos\Delta \end{bmatrix}, \tag{3}$$

where Ψ and Δ are the two classical ellipsometric angles found taking the ratio of the Fresnel coefficients $r_{pp}/r_{ss} = \tan\Psi \exp(i\Delta)$, see *e.g.* Azzam and Bashara [27]. In Mueller matrix ellipsometry the Mueller matrix is measured directly, and may, for anisotropic samples, have no elements that are zero. Then the coupling between the *s* and *p* polarized light becomes important, and the corresponding Mueller matrix expressed using the Fresnel reflection coefficients from the Jones matrix (Eq. (1)) becomes

$$\mathbf{M}_{\text{aniso}} = \begin{bmatrix} \frac{1}{2}(|r_{pp}|^2 + |r_{sp}|^2 + |r_{ps}|^2 + |r_{ss}|^2) & \frac{1}{2}(|r_{pp}|^2 + |r_{sp}|^2 - |r_{ps}|^2 - |r_{ss}|^2) & \dots \\ \frac{1}{2}(|r_{pp}|^2 - |r_{sp}|^2 + |r_{ps}|^2 - |r_{ss}|^2) & \frac{1}{2}(|r_{pp}|^2 - |r_{sp}|^2 - |r_{ps}|^2 + |r_{ss}|^2) & \dots \\ \mathrm{Re}(r_{pp}r_{sp}^* + r_{ps}r_{ss}^*) & \mathrm{Re}(r_{pp}r_{sp}^* - r_{sp}r_{ss}^*) & \dots \\ -\mathrm{Im}(r_{pp}r_{sp}^* + r_{ps}r_{ss}^*) & -\mathrm{Im}(r_{pp}r_{sp}^* - r_{ps}r_{ss}^*) & \dots \end{bmatrix}$$

$$\begin{bmatrix} \mathrm{Re}(r_{pp}r_{ps}^* + r_{sp}r_{ss}^*) & \mathrm{Im}(r_{pp}r_{ps}^* + r_{sp}r_{ss}^*) \\ \mathrm{Re}(r_{pp}r_{ps}^* - r_{sp}r_{ss}^*) & \mathrm{Im}(r_{pp}r_{ps}^* - r_{sp}r_{ss}^*) \\ \mathrm{Re}(r_{pp}r_{ss}^* + r_{ps}r_{sp}^*) & \mathrm{Im}(r_{pp}r_{ss}^* - r_{ps}r_{sp}^*) \\ -\mathrm{Im}(r_{pp}r_{ss}^* + r_{ps}r_{sp}^*) & \mathrm{Re}(r_{pp}r_{ss}^* - r_{ps}r_{sp}^*) \end{bmatrix}. \tag{4}$$

When reporting Stokes vectors and Mueller matrices, they are normalized to the first (s_0 and $\mathbf{M}_{11}$) element.

Spectroscopic Mueller matrix can through the appropriate modelling be used to invert for the dispersive optical properties of thin plasmonic layers/plasmonic surfaces. Commonly available effective medium theories, such as Yamaguchi [28, 29], anisotropic Bruggeman [30] and anisotropic Maxwell-Garnett [31], do not well capture the plasmonic response of nanoparticles on a substrate. Furthermore, tabulated reference optical properties of metallic nanoparticles are uncertain. On the other hand, recent rigorous numerical approaches [2, 32, 33] require the particles to be of regular shape and regularly distributed, and in [2] not in direct contact with the substrate. However, the latter approach supplies useful physical insight into the line shape of the dielectric function. An appropriate and practical approach to extract the intrinsic optical response of the nano-plasmonic layer, is to make an anisotropic parametric dispersion model based on oscillators in order to capture the plasmonic, interband and free electron response, in addition to appropriate Euler angles to capture the possibility of a biaxial dielectric tensor with principal axes tilted away from the substrate normal. This model allows to simulate and compare to the large Mueller matrix data set. By trial an error, a reasonable set of starting parameters can be found, and finally fitted to the full data-set. As the nanowires are anisotropic, the dielectric function is a tensor with at most three orthogonal axes with different properties when assuming an orthogonal coordinate system. The inherent tilt and the truncation of the gold nanoparticles on the rippled surface, suggested a *biaxial* tensor with appropriate Euler angles. The anisotropic dispersion model approach is here used to determine the biaxial dielectric tensor and the Euler angles for the gold nanowires deposited on the quartz rippled substrate.

4. Results and discussions

Figure 3 shows the fascinating information captured by the full spectroscopic Mueller matrix recorded at 50° incidence for a complete azimuthal rotation of the sample. The Mueller matrix

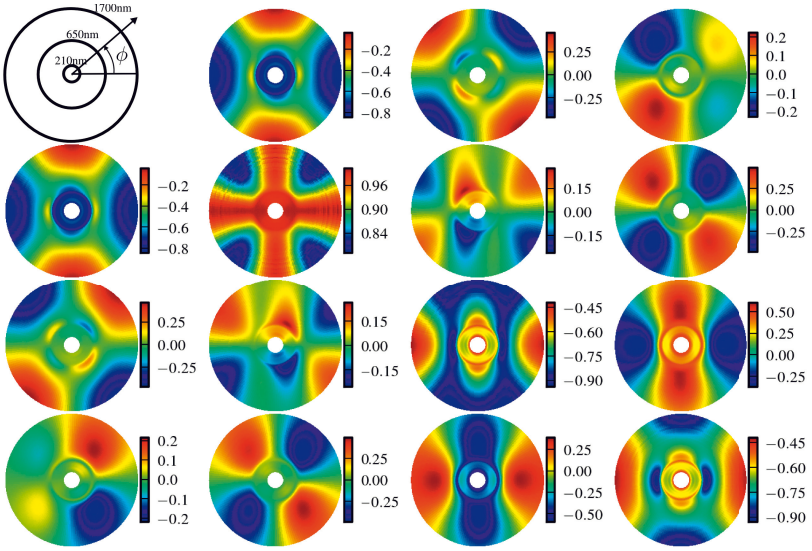

Fig. 3. A polar color map of the experimental spectroscopic Mueller matrix measured at 50° incidence. The radius correspond to the wavelength from 210 nm (5.9 eV) at the inner radius circle to 1700 nm (0.73 eV) at the outer edge. The Mueller matrix is normalized to the m_{11} element. The color bar shows the scale at each element.

is here presented as a polar color map, where the wavelength is mapped linearly to the radial direction, and the incidence plane orientation is mapped to the polar angle. The color map shows the numerical value of the Mueller matrix element at a particular incidence plane and wavelength, at the given incidence angle. The incidence plane has initially been rotated so that 0° and 90° correspond to the directions where the block off-diagonal elements are at a minimum, a close to pseudo isotropic orientation where the Mueller matrix may be approximated using Eq. (3), i.e. the incidence plane is coinciding with the long and short axis of the nanowires.

In Fig. 4 the Mueller elements m_{12}, m_{33} and m_{34}, the standard ellipsometry N, C and S parameters respectively, are plotted for these two incidence planes ($\phi = 0°$ and 90°) for the incidence angles $\theta = 50°$, 60° and 70°, as a function of photon energy. All three elements shows large differences between the two incidence planes. In particular below 3 eV the difference is largest, while for higher energies the data is similar.

The fabrication method employed leads to the formation of gold nanowires which are preferentially aligned along the side of the quartz nano ripples illuminated by the gold atom flux during evaporation, as illustrated in Fig. 2. For the optical model, localized surface plasmon resonances from strictly monodisperse noble metal nanoparticles in a well defined infinite regular array can be modelled by a Lorentzian line shape given by [34]

$$\tilde{\varepsilon}_{\text{Lor.}}(E) = \frac{A_k}{E_k^2 - E^2 - i\gamma_k E}, \tag{5}$$

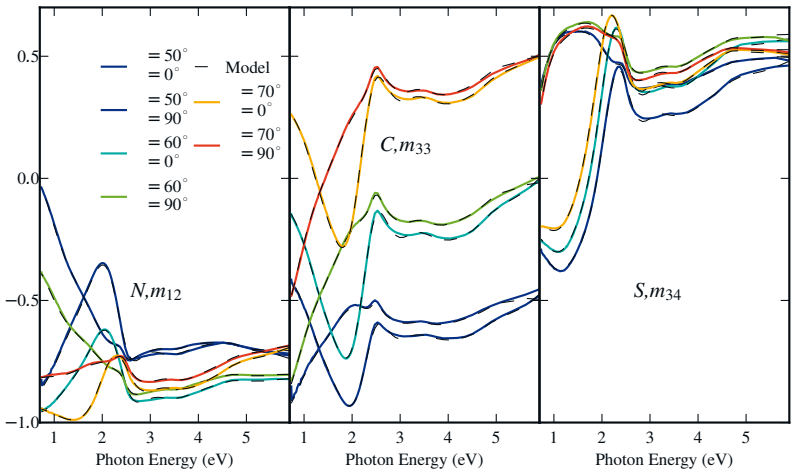

Fig. 4. The spectroscopic Mueller matrix elements m_{12}, m_{33} and m_{34} for the incidence angles 50° and 70° and incidence planes 0° and 90°. The solid colored lines show the experimental data, while the dashed black lines show the simulated data.

where A_k is the amplitude, E_k energy location, γ_k a broadening parameter and E the photon energy. Such a Lorenzian model may be readily understood also in terms of Maxwell-Garnett theory for particles within a host matrix. Normal to the local plane surface supporting the gold particles (z-direction), the model also includes a standard Drude dispersion term

$$\tilde{\varepsilon}_{\mathrm{D}}(E) = -\frac{E_p^2}{E^2 + i\gamma_k E}, \tag{6}$$

where E_p is the plasma energy and γ_k is the broadening parameter.

The self-organized formation of the nano ripples recurring to a stochastic process of sputtering may result in small variations of the plasmon resonance energy. This can be represented by a sum of Lorentzians distributed around a center energy E_k. The resulting line shape may for the imaginary part of the dielectric function then more simply be expressed by a Gaussian line shape

$$\varepsilon_{2\mathrm{Gauss.}} = A_k \left[\exp\left\{ -\left(\frac{E - E_k}{\gamma_k} \right)^2 \right\} + \exp\left\{ -\left(\frac{E + E_k}{\gamma_k} \right)^2 \right\} \right], \tag{7}$$

where the parameters γ_k is the broadening, A_k the amplitude and E_k the center energy position. Equation (7) is a sum of two Gaussians with positive and negative center energy making it an odd function which is needed for Kramers-Kronig consistency [35]. The real part of the dielectric function is calculated using Kramers-Kronig relations, and results

$$\varepsilon_{1\mathrm{Gauss.}} = A_k \left[\Gamma\left(\frac{E - E_k}{\gamma_k} \right) + \Gamma\left(\frac{E + E_k}{\gamma_k} \right) \right]. \tag{8}$$

Here Γ is a convergence series that produces the Kramers-Kronig consistent line shape.

We let the localized plasmons be described by one or several Gaussians, where each localized plasmon is denoted $\varepsilon_{\mathrm{Loc}}$. Several localized plasmons was found necessary to account for a distribution of nano particle sizes, and a distribution of connectivity between the particles. The Drude contribution ε_D is the special case of near bulk gold behaviour such as expected for completely connected nanowires. We also let, for the simplicity of the model, the interband contribution be accounted for by a Gaussian (Eq. (7)), and denote it ε_{IB}. The dielectric function for the three tensor components $q = x, y, z$ is then proposed described by:

$$\tilde{\varepsilon}^q_{\mathrm{Total}}(E) = \varepsilon^q_\infty + \sum \varepsilon^q_{\mathrm{Loc}} + \varepsilon^q_{\mathrm{IB}} + \varepsilon^q_{\mathrm{D}} \tag{9}$$

A total of 9 oscillators were needed in order to have an acceptable mean square error between the simulated and measured data for the whole spectral range, three for each orthogonal direction. The complex inverse problem was found to be most easily solved using an iterative process. First, the common ellipsometric parameters (N, C and S) were used to determine an approximate solution to the biaxial effective dielectric tensor by assuming that the principal axes of the tensor were in the sample plane. All incidence planes and the different incidence angles were used in order to increase the sensitivity to the effective properties normal to the surface (z-direction). The (N, C and S) parameters were also found to be most sensitive to the effective layer thickness, such that the first analysis supplied an estimate of the effective film thickness in addition to a first estimate to the dielectric tensor.

Upon rotation of the incidence plane it is observed from the polar plots in Fig. 3 that the block-diagonal Mueller elements have a 180° symmetry. The off block-diagonal elements, which are probing the cross polarization *i.e.* the anisotropy (cf. Eq. (4)) show a more complex behaviour. It is particularly observed that they are oscillating with a different amplitude for the maxima and mimima. The m_{23} and m_{32} elements have an additional feature at about 2.2 eV (560 nm) near $\phi = 90^\circ$ (incidence plane along the nanowires), which is strongly asymmetric. This may be explained by some randomness that can be found in the structure along the ripples by examining the AFM image in Fig. 1. Further, for $\phi = 0^\circ$ (incidence plane normal to the nanowires) the Mueller matrix is pseudo-isotropic (i.e. a diagonal Jones matrix).

The metallic nano particles on a substrate indicate that the dielectric tensor has principal axes aligned with, and perpendicular to the local surface normal. The local slope (θ in Fig. 2) is approximated to be the the Euler rotation angle for the dielectric tensor. The $z-$axis of the tensor is then no longer orthogonal to the global sample plane and does also have a component in the $y-$direction, in principle one could expect that the plasmonic resonance may also be weakly observed in this part of the dielectric tensor. The off-diagonal elements were therefore used to fit the tilt angle θ by applying an Euler rotation of the dielectric tensor. This process was repeated until convergence.

The tilt angle converged to 12.8° and the effective thickness of the nanoparticle film amounts to 28 nm. The parameters were found to have an accuracy within ± 4 nm and $\pm 2^\circ$. The parameters of the dielectric tensor is summarized in Table 1, while Figure 5 shows the real and imaginary part of the dielectric functions for the principal axes, where we have used the fitted dispersion model parameters in Table 1.

The most striking feature is the localized plasmonic absorption peak at 1.58 eV for the ε_y component (normal to the wires, but in the sample plane), although it also appears to contain an additional localized plasmonic feature around 0.9 eV. The ε_x component appears to contain strong contributions from two localized plasmons located in the IR region of the spectrum. The exact locations of these plasmons are uncertain, and may be further revealed in upcoming work using IR Mueller matrix ellipsometry. As previously mentioned, it is speculated that several such localized plasmons may be the result of incomplete connectivity within the chains of

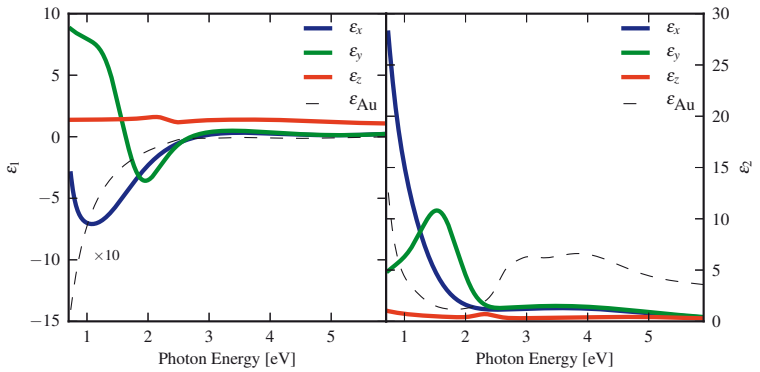

Fig. 5. The complex dielectric tensor parametrized using Eq. (9) and Table 1. The dielectric function of Au [36] is shown for comparison.

Table 1. The parametrization of the dielectric tensor of the film. The amplitudes, broadening and energy corresponds to the parameters of a Lorentzian, Drude and Gaussian line shapes in Eq. (5), Eq. (6) and Eq. (7). The blank fields indicate that the oscillator was not included for the corresponding axis.

	x			y			z			
	A_k	γ_k	E_k	A_k	γ_k	E_k	A_k	E_p	γ_k	E_k
$\varepsilon_{\mathrm{Loc1_{Gauss}}}$	53.43	0.92	0.13	8.67	0.43	1.58	0.48	–	0.20	2.33
$\varepsilon_{\mathrm{Loc2_{Gauss}}}$	–	–	–	4.30	0.68	0.87	–	–	–	–
$\varepsilon_{\mathrm{Loc2_{Lorentz}}}$	22.69	0.47	0.60	–	–	–	–	–	–	–
$\varepsilon_{\mathrm{IB_{Gauss}}}$	1.39	2.22	3.75	1.66	2.31	3.57	0.42	–	1.69	4.83
ε_{D}	–	–	–	–	–	–	–	2.47	6.58	–
ε_∞		1.41			1.41			1.43		

particles making up the ”nanowires” along the x-axis. A completely connected chain should thus be represented by the Drude model, while the reduced chain lengths may result in the IR localized plasmons. For comparison a typical dielectric function for Au is included in Fig. 5. The interband transitions in the plasmonic film are strongly attenuated compared to Au, and the plasmon resonances in ε_x, ε_y and ε_z makes $_1$ increasing in the infrared.

An interband contribution with center energy 3.75 eV and 3.57 eV was found for both the ε_x and ε_y components. The ε_z component was found to be dominated by a weak Drude component in the near infrared and some weak interband contribution with center energy 4.83 eV. Another weak localized plasmon contribution at 2.33 eV appeared in ε_z. The blue shift for the out of plane resonance follows the the results of polarizability calculations for silver hemispherical islands on MgO substrate by Lazzari and Simonsen [32]. The ε_z component also has a Drude component, which was also found for silver hemispherical nanowires supported on silicon substrate in [10], while the effective film appears much less dense than bulk gold properties. The blue shifted out of plane resonance predicted by Lazzari and Simonsen was, however, not reported by Oates *et al.* [10]. The effective thickness of the layer is probably much larger than the truncated particle thickness on the ”hills” of the ripple along the z-axis, i.e. the local surface normal. This may be correlated by the weak Drude contribution.

In Fig. 6 the measured spectroscopic Mueller matrix at 50° incidence for the incidence planes 0°, 45°, 135°, 180°, 225° and 270° is plotted together with the simulated data using the fitted parametric model. The simulated data is also plotted as dashed lines for different incidence angles in Fig. 4. The figure of merit was calculated using the root mean square error of the entire data set, where the weighting on all Mueller matrix elements and measured wavelengths in nm are the same.

In order to verify the optical model, a direct analysis of the slope distribution of the AFM image in Fig. 1(a) is performed. Fig. 7 shows a histogram of the slope in the image. It is found that the most dominant inclination is 12°-13°, which much verify the tilt angle found by Mueller matrix ellipsometry.

The polarizing properties of the sample was investigated by spectroscopic transmission Mueller matrix measurements. Figure 8 shows the measured data at normal incidence as a solid curve and the simulated data using the model from above where only the relative orientation of the sample was refitted. The simulations reproduce all features of the measurement, except a very small Gaussian like "bump" (amplitude 0.002) in the $m_{14/41}$ elements indicating an induced circular dichroism. The Mueller matrix is largely block-diagonal, meaning that the optical axis of the sample coincide with the axes of the instrument, only small deviations of a few per cent origin from sample orientation misalignment of approximately 3°.

The linearly polarizing properties are directly observed in the $m_{12/21}$ elements, and through the model, we can now observe that the main features are related to the plasmon resonances in

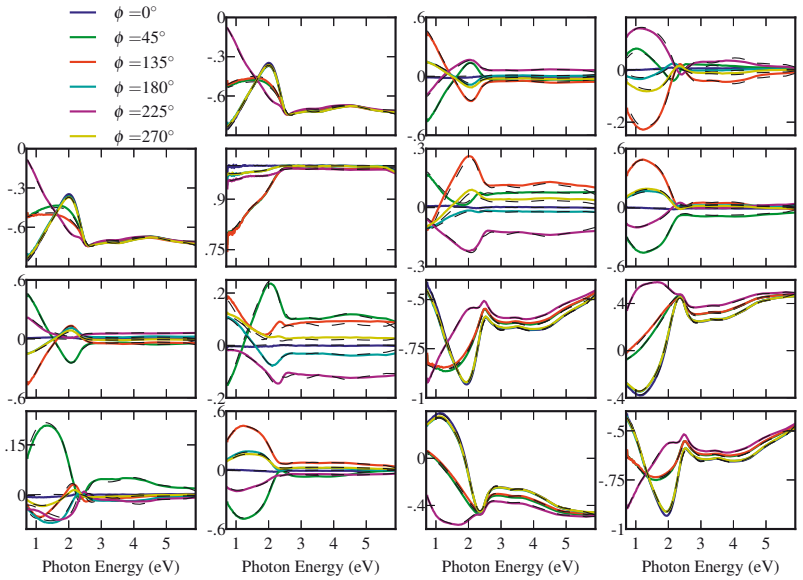

Fig. 6. The spectroscopic Mueller matrix at 50° incidence for six incidence planes (0°, 45°, 135°, 180°, 225° and 270°). The solid colored curves show experimental data, while the dashed black curves show the simulated data.

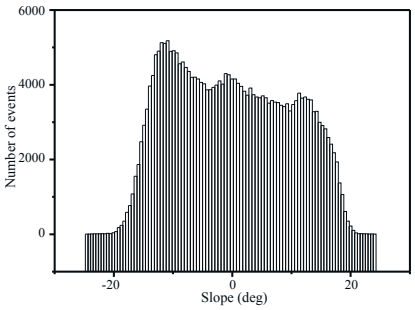

Fig. 7. Histogram showing the distribution of slope for the AFM image in Fig. 1(a).

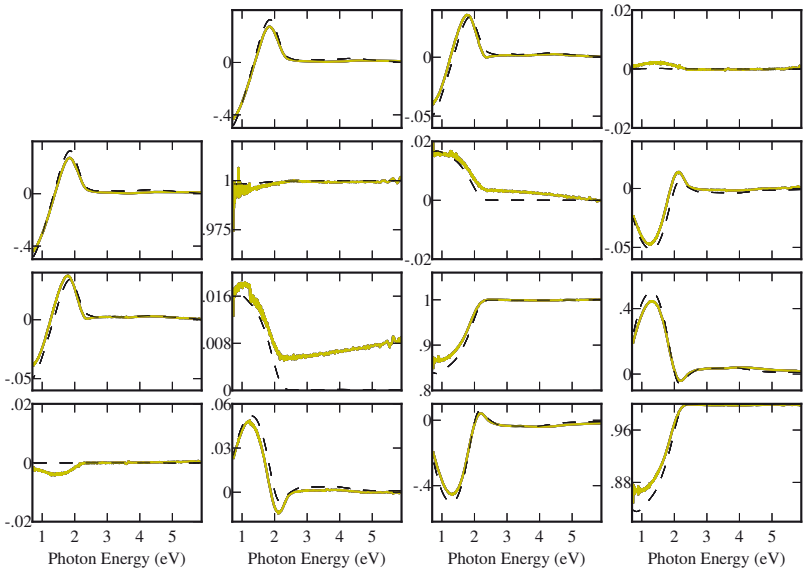

Fig. 8. Spectroscopic Mueller matrix measurement in transmission. The solid line indicates the measurement, while the dashed line is the simulated data using the model in Table 1

ε_y and ε_x.

For the y direction the transmission measurements show a peak at 1.84 eV that is the maximum in the extinction coefficient $\kappa = \varepsilon_2/2n$, where n is the real part of the refractive index $n^2 = \frac{1}{2}\varepsilon_1 + \frac{1}{2}\sqrt{\varepsilon_1^2 + \varepsilon_2^2}$. The $m_{12/21}$ elements go to negative values for the oscillator in the ε_x on the edge of the spectral range in the infrared. This anisotropy is of inverse polarizing character [37, 38], where the polarization shifts spectrally.

The features in the lower right 2×2 matrix comes from the spectral birefringence ($\Delta n = n_x - n_y$). A polar decomposition [39] of the Mueller matrix supplies the magnitude and orientation of the retarding and diattenuating (polarizing) properties. Figure 9 shows the linear retardance (δ), linear diattenuation, and the orientations of the two. It is interesting to observe that as ε_{2y} crosses ε_{2x} (see Fig. 5), the orientation of the diattenuator (polarizer) changes abruptly from x-axis to y-axis. In the infrared the sample is a polarizer with transmission axis in the y-direction (with respect to the coordinate system in Fig. 2), at ~ 1.4 eV a retarder with slow axis in the y-direction, and ~ 2 eV the sample is a polarizer with transmission axis along the x-direction. These interesting properties can in principle be shifted spectrally by varying the period of the rippled structure, and the distance between the Au nanoparticles forming the nanowire.

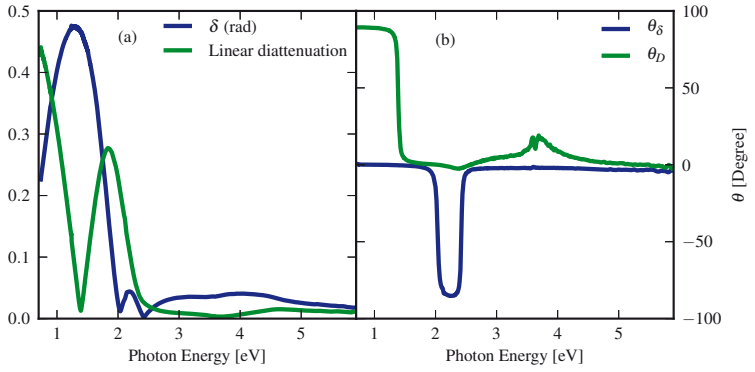

Fig. 9. The decomposed and orientation of slow axis of retardance and transmission axis of polarizer

5. Conclusion

The localized plasmonic optical properties of in plane gold nanowire array deposited at grazing incidence on a nano-rippled quartz substrate has been determined by variable angle spectroscopic Mueller matrix ellipsometry (MME) with complete azimuthal rotation of the sample. The sensitivity to the anisotropy is strong in all Mueller elements, including the elements measured in standard ellipsometry. The off block-diagonal elements show a lower symmetry, suggesting that the shadowing effects during deposition leaves the nano-wires tilted with respect to the surface normal. The dielectric tensor axes are proposed tilted by the same angle, as was found non-destructively by MME. The three components of the dielectric tensor were determined through parametric dispersion models for each component. The extracted dielectric functions complete the understanding of the observed wire-grid and inverse polarizing properties. The parametric dispersion models extracted from the effective thin surface layer com-

posed of aligned gold nanoparticles on the nano-rippled glass surface, is expected to be a useful model starting point for many similar nano-plasmonic systems. Finally, a systematic approach was proposed to attack the complex modelling issue with such a large MME data-set.

Acknowledgments

L.M.S.A acknowledges financial support from “The Norwegian Research Center for Solar Cell Technology” (project num. 193829).
This work has been partly supported by MAE under program Italia-Polonia, and by MSE in the framework of the Operating Agreement with ENEA for research on the Electric System.

Z. Ghadyani, M. Kildemo, L. M. S. Aas, Y. Cohin, and E. Søndergård, Spectroscopic Mueller matrix ellipsometry of plasmonic resonant Cu in mixed oxide nanopillars, Preprint, subm. to Opt. Express (2013)

Paper 13

Anisotropic plasmonic Cu nanoparticles in sol-gel oxide nanopillars studied by spectroscopic Mueller matrix ellipsometry

Z. Ghadyani,[1] M. Kildemo,[1,*] L. M. S. Aas,[1] Y. Cohin,[2] and E. Søndergård[2]

[1]*Department of Physics, Norwegian University of Science and Technology (NTNU), NO-7491, Norway*

[2]*Surface du Verre et Interfaces, Unit Mixte de Recherche CNRS/Saint-Gobain, UMR 125, 39 Quai Lucien Lefranc, F-93303 Aubervilliers Cedex, France*

morten.kildemo@ntnu.no

Abstract: Broadened plasmon resonances of Cu nanoparticles in nanopatterned mixed oxide sol-gel nanopillars are shown to be readily detected by spectroscopic Mueller matrix ellipsometry. The plasmonic nanomaterials are obtained by low energy ion sputtering of a CuO sol-gel film. Both s- and p-polarized plasmon resonances are present in the off-block-diagonal and the block-diagonal Mueller matrix elements as well as generalized ellipsometric parameters. The resonant features in all elements correlate with both maximum depolarization and a minimum in the reflected intensity. Analyzing the spectral position of s- and p-polarized plasmon resonances using effective medium theory provide information about the size and shape of the Cu nanoparticles as well as of the host medium.

OCIS codes: (300.0300) Spectroscopy, (120.2130) Ellipsometry and polarimetry, (250.5403) Plasmonics, (040.5350) Photovoltaic, (160.4236) Nanomaterials.

References and links

1. H. Tompkins and E. Irene, *Handbook of ellipsometry* (2005).
2. H. Fujiwara, ed., *Spectroscopic ellipsometry: principles and applications* (John Wiley & Sons Ltd., 2007).
3. N. Guth, B. Gallas, J. Rivory, J. Grand, A. Ourir, G. Guida, R. Abdeddaim, C. Jouvaud, and J. de Rosny, "Optical properties of metamaterials: Influence of electric multipoles, magnetoelectric coupling, and spatial dispersion," Phys. Rev. B **85**, 115138 (2012).
4. D. Schmidt, B. Booso, T. Hofmann, E. Schubert, A. Sarangan, and M. Schubert, "Monoclinic optical constants, birefringence, and dichroism of slanted titanium nanocolumns determined by generalized ellipsometry," Appl. Phys. Lett. **94**, 011914 (2009).
5. I. Nerbø, S. L. Roy, M. Foldyna, E. Søndergård, and M. Kildemo, "Real-time in situ Mueller matrix ellipsometry of GaSb nanopillars: observation of anisotropic local alignment," Opt. Express **19**, 571–575 (2011).
6. I. S. Nerbø, S. Le Roy, M. Foldyna, E. Søndergård, and M. Kildemo, "Real-time in situ Mueller matrix ellipsometry of GaSb nanopillars: observation of anisotropic local alignment." Opt. Express **19**, 12551–61 (2011).
7. T. Oates and A. Mücklich, "Evolution of plasmon resonances during plasma deposition of silver nanoparticles," Nanotechnology **16**, 2606 (2005).
8. I. Nerbø, S. L. Roy, M. Kildemo, and E. Søndergård, "Real-time in situ spectroscopic ellipsometry of GaSb nanostructures during sputtering," Appl. Phys. Lett. **94**, 213105 – 213105–3 (2009).
9. I. S. Nerbø, S. Le Roy, M. Foldyna, M. Kildemo, and E. Søndergård, "Characterization of inclined GaSb nanopillars by Mueller matrix ellipsometry," J. Appl. Phys. **108**, 014307 (2010).

10. L. Aas, M. Kildemo, Y. Cohin, and E. Søndergård, "Determination of small tilt angles of short gasb nanopillars using uv-visible mueller matrix ellipsometry," Thin Solid Films **541**, 97–101 (2012).
11. P. Wang, X. Zhao, and B. Li, "ZnO-coated CuO nanowire arrays: fabrications, optoelectronic properties, and photovoltaic applications," Opt. Express **19**, 11271 (2011).
12. Y. Cohin, E. Barthel, N. Brun, C. Goldman, S. Le Roy, and E. Søndergrd, "Spontaneous formation of copper-silica nanostructures by ion abrasion," Adv. Mater. (Submitted).
13. S. L. Roy, E. Barthel, N. Brun, A. Lelarge, and E. Søndergård, "Self-sustained etch masking: A general concept to initiate the formation of nanopatterns during ion erosion," J. Appl. Phys. **106**, 094308 – 094308–5 (2009).
14. S. Maier, *Plasmonics: Fundamentals and Applications* (Springer, 2007).
15. K. Willets and R. V. Duyne, "Localized surface plasmon resonance spectroscopy and sensing," Annu. Rev. Phys. Chem. **58**, 267–297 (2007).
16. P. C. Wu, M. Losurdo, T.-H. Kim, S. Choi, G. Bruno, and A. S. Brown, "In situ spectroscopic ellipsometry to monitor surface plasmon resonant group-III metals deposited by molecular beam epitaxy," J. Vac. Sci. Technol. B **25**, 1019 (2007).
17. G. F. Walsh, C. Forestiere, and L. Dal Negro, "Plasmon-enhanced depolarization of reflected light from arrays of nanoparticle dimers." Opt. Express **19**, 21081–90 (2011).
18. N. G. Khlebtsov, A. G. Melnikov, V. a. Bogatyrev, L. a. Dykman, A. V. Alekseeva, L. a. Trachuk, and B. N. Khlebtsov, "Can the light scattering depolarization ratio of small particles be greater than 1/3?" J. Phys. Chem. B **109**, 13578–84 (2005).
19. T. Oates, M. Ranjan, S. Facsko, and H. Arwin, "Highly anisotropic effective dielectric functions of silver nanoparticle arrays," Opt. Express **19**, 2014–2028 (2011).
20. J. Pérez-Robles, F. Garcia-Rodriguez, J. Yáñez Limón, F. Espinoza-Beltrán, Y. Vorobiev, and J. González-Hernández, "Characterization of sol-gel glasses with different copper concentrations treated under oxidizing and reducing conditions," J. Phys. Chem. Solids **60**, 1729–1736 (1999).
21. P. Hauge, R. Muller, and C. Smith, "Conventions and formulas for using the Mueller-Stokes calculus in ellipsometry," Surf. Sci. **96**, 81–107 (1980).
22. J. Gil and E. Bernabeu, "Depolarization and polarization indices of an optical system," J. Mod. Optic. **33**, 185–189 (1986).
23. R. Azzam and N. Bashara, *Ellipsometry and polarized light* (North-Holland, 1987).
24. M. Schubert, *Handbook of Ellipsometry* (2005), chap. Theory and Application of Generalized Ellipsometry.
25. J. Spanier and I. Herman, "Use of hybrid phenomenological and statistical effective-medium theories of dielectric functions to model the infrared reflectance of porous SiC films," Phys. Rev. B **61**, 10437–10450 (2000).
26. D. E. Aspnes, "Local-field effects and effective-medium theory: A microscopic perspective," Am. J. Phys. **50**, 704 (1982).
27. T. Yamaguchi, S. Yoshida, and A. Kinbara, "Optical effect of the substrate on the anomalous absorption of aggregated silver films," Thin Solid Films **21**, 173–187 (1974).
28. T. Yamaguchi, H. Takahashi, and A. Sudoh, "Optical behavior of a metal island film," J. Opt. Soc. Am. **68**, 1039 (1978).

1. Introduction

The spectacular properties of photonic crystals and metamaterials have spurred an increasing interest for the synthesis and characterization of complex biological and manmade nanomaterials. In many cases these materials exhibit a complex 3D organization obtained through self-assembly where objects of various composition, form and size are localized in more or less organized patterns. A systematic approach to the characterization of such materials is often a major hurdle and it hampers the progress in the synthesis. Spectroscopic ellipsometry (SE) and Generalized Ellipsometry (GE) measures the change in polarization state of light upon reflection from a surface over a wavelength range [1, 2]. SE and GE are particularly useful for investigating the pattern formation in self assembly nanostructuring processes [3–5], while for a complete measurement of anisotropic and depolarizing samples, a full Mueller matrix ellipsometry (MME) measurement is generally required. Although SE is an established technique for in line production control and real time study of thin film processes, GE and MME have recently been demonstrated as promising techniques for in-situ real time studies of nanostructuring processes [6, 7]. For example, spectroscopic MME in the visible range has been successfully utilized to investigate formation mechanism of GaSb nanopillars in ion beam sputtering of GaSb films [6, 8–10]. Furthermore, it has recently been shown that ex-situ UV-VIS-NIR spec-

troscopic MME over a complete azimuthal rotation of the sample and multiple incidence angles is highly sensitive to small tilts of nanopillars away from the surface normal [10]. The spectroscopic MME method is thus a powerful tool to characterize self assembly nanomaterials, and we here aim at extending the use of MME as an additional tool to nano-structured sol-gel materials with plasmonic nanoparticles. Indeed, such a non-destructive characterisation method, can have major advantages compared to the more commonly used direct imaging methods such as Atomic Force Microscopy (AFM), Scanning Electron Microscopy (SEM) and Transmission Electron Microscopy (TEM).

The abundance and interesting optoelectronic properties of CuO has made it an appealing choice for photovoltaic applications [11]. Self assembly of mixed oxide sol-gel film of CuO can introduce new possibilities in photonics and plasmonics. Low energy ion sputtering of CuO sol-gel film is a simple and low cost technique for fabricating a large area of dense nanopillars [12]. Variations of film temperature and ion energies result in the formation of different patterns. The nanopillar formation mechanism can partially be explained by the theory of self-sustained etching mask [13]. According to the latter theory, the metallic Cu on top of the pillars plays the role of an etching mask [12]. Indeed, real time spectroscopic ellipsometry can provide more evidences for the evolution and growth mechanism of nanopillars [6, 8, 9, 13]. Since the presence of metallic copper nanoparticles in the oxide nanopillars supports plasmonic resonances, a strong sensitivity of spectroscopic MME to these resonances can be exploited to reveal more information both about the formation mechanism, and the characteristics of the resonances.

Strong field enhancement and confinement in metallic nanoparticles at localized surface plasmon resonances (LSPR) has inspired many applications in nanophotonics [14]. The spectral position of these resonances can be measured with various spectroscopic methods [15]. The common far field method is to measure either scattering, absorption or extinction cross section over the desired spectral range. The position of LSPRs are highly sensitive to the size and shape of metal nanoparticles as well as optical properties of the host medium. Therefore, any non-uniformity in the sample, leads to broadening of the resonance over the spectral range. Thus the characterization of LSPRs in highly nonuniform self assembled samples become problematic with common methods. LSPRs are resonances in polarizability of a scattering medium, and consequently the polarization of the light scattered from this medium contains information about these plasmon resonances. As a result, ellipsometry is an appropriate tool to study the evolution of such plasmon resonances [16].

Recently, it has been demonstrated analytically and experimentally that a maximum depolarization occurs in the spectral regions of LSPRs [17], and that for anisotropic randomly oriented nanoparticles, the crossed polarized scattering events increase near the plasmon resonance region [18]. However, spectroscopic MME is the most appropriate method to fully measure the polarization properties of a complex scattering medium that show strong anisotropies [19] and is partially depolarizing. Indeed, we expect that the LSPRs will exhibit sharp resonances in both the on and off-block-diagonal Mueller matrix elements, and consequently also in the generalized ellipsometric parameters derived from the so-called Mueller-Jones matrix. Thus we expect that MME is sensitive to both the polarization, here referring to the tensor properties, and the spectral position of the plasmon resonances.

In this paper we use spectroscopic MME with azimuthal rotation of the sample to characterize the nanopillars fabricated by low ion-energy sputtering of CuO sol-gel film [12]. The fabrication and characterization methods are briefly reviewed in section 2, while the measured spectroscopic Mueller matrix elements are presented in section 3. The spectral behavior of the Mueller matrix elements near the plasmon resonance regions are further investigated in section 3. The GE parameters are utilized to further reveal the polarization characteristic of each plasmon resonance. Finally, the measured position of two sets of s-polarized and p-

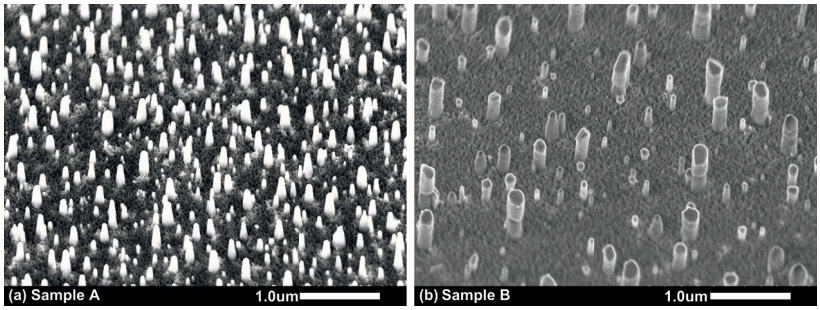

Fig. 1. SEM images of the surface of samples A and B. The view angle is 40° in both images.

polarized plasmon resonances are discussed in terms of the shape of the Cu particles inside the mixed oxide-void matrix.

2. Fabrication and characterization methods

The oxide nanopillars were fabricated by low ion-energy sputtering of a sol-gel film of mixed copper oxide and silica [12], with further details of the sol-gel procedure in e.g. Ref. [20]. The nanopillar growth is initiated when the film is heated and exposed to low energy Ar^+ ions. The pillars tend to point in the direction of the incident ion beam similar as for the formation of GaSb nanopillars reported in previous work [6, 8, 9]. In practice, the ion incidence will slightly deviate from the normal incidence (unless carefully aligned with e.g. optical methods). As a result, the fabricated nanopillars become slightly inclined and consequently the samples have small in-plane anisotropies [10]. Optical studies of two different samples with the fabrication parameters given in Table 1 are reported here.

Table 1. Fabrication parameters for the samples

Sample	Temperature °C	Flux mA cm^{-2}	Exposure time s	Ion energy kV	Pillar density μm^{-2}
A	300	0.2	360	1	10.7
B	400	0.6	120	1	3.2

Figure. 1 shows representative SEM images of the two samples. It is observed that the distribution of the pillars is spatially non-uniform. A further analysis of the corresponding AFM images, shows that the height of the pillars in sample A is normally distributed around an average value, while the height of the pillars in sample B has two (or more) populations of long and short pillars, see Ref. [12] for further details. As a result, it is expected that the plasmon resonances will be broadened in the far field.

The spectroscopic MME measurements were performed using a RC2 spectroscopic Mueller matrix ellipsometer from *J.A.Woollam Co.*. The instrument is a complete Mueller matrix system based on two rotating retarders. The illumination part consists of a 150 W Xe lamp with a source pin-hole of 100 μm and collimation optics giving an initial beam waist diameter of approximately 3 mm. The detection system consists of a combination of an InGaAs and a Si spectrograph, where the data are recorded at wavelength from 210 to 1700 nm (0.73 to 5.9 eV) with a resolution of 2 nm for wavelengths > 1000 nm, and 1 nm for wavelengths < 1000

nm. The measurements were performed using multiple angles of incidence from 45° to 70° and complete 360° rotation of the incidence plane, both in steps of 5°. Micro focusing probes of 80 mm focal length is used to limit the spot size to approximately 150 µm at normal incidence, consequently reducing the influence of spatial inhomogeneities.

3. Results and analysis

Figure 2 shows the measured spectroscopic 4×4 Mueller matrix as a polar color map where the photon energy in the range 0.73 - 5.9 eV is mapped to the radial direction, and the azimuthal angle in the plane of incidence is mapped to the polar angle. This is thus a complete presentation of the spectroscopic data with azimuthal rotation of samples A and B. In the figure, the Mueller matrices of samples A and B are plotted for incidence angles of 65° and 70°, respectively. Note that all m_{ij} elements have been normalized to the total intensity m_{11}.

It is observed that for both samples in Fig. 2, the block-diagonal elements have higher amplitudes compared to the off-block-diagonal elements, and they contain spectral features that can be mistaken as interference fringes. There are also small variations in the block diagonal elements upon azimuthal rotation in Fig. 2, but these variations are masked by the much larger amplitudes of the spectrally dependent features. On the other hand, the off-block-diagonal elements, which are nominally zero for isotropic materials and uniaxial materials with the extraordinary axis perpendicular to the sample surface, show features that appear anti-symmetric by 180° upon rotation of the incidence plane. Two sets of rings are observed in the off-block-diagonal elements. An inner ring that is typically located in the range of 1 to 3 eV and an outer ring that is typically located in the range of 3 to 5 eV.

The Mueller Jones matrix for a non-depolarizing anisotropic sample [21] shows that these rings are the result of polarization coupling between s- and p-polarized light. Furthermore, the observed 180° asymmetry is similar to the uniaxial anisotropy observed for tilted and slightly tilted GaSb nanopillars in previous work [9, 10]. In the latter case, the in plane projection of the direction of the tilt-axis resulted in an in-plane anisotropy. However, a small tilt of the low density CuO pillars should not result in an anisotropy with such large amplitudes in the off-diagonal elements. It is therefore proposed that these rings are indeed localized plasmon resonances resulting from Cu nanoparticles within the pillars. The Cu particles are directly observed in scanning transmission electron microscope images reported by Cohin et. al. [12], and they form as a combined result of the sputtering process and the substrate temperature during sputtering. Cohin et al. further reported that single-crystal Cu particle segregate to the top of the pillars, whereas the pillars were determined to be mainly of silica. The top Cu particles most likely contribute as sputtering masks in the abrasion process during the growth of the pillars. However, smaller Cu particles are also found within the pillars, while thin Cu wires were observed on one side of very long pillars. A schematic diagram summarizing the latter a-priori information is shown in Fig. 3 [12].

Having studied the symmetry of the spectroscopic Mueller matrix upon azimuthal rotation, we now focus on the spectroscopic features. We select to study the spectroscopic data for azimuthal rotations of the samples with steps of 45°, as these angles will capture most of the symmetric features observed in Fig. 2. Fig. 4 shows the upper right triangular elements of the Mueller matrix as a function of photon energy for samples A and B. The calculated depolarization index [22] is also shown in the bottom of the figure, while the total intensity is shown in the top. We observe that there is a distinct correlation between the structures in the off-block-diagonal elements $(m_{13}, m_{23}, m_{14}, m_{24})$ and the block-diagonal elements (m_{12}, m_{33}, m_{34}). There is also a certain correlation with the depolarization index and the total intensity. The positions indicated by the red lines show the maxima of the m_{33} element.

A careful comparison of the structures in the Mueller matrix elements in Fig. 4, shows that the

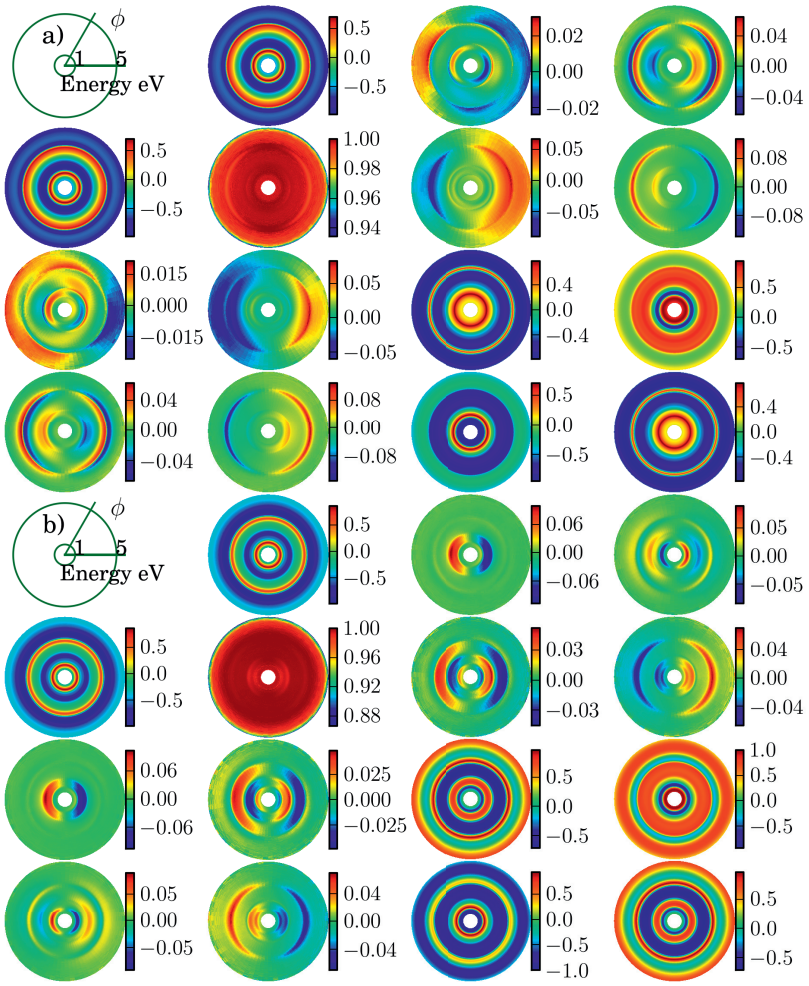

Fig. 2. Measured spectroscopic Mueller matrix for a complete 360° azimuthal rotation of the samples a) A and b) B with incidence angles of 65° and 70°, respectively. The radial and azimuthal axes correspond to photon energy and in plane rotation, respectively.

peaks in the m_{33} element correlate to the zero crossing in the m_{14} element, and simultaneously a maximum of the m_{24} element. The m_{34} element shows certain corresponding extrema. On the other hand, the m_{12} element shows a maximum and a minimum around the peaks of the m_{33} element. Furthermore, the extrema of the m_{12} element correlate to the peaks of the m_{14} element. Finally the dip in the intensity occurs at the positions of the peaks in the depolarization. It should be noted that the m_{33} element of sample B have two broad maxima between photon energies of 1.5 eV and 1.59 eV that are not resolved, and form a wide maximum in this region. However, the Mueller matrix elements follow the same trend as above at the photon energy in the center of this region, as shown by the shaded red region in Fig. 4.

These observations allow us to infer that the rings in the block-diagonal elements in Fig. 2 are also strongly related to the localized plasmons, and are not interference fringes. As a result, the oxide nanopillars studied here should not be regarded as a film on a substrate, but rather as free standing scattering particles on top of, within or on the side of oxide-pillars on a substrate. Consequently, the system is proposed to be more appropriately modelled as a combination of a scattering problem and a standard dichroic retarder for the bottom film-substrate reflection. The fully developed nano-pillars can possibly be modelled by forming the scattering Mueller matrices for the localized plasmons $\mathbf{M}_{LP}^{\text{in}}$ and $\mathbf{M}_{LP}^{\text{out}}$, in addition to the film-substrate reflection Mueller matrix $\mathbf{M}(\psi,\Delta)$, where one further assumes that for the particles, it is mainly the forward scattered light that is detected.

$$\mathbf{M} = \mathbf{M}_{LP}^{\text{out}}\mathbf{M}(\psi,\Delta)\mathbf{M}_{LP}^{\text{in}} \tag{1}$$

It is clear that a complex situation will take place during the initial phase of the sputtering process, where the sol-gel film will remain underneath the pillars, giving rise to interference fringes represented by the matrix $\mathbf{M}(\psi,\Delta)$.

The plasmon resonances are not as easily detected for all samples, as is demonstrated by sample B. Sample B has a lower density of pillars and a larger distribution of pillar heights compared to sample A, but it can still be favourably studied with MME, as shown in Fig. 4. The correlation between the m_{24} and m_{14} elements is less obvious for sample B, and similarly m_{33} only shows a single broad low energy peak. Furthermore, the depolarization appears to take place somewhat below the apparent dip in the intensity, particularly for the resonance around 2.2 eV.

With a complete Mueller matrix ellipsometer one may choose between analyzing the complete Mueller matrix, or by neglecting the depolarization, find the closest corresponding Jones matrix and study the generalized ellipsometric parameters [23, 24]. This method can be used as long as the depolarization is small. The ellipsometric parameters are defined as the ratio of the reflection coefficients of orthogonal polarization states. In isotropic materials there are no coupling between orthogonal polarization states and therefore the Fresnel coefficients r_{sp} and

Fig. 3. Sketch of the nanopillars with Cu nanoparticles on top, inside or on the side of the nanopillars [12].

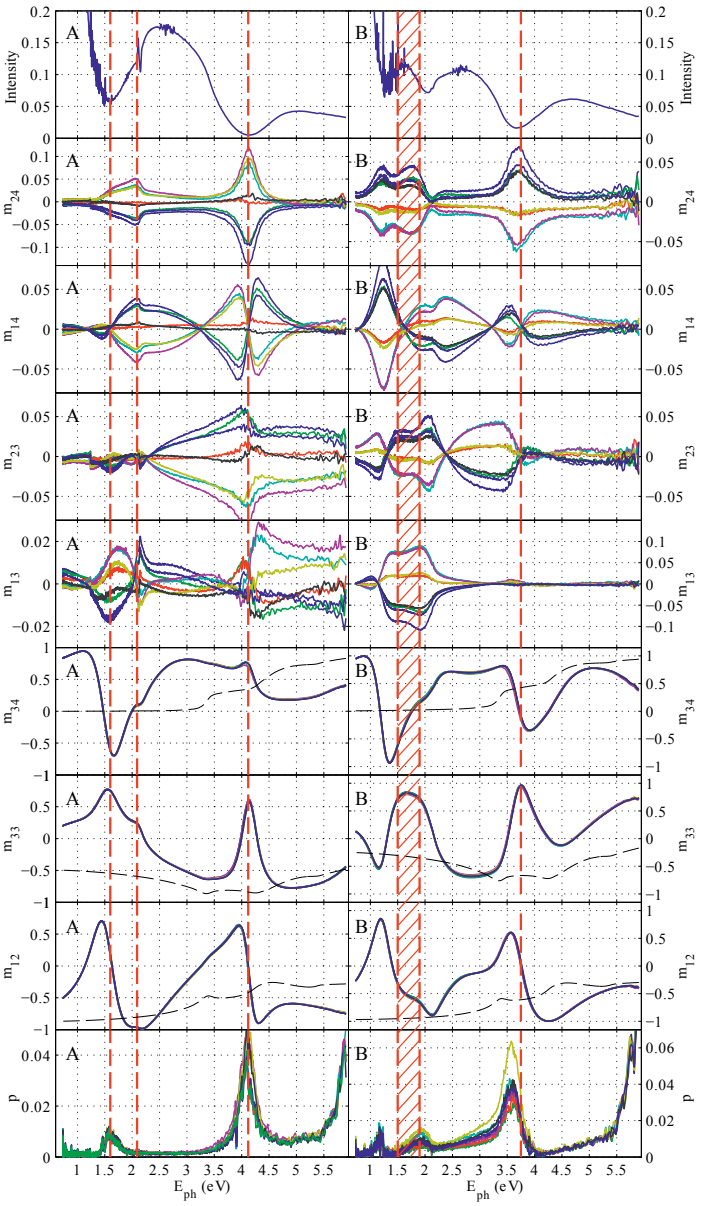

Fig. 4. Reflected intensity, selected Mueller matrix elements and depolarization factor for a complete azimuthal rotation of samples A and B versus photon energy with incidence angles of 65° for sample A and 70° for sample B. The positions indicated by the red lines show the maxima of m_{33} element and dashed black lines are calculated reflection Mueller matrix elements of c-Si substrate.

r_{ps} are zero, corresponding to zero off-block-diagonal elements of the Mueller matrix. Here r_{ps} denotes conversion from p-polarized to s-polarized light, while r_{sp} denotes conversion from s-polarized to p-polarized light. In this case the generalized ellipsometric parameters, i.e. the relative amplitudes ψ, ψ_{ps},ψ_{sp} and the phase shifts Δ, are defined by:

$$\frac{r_{pp}}{r_{ss}} = \tan\psi e^{i\Delta}, \quad \frac{r_{sp}}{r_{ss}} = \tan\psi_{sp} e^{i\Delta_{sp}}, \quad \frac{r_{ps}}{r_{pp}} = \tan\psi_{ps} e^{i\Delta_{ps}}. \tag{2}$$

Figure 5 shows the generalized ellipsometric parameters of samples A and B with azimuthal angle of 0°, where the parameter ψ basically conveys the same information as m_{12}. However, ψ_{sp} and ψ_{ps} appears to take more appropriate peak shapes that can facilitate the localization of the plasmon resonances. Due to the non-uniformity of the nanopillars in these samples, the plasmon resonances are broadened.

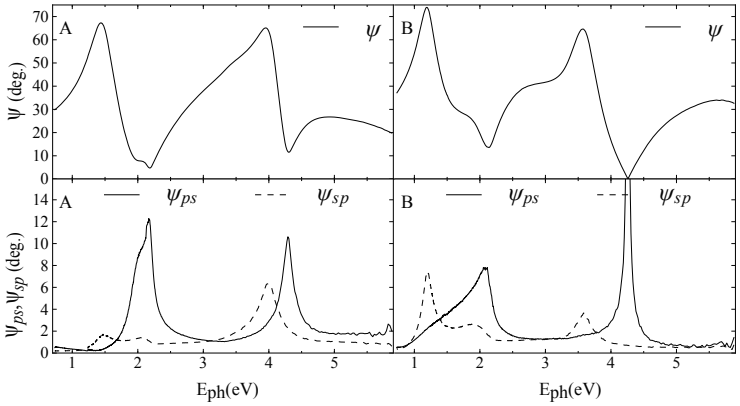

Fig. 5. Generalized ellipsometric parameters ψ, ψ_{sp} and ψ_{ps} of samples A and B for the azimuthal angle 0°. The parameters are calculated using the Mueller matrix in Fig. 4.

The data are proposed interpreted as follows. The peaks in ψ, or m_{12}, are related to dichroism as a result of the localized plasmon resonance, with the principal "absorption"-axis in the s-polarized component (perpendicular to the oxide pillars). Indeed, the maximum in m_{12} and the dip in the intensity may be understood as the combination of a Brewster effect from the c-Si substrate (working nearly as a s-polarized polarizer near the pseudo-Brewster angle) and absorption of s-polarized light. This resonance results further in a peak in ψ_{sp} which correlates to a peak in the m_{33} element, i.e. a strong retardance effect. The dips in ψ, or m_{12}, are believed to be related to a dichroism due to the localized plasmon resonance with the principal axis in the p-polarized component (here this notation is redefined to be parallel to the oxide pillars, and not along the p-component of the electromagnetic field with respect to the incidence plane). As mainly s-polarized light is reflected from the substrate near the pseudo-Brewster angle, the latter resonance only results in a minor dip in the total intensity, but gives a peak in ψ_{ps}, which also correlates to a peak in the m_{33} element.

A combined analysis of the above data, allow us to make an approximate determination of the spectral position of the modes as well as its polarization characteristics. The resonances are divided into four main resonances LP1-LP4 and their position and polarization characteristics are given in Table 2.

Table 2. Rough estimate of position of the localized plasmon resonances and their polarization characteristics for samples A and B

Sample	LP1 (eV)	LP2 (eV)	LP3 (eV)	LP4 (eV)
A	1.6 (s-pol)	2.1 (p-pol)	3.9 (s-pol)	4.3 (p-pol)
B	1-1.3(s-pol)	1.5-2.3 (p-pol)	3.4-3.7(s-pol)	4-4.3(p-pol)

Two pairs of resonances are found for both samples. For sample A, the resonances are split in a low energy resonance at 1.6 eV of principally s-character and a high energy resonance at 4.3 eV of principally p-character, a low energy resonance at 2.2 eV of p-character and a high energy resonance at 3.9 eV of s-character. Sample B does on the other hand show a large distribution of resonances, which correlates well with the analysis of the AFM and SEM images.

We infer that the observed depolarization is due to a physical effect taking place at the resonance, and not a system calibration artifact due to e.g. low light intensity, based on the following arguments. It is expected an incomplete coverage or inhomogeneous spatial distribution of the pillars and Cu particles results in a depolarization. Furthermore, small Cu particles are strongly radiating at the resonance, and some of this radiation is collected by the micro-focus lens used in the system. Depending on the radiation pattern and hence the type of scatterer, the detected light may become depolarized. This is in principle similar to including a small contribution of reflected light from the particles, which add incoherently to the forward scattered light reflected by the substrate. However, we were not able to detect such radiation with a commercial scatterometer using monochromatized white light illumination.

An accurate interpretation of the data involves scattering calculations of small anisotropic shaped metal particles that have an orientation which resembles the nanopillar orientation. However, since the particles may be on top of the pillars, inside the pillars or on the side of the pillars (Fig. 3), a rigorous determination of the resonances for such a disordered system is challenging. On the other hand, effective medium theory (EMT) can be used to explain the localization and splitting of the resonances as well as the measured anisotropy. For a phenomenological model, it is useful to consider the particle scattering matrix in terms of EMT [25–28], similar to e.g. liquid crystals. Note that the variation of the EMT proposed by Yamaguchi et al. [27,28], takes the substrate effect (here c-Si) into account. However, in the current case, the substrate effect is negligible as the Cu particles are suspended in the nano-pillars several hundred nanometers away from the substrate.

First we consider spherical Cu particles within the anisotropic host medium of an oxide pillar in air that are slightly tilted away from the sample normal. The depolarization factors along and perpendicular to the pillars are different for biaxial materials in the generalized EMT [6, 25]. Therefore, the dielectric function of the effective host medium is a tensor. Assuming the pillars to be mainly silica [12], one can then obtain two orthogonal resonance modes that are slightly split, but both located around 3.4 eV. Note that a host medium of Cu_2O, SiO_2 and air would result in a wider range of resonances and a larger splitting.

Now, we consider the case where the Cu particles take a prolate shape. We further assume that the Cu particle have the same principal axis as the surrounding oxide pillar. A s-polarized resonance defined by an absorption line perpendicular to the incidence plane is only allowed for lower energies for a disk-shaped Cu particle. In this case, the p-polarized resonance defined here by an absorption line parallel to the pillars will be shifted to higher energies. As a result, the observed low energy s-polarized resonance accompanied with a high energy p-polarized resonance must then be dedicated to disk shaped particles. On the other hand, needle shaped Cu particles parallel to the oxide pillars have p-polarized resonances located at lower energies,

accompanied with an s-polarized resonance at higher energies.

The pair of resonances at 1.6 eV (s-pol) and 4.1-4.3 eV (p-pol) for sample A are thus a result of disk shaped Cu particles, while the resonance at 2.1 eV (p-pol) accompanied with resonances around 3.9 eV (s-pol) are a result of a more needle shaped Cu particles. A similar trend can be observed for sample B, although the resonances are here smeared out due to a larger distribution of the pillar heights. The disk shaped Cu particles are on top of the pillars, i.e. acting as the self-sustained etching mask during the nanopillars growth, while the needle shape is on the side of the pillars as shown in Fig. 3.

4. Conclusion

We have shown that spectroscopic Mueller matrix ellipsometry is an appropriate far field method to investigate the broadened plasmon resonances of non-uniform self assembled samples, such as the mixed oxide nanopillars fabricated by low energy ion sputtering of sol-gel mixed oxide films containing Cu-oxide nanoparticles. Dips in the total intensity, peaks in the depolarization, peaks in m_{33}, and minima and maxima of m_{12} are observed to be correlated at the spectral position of the localized plasmon resonances resulting from Cu particles on top of, inside or on the side of the nanopillars that mainly consist of silica. Since the slight tilt of oxide pillars without Cu particles can only result in minor deviations of the off-block-diagonal elements from zero, the strong signal in these elements at the plasmon resonances is a result of the Cu nanoparticles, which further supports the interpretation of the features in the block-diagonal elements. The generalized ellipsometric parameters ψ_{ps} and ψ_{sp} exhibit clear peaks at plasmon resonance regions as a result of the slight anisotropy in the samples. These parameters present two sets of the s-polarized and p-polarized plasmon resonances. An interpretation of the position of these resonances using effective medium theory, indicates the presence of both disk shaped and needle shaped Cu particles. The strong sensitivity to the localized plasmons produced by the Cu particles in the low density nanopillar matrix, makes Mueller matrix ellipsometry a suitable technique for studying the related complex polarization phenomena. However, commercial ellipsometric thin film software appears unsuited for the exact modeling, and future work will focus on developing suitable modeling which will allow us to directly fit the lineshapes of the plasmon resonances. Finally, real time in-situ investigation using MME during the fabrication process is envisaged to reveal more details of the formation process.